Tri-layer tissue engineering heart valve based on collagen, elastin and hyaluronic acid



Zhaoying Ma

St Cross College

Department of Materials

University of Oxford

A thesis submitted for the degree of *Doctor of Philosophy*

Hilary term 2024

Acknowledgement

One thing I will miss about the PhD life is being able to enjoy research while being able to hang out with all my lovely friends when the research is not researching.

Thank you to my supervisor, Prof Jan Czernuszka, for the support and advice throughout the years, and the many fully loaded fries and good chats. Thank you to my parents, who taught me to be who I am today, who have been encouraging and not holding me back in any form despite me being the only child, and who generously funded me along this journey. Thank you to my labmates: Dr Hazal Gezmis, Dr Sasza Nabilla, Dr Ilayda Karadag, and Stephanie Budenburg for providing guidance, company, and comfort through difficult times. Thank you to Robin Scales for being THE material scientist in the building and for always helping me with my problems (they are also the co-author of my paper now!). Lastly, Thank you to my part II student from 2021-2022, Jinghao Dong, for being my best friend and being there for me, and most importantly, for teaching me to be there for myself.

Thank you to Anna Jones and David Geldbach for an amazing year of co-captaining Wolfson College Boat Club and for getting me out of my shell, Oxford would never have felt like home without them. Thank you to Reuben Boat Club for the opportunity to coach such an enthusiastic squad and for the most welcoming and supportive club culture. Thank you to Dr Ester Paolocci and Mei Takehana for the many post-outing coffee/brunch/gossip and for lighting up my gloomy days. Thank you to Sophia Ungermann for being the double agent of a materials scientist and a dedicated rowing friend and for the many amazing Live Laugh Loaf events. Thank you to many other friends I've made in the Oxford (and even Cambridge) rowing community who indulged me with endless support and encouragement.

Some rowing friends turned out to be more. Dr Alexandra Blackwell always makes me feel heard and less stressed, she also is a main supply of the courage to find myself. Juliana Mota and Oana Diaconescu provided top-tier company and community when it was

the most needed, I wouldn't know what to do with my spare time without the countless brunch, writing sessions, gym, dinners, bops, and Catan and such. Ricardo Le is always a delight to see whenever he graces Oxford with his presence, many events for sure could've been less memorable without him. Grant Rowley is the best mixed double mate there ever is, always very mindful and very demure about my steering and the tree adventures. Cumbria round two has made a comeback this year, thank you to Grant Rowley again for letting me steal his friends, Kay Gupta, Ashwin Banarsee, and Thomas Johnston, a friend group in London before I moved here is a true luxury. Lastly, Dr Filomena who wishes to remain unnamed is thanked for being my dearest friend, a role model and an inspiration, and low-ley my Oxford mum, and for truly making me a better person. And upon popular request, I would like to deeply thank everyone who fed me, without your kind invites, I would be left alone with a life of having to cook for myself, which I can but would rather not ;)))

2024.02.14

[Epilogue]

Life after first submitting my thesis was no easier, although I did manage to run two half marathons and a 10k and also went rowing in France, so I guess it wasn't too bad after all. Thanks to my mum again for flying all the way here and spending three weeks and my 26th birthday with me in Oxford. Thanks to my friends again for even more precious memories.

Most importantly, thank you to Dr Matt Rigby, for providing the needed academic and technical support for the thesis correction itself, for taking care of daily life and house chores as well as my mental health during the final week of writing, for taking up as much responsibility during the stressful time of relocating and job and life in general, for making silly puns that are actually quite funny and always make me giggle, and for being the most loving, caring, supportive partner I could ever wish for.

2024.10.15

Abstract

Valvular heart disease is one of the leading causes of death globally, nonetheless, it is treatable via clinical heart valve replacement. Between the clinically used mechanical and bioprosthetic valves, thrombosis, calcification, and incompatibility to somatic growth have been the limiting factors. Tissue engineering heart valve scaffolds, especially those constructed with naturally derived materials, have proven biocompatible and promising candidates for future-generation heart valve replacements.

Instead of the commonly used polymeric collagen, this thesis selected type I bovine atelocollagen, together with hyaluronic acid (HA) and a novel type of fibrillar gel elastin, as the scaffold-constructing materials, for the anti-immunogenicity of atelocollagen and the composition resemblance of the natural aortic heart valve extracellular matrix. The self-assembly of atelocollagen into fibrillar collagen was successfully proven, and highly porous (> 98 %) collagen-based single-layer scaffolds with desired interconnective microstructure were subsequently fabricated and crosslinked by lyophilisation and the EDC/NHS chemistry. The effect of collagen sources, crosslinking, and HA incorporation was studied in microstructure, chemical structure, and mechanical properties. It was shown that crosslinking improved the scaffold stiffness but compromised the extensibility. HA infiltration further stiffened the structure, whereas premixing HA with collagen yielded mechanically inferior structures in the non-hydrated state. Hydration was shown to drastically reduce scaffold stiffness in the self-deflection bending test.

Two designs of tri-layer scaffolds resembling the natural heart valve structurally were subsequently fabricated, with smooth interlayer transition and no visible sign of structure delamination. The average pore size ranging from 147 to 220 μm is deemed to be suitable for cell adhesion, proliferation, and differentiation. Both designs demonstrated the desired bending anisotropy in the non-hydrated and hydrated state tested by the three-point bending

test, with the bending modulus being 1208 ± 178 kPa in the with curvature (WC) direction and 1452 ± 392 kPa in the against curvature (AC) direction for non-hydrated tri-layer(ipn) scaffolds, 290 ± 48 kPa in the WC direction and 571 ± 169 kPa in the AC direction for the non-hydrated tri-layer(mix) scaffolds. Hydration reduced the bending stiffness; however, hydrated scaffolds exhibited the desired J-curve stress-strain response for biomedically oriented applications. The hydrated bending modulus tested by the self-deflection test was 5 ± 1 kPa for tri-layer(ipn) in the WC direction and 8 ± 2 kPa in the AC direction, and 4 ± 2 kPa for tri-layer(mix) WC and 6 ± 3 kPa AC.

Despite the lowering effect on mechanical properties, hydration eliminated the mechanical strength difference between the two designs, rendering them both promising candidates for future *in vitro* and *in vivo* studies. In potential future applications, the interconnected and widely distributed pore size range makes the designs suitable for a variety of biomedical applications not limited to aortic heart valve replacement. Dermal tissue engineering, for example, can benefit from the designs included in this thesis for their similar composition requirements (collagen, HA, and elastin), suitable pore size range (219 ± 34 μm) [1], and less demanding mechanical properties.

Preface

The research in this thesis was carried out by the author at the Department of Materials, University of Oxford, between October 2020 and February 2024, under the supervision of Professor Jan Czernuszka. The content of this thesis is the product of the author's work and all the assistance and resources in the completion of this thesis have been acknowledged. No part/s of this thesis has been submitted or approved for any other degree at this university or elsewhere.

Parts of this thesis were presented at an international conference:

- Ma Z., Czernuszka J., Brand D. Fabrication and Characterisation of Monomeric Type I Collagen Scaffolds as Tissue Engineering Heart Valve, Tissue Engineering and Regenerative Medicine International Society European Chapter 2023 (TERMIS EU-2023), (Abstract: PP-273), Manchester Central Conference Centre, Manchester, UK, March 28-31, 2023. (Poster presentation)

Parts of this thesis were published in a journal:

- Ma Z, Scales RJ, Brand DD, Czernuszka JT. A tri-layer tissue engineering heart valve scaffold based on atelocollagen, hyaluronic acid, and elastin. Explor BioMat-X. 2024;1:215–30. https://doi.org/10.37349/ebmx.2024.00016

Table of Contents

ACKNOWLEDGEMENT II

ABSTRACT IV

PREFACE VI

CHAPTER 1 INTRODUCTION 1

CHAPTER 2 LITERATURE REVIEW 6

2.1 Valve Development and Tissue Engineering **7**
2.1.1 Non-regenerative valves 7
2.1.2 Tissue Engineering Heart Valves (TEHVs) 11
2.2 Native Heart Valves **12**
2.2.1 The Layered Structure 13
2.2.2 Chemical Composition 18
2.2.3 Biomechanics 25
2.3 Mechanical Properties and Characterisation **28**
2.3.1 Tensile Properties 29
2.3.2 Flexural Properties 30
2.3.3 Viscoelasticity and Time-dependent Properties 33
2.4 TEHVs Construction **35**
2.4.1 Fabrication and Crosslinking Methods 35
2.4.2 Single-layer Scaffolds 40
2.4.3 Layered Scaffolds 44
2.5 Summary **46**

CHAPTER 3 FABRICATION AND CHARACTERISATION OF SINGLE-LAYER SCAFFOLDS 48

3.1 Introduction **49**
3.2 Materials and Methods **50**
3.2.1 Materials 50
3.2.2 Characterisation 53
3.3 Result **60**
3.3.1 SDS-PAGE 60
3.3.2 Fibrillogenesis 62
3.3.3 Rheology 64
3.3.4 FTIR 70
3.3.5 Microstructure 77
3.3.6 Swelling ratio 86
3.3.7 Degradation 88
3.4. Discussion **92**
3.4.1 Collagen-Elastin Layer 92
3.4.2 Viscosity and Shear Thinning 95

3.4.3 FTIR 98
3.4.4 Porosity and Pore Size 99
3.4.5 Swelling 101
3.5 Conclusion 103

CHAPTER 4 MECHANICAL PROPERTIES OF COLLAGEN-BASED SCAFFOLDS 106

4.1 Introduction 107
4.2 Materials and Methods 108
4.2.1 Viscoelasticity 108
4.2.2 Static Uniaxial Compression and Tension 109
4.2.3 Self-deflection 110
4.2.4 Statistics 111
4.3 Results 111
4.3.1 Rheology 111
4.3.2 Scaffold viscoelasticity 114
4.3.3 Compression 118
4.3.4 Tension 122
4.3.5 Bending 126
4.4 Discussion 128
4.4.1 Suspension Viscoelasticity 128
4.4.2 Scaffold Viscoelasticity 134
4.4.3 Deformation Mechanism 136
4.4.4 Effects of Modification 138
4.4.5 Bending 140
4.5 Conclusion 142

CHAPTER 5 FABRICATION AND CHARACTERISATION OF TRI-LAYER SCAFFOLDS 144

5.1 Introduction 145
5.2 Materials and Methods 145
5.2.1 Fabrication 145
5.2.2 SEM 147
5.2.3 Mechanical Properties (Non-hydrated) 147
5.2.4 Mechanical Properties (Hydrated) 149
5.2.5 Degradation 149
5.2.6 Statistics 150
5.3 Results 150
5.3.1 Pore Morphology 150
5.3.2 Viscoelasticity 152
5.3.3 Compression 154
5.3.4 Tension 157
5.3.5 Bending 159
5.3.6 Degradation 161
5.4 Discussion 162
5.4.1 Pore Morphology 162
5.4.2 Compression 164
5.4.3 Tension 171
5.4.4 Bending and the "ideal design" 172

5.5 CONCLUSION 178

CHAPTER 6 CONCLUSIONS 180

CHAPTER 7 FUTURE WORK 185

REFERENCES 191

Chapter 1 Introduction

The heart is one of the most vital organs in the human body. Yet, it is subjected to various diseases including valvular heart diseases (VHDs), including stenosis (valve narrowing causing blood flow hindrance) and regurgitation (valve weakening causing blood flow reversal). Stenosis is often caused by valve thickening or calcification for patients over 70 and largely by congenital defects for patients under 70. Regurgitation could be caused by congenital bicuspid valves, calcific degeneration, rheumatic disease, and systemic hypertension [2]. Overall, ageing and congenital malfunction are the two main reasons for the increasing VHD cases, because they both disrupt the opening and closing of the valves by introducing degeneration or calcification [3].

In the United Kingdom, around 1.5 million people aged 65 or over are diagnosed with VHDs, and estimates suggest that this number will double by 2046 and rise to 3.3 million in 2056 [4]. In the United States, 8,250,000 people suffer from VHDs each year, with the number being approximately 2.5 % of the country's population [5]. Among adults diagnosed with VHDs, 75 % experience mitral or aortic valve malfunction [6]. The current solution focuses on heart valve replacement; over 300,000 valve replacement surgeries are estimated to be performed annually around the globe [7]. Two categories of valve replacements are common clinically: the mechanical valve (about 55 %) and the bioprosthetic valve (about 45 %) [8], and the number of bioprosthetic valves required worldwide is estimated to reach 850,000 per annum by 2050 [9]. Despite being sufficiently stiff, the mechanical valves are limited by their low extensibility, the possibility of causing thrombosis, and insufficient haemodynamic properties. The bioprosthetic valves, on the other hand, are mechanically insufficient and immunogenic, and the perfect match is often required.

With the aforementioned drawbacks together and the lack of biocompatibility, both mechanical and bioprosthetic valves will eventually be outcompeted by more advanced technologies, among which tissue engineering heart valve (TEHV) is the most promising.

Being a newly emerging field, studies of TEHVs are still at an early stage. This thesis aims to develop two tri-layer TEHV designs that structurally, mechanically, and in composition mimic the natural heart valve. Instead of choosing traditional metallic or synthetic polymeric materials, natural polymers such as collagen, elastin, and hyaluronic acid (HA) are the starting materials. Additionally, atelocollagen is substituting the widely used polymeric collagen for better anti-immunogenicity. Functionally, the aortic heart valve leaflets experience the systole-diastole cycle, during which the structure is subjected to a transvalvular pressure of 12 kPa and elongations of about 31 % radially and 12 % circumferentially. Structurally, the layered structure with different components and properties of each layer is crucial to the bending anisotropic behaviour vital to the prevention of blood backflow. Mechanically, the "J-curve" stress-strain response is of great significance in allowing the structure to reach the desired elongation within the physiological stress. These biomechanics of the aortic valve leaflets serve as a guideline for this thesis.

Chapter 2 reviews the development of current heart valve replacement, drawing out the advantages of TEHVs. The key properties of the native heart valves are then summarised to understand and benchmark standards for the tri-layer designs. The chemical structure and mechanical properties of each starting material are studied, and the current development of collagen-based TEHVs is reviewed. In short words, the benchmark standards that need to be met are the suitable microstructure (interconnected pores and a suitable pore size range for cardiovascular cell activities), sufficient mechanical properties (being able to withstand the transvascular pressure and support the structure elongation, as well as displaying the "J-curve" when hydrated and has bending anisotropy), and good biological properties (physiological condition affinity, resistance to degradation, and cell affinity).

Chapter 3 focuses on the fabrication and characterisation of the collagen-based single-layer scaffolds, and the effect of collagen source, crosslinking, and HA modification are

investigated. Scanning electron microscopy (SEM), Fourier transform infrared spectroscopy (FTIR), rheometer, swelling test, and degradation test are conducted to determine the microstructure, chemical structure, flow properties, water uptake ability, and degradation resistance of the starting materials and the resultant single-layer scaffolds. Atelocollagen was proven to successfully undergo the fibrillogenesis and the scaffold fabrication process, bringing the anti-immunogenicity of atelocollagen into the design. The interconnected microstructure with widely distributed pores was achieved, creating channels for cell activity. HA was successfully incorporated using two different methods, rendering the proposed design composition more adjacent to that of the native aortic valves. The single-layer scaffolds also exhibited good water uptake abilities and decent non-enzymatic degradation.

Chapter 4 is dedicated to investigating the mechanical properties, including the viscoelastic, compressive and tensile properties in the non-hydrated state and the bending behaviours when hydrated of the collagen-based single-layer scaffolds. The effect of collagen source, crosslinking, and HA modification are further studied in a mechanical context, with the previous microstructure and chemical structure information being considered for explanation. The EDC/NHS partial crosslinking was proven to improve the mechanical properties in both the non-hydrated and hydrated states in all testing modes, however, the extensibility was compromised. HA infiltration was shown to further strengthen the mechanical properties while premixing HA and collagen resulted in far inferior non-hydrated stiffness. Nonetheless, hydration has brought the bending stiffness of the two designs to a similar level again.

Chapter 5 carries the successful production of the single-layer scaffolds further and focuses on the assembly and characterisation of two tri-layer designs with slightly different middle-layer compositions. Similar sets of characterisation are performed as the single-layer scaffolds for comparison. In addition, the bending behaviours were further investigated in

both non-hydrated and hydrated states in two directions to examine the bending anisotropy, which is desired for TEHVs. Like the single-layer components, the tri-layer designs showed the desired structure with interconnected and intact pores as well as a smooth transition between layers with no visible delamination, and the pore size and distribution are deemed sufficient in meeting the cell activity standards. The assembly of the layers has successfully introduced the bending anisotropy desired. In the non-hydrated states, the bending modulus is tested to be higher in the AC direction (1.5 ± 0.4 versus 1.2 ± 0.2 MPa for the tri-layer(ipn) structure and 0.29 ± 0.05 versus 0.6 ± 0.2 MPa for the tri-layer(mix) scaffolds); in the hydrated states, the bending moduli were reduced yet the bending anisotropic behaviours remained, with the bending moduli in the two directions ranging 4–8 kPa. The two designs are deemed to be equally suitable for TEHV applications, and both designs have shown promising conditions for cells to populate and modify their mechanical properties.

Chapter 2 Literature Review

2.1 Valve Development and Tissue Engineering

Artificial heart valves have developed from the originally used mechanical valves and bioprosthetic valves to synthetic polymer valves with adjustability (Figure 2.1), and together they are classified as non-regenerative valves due to their incapability to regenerate. Furthermore, studies including this thesis on natural polymer-based valves under the concept of tissue engineering shed light on a new potential valve replacement. This section will first focus on the advantages and disadvantages of the three non-regenerative valves, then the emphasis will be redirected to tissue engineering and TEHVs.

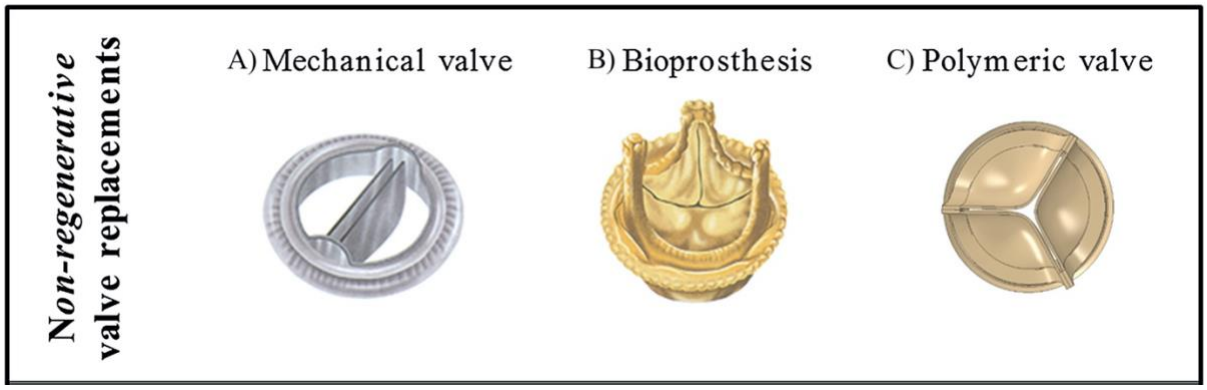


Figure 2.1 Illustration of the three types of non-regenerative valves [8].

2.1.1 Non-regenerative valves

As the name suggests, the mechanical valves focus on mimicking the native heart valves (NHVs) in mechanical functions. Figure 2.2 organises the development of various mechanical valve designs over time. To avoid the gross enlargement, distortion, and actual fragmentation of the ball-in-cage design, a study proposed a lightweight titanium ball design with a mirror-like finish to minimise the fibrin deposit. The lighter-than-blood weight ensured no inertial delay in the opening and closing, and the design was proven to have great flow dynamics both *in vitro* and *in vivo* [10]. However, compared to the ball valves, disc valves were reported to interfere less with myocardial contraction and less prone to complications. A study then presented the Kay-Suzuki disc valve with the optimal ratio of the orifice area to the frustum

area being 1 to 1.5, effectively lowering operative mortality and lessening thromboembolism incidence, demonstrating superior physiological response than the Starr-Edwards ball valves [11]. A more advanced design bi-leaflet valve later gradually replaced the ball valves and disc valves, however, the fast valve closing speed resulted in extremely high local reverse flow, increasing the risk of thromboembolic complications. One recent study therefore reported a tri-leaflet design with favourable haemodynamic behaviour that was reported to address this issue [12]. Despite the occasional innovations, the mechanical valve development has stagnated since the 70s, due to the lack of optimal biocompatibility.

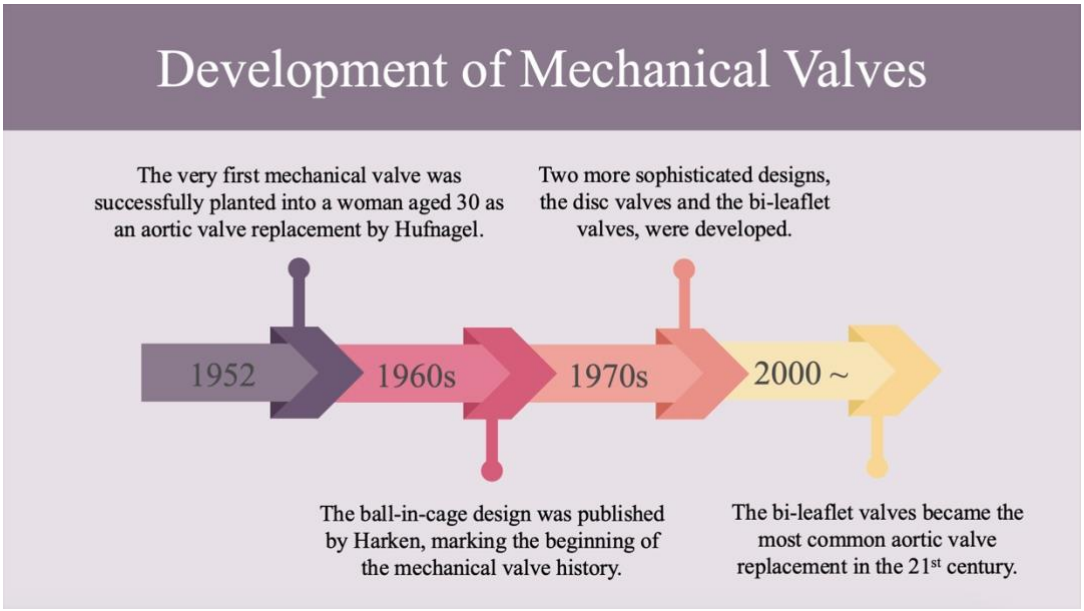


Figure 2.2 The timeline of mechanical valve development [13–15].

The bioprosthetic valves are categorised into three types: the homograft, the allograft (or the autograft), and the xenograft. The donor and the acceptor tissues originate from the same species in homograft, whereas in xenograft both tissues are sourced from different animal types. Allograft, on the other hand, focuses on an individual level; that is, the grafted tissue is to be obtained from the patient themselves. The first bioprosthetic valve implantation succeeded in 1965 with a glutaraldehyde-fixed porcine aortic valve [16]. Two years later, the Ross procedure replaced a patient's pulmonary valve with a xenograft while autografting the original pulmonary valve as the patient's aortic valve replacement [17,18]. Due to degradation

and failure, bioprosthetic valves sometimes need reoperation, and transcatheter aortic valve-in-valve implantation is an emerging therapeutic alternative [19]. In alleviating the patient/prosthesis mismatch issue often found in valve-in-valve implants, the Bioprosthetic Valve Fracture method was reported successful [20]. Moreover, the BASILICA procedure where the old leaflet is sliced when the new valve is put in can be adopted to reduce the coronary obstruct [21]. All these emerging technologies revolving around bioprosthetic valves keep this replacement method in the clinical market; however, the long-standing calcification and higher incidence of thrombosis with the valve-in-valve designs limit the broader application of bioprosthetic valves [22].

Compared to metals and biological materials, polymers exhibit excellent tunability towards their mechanical properties, microstructure, and swelling degree through material selection, molecular weight distribution control, crosslinking, and modification. Therefore, synthetic polymer valves are promising in meeting the different individual requirements of patients. Additionally, synthetic polymers are less subjective to calcification due to their chemical inertness and lack of calcification-inducing elements [23], and they can be designed to be fatigue and failure-resistant. Although a polyurethane (PU) valve was among the first implanted valves into human bodies [24], it wasn't until recent years that the development of polymers showed potential to prolong the material durability. A few polymeric valves using polytetrafluoroethylene (PTFE) and expanded PTFE (ePTFE) were reported to be successful in bicuspid and tricuspid forms to have good durability and flexibility, yet were still subjective to increasing pressure gradient, stiffness, and limited application in the paediatric population [25]. The triblock copolymer of styrene and isobutylene (SIBS) was studied to perform better *in vitro*, with better cell adhesion and proliferation performance than ePTFE and better calcification resistance [26]. Admittedly, polymeric valves are promising candidates in valve replacement surgeries, yet there has yet to be a design that combines the required

biocompatibility, hemocompatibility, anti-thrombogenicity, degradation and calcification resistance, and good endothelial cell affinity [27].

Mechanical valves		
Materials	**Advantages**	**Disadvantages**
titanium stainless steel nylon	traditional rigid materials with high moduli lifespan of over 20 years	insufficient haemodynamic properties thrombosis: life-long treatment, limited activities pregnancy: anomalous foetus development
pyrolytic carbon	biocompatible and resistant to thrombosis	low fracture toughness and extensibility (< 1 %)
Bioprosthetic valves		
Valve type	**Advantages**	**Disadvantages**
bioprosthetic	native heart valve structure desired haemodynamic low thrombosis rate and biocompatible	insufficient mechanical strength and short lifespan immunogenic and possibly infectious limited quantities and requires perfect match
decellularized	reduced immune reactions	calcification and compromised mechanical strength
Synthetic polymer valves		
Materials	**Advantages**	**Disadvantages**
PU	biocompatible with low biodegradation rate adjustable moduli and good viscoelasticity resistant to hydrolysis and oxidation	susceptible to thrombosis and calcification material failure by cracking material degradation by oxidation and hydrolysis
PTFE	haemodynamic properties	susceptible to thrombosis and calcification subjective to tearing and stiffening
SIBS	good mechanical properties	subjective to calcification, creep, and failure
biodegradable elastomers	sufficient mechanical strength controlled biodegradation rate cytocompatibility and hemocompatibility low inflammatory and non-toxic	subjective to hydrolysis short life circle
hydrogel	mechanically tuneable	limited application

Table 2.1 The advantages and disadvantages of non-regenerative valves [28–34].

The advantages and disadvantages of the non-regenerative valves are summarised and listed in Table 2.1. From the author's perspective, mechanical valves have the dominant advantage of providing robust and long-lasting support, which is challenging for most bioprosthetic and polymeric valves. The early-developed types were reported to cause thrombosis, yet the use of pyrolytic carbon was proven to alleviate the issue. Sourced from

biological donors, the bioprosthetic valves have a bio-mimicking structure more recognisable to cells and better flexibility than the traditionally used metallic ones in mechanical valves. However, issues such as calcification, the need for reoperation, and the inducing of immunogenic response remain to be overcome. The most promising of the three is the polymeric valve for its tunability based on adjustable molecular weight, crosslinking density, and microstructure, yet the lack of biodegradability from most of the synthetic polymers still introduces immunogenic response and potential thrombosis from poor hemodynamics. That being said, the non-regenerative valves all share proven success in clinical applications for being mechanically sufficient, and emerging engineering designs to address the aforementioned issues caused by materials alone.

2.1.2 Tissue Engineering Heart Valves (TEHVs)

Despite the wide application clinically, the non-regenerative valves face a major limitation of their incapability in regeneration. This hinders their clinical application in younger patients, as they cannot keep up with the somatic growth. Therefore, new concepts need exploration to tackle this challenge, which led to the development of tissue engineering. The main concept of tissue engineering is to rely on cells either pre-embedded onto the scaffold before implantation or *in-situ* migrated onto the scaffold after implantation to generate new tissues. The cells at the same time would feed on the implanted scaffold and gradually degrade it, leaving no foreign materials eventually. Biodegradable synthetic polymers such as polylactic acid (PLA) and polyglycolide (PGA) are reported to be promising starting materials for TEHV construction, yet natural polymers like collagen, elastin, and glycosaminoglycans (GAGs), compositions of native human extracellular matrix (ECM), are preferred for their superior *in vivo* biocompatibility.

In general, a few other requirements are to be met for TEHVs other than biocompatibility, for example, somatic growth ability, non-thrombogenicity, non-immunogenicity, and suitable physical, chemical, and mechanical properties [17]. Of all required properties, three are of great significance: biocompatible surfaces favouring and promoting cell activities (including proliferation, migration, and alignment), abundant biomechanical strengths supporting new tissue growth, and a degradation rate matching the regeneration rate of the new tissue [35,36]. In simpler words, the key to a successful TEHV fabrication is to mimic the mechanical properties, the biological properties, and the microstructure (haemodynamic properties) of the native valves. This thesis is going to focus mostly on the microstructure, mechanical properties, and other physical and chemical properties as a proof-of-concept study for potential future studies on the biological front.

2.2 Native Heart Valves

Heart valves are categorised into the atrioventricular and semilunar valves based on their locations. As shown in Figure 2.3, the atrioventricular valves, including the tricuspid and mitral valves, are situated between the atria and ventricles, and the semilunar valves including the aortic and pulmonary valves sit at the base of the aortic and pulmonary arteries. The aortic valve, being the target application of this thesis, has three half-moon-shaped leaflets symmetrically arranged, each of which has one end connecting to the artery wall and the other free to coapt with the other two leaflets, preventing the backward blood flow during diastole.

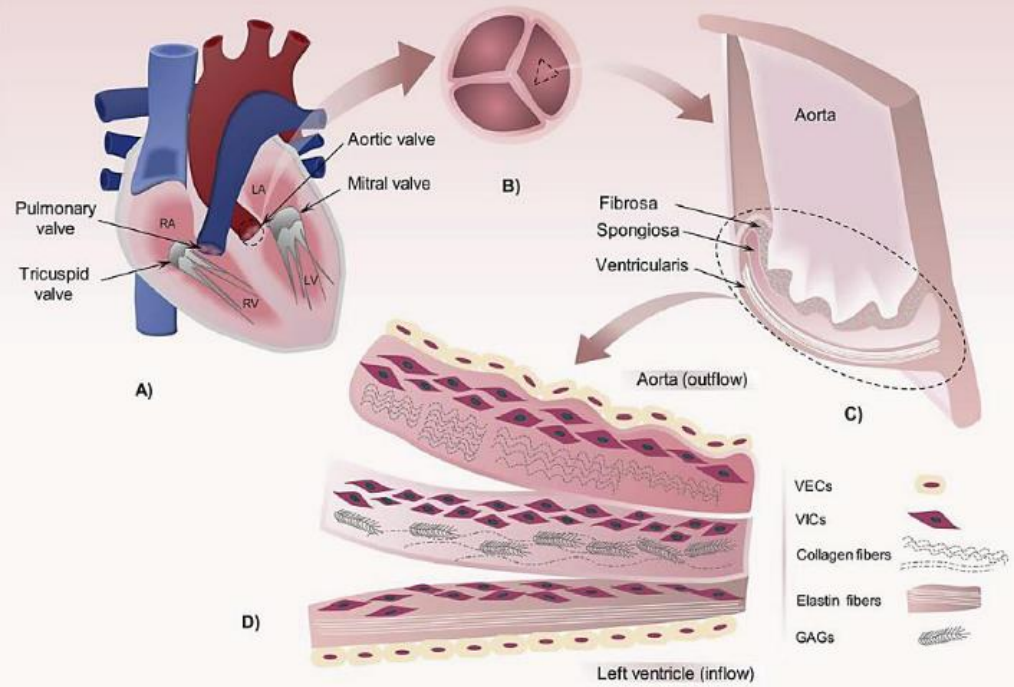


Figure 2.3 Illustration of a) the four types of heart valves and their locations, b) the aortic valve constituting the three symmetrically distributed half-moon-shaped leaflets, c) the layered structure of one aortic valve leaflet and the corrugated structure of the fibrosa, and d) the chemical and cell composition of each layer [37].

2.2.1 The Layered Structure

Three distinct layers are found to constitute the aortic valve leaflet: the fibrosa, the spongiosa, and the ventricularis. The fibrosa is the layer closer to the aorta surface while the ventricularis faces the ventricle, and the spongiosa sits as the middle layer. Several studies have successfully measured the thickness of each layer of porcine and human aortic valve leaflets, and the data and details are organised in Table 2.2. As can be concluded, different methods and sample types were employed, which resulted in slightly different layer thickness. Nonetheless, a tri-layer heart valve scaffold design with equal thickness for each layer is a good starting point.

Sample	**Pretreatment**	**Thickness**					
			F	**S**	**V**	**C**	**Condition**
6 porcine valves young (~10 months)	sliced (belly region) GA-fixed	%	33	57	10		stained

6 porcine valves	fresh and intact	mm (%)	0.26 (35)	0.22 (30)	0.26 (35)	0.73	CPS
	CPS or distilled water	mm (%)	0.39 (34)	0.41 (36)	0.35 (30)	1.15	distilled water
18 human valves from 6 autopsy male/female: 5/1 age 18-42	vertically sliced central of each cusp 10% formalin-fixed embedded in paraffin	mm (%)	0.25 (33)	0.36 (48)	0.14 (19)	0.75	middle
		mm (%)	0.57 (43)	0.48 (37)	0.26 (20)	1.20	base
13 porcine valves	intact and fresh	mm (%)	0.3 (36)	0.23 (27)	0.32 (37)	0.81	CPS
4 porcine valves	sliced (belly region)	mm	0.16 (41)	0.12 (30)	0.11 (29)	0.39	PBS
120 porcine valves	split spongiosa fresh or GA-fixed fixing before split fixing after split circumferentially radially	mm	0.42		0.21		fresh-cir
		mm	0.37		0.19		fresh-rad
		mm	0.34		0.22		fixed-cir
		mm	0.29		0.20		fixed-rad
		mm	0.37		0.17		intact-cir
		mm	0.40		0.21		intact-rad

Table 2.2 The thickness value and percentage of the fibrosa (F), the spongiosa (S), the ventricularis (V), and the entire cusp (C) were summarised from six different research. Glutaraldehyde (GA), coronary perfusion solution (CPS), and phosphate buffer saline (PBS) are abbreviated. In the last research, "fixed" refers to the samples that were fixed after dissection, and "intact" the samples that were fixed first and then had layers separated [38–43].

2.2.1.1 Fibrosa

The fibrosa serves as the main load bearer in the circumferential direction. Vesely et al. measured the stress-strain response of the separated fibrosa, and Young's modulus was calculated to be 13 ± 5 kPa at a stress of 300 kPa [44]. The result matched his earlier finding, where Young's modulus of fresh porcine aortic valves was tested to be 13 ± 2 kPa under the same conditions [45]. The high stiffness can be attributed to the structural composition of the layer, where a dense pack of circumferentially arranged collagen fibres can be observed. Collagen is the provider of tissue stiffness; therefore, its fibre orientation affects the elastic behaviours of the tissues. When radially aligned, Young's modulus of the heart valve is 5 ± 2 kPa, much less compared to its circumstantial counterpart due to fewer oriented collagen bundles [44]. It is, however, still worthwhile to mention that there exists collagen fibre

alignment in other directions; therefore, the data obtained from the uniaxial tensile test may only serve as a guide on a magnitude level when it comes to understanding the elasticity of the fibrosa.

The same study also shed light on the extensibility of the fibrosa. The failure strain was reported to be 19 ± 5 % circumferentially and 28 ± 10 % radially [44]. Lee et al., however, reported the radial failure strain of fresh porcine aortic valves to be 62 ± 3 %, marking a significant inconsistency [46]. This difference is assumed to result from the corrugated conformation of the layer, which only exists in its physiological conditions, which was only the case in Lee's study. In the native environment, valve leaflets unload during the systole, leaving the fibrosa layer under compression and the collagen bundles inside highly undulated [42]. The corrugated fibrosa can stretch to match the extensibility of other layers, yet this unique characteristic was lost when the layers were separated and flattened during Vesely's study, resulting in inconsistency in the extensibility.

2.2.1.2 Ventricularis

The ventricularis provides the necessary radial extensibility for valves to efficiently open and close. The failure strain of this layer goes up to 63 ± 20 % measured by Vesely [44]. The result matches that of the fresh porcine aortic valve tissue (62 ± 3 %), indicating that the ventricularis dominates the stretching behaviour of the whole valve leaflet [46]. This behaviour in the radial direction originates from the radially oriented elastin fibres, which act as the elasticity contributor [47]. The circumferential extensibility, on the other hand, does not vary much from that of the fibrosa (22 ± 7 % versus 19 ± 5 %), suggesting a matching stretching ability that allows the layered leaflet to function as a whole [44]. The high extensibility and low hysteresis enable the ventricularis to mitigate radial strains [48], therefore giving this layer a physiological role of bearing compressive forces [49].

With the fibrosa carrying the most circumferential loads, Young's modulus of the ventricularis in this direction is only 7 ± 2 kPa, about half of that of the fibrosa [44]. The radial loads, on the other hand, are split and shared equally between the two layers, which is corroborated by the close radial Young's modulus data (5 ± 2 kPa for the fibrosa and 3.7 ± 0.6 kPa for the ventricularis) [44]. This similarity in elastic moduli of these two layers indicates that the proportion of radially aligned collagen fibres is of the same level, which also suggests that the ventricularis contains not only radially arranged elastin but also some collagen fibres [47]. These collagen fibres are still more circumferentially oriented, resisting undesired deformation by reorienting in the loading direction; this mechanism limits the extension of the elastin fibres and provides a certain level of strength.

2.2.1.3 Spongiosa

The spongiosa has a hydrated and gelatinous structure and is comprised of mostly hydrophilic GAGs (resulting in the gelatinous structure) and some randomly aligned collagen fibres [42]. Due to the lack of organised collagen or elastin fibres, the spongiosa layer provides no noteworthy influence on Young's modulus and extensibility of the leaflet. However, with the GAGs being highly hydrophilic and negatively charged, the layer can trap a large amount of water, introducing other essential functions [50]. With further investigation into the biomechanical role of this layer, it is widely accepted that the spongiosa is indispensable in the reduction of shearing, allowing relative movements between the fibrosa and the ventricularis in the prevention of delamination and the damping of the shocks generated during the systole-diastole cycle [51].

Talman et al. related the leaflet shear modulus to the hydration and stretching extent of the spongiosa by comparing the moduli tested under different strains between porcine leaflets treated with the high-concentration low-molecular-weight dextran solution

(dehydrated) and the Hank's solution (physiological) [52]. As the data summarised in Table 2.3 suggests, the shear modulus is higher when deprived of water. Moreover, further stretching (increased strain) improved the shear modulus as well. This experiment was conducted on the whole leaflet rather than on the separated layers, which further demonstrates that the changes in shear properties are predominantly attributed to the hydrated spongiosa layer [52].

Strain	0	0.25	0.50
Shear modulus, physiological (kPa)	0.54	1.05	2.89
Shear modulus, dehydrated (kPa)	2.79	3.93	6.32

Table 2.3 The shear moduli (kPa) under different strains (0, 0.25, 0.50) of the dehydrated and physiological porcine aortic valve leaflets [52].

The shock-dampening effect of the spongiosa can be quantified by its hysteresis, which describes the energy dissipation within the tissue. Talman et al. found out that the porcine valve leaflet has a lower hysteresis under physiological conditions than being rid of water (44 ± 2 % versus 68 ± 3 %), indicating that the water-absorbing layer could be responsible for the better shock dampening of the leaflets [52]. Eckert et al. explored the role of the spongiosa by removing its main component using enzymes and putting it under planar tension as well as flexion [53]. Figure 2.4 suggests that the spongiosa has no detectable influence on the stretching properties in both circumferential and radial directions and no significant difference between the tensile hysteresis under physiological tensile stress (90 N/m) and low tensile stress (10 N/m), which supports the assumption that the spongiosa has little effect on the elastic behaviours of the leaflets. However, the flexure tests yielded the result that when loaded within a low-force range, the hysteresis reduced from 36 ± 3 % to 25 ± 2 % after enzymatic removal of the GAGs, confirming that the dampening function of the spongiosa under flexion.

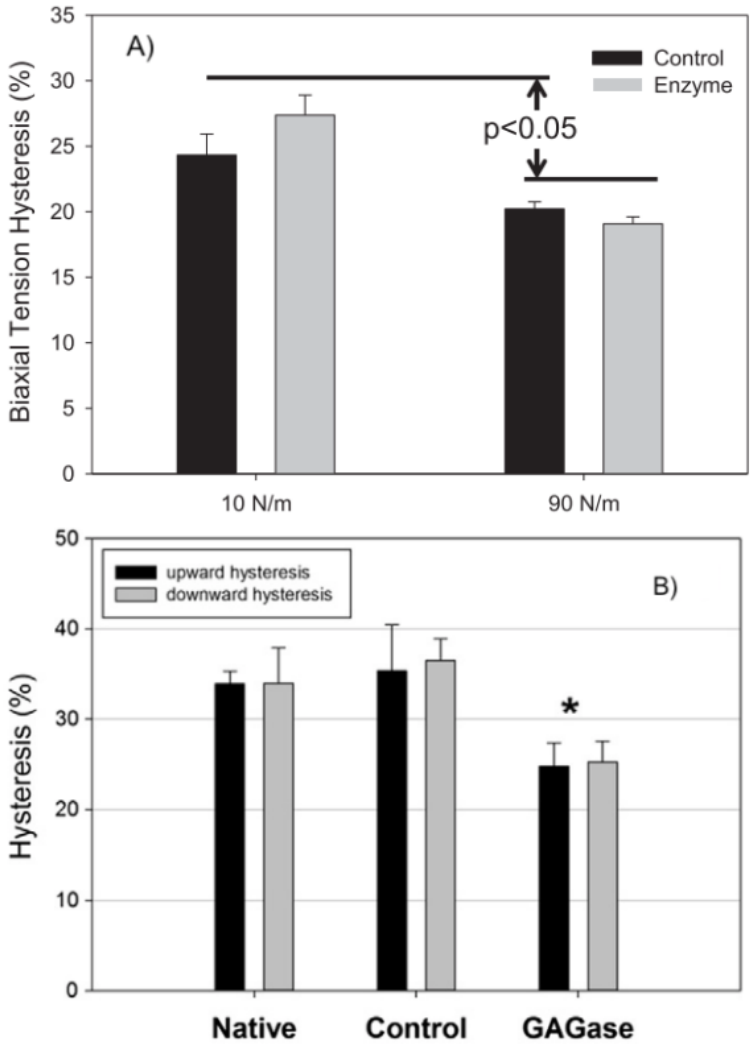


Figure 2.4 Experimental results of a) planar tensile hysteresis of the control and enzyme-treated groups at low tensile stress (10 N/m) and physiological tensile stress (90 N/m), b) flexural hysteresis values for the native, control, and enzyme-treated groups in both flexural directions. Note that the unit here is N/m instead of N/m^2 due to the neglectable nature of the thickness of thin film materials [53].

2.2.2 Chemical Composition

The application of ECM natural polymers as TEHV materials is advantageous for that they provide a familiar environment for cells to seed on and feed on them. It is essential to further investigate the microarchitecture, the microstructure, and the compositions of the aortic valves for a better understanding of materials selection for this thesis and better structural and mechanical imitation for scaffold construction. A more detailed distribution of collagen,

elastin, and GAGs in the aortic valve leaflets is shown in Figure 2.5. In addition, functional proteins in the ECM are essential in signalling, cell activities, and metabolism, yet their impact on structural properties is neglectable [54]. The other important substance is the proteoglycan, which is a protein-glycosaminoglycan complex that is reported to provide minor compressive resistance [55]. Collagen, elastin, and GAGs are the structural components of the aortic valve ECM, therefore, are selected as the materials in this thesis.

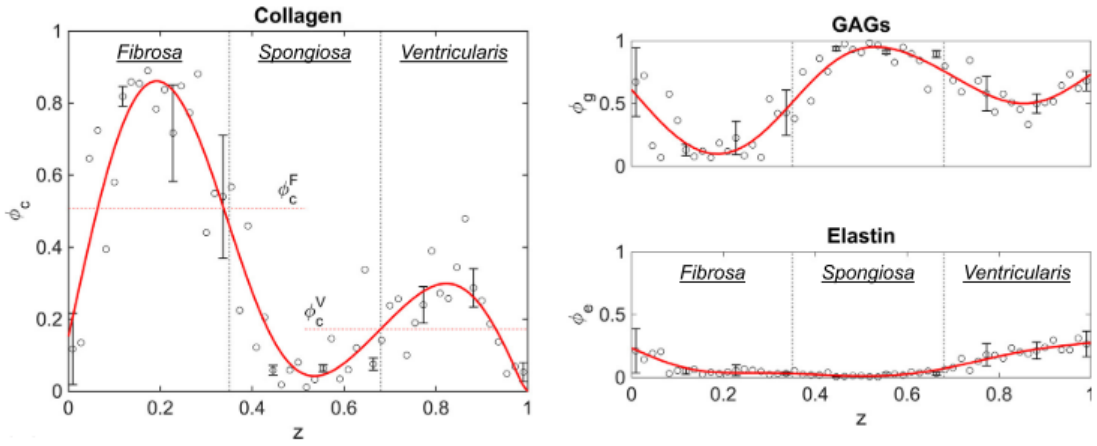


Figure 2.5 The average volume fractions of collagen, elastin, and GAGs in aortic valve leaflets [56].

2.2.2.1 Collagen

Collagen can be found in all three layers in different orientations, contributing to half of the valvular dry mass [56,57]. Figure 2.6 shows the representative conformation of the collagen basic unit, which contains three intertwined peptide chains (α-chain) with a repeating sequence of three amino acids, G-X-Y [50]. G stands for the smallest amino acid glycine, which occupies the inside of the triple helix pointing towards the axis. X and Y groups, commonly proline and hydroxyproline, are forced to face the outside due to their bulky volume [58]. Based on the slight difference in the exact amino acid groups, collagen is divided into 29 types. Type I collagen predominantly exists in heart valve tissue, taking up 74 % while 24 % is type III collagen and 2 % is type V collagen [59].



Figure 2.6 The triple helix structure of the collagen basic unit [50].

As mentioned, the higher circumferential Young's modulus of the fibrosa is attributed to collagen fibres and their alignment. The tensile resistance of collagen fibres originates from the triple helical structure. The chemical structures of glycine, proline, and hydroxyproline are shown in Figure 2.7. The backbone N-H bond of glycine and the C-O bond in proline would form hydrogen bonds to stabilise the helix, resulting in tension resistance [50].

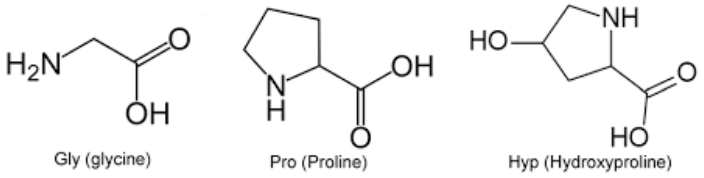


Figure 2.7 The chemical structures of glycine, proline, and hydroxyproline.

After being secreted from the cell, the triple helices are tailored into tropocollagen with a length of about 300 nm and a diameter of roughly 1.5 nm. Every five of these tropocollagen molecules further stagger along their axes and aggregate into microfibrils with an average diameter of 4 nm, creating an overlap-gap structure [60]. This 67 nm gap within this alignment is unique to collagen and is named the 'D-period' or the 'D-band'. The microfibrils then further upscale as fibrils and eventually bundle up to form the collagen fibres existing universally in the heart valve extracellular matrix. The formation of the D-banding pattern is demonstrated in Figure 2.8.

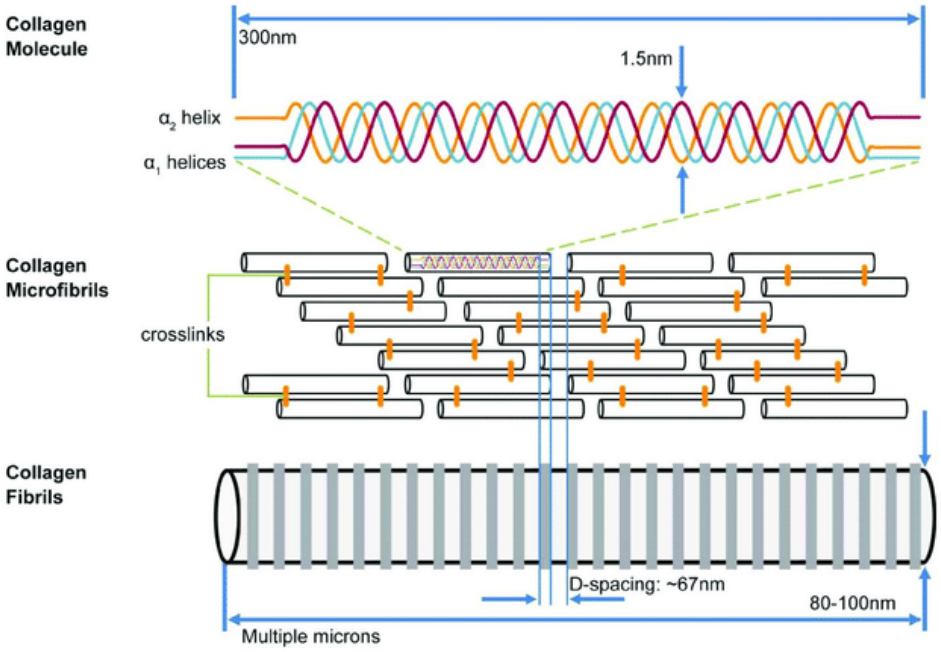


Figure 2.8 The triple helices forming microfibrils, which then further aggregated into collagen fibrils with the overlap-gap pattern [61].

Collagen can be classified based on its microstructure into two categories: polymeric collagen and monomeric collagen [62]. The polymeric collagen is naturally crosslinked and polymerised and can be extracted by mucopolysaccharide and soluble protein cleansing [63,64]. When rid of the intermolecular crosslinks, the polymeric collagen is downscaled to monomeric collagen, which is the isolated triple helical tropocollagen form. The monomeric collagen can be obtained by treating the polymeric ones with acidic conditions to break the crosslinks [65,66]. It is experimentally confirmed that monomeric collagen can be reconstructed into a polymeric collagen equivalent fibrillar structure with the characteristic D-period by a self-assembly process termed fibrillogenesis [67,68]. Monomeric collagen was first introduced into biotechnology as a molecular sieving and dialysis separation membrane. It was also used as an additive in calcium phosphate cement bone grafts in the late ‘90s but was found to compromise the structural tensile strength [69]. Polymeric collagen, on the other hand, shows better mechanical properties due to its intermolecular crosslinking [70]. However, these natural crosslinks can lead to potential antigenic reactions and batch-to-batch differences [71].

Within monomeric collagen, two subtypes were distinguished from each other, tropocollagen and atelocollagen. Tropocollagen can be obtained by acid treatment, whereas atelocollagen is commonly extracted by pepsin digestion. A collagen molecule contains a terminal amino telopeptide (N-), the triple helix part, and a terminal carboxy telopeptide (C-) [72]. The telopeptide area does not contain the G-X-Y sequence or the helical structure that is important for fibril formation and stabilisation [73,74]. By enzyme treatment (often pepsin), terminal telopeptides of tropocollagen can be cleaved, leaving the triple helix structure intact and yielding atelocollagen, which is proven to retain the self-assemble properties and can be more effective in aggregation during fibrillogenesis [75–77]. It is studied that collagen antigenicity can be attributed to the telopeptides; therefore, atelocollagen stands out in tissue engineering as it potentially eliminates immunogenicity [78].

2.2.2.2 Elastin

Elastin is the main component of the ventricularis and is crucial to the layer reaching the required extensibility. Together with the trace amount that exists in the fibrosa, elastin contributes to about 13 % of the total valve leaflet weight [57]. Similar to collagen, glycine forms almost one-third of the elastin peptide chain, yet the low fraction of proline and hydroxyproline combined with the presence of other nonpolar amino acids, i.e., alanine and leucine, makes elastin strongly hydrophobic [79]. Other amino acids found in elastin include lysine, valine, aspartate, glutamate, and arginine [80]. Different from the hierarchical structure of collagen, elastin molecules form a network that can stretch and recoil freely like a rubber band under tension as shown in Figure 2.9, and it coils into a globular structure when in contact with water due to a certain amount of polar side groups [81].

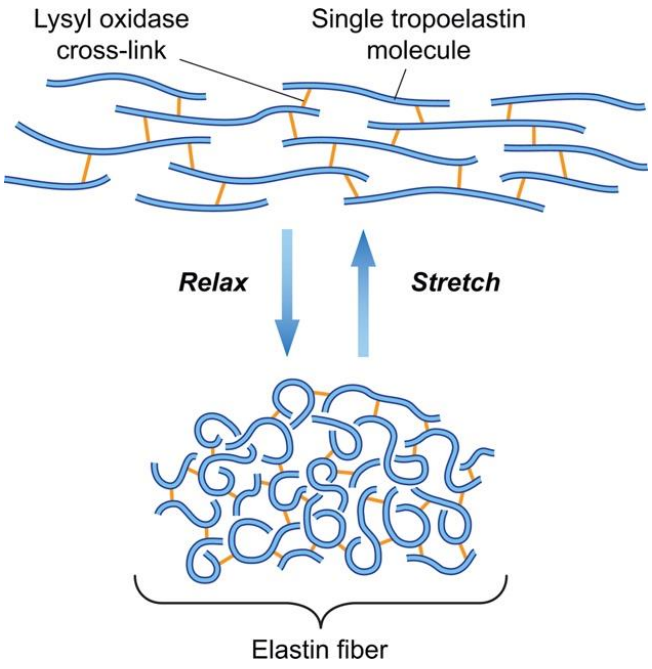


Figure 2.9 The elastin network in its relaxed and stretched states [82].

Unlike the triple helical structure of collagen, elastin peptide chains are arranged more randomly, with two distinguishable conformations found in the network. As shown in Figure 2.10, the α-helical conformation is present in the crosslinked area where the two outward-facing lysine residues from two adjacent tropoelastin molecules form the intermolecular desmosine or isodesmosine crosslinks (Figure 2.11), turning the dissolvable tropoelastin molecules insoluble in water. The α-helix is the only conformation where the lysine residues can protrude perpendicularly to the axis and establish the desmosine and isodesmosine interactions, therefore is crucial to the crosslinking-related properties such as extensibility and low hysteresis. The β-turn occurs in the region in between crosslinks with the often-present valine residues participating in the intramolecular hydrogen bonding [83]. These two conformations each dominate 10 % (α-helix) and 35 % (β-turn) of the whole elastin structure, leaving the rest 55 % undefined [84].

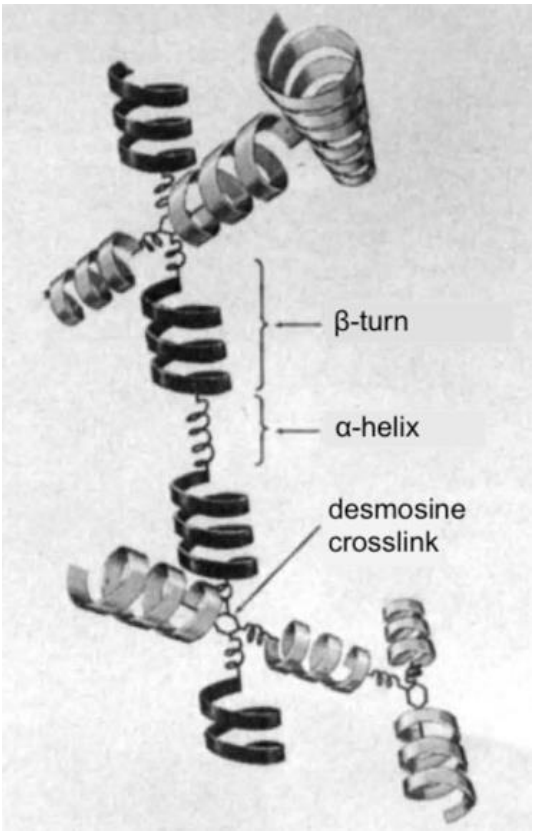


Figure 2.10 The α-helix and β-turn conformations within the elastin molecule [83].

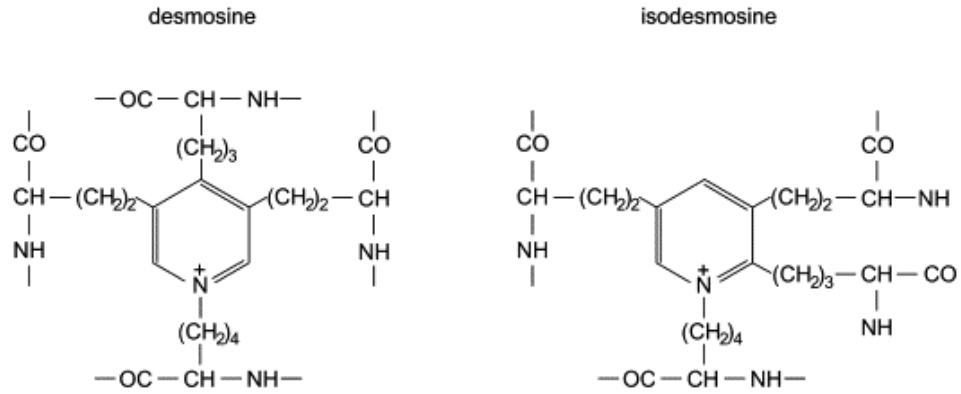


Figure 2.11 The desmosine and isodesmosine crosslinks [85].

2.2.2.3 Glycosaminoglycans (GAGs)

GAGs are a group of linear polysaccharides containing repeating units of hexose-hexosamine and are generally sulphated except for hyaluronic acid (HA) [86]. The hexose and hexosamine constituting HA are β-1,4-D-glucuronic acid and β-1,3-N-acetyl-D-glycosamide, and their chemical structures are shown in Figure 2.12 [87]. HA takes up 50–60 % of the total GAGs in

human aortic valves and mainly appears in the spongiosa layer [88]. The higher HA percentage in aortic valves is due to the mechanical requirement of bearing greater compression caused by the higher blood pressure which reaches about 80 mmHg [89]. With ageing, the HA proportion is expected to show a downward trend.

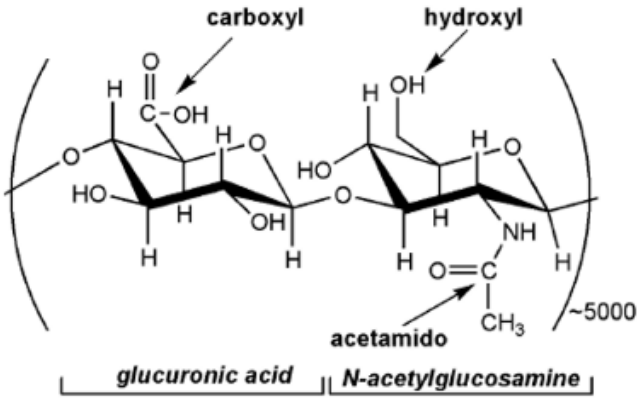


Figure 2.12 The structure of the disaccharide repeating unit of HA [90].

The mechanical function of the spongiosa focuses on preventing delamination and shock dampening, of which the latter is hypothesised to be achieved by GAGs. The carboxyl groups in the glucuronic acid unit are negatively charged, which together with the helical configuration constructed by the hydrogen bonds formed between the hydroxyl groups and water molecules, guarantees the absorption and retainment of a large amount of water [91]. This water uptake renders the spongiosa a cushion-like structure, which is effective in resisting impacts and preserving energy. Meanwhile, water serves as a lubricant during the relative movement between layers, preventing excessive shearing force and therefore avoiding delamination [90]. Apart from mechanical roles, the GAGs are crucial physiologically in supporting the extracellular matrix and facilitating cell activities [92].

2.2.3 Biomechanics

Besides the layered structure and the chemical composition, the biomechanics of the aortic valves are equally important for a successful leaflet reconstruction. Functionally, the heart

pumps blood containing oxygen, nutrition, and waste through the human body, which is achieved by repeating the cycle of systole and diastole. During systole, the valve leaflet relaxes and opens while the blood flows from the ventricles to the artery, rapidly achieving its peak velocity before deceleration [93]. The valve remains closed in diastole, withstanding a transvalvular pressure of up to 12 kPa [94]. The axial pressure gradient towards the leaflets is built during systole, accompanying an uneven distribution of blood flow momentum. This further leads to blood vortices that can impose a quick close on the leaflets [95]. During this process, the corrugated fibrosa layer unfolds and matches with the extension of the ventricularis layer [96]. For canines, the valve leaflets can experience a length increase of 30.8 % radially and 11.9 % circumferentially *in vivo*, which can be mimicked by constructing TEHVs with biaxial extensibility [97,98]. For humans, the transition strain is measured to be within the range of 16–32 % *in vitro*, providing another mechanical standard for TEHVs [99].

Structurally, the leaflet in its natural state bends slightly towards the ventricularis side, generating different loading modes in different layers (the fibrosa in compression and the ventricularis in tension as shown in Figure 2.13). The curvature increases during systole and this flexural state is known as “with curvature” (WC), of which the effective bending modulus is related to both mechanical behaviours of the fibrosa and the ventricularis. Due to the lack of compression resistance of collagen fibres in the fibrosa, the bending modulus in the WC direction is majorly determined by the tensile strength of the elastin fibres in the ventricularis. When the valve closes, the curving direction changes with the blood flow and the leaflets bend towards the fibrosa in resistance to the backflow, this state is known as “against curvature” (AC). The fibrosa is under tension in the AC direction, where the collagen fibres with better tensile properties are the main contributors to the effective bending modulus [100]. Merryman et al. measured the effective bending moduli of the porcine aortic valve in both WC and AC directions and concluded that the valve is more resistant to bending

in the AC direction (bending modulus being 700 kPa in the AC direction and only 500 kPa in the WC direction), which coincides with the hypothesis that the fibrosa under tension dominates the AC direction bending [38]. This bending anisotropy is crucial to heart valve function, for the higher modulus in the AC direction can efficiently prevent the leaflet from any sudden reverse movements, reducing the flexure fatigue occurrence [101]. Therefore, this bending anisotropy is of great significance in TEHV construction.

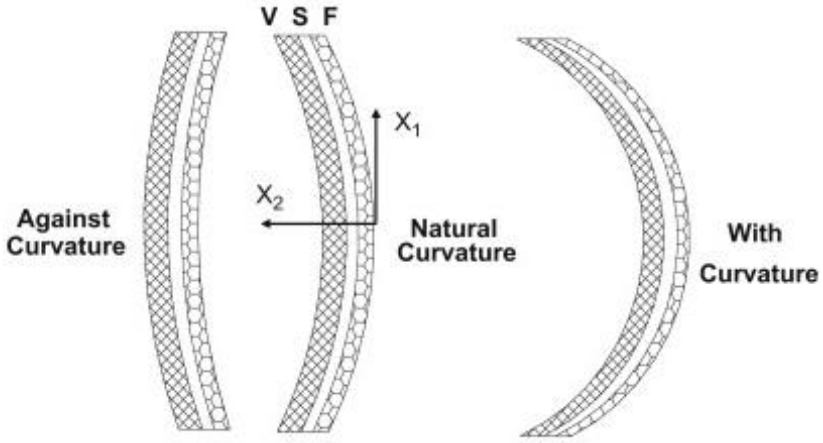


Figure 2.13 The heart valve leaflet in different bending states. V, S, and F each stand for the ventricularis, the spongiosa, and the fibrosa [49].

Mechanically, many soft tissues including the heart valves follow a J-shaped stress-strain curve termed "J-curve". When subjected to tension, the stress-strain curve of the valve leaflet experiences three stages: the "toe" region, the transition region, and the linear region as shown in Figure 2.14. In the "toe" region, the crimped collagen fibres unfold, and this unfolding is manifested by a relatively large strain under minimal stress. When the fibres cannot be further uncrimped and can only be stretched, the leaflet enters the linear region, where the tissue rapidly stiffens with elevated Young's modulus. This characteristic feature of soft tissues prevents them from elastic instability and potential fracture failure. Moreover, the J-curve behaviour effectively reduces the bending stress, for the aforementioned large extension during systole enables the leaflet to function in the low modulus "toe" region. It is also worth mentioning that both the large length changes brought in by valve stretching and

the extremely frequent flexure can potentially introduce fatigue failure, which surprisingly eludes the billions of loading-unloading cycles. Two possible explanations are that either the valve is less sensitive to fatigue or that the damage caused is reversible, with the actual mechanism of this fatigue resistance remaining unknown [97]. Stella et al. reported a negligible creep deformation during a three-hour experiment where biaxial planar tension was applied to porcine aortic leaflets [102]. This study indicated that the creep deformation is also prevented by the minimal stress within the "toe" region.

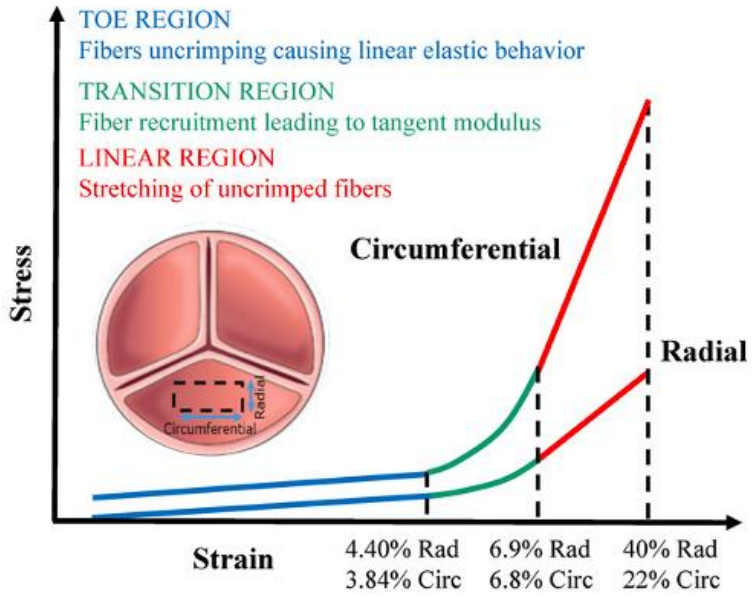


Figure 2.14 The characteristic stress-strain J-curve of the heart valve leaflets [103].

2.3 Mechanical Properties and Characterisation

The valve leaflet biomechanics regulates both the blood flow pattern and the cell behaviours; cell shape and its proliferation rate in turn influence the constructive fibre formation, which determines the mechanical properties of the valves [104]. The completed stress cycle the leaflet undergoes comprises four loading stages, the flexure during valve opening, the shear generated by blood flowing, the flexure during valve closing, and the tension created by the backward blood flow on the closed valve [49]. Therefore, constructing TEHVs that

mechanically match the native valves is one of the priorities of future research. Among the mechanical properties, the tensile, bending, and viscoelastic properties, are of interest.

2.3.1 Tensile Properties

Robust tensile behaviours are required due to the transvalvular pressure imposed on the closing valve, therefore the relevant properties such as the elastic modulus (E_{ten}), the ultimate tensile stress (UTS) and the failure strain (ε_{max}) are of the main focus. As demonstrated in Figure 2.15, UTS and ε_{max} data can be directly obtained from the stress-strain curve, and E_{ten} can be calculated from the slope of the linear region. Uniaxial tensile tests were performed on both porcine and human aortic valves and the data is organised in Table 2.4. The data suggests anisotropic tensile behaviours, where the valves are stiffer circumferentially and more compliant radially [105–110].

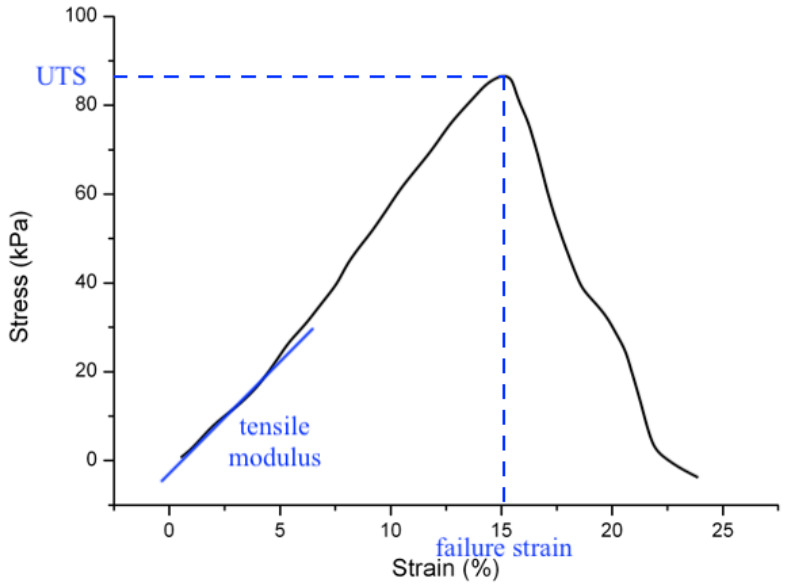


Figure 2.15 A stress-strain curve of collagen scaffold under unidirectional tension.

	E_{ten} (kPa)	**ε_{max} (%)**	**UTS (kPa)**	**condition**
Circumferential	15600 ± 6400	22 ± 11	2600 ± 1200	load: 20 N strain rate: l_0/min
Radial	2000 ± 1500	30 ± 14	420 ± 240	

Table 2.4 Uniaxial tensile properties of healthy human aortic valves [109].

Despite being convenient, uniaxial testing cannot reveal the bi-directional response found in physiological valves under planar tension [111]. The understanding of the biaxial tensile properties of the leaflet is often hindered by the heterogeneous and curved structure as well as the small size [112]. One study reported a unique negative circumferential strain under planar tension, which resulted from the contraction caused by collagen bundle rotation as shown in Figure 2.16; this rotation movement was hypothesised to facilitate the radial extension [49,112]. Nonetheless, the uniaxial test is still widely used in scaffold mechanical characterisation for its sufficiency in illustrating tensile anisotropy and measuring UTS.

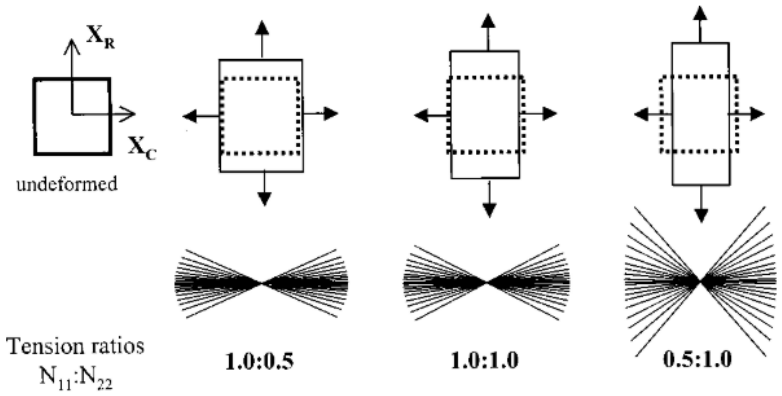


Figure 2.16 A schematic of collagen bundle rotation caused by larger radial stretching [112].

2.3.2 Flexural Properties

The heart valve leaflets constantly shift between the WC and AC directions; therefore, sufficient bending stiffness (measured by the effective bending modulus E_{bend}) and bending anisotropy are required for a functioning valve replacement. The changes in stiffness in the transition region and the contribution and interaction of individual layers can be studied by bending tests. The commonly adopted testing methods include cantilever bending and three-point bending as shown in Figure 2.17. The cantilever bending test is more applied in the commissural region measurement whereas the three-point bending is more suitable for the belly region of the native heart valves and the scaffolds in the non-hydrated state [113]. It is

more difficult to measure the bending properties of the hydrated scaffolds, however, a "self-deflection" test was developed to bypass the limitation of equipment sensitivity existing in three-point bending [114].

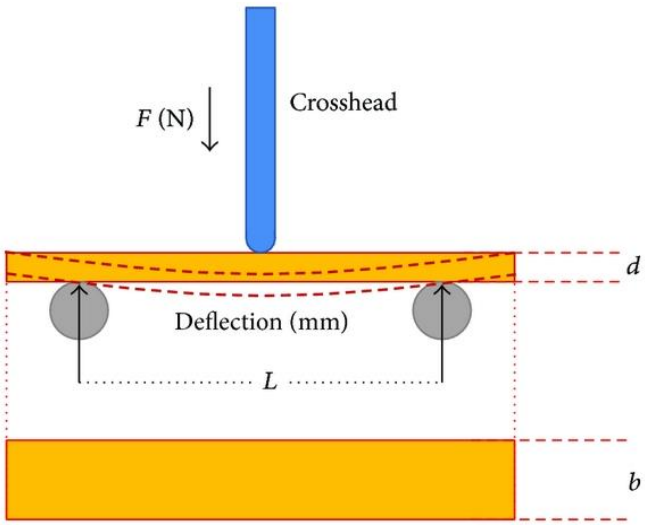


Figure 2.17 The setup for the three-point bending test. F(N), d, L, and b respectively represent the loading force, sample thickness, the span of the support, and sample width [115].

Gloeckner et al. performed three-point bending on porcine aortic leaflets and concluded that they are stiffer circumferentially and that they are more resilient in that AC direction [116]. Engelmayr et al. later conducted three-point bending on polymeric scaffolds and calculated the bending modulus from the slopes of the M-Δκ curve as shown in Figure 2.18, where M and Δκ stand for the moment and the change in curvature [117]. The bending modulus can be calculated from Equation 2.1, where I stands for the second moment of inertia, and for rectangular samples, which can be calculated using Equation 2.2, where t and w are the sample thickness and width.

$$M = E_{bend} I \Delta\kappa \qquad \text{Equation 2.1}$$

$$I = \frac{t^3 w}{12} \qquad \text{Equation 2.2}$$

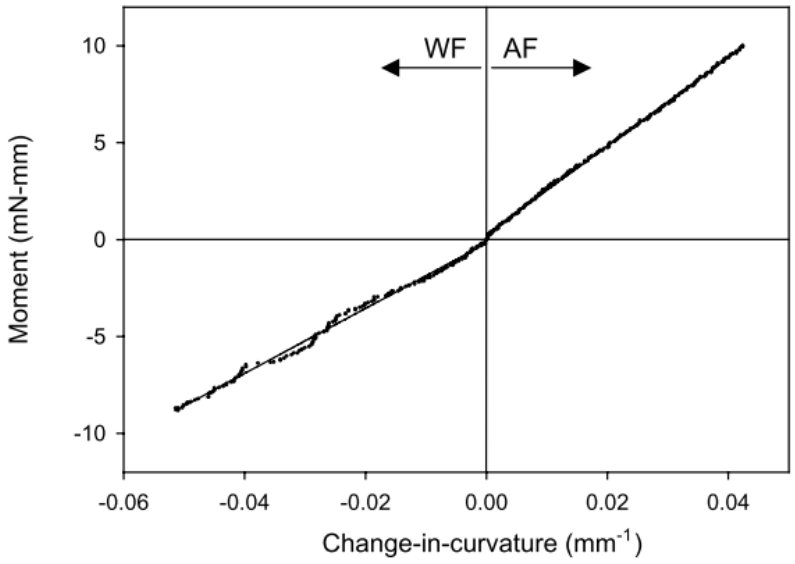


Figure 2.18 The plot of a M-Δκ curve for the calculation of the bending modulus, with AF being against flexure and WF being with flexure [117].

Evolving from the methods above, a more convenient way of the bending modulus calculation is adopted [118]. Using Equation 2.3, the bending modulus can be calculated by knowing the slope of the load-deflection curve (Figure 2.19), the loading span distance (l), and the second moment of inertia (I).

$$E_{bend} = \left(\frac{\delta P}{\delta D}\right)\frac{l^3}{48I} \qquad \text{Equation 2.3}$$

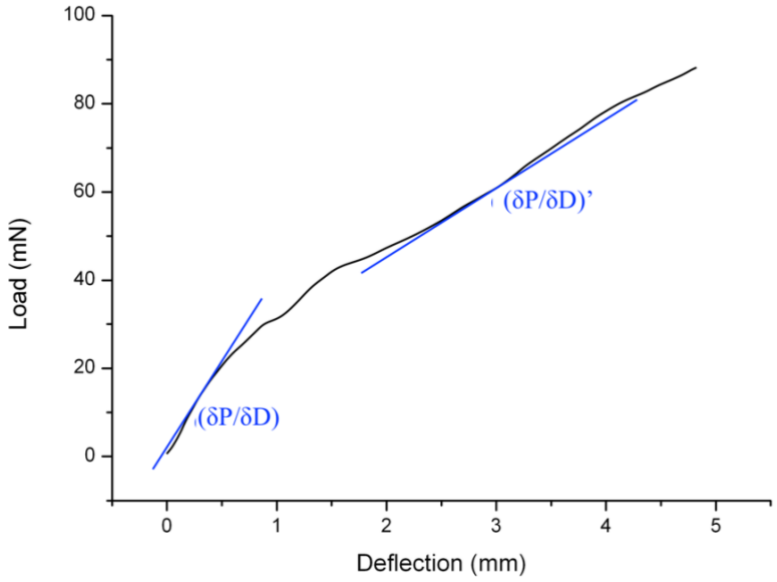


Figure 2.19 The plot of a typical two-stage load-deflection curve for a collagen-based scaffold, with δP/δD being the load deflection rate.

2.3.3 Viscoelasticity and Time-dependent Properties

The heart valve leaflets demonstrate viscoelasticity in the physiological environment; therefore, dynamic behaviours of the leaflets need to be understood through properties such as the storage modulus (G'), the loss modulus (G"), and the loss tangent (tanδ). Storage modulus measures the energy stored and represents the elastic portion of the complex modulus while loss modulus quantifies the energy dissipated as heat and corresponds to the viscous part, and tanδ shows the dampening effect by being the ratio of storage to loss modulus. Jiao et al. measured the shearing storage modulus and tanδ of fresh human aortic leaflets to be 0.54 ± 0.08 kPa and 0.3–0.4, providing the viscoelastic benchmark for future scaffold construction [119].

Time-dependent properties such as stress relaxation, creep deformation, and hysteresis are worth investigating since the implanted scaffold should be able to function normally until the new tissue regeneration. Grashow et al. made an early attempt to map the planar mechanical response of porcine mitral valves at different strain rates and concluded that the valves exhibited completed strain rate independence at physiological conditions [120,121]. Stella et al. later performed analogous experiments on porcine aortic valves and revealed similar outcomes of low and strain rate-independent hysteresis, large stress-relaxation, and minimal creep deformation as shown in Figure 2.20, providing another benchmarking requirement for TEHV designs [102]. It should be pointed out that uniaxial tests lack accuracy in characterising time-dependent properties due to the rate dependency and the lack of anisotropic relaxation [121,122]. The data from the studies mentioned above are listed in Table 2.5.

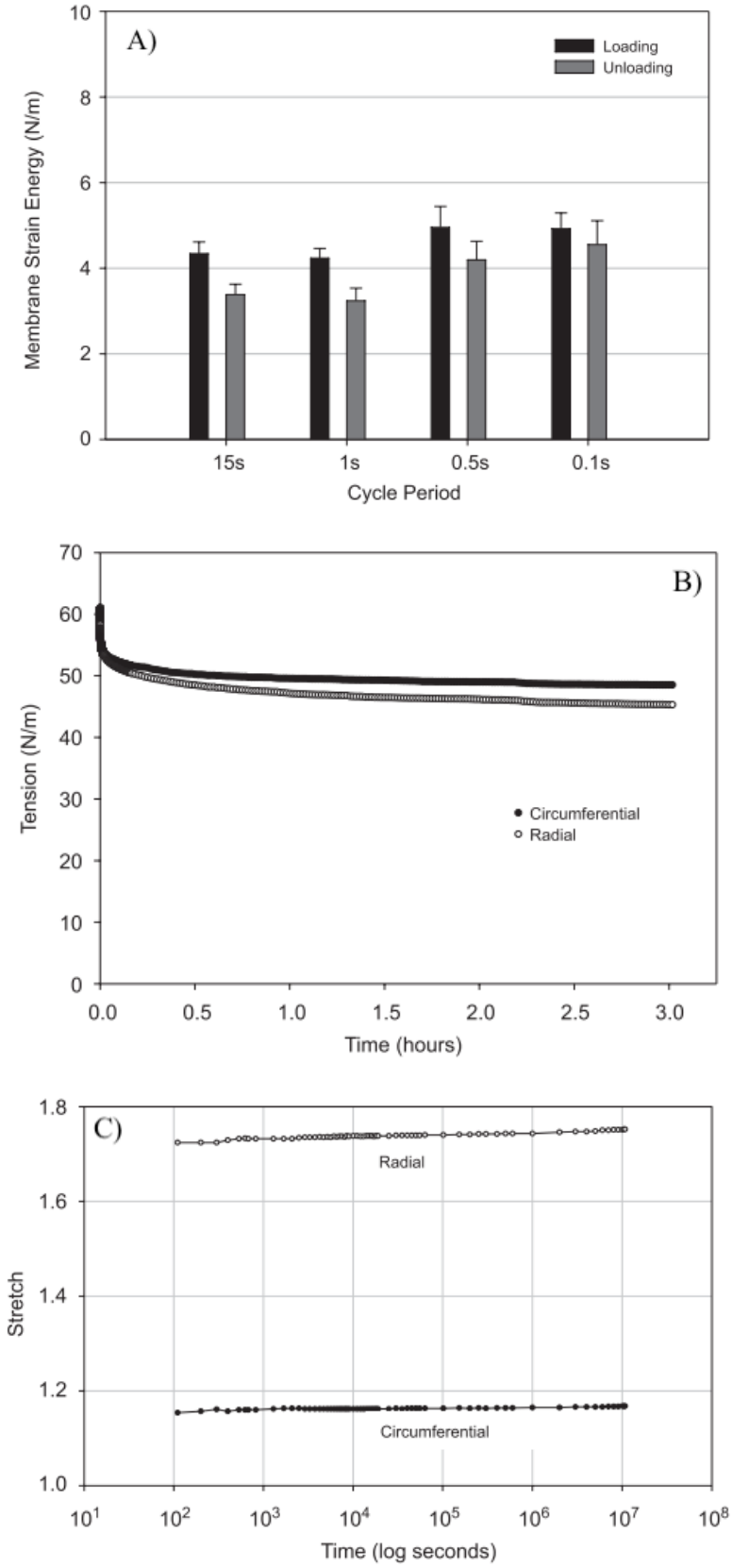


Figure 2.20 Representative illustrations of a) hysteresis, b) stress-relaxation curve, and c) creep behaviours of porcine aortic valve [102].

Valve Type	Relaxation (%)		Creep	Hysteresis	Loading
	circumferential	radial			
mitral valve			negligible	~ 17 %	90 N/m
mitral valve	24.7 ± 0.9 biaxial	32.1 ± 0.8 biaxial	negligible		90 N/m
	25 ± 2 uniaxial	25 ± 2 uniaxial			90 N/m
aortic valve	28 ± 1 biaxial	33 ± 1 biaxial	negligible	~ 12 %	60 N/m

Table 2.5 The organised time-dependent properties of the porcine valves from various studies [102,120,121].

2.4 TEHVs Construction

2.4.1 Fabrication and Crosslinking Methods

Electrospinning, freeze-drying (lyophilisation), critical point-drying, and 3D bioprinting are TEHV scaffold manufacturing methods most commonly used. As shown in Figure 2.21, dry polymer fibres form from a charged polymer solution under an electric field through a syringe nozzle, which makes the product's porosity, pore size, and fibre diameter controllable with electrospinning [123].

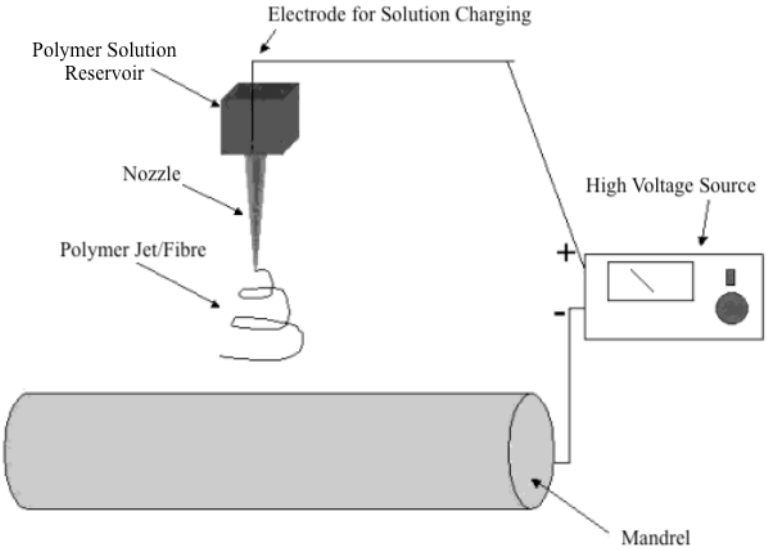


Figure 2.21 A schematic illustration of the electrospinning apparatus [124].

Both the free-drying and the critical point-drying methods create scaffolds with a porous structure by avoiding crossing the liquid-gas phase boundary. As shown in Figure 2.22,

freeze-drying utilises the low temperature to introduce the ice crystals and low pressure to sublimate them. After the polymer solution is moulded in the liquid phase, the temperature is brought below the freezing temperature, the solution enters the solid phase. The close-to-vacuum pressure inside the freeze-dryer bypasses the liquid phase entirely when the temperature goes up again, leaving the negative replica of ice crystals, the pores, behind.

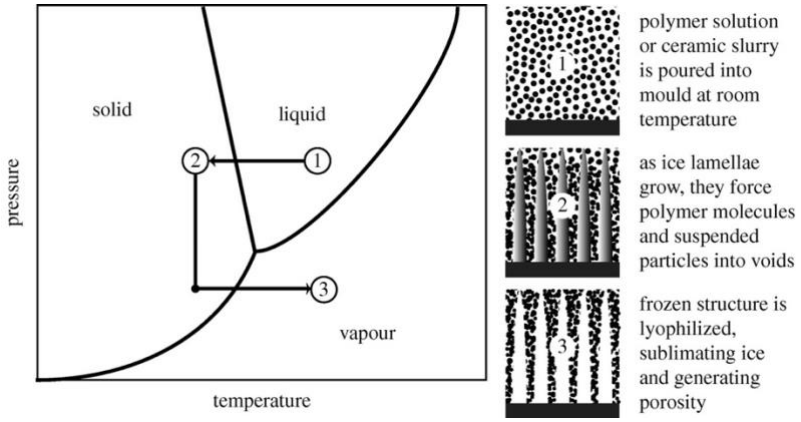


Figure 2.22 The phase diagram of water (solid, liquid, and vapour) and the freeze-drying procedure [125].

Bioprinting uses polymer-based bio-ink as the starting material and has the advantage of accurate structure design due to the incorporation of computed models, it can be used to print scaffolds and even living cells, allowing for both cell integration and ECM remodelling [126,127]. The advantages and disadvantages of each method are organised in Table 2.6. Both electrospinning and 3D printing can introduce intricate pore structures, yet the dense structure obtained by electrospinning shows restricted waste/oxygen exchange and cell infiltration, and the 3D printing procedure poses extra requirements on the viscosity and sol-gel temperature of the starting materials. Critical point-drying, on the other hand, has a more complex protocol and is reported to directly link to structure shrinkage and deformation. Therefore, freeze-drying is considered the optimal approach for constructing the porous TEHV scaffolds in this thesis.

Fabrication Method	Advantages	Disadvantages
Electrospinning	nanoscale control, efficient, inexpensive	dense product, poor reproducibility, potential cytotoxicity

Freeze-drying	highly porous structure, interconnected network, tuneable pore morphology, no disruption of water	time/energy consuming, surface skin
Critical point-drying	highly porous structure	complex protocol, drastic volume shrinkage
3D bioprinting	homogeneous porosity, customised to patient, complex structure, different cell type	high printability requirements, shrinkage and deformation, high cost

Table 2.6 The advantages and disadvantages of different fabrication methods [128–134].

With the inherently low mechanical strength, the scaffolds are preferred to be crosslinked for enhanced mechanical properties and degradation resistance [73]. The commonly used physical crosslinking methods include dehydrothermal treatment (DHT) [135] and UV irradiation [136,137], and the reagents used to introduce chemical crosslinks include glutaraldehyde [138,139], carbodiimide [140,141], isocyanate [142], and Genipin [143]. Physical crosslinking is reported to effectively increase the mechanical properties, especially the tensile strength, yet can cause inevitable fragmentation and denaturation of the biopolymers; chemical crosslinking, on the other hand, avoids compromising the structure by forming covalent bonds [135]. It should be pointed out that although higher crosslinking density would result in improved mechanical properties as many studies suggest, a moderate degree of crosslinks should be maintained so that enough sites are left for cell binding [144–148]. EDC (1-ethyl-3-(3-dimethylaminopropy) carbodiimide) and NHS (N-hydroxysuccinimide) are chosen as the crosslinking agents based on carbodiimide chemistry shown in Figure 2.23 [144–148]. The advantages and disadvantages of different crosslinking methods are organised in Table 2.7. It can be seen that EDC/NHS chemistry has the advantage of improved denaturation resistance, high cell attachment potential brought in by the strong covalent bond, surface hydrophilicity, efficient attachment of the adhesion-promoting molecules [149], and low cytotoxicity. Therefore, EDC/NHS chemistry is chosen as the crosslinking method for this thesis.

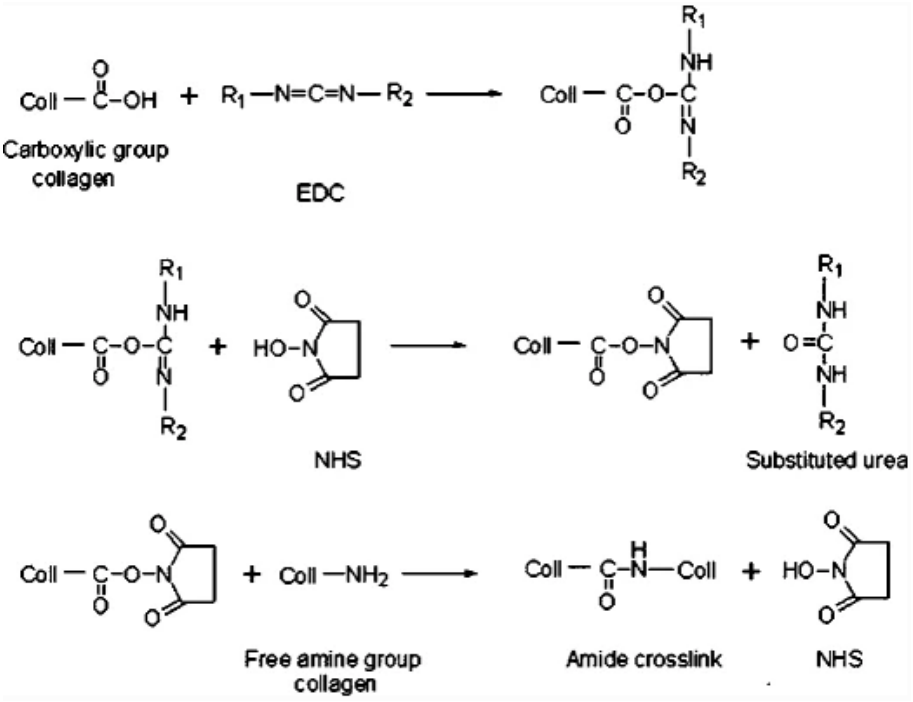


Figure 2.23 The crosslinking of collagen based on the EDC/NHS chemistry [150].

Method	Advantages	Disadvantages
DHT	controlled mechanical properties	time-consuming (3–5 days), fragmentation and denaturation
UV irradiation	time-effective (15 min), enhanced enzymatic resistance, reduced fragmentation with glucose	effective for thin scaffolds, limited available sites
glutaraldehyde	enhanced thermal strength	poorly understood mechanism, side reaction with primary amides, toxic by-products
EDC/NHS	increased denaturation temperature, enhanced enzymatic resistance, high cell attachment potential, controlled swelling behaviour, least cytotoxicity, water-soluble by-products	time-consuming (3–4 h)
genipin	low toxicity	Expensive, low crosslinking density

Table 2.7 The advantages and disadvantages of different crosslinking methods [73,151–163].

Various studies successfully fabricated interconnected scaffolds based on natural polymers with high porosity using freeze-drying and EDC/NHS crosslinking, showing promising applications of these types of scaffolds and fabrication methods in heart valve

tissue engineering. The data is organised in Table 2.8. Divakar et al. concluded that crosslinking is necessary for *in vivo* experiments after observing that the uncrosslinked scaffolds became highly compacted after two weeks while the crosslinked ones maintained their porous structures and elliptical pore shapes [164]. Li et al. reported elevated biodegradation resistance after EDC-crosslinking with no pore morphology damage, and that pressing before crosslinking alters the original nearly globular pores into a flatter shape [165]. Mechanical properties were reported to be improved after EDC/NHS crosslinking, with Young's modulus and the failure strain of a crosslinked fibroin/collagen/chitosan scaffold reaching 32 kPa and 70 % respectively [166]. Nong et al. determined that the optimal crosslinking condition is with 75 % ethanol at 37 ºC by comparing the swelling and degradation properties of type II collagen scaffolds with 33 mM/20 mM/50 mM EDC/NHS/ethyl sulfonic acid (MES), while other studies commonly choose 50 mM/25 mM EDC/NHS in 98 % ethanol or 33 mM/6 mM EDC/NHS as crosslinking conditions [167].

Ref	**Materials**	**Methods**	**Porosity** **Pore Size**
Grabska-Zielińska (2021)	collagen chitosan silk fibroin	freeze-drying EDC/NHS 50/25 mM in 98 % EtOH	~ 90 % ~ 200 μm
Divakar (2020)	1 % w/v collagen	freeze-drying EDC/NHS 33/6 mM in 200 proof EtOH	98.98 ± 0.02 % 275 ± 127 μm for length 48 ± 3 μm for width
Nong (2019)	collagen	freeze-drying EDC/NHS/MES 33/20/50 mM in 75 % EtOH	84 ± 16 μm
Kaczmarek (2018)	chitosan/collagen + 1 % HA	freeze-drying EDC/NHS 50/25 mM in 98 % EtOH	95.9 ± 0.6 %
	chitosan/collagen + 2 % HA		95.1 ± 0.4 %
	chitosan/collagen + 5 % HA		98.9 ± 0.8 %
Li (2017)	chitosan/collagen	freeze-drying EDC/NHS 33/6 mM in MES buffer	93 ± 1 % 50–100 μm
	pressed chitosan/collagen		90 ± 1 % 50–150 μm

Table 2.8 Studies on natural polymeric scaffolds fabricated by freeze-drying and crosslinked by EDC/NHS chemistry [164–168]. *EtOH stands for ethanol.

2.4.2 Single-layer Scaffolds

Collagen is the most widely studied tissue engineering scaffold construction material, either as the sole material or forming a composite structure with others. Different collagen concentrations were attempted in fabricating collagen-only scaffolds with suitable porosity (over 90 %) and pore size (between 50 and 200 μm) for cardiovascular applications, and the relevant studies are organised in Table 2.9 [169–171]. Chitosan, silk fibroin, hydroxyapatite (HAp), and poly-L-lactide (PLLA), are the common materials to form collagen-based composite scaffolds. The representative studies involved are organised in Table 2.10. 1,2,7,8-diepoxyoctane (DEO) crosslinked nano-hydroxyapatite (nHAp) scaffolds exhibit a less-desired pore size range for cardiac applications, nonetheless the design shows potential in bone tissue engineering. Significant improvements in scaffold mechanical properties are made possible by infiltrating collagen fibres into the PLLA matrix as reinforcement, providing a structural way to strengthen the natural polymeric structure. However, the inherent lack of strength remains a problem for collagen and other natural polymer-based scaffolds despite the strengthening effect of crosslinking, increased concentration, and structural engineering.

Ref	**Materials**	**Methods**	**Porosity Pore Size**	**Mechanical Properties**
Antipova (2021)	1 wt% type II collagen	freeze-drying uncrosslinked		E_{ten}: 123 ± 22 MPa UTS: 6 ± 1 MPa
Khajav (2021)	1 %w/v collagen	freeze-drying EDC/NHS 33/6 mM in 80% EtOH	98.0 ± 0.2 % 155 ± 44 μm	E_{comp}: 1.30 ± 0.06 kPa
	2 %w/v collagen		97.47 ± 0.01 % 145 ± 23 μm	E_{comp}: 3 ± 1 kPa
	3 %w/v collagen		96.6 ± 0.2 % 122 ± 25 μm	E_{comp}: 6 ± 1 kPa
	4 %w/v collagen		96.0 ± 0.3 % 110 ± 26 μm	E_{comp}: 9 ± 1 kPa

Newman (2020)	0.2 %w/v type I collagen	freeze-drying (hydrated)		E_{comp}: 0.8 ± 0.2 kPa σ_{max}: 0.12 ± 0.08 kPa
	0.6 %w/v type I collagen			E_{comp}: 7 ± 1 kPa σ_{max}: 0.82 ± 0.05 kPa
	0.6 %w/v type I collagen	freeze-drying EDC:NHS = 1:1		E_{comp}: 11 ± 1 kPa σ_{max}: 1.22 ± 0.05 kPa
Kaczmarek (2018)	1 % collagen	freeze-drying EDC/NHS 50/25 mM in 98% EtOH	95.1 ± 0.7 %	E_{comp}: 17 kPa σ_{max}: 18 kPa
Kozlowska (2017)	1 wt% type I collagen	freeze-drying EDC/NHS 50/25 mM in 98% EtOH + DHT	92 %	E_{comp}: 27 kPa
	2 wt% type I collagen		93 %	E_{comp}: 55 kPa

Table 2.9 A summary of the collagen-only scaffolds published in recent studies focusing on materials, methods, pore morphology and mechanical properties [168,172–175].

Ref	Materials	Methods	Porosity (%)	Mechanical Properties
Antipova (2021)	0.1 wt% type II collagen + PLLA	electrospinning freeze-drying uncrosslinked		E_{ten}: 348 ± 22 MPa UTS: 12 ± 2 MPa
	0.5 wt% type II collagen + PLLA			E_{ten}: 386 ± 14 MPa UTS: 14.6 ± 0.8 MPa
	1 wt% type II collagen + PLLA			E_{ten}: 393 ± 28 MPa UTS: 20 ± 2 MPa
Liu (2020)	collagen + nHAp 4 %v/v DEO	freeze-drying DEO	75 ± 2	E_{comp}: 40 ± 3 MPa σ_{max}: 2.8 MPa
	collagen + nHAp 6 %v/v DEO		82 ± 3	E_{comp}: 46 ± 2 MPa σ_{max}: 3.9 MPa
	collagen + nHAp 8 %v/v DEO		84 ± 4	E_{comp}: 48 ± 4 MPa σ_{max}: 4.3 MPa
Kaczmarek (2019)	1 % collagen + 1 wt% GAG	freeze-drying EDC/NHS 50/25 mM in 98% EtOH	97 ± 1	E_{comp}: 51 kPa σ_{max}: 13.5 kPa
	1 % collagen + 5 wt% GAG		96 ± 1	E_{comp}: 54 kPa σ_{max}: 14.5 kPa
	collagen + chitosan + 1 wt% GAG		97 ± 1	E_{comp}: 67 kPa σ_{max}: 17.5 kPa

	collagen + chitosan + 5 wt% GAG		97 ± 1	E_{comp}: 72 kPa σ_{max}: 17.5 kPa
Kozlowska (2017)	1 wt% type I collagen + HAp (80:20)	freeze-drying EDC/NHS 50/25 mM in 98% EtOH + DHT	93.5	E_{comp}: 75 kPa
	1 wt% type I collagen + HAp (50:50)		92.4	E_{comp}: 60 kPa
	2 wt% type I collagen + HAp (80:20)		93.6	E_{comp}: 110 kPa
	2 wt% type I collagen + HAp (50:50)		91.8	E_{comp}: 460 kPa
Sionkowska (2016)	1 wt% collagen + silk fibroin (90:10)	freeze-drying EDC/NHS in 98% EtOH (hydrated)	85 ± 12	E_{comp}: 20 kPa σ_{max}: 15 kPa
	1 wt% collagen + silk fibroin (75:25)		66 ± 3	E_{comp}: 51 kPa σ_{max}: 50 kPa
	1 wt% collagen + silk fibroin (50:50)		43 ± 6	E_{comp}: 50 kPa σ_{max}: 80 kPa

Table 2.10 A summary of collagen-based composite scaffolds published in recent studies focusing on materials, methods, porosity and mechanical properties [168,172,173,176–178].

Elastin and hyaluronic acid (HA) are the other two essential components of the native valve leaflets, and both show potential as scaffold materials. Chen et al. successfully fabricated the type I collagen and elastin composite scaffold with various collagen-elastin ratios, and the structures were reported to have suitable pore size and proportionally matching mechanical properties [179]. Studies using elastin-like polypeptide (ELP) as scaffold material concluded that the scaffolds with either high collagen concentration or crosslinking density exhibited dense structures and better mechanical properties and that the optimal ratio of collagen to ELP to achieve better tensile resistance is 1:3; however, this ratio is less favourable once cell behaviours were considered [174,180]. Nazir et al. synthesised type I collagen and HA hybrid scaffolds with different crosslinking conditions under both the non-

hydrated and hydrated statuses and the scaffolds produced showed interconnected microstructure and a promising dynamic mechanical response to mimic the spongiosa layer with the tanδ being 0.38 of the hydrated S-1 compared to 0.3–0.4 of human aortic valves [119], yet the hydrated bending stiffness is still far below the TEHV application requirements [114,181]. Despite the seeming lack of mechanical strength, both elastin and HA are still considered ideal TEHV materials based on the promising results from the existing studies, which are organised in Table 2.11 and Table 2.12.

Ref	Materials	Methods	Pore Size (μm)	Mechanical Properties
Newman (2020)	0.2 %w/v type I collagen + 0.6 %w/v ELP	freeze-drying (hydrated)		E_{comp}: 2.9 ± 0.5 kPa σ_{max}: 0.45 ± 0.07 kPa
Gurumurthy (2018)	0.6 %w/v type I collagen + 1.8 %w/v ELP	gel formation		E_{ten}: 62 ± 23 kPa UTS: 20 ± 10 kPa
	0.7 %w/v type I collagen + 1.2 %w/v ELP			E_{ten}: 15 ± 4 kPa UTS: 10 ± 2 kPa
	0.6 %w/v type I collagen + 1.2 %w/v ELP			E_{ten}: 9 ± 2 kPa UTS: 2.7 ± 0.5 kPa
Chen (2012)	1 %w/v 50 % type I collagen + 50 % elastin	freeze-drying	180 ± 36	E_{ten}: 230 ± 22 kPa E_{comp}: 13 ± 2 kPa ε_{max}: 7 ± 2 %
	1 %w/v 20 % type I collagen + 80 % elastin		188 ± 36	E_{ten}: 40 ± 9 kPa E_{comp}: 10 ± 2 kPa ε_{max}: 15 ± 2 %

Table 2.11 A summary of collagen-elastin scaffolds published in recent studies focusing on materials, methods, pore size and mechanical properties [174,179,180].

Ref	Materials	Methods	Pore Size	Mechanical Properties
Nazir (2021, 2019)	1 %w/v type I collagen + HA2	freeze-drying 2 mM EDC or 20 mM EDC for HA	126 ± 4 μm	E_{comp}: 41 ± 4 kPa (dry) E_{bend}: 711 ± 29 kPa (dry) 1.0 ± 0.2 kPa (wet) G': 52 ± 6 kPa (dry) 11 ± 3 kPa (wet) G": 6 ± 1 kPa (dry) 4 ± 1 kPa (wet) tanδ: 0.12 (dry) 0.38 (wet)

	1 %w/v type I collagen + HA20		125 ± 5 μm	E_{comp}: 73 ± 5 kPa (dry) E_{bend}: 817 ± 17 kPa (dry) 1.0 ± 0.3 kPa (wet) G': 64 ± 4 kPa (dry) 15 ± 3 kPa (wet) G": 7 ± 2 kPa (dry) 2.0 ± 0.6 kPa (wet) tanδ: 0.12 (dry) 0.24 (wet)
	1 %w/v type I collagen + HA2	freeze-drying EDC/NHS 60/30 mM for collagen 2 mM EDC or 20 mM EDC for HA	84 ± 16 μm	E_{comp}: 68 ± 5 kPa (dry) E_{bend}: 980 ± 20 kPa (dry) 2.0 ± 0.3 kPa (wet) G': 68 ± 5 kPa (dry) 53 ± 4 kPa (wet) G": 7 ± 2 kPa (dry) 5 ± 2 kPa (wet) tanδ: 0.11 (dry) 0.1 (wet)
	1 %w/v type I collagen + HA20		66 ± 9 μm	E_{comp}: 95 ± 4 kPa (dry) E_{bend}: 1660 ± 25 kPa (dry) 3.0 ± 0.2 kPa (wet) G': 113 ± 6 kPa (dry) 55 ± 3 kPa (wet) G": 10 ± 2 kPa (dry) 6 ± 1 kPa (wet) tanδ: 0.09 (dry) 0.1 (wet)

Table 2.12 A summary of collagen-HA scaffolds published in recent studies focusing on materials, methods, pore size and mechanical properties [114,181].

2.4.3 Layered Scaffolds

As established previously, the function of the native aortic valve derives from the combined contributions of the fibrosa, the spongiosa, and the ventricularis, which in other words means that the single-layer scaffolds reviewed above are not structurally nor functionally sufficient to act as TEHVs. To address this deficiency, Chen et al. developed bi-layer scaffolds based on collagen and elastin [182]. The multi-step freeze-drying successfully produced scaffolds with well-connected interfaces, uniform microstructure, and bending anisotropy (Table 2.13), showing that the layered scaffold is the future of TEHV research.

Bi-layer Scaffolds	100% collagen / 50% collagen-50% elastin	100% collagen / 20% collagen-80% elastin

	WC	AC	WC	AC
E_{bend1} (kPa)	71 ± 8	74 ± 5	21 ± 5	21 ± 4
E_{bend2} (kPa)	22 ± 4	39 ± 4	10 ± 2	18 ± 1

Table 2.13 The effective bending modulus of the bi-layer scaffold designs exhibiting the desired bending anisotropy in both the WC and the AC directions [182].

After confirming the feasibility of constructing layered structures, a tri-layer scaffold design with 100 % collagen as the fibrosa, 50 %–50 % collagen-chondroitin-4-sulfate (C4S) as the spongiosa, and 20 %–80 % collagen-elastin as the ventricularis was successfully fabricated, maintaining the desired bending anisotropy in both the non-hydrated and hydrated states (Table 2.14) [183]. Although lacking characterisation of the inter-layer shear force and the dampening effect of the middle layer, this study laid the foundation for later research on natural polymeric tri-layer scaffolds aimed at TEHV applications including this thesis. Another tri-layer scaffold design of similar compositions with 100 % as the fibrosa, collagen-HA interpenetrating polymer network (IPN) as the spongiosa, and 50 %–50 % collagen-elastin as the ventricularis was successfully developed with satisfying microstructure and no delamination between layers (Table 2.15), further confirming the potential of the tri-layer designs and the importance of the research conducted in this thesis [114,181].

	WC	**AC**
E_{bend1} (kPa)	55 ± 5	51 ± 5
E_{bend2} (kPa)	13 ± 2	30.0 ± 0.9
$E_{bend, wet}$ (kPa)	1.6 ± 0.2	2.5 ± 0.2

Table 2.14 The effective bending modulus of the 100 % collagen / 50 %–50 % collagen-C4S / 20 %–80 % collagen-elastin scaffold in both the non-hydrated and hydrated states, exhibiting the bending anisotropy.

low strain modulus (kPa)	10 ± 5
high strain modulus (kPa)	83 ± 6
extensibility (%)	18 ± 5
failure strain (%)	35 ± 5
E_{bend} in WC (kPa)	35 ± 5
E_{bend} in AC (kPa)	45 ± 3

Table 2.15 The mechanical properties of the 100 % collagen / C0-HA20 / 50 %–50 % collagen-elastin scaffold.

Based on the current progress, several challenges remain unresolved with the tri-layer scaffold being native valve leaflet replacement, especially with atelocollagen being the starting material. As can be seen from the tables, the mechanical properties of most natural polymeric scaffolds are still notably lower than those of the native heart valves, especially in the hydrated state, which is the physiological condition for their application. Crosslinking has the potential to improve the structural mechanical strength to a certain extent, yet an extreme degree of crosslinking poses a counterproductive impact on cell behaviours. Therefore, this thesis intends to explore a partial crosslinking technique to find the middle ground between sufficient mechanical strength and enough leftover reactive sites for cell bonding. Moreover, the most recent study mentioned that due to the different water uptake abilities of collagen, elastin, and HA, the tri-layer scaffold fabricated could potentially be subject to a mismatching swelling behaviour when hydrated, which further leads to delamination [184]. It is also important to characterise the time-dependent properties such as stress relaxation, creep deformation, and fatigue, ensuring the structural duration during the temporary implantation before the new tissue is regenerated.

2.5 Summary

Compared to mechanical and bioprosthetic valves, natural polymeric TEHVs are the future alternatives for aortic valve replacement due to their regeneration and biodegradation abilities. Collagen, elastin, and HA are abundantly distributed in the human aortic valve ECM, rendering them suitable candidates as scaffold materials for their cell affinity and structural importance. The ideal TEHV construction aims to mimic the native heart valve leaflet in aspects of structure, composition, and mechanical properties. The three layers in the native aortic valve, the fibrosa, the spongiosa, and the ventricularis, each exhibit distinct composition and hence functions, therefore, it is important for this thesis to match the tri-

layer structure with corresponding compositions for each layer to achieve matching mechanical properties with native valves, among which the most important aspect to recreate is the characteristic bending anisotropy introduced by different tensile and compressive responses of each layer.

Freeze-drying is one most commonly used scaffold fabrication methods, which is chosen for its ability to create the porous structure needed for cell penetration, nutrient-waste exchange, and vasculogenesis. Chemical crosslinking is proven to effectively enhance the inherently weak mechanical strength of natural polymers, and EDC/NHS chemistry is chosen for this thesis as the crosslinking agent for effective crosslinking and avoidance in denaturation. Moreover, partial crosslinking is chosen for this thesis, aiming to create a balance between sufficient mechanical properties and enough reactive sites for cell bonding. Several single-layer collagen-only and tri-layer scaffolds were successfully fabricated, and they demonstrated interconnected porous structures, proportionally matching mechanical properties, and the desired bending anisotropy. However, no tri-layer tissue engineering scaffold aimed at cardiovascular applications based on atelocollagen has been reported, leaving an important and necessary gap for this thesis to fill. Additionally, the further challenges lay in poor mechanical behaviours in the hydrated state and possible delamination due to mismatching swelling abilities across the layers are to be addressed in this thesis.

Chapter 3 Fabrication and characterisation of single-layer scaffolds

3.1 Introduction

This chapter is dedicated to the fabrication and characterisation of the single-layer scaffolds that would be used for tri-layer scaffold construction, from the atelocollagen fibrillogenesis and fibrillar elastin gel synthesis to scaffold non-enzymatic degradation, with a focus on suspension flow properties, scaffold microstructure and pore morphology, and scaffold chemical structure and crosslinking effectiveness. The purity of the pepsin-extracted atelocollagen was confirmed immediately after extraction with sodium dodecyl sulfate-polyacrylamide gel electrophoresis (SDS-PAGE). The successful fibrillogenesis occurrence was inspected on macroscopic and microscopic levels, with the signature D-banding pattern imaged using scanning electron microscopy (SEM), ensuring the feasibility of atelocollagen as a commercial polymeric collagen replacement as the scaffold material. The flow properties of the scaffold precursors, the suspensions, were characterised for a better understanding of the microstructure and interactions between the polymeric chains while providing a benchmarking viscosity standard for repeatability and minimising the batch-to-batch difference. With the porous scaffold structure being formed, the characterisation spotlight shifted to pore morphology and the chemical structure alteration introduced by crosslinking, with the former being examined by SEM and the latter by Fourier-transform infrared spectroscopy (FTIR). The water uptake ability and the degradation resistance were studied via the swelling test and the non-enzymatic degradation test, aiming to understand the interaction between the scaffolds and their intended application physiological environment. This chapter aims to demonstrate the fabrication and characterisation of the single-layer scaffolds in an experimentally chronological manner, laying the foundation for the next step, the tri-layer scaffold construction.

3.2 Materials and Methods

3.2.1 Materials

Type I atelocollagen, hyaluronic acid, and elastin were chosen as the tissue engineering heart valve materials in this thesis. Three batches of pepsin-extracted collagen of slight differences were kindly gifted by Dr. David Brand (Collagen Research Core, Memphis Veterans Affairs Medical Centre's Research Service), including type I collagen from bovine skin (skin collagen), type I collagen from bovine amnion (amnion collagen), and type I with trace amount of type III, IX, and XI collagen from bovine amnion (amnion* collagen). Amniotic membranes from *Bos tarus* were obtained from a farm with a closed (certified BSE-free) herd, separated from other placental tissues, washed and homogenised in deionised water and centrifuged. Several cycles of resuspension and centrifugation were used to remove any residual blood. Homogenates were resuspended in acid and subjected to a limited pepsin digest to degrade serine-protease-sensitive proteins. The product was subjected to repeated rounds of differential salt precipitation to separate type I collagen from other collagen moieties. Purified bovine amnion type I collagen was subjected to analysis by SDS-PAGE, lyophilised and shipped in bulk to the UK.

Fibrillar gel elastin (FEG), a gel-formed elastin discovered by a previous group member, is reported to be both soluble and structurally intact with self-assembly properties, exhibiting the desired qualities from both monomeric and polymeric elastin. It was concluded that the mechanical properties especially the low loss factor of FEG are closer to those of natural elastin, making it more suitable for biomedical applications compared to the synthetic elastin variants currently used [184]. Another follow-up research on the effect FEG has on cell activities and *in vivo* implantation revealed that it promoted cell adhesion and endothelisation, reduced the structural stiffness for better cell response, and facilitated *in vivo*

ECM deposition and angiogenesis [185]. Therefore, FEG was chosen as the elastin variation used in this thesis.

6 mg/ml lyophilised collagen was weighed and transferred into 0.05 M ethanoic acid solution (pH 3.20), which was subsequently homogenised using a hand-held blender until the collagen had fully dissolved. The suspension continued to be centrifuged at 5000 rpm for 5 minutes, separating the air bubbles created from blending, which were later removed using a spatula. Tris-buffered saline (TBS, pH 7.60), consisting of 50 mM tris(hydroxymethyl)aminomethane, 150 mM NaCl, and drops of HCl, was prepared in advance, serving to facilitate the fibrillogenesis process. The de-bubbled afibrillar collagen suspension was added into TBS, with the solution pH adjected to physiological conditions (pH 7.20–7.50). The neutral-pH mixture was then placed into an incubator at 37 ºC for a few hours to allow fibrillogenesis, and the resulting fibrillar collagen suspension produced was centrifuged again, with the excessive TBS disposed of, yielding the non-crosslinked collagen suspension ready for subsequent steps.

EDC hydrochloride and *N*-hydroxysuccinimide (NHS) were chosen as crosslinking agents. 30 mM EDC and 15 mM NHS were added to deionised water instead of ethanol to preserve the structural integrity of atelocollagen, and the pH was adjusted to 4.70–4.80 using ethanoic acid. The non-crosslinked collagen suspension was gently poured into the crosslinking solution with gentle and continuous stirring and the mixture was left to react at room temperature for 4 hours. Two consecutive washing steps with 1 M NaCl solution and deionised water were carried out for 2 hours each, with the mixture being centrifuged after each step to get rid of the unreacted crosslinking chemicals. The yield is referred to as the crosslinked collagen suspension.

4 mg/ml sodium hyaluronate (Fisher Scientific, USA) was weighed and slowly added into deionised water with continuous stirring until fully dissolved. 35 times excessive adipic

acid dihydrazide (ADH) was then added to the SHA solution, with the pH adjusted to 4.75 after the solution reached homogeneity. 20 mM EDC was then added while maintaining the pH, and the reaction was left to stir for 24 hours. The reaction was terminated by adding drops of NaOH to return the pH level to neutral, with the reacted solution pipetted into a dialysis cellulose membrane tube (Merck Life Science UK Limited) for further dialysis against 150 mM NaCl and deionised water for 24 hours each. The final product of the ADH-modified HA solution was obtained.

The collagen-HA mixture was obtained by simply mixing the crosslinked collagen suspension with the ADH-modified HA solution, with 24 hours of gentle stirring to reach homogeneity. Excessive HA solution was discarded after centrifuging the mixed solution, leaving the desired collagen-HA mixture ready for the next steps.

The protocol for FEG production adopted in this thesis was constructed by Dr. Sonia Iftekhar with refined adjustments [184]. 10 %wt insoluble elastin from bovine neck ligament (Merck Life Science UK Limited) was weighed and funnelled into a round bottom flask, and 0.25 M oxalic acid solution was subsequently added. The mixture was then put into a boiled water bath for 70 minutes, and this hydrolysis process was facilitated with gentle stirring and a condenser with a continuous cold-water flow. The reaction was quenched by immersing the round bottom flask into a 0 ºC ice bucket for 10 minutes, and the partially hydrolysed mixture was transferred to be centrifuged at 5000 rpm for 5 minutes. After discarding the supernatant, the pellet was mixed with 0.25 M oxalic acid solution and transferred back to the round bottom flask, ready for the second round of hydrolysis. The hydrolysis process was repeated in total three times. After the last hydrolysis, the pellet produced was rinsed against deionised water with constant stirring for an hour at room temperature, followed by four more washing steps lasting 30 minutes each to get rid of excessive oxalic acid. In between each washing cycle, the mixture was centrifuged at 5000 rpm for 5 minutes to ensure no excessive oxalic

acid was left in the system. Lastly, the pellets were merged into one tube and stored at 4 ºC overnight for further swelling and storage.

All single-layer scaffolds were fabricated using the freeze-drying method. In general, the suspensions were gently mixed before being transferred into the polytetrafluoroethylene (PTFE) moulds to maximise the homogeneity level. Spatulas were employed to assist with the moulding process, including transferring the surface flattening. The moulded samples were first stored in a -20 ºC freezer overnight and moved into a freeze-dryer (Christ I-5, Martin Christ Gefriertrocknungsanlagen GmbH, Germany) for 24 hours. For the HA-infiltrated collagen scaffolds, the freeze-dried crosslinked collagen parent network scaffold was immersed in ADH-modified HA solution with gentle stirring, and 24 hours were allowed for the establishment of the collagen-HA interpenetrating network (IPN) system. Subsequently, the infiltrated scaffold was washed in 150 mM NaCl and deionised water for 2 hours each to get rid of excessive HA solution. The washed scaffolds were then transferred back into the moulds, with a suitable amount of deionised water added to maintain the shape during further freeze-drying. The freeze-drying cycle was repeated to yield the final collagen-HA(IPN) scaffolds.

non-crosslinked skin collagen scaffold	skin unxl-col
crosslinked skin collagen scaffold	skin xl-col
crosslinked amnion* scaffold	amnion* xl-col
HA infiltrated amnion collagen scaffold	amnion col-HA(IPN)
HA infiltrated amnion* collagen scaffold	amnion* col-HA(IPN)
HA and amnion* collagen mixture scaffold	amnion* col-HA(mix)

Table 3.1 A summary of the scaffold nomenclature.

3.2.2 Characterisation

3.2.2.1 SDS-PAGE

SDS-PAGE is an electrophoresis method that separates proteins based on their molecular weight differences. The sodium dodecyl sulphate serves as a surfactant that combines with amino acids, resulting in the shielding of the intrinsic charge of the protein, leading to almost identical charge-per-unit-weight ratios. Together with the size exclusion effect of the polyacrylamide matrix, proteins start to "swim" towards the anode at various speeds when an external electric field is applied. With the assistance of staining, the separation based on protein molecular weight can be manifested.

SDS-PAGE on skin and amnion* collagen was kindly performed by Dr. David Brand immediately after extraction, and the raw data was provided for further analysis. Extracted collagen samples were first heated to about 45 ºC in Laemmli buffer, which compelled the dissociation of the collagen triple helices into randomly coiled α-chains. Approximately 5 – 15 μg sample was placed onto the gel containing 4 % stacker and 7.5 % resolver, which is more suitable for the size and shape of the rod-like collagen molecules instead of the commonly used 15 % resolver for globular structures. Coomassie Brilliant Blue was chosen to visualise the result by staining the α-chains separated and settled as different lines under electric field influence.

3.2.2.2 SEM

SEM is a type of electron microscope that characterises surface topography/microstructure by scanning the sample surface with a focused electron beam. The electron beam is emitted by the electron gun commonly made of either tungsten (W) or lanthanum hexaboride (LaB_6) and is accelerated through a controlled magnetic field onto the sample surface. Different signals including secondary electrons, backscattered electrons, and X-rays can be detected for different purposes, with secondary electron signals being collected in this study. A built-in

detector for secondary electrons (Everhart-Thornley detector) is used to collect the signal for SEM image generation.

Zeiss Merlin SEM was used to examine the successful fibrillogenesis process by visualising the occurrence of the characteristic D-banding pattern of polymeric collagen. Amnion* collagen suspensions with (fibrillar) and without (afibrillar) incubation were prepared and deposited onto aluminium SEM pin stubs with carbon tape, which were then put into a sealed desiccator under a near vacuum until fully dehydrated. The dried samples were coated with a thin layer of platinum (Leica EM ACE600) at least 24 hours before testing. The probe current and the accelerating voltage were chosen to be 100 pA and 5.00 kV due to the delicate nature of the samples. Images with various ranges of magnification were taken. The D-banding pattern was further analysed using ImageJ (National Institutes of Health, USA), with the average value calculated and compared with the data from the literature.

Zeiss EVO SEM was used to characterise the microstructure of the collagen-based scaffolds fabricated. The samples were sectioned into thin slices of 1–2 mm using a sharp surgical scalpel and were then placed on an aluminium stub with carbon tape. To create a conductive path, the samples were subsequently coated with platinum (Leica EM ACE600), and extra coating with the silver dag (Agar Scientific Ltd, UK) was brushed on the side to connect the top coating and the bottom carbon tape. The cross-section was examined with a 10.00 kV accelerating voltage and a 200 pA probe current. The pore area was analysed using ImageJ, where 100 pores were arbitrarily selected and measured in each image (N=5). The circularised pore diameter (the diameter of the circle that has the same area) was calculated for comparison between samples using Equation 3.1, with d being the diameter and A being the pore area.

$$d = 2\sqrt{\frac{A}{\pi}}$$ Equation 3.1

The overall porosity of the scaffolds was determined with gravimetry, which is of sufficient accuracy for this thesis. The mass and dimensions of each sample were measured using an analytical balance (BDH AA-200DS, VWR International GmbH, Germany) and a digital calliper (CD-6" CSX, Mitutoyo, UK), and the density of the samples was calculated using Equation 3.2. The porosity is in its essence the hollow space within the porous structure, which can therefore be deduced based on the scaffold density and the pure material according to Equation 3.3. The density of pure collagen adopted here is 1.35 g/cm^3 according to the literature [186].

$$\rho_{scaffold} = \frac{mass\ (g)}{volume\ (cm^3)} \qquad \text{Equation 3.2}$$

$$porosity = 1 - \frac{\rho_{scaffold}}{\rho_{pure\ material}} \qquad \text{Equation 3.3}$$

3.2.2.3 Rheology

Rheology is the science of the flow and deformation behaviours, among which viscosity is one of the main parts. Viscosity is the macroscopic manifestation of the internal friction between adjacent layers of fluid that are in relative motion. In other words, viscosity represents the resistance to shear deformation. Static (or apparent) viscosity can be defined using Equation 3.4, where η represents viscosity (mPa·s), τ shear stress (mPa), and γ shear rate (s^{-1}). Viscosity can be measured using the rotational mode of the rheometer, with the measuring bob turning in one direction. The measurement is often presented as the flow curve, which displays the viscosity change with a gradually changing shear rate. Complex viscosity (η*), on the other hand, is obtained with the geometry oscillating around the axis under different angular frequencies.

$$\eta = \frac{\tau}{\gamma} \qquad \text{Equation 3.4}$$

Both types of viscosity were characterised using an Anton Paar MCR702 Rheometer at the Laboratory for In-situ Microscopy and Analysis, Department of Engineering Science, University of Oxford. All suspensions were produced shortly before testing, and the experiment temperature was controlled at 4 ºC achieved by a Peltier temperature control (Deben, UK). A geometry of 25 mm stainless steel parallel plate was chosen with sandpaper stuck on for better grip, and the initial gap was set at 1 mm. After lowering the geometry down, the excessive sample volume was trimmed off along the edges using a spatula. The samples (N=5) were first subjected to a series of angular frequencies (0.1–10 Hz), with the constant shear strain being 0.3 %. Immediately after the frequency sweep, a static flow curve was generated by shearing the sample under a continuously changing shear rate ranging from 0.001–1000 s^{-1}. All collagen-only suspensions were crosslinked. The data was analysed using OriginLab 2021b.

3.2.2.4 FTIR

FTIR is a widely used chemical structure characterisation method for detecting existing functional groups in organic compounds, which measures the light absorbance as a function of wavelength. This technique relies on the interferometer built in to generate an interferogram that consists of all frequencies of light, which in turn shine through the sample compartment and reach the detector. The interference patterns were created by the centre 45 º beamsplitter simultaneously transmitting and reflecting the beam from the light source into two beams, which respectively strike a fixed mirror and a mirror moving at a constant speed and converge at the beamsplitter again. The energy absorbed at each wavelength corresponds to a certain bond vibration, which makes FTIR a powerful instrument that highlights the possible existence of specific functional groups and their relative intensity. The correlated

intensity information can also be transformed into the concentration molecules or functional groups via Beer-Lambert's Law.

Varian Excalibur FTS 3500 FT-IR Spectrometer was used to perform FTIR characterisation on the three types of lyophilised collagen samples as received, the insoluble elastin as purchased, the FEG produced, the SHA as purchased, and the ADH-modified HA as synthesised. The samples (N=3) were examined at a resolution of 4 cm^{-1} under the aperture setting of 0.5 cm^{-1} at 2000 cm^{-1}, with each test repeated in total of three times. The resultant spectrum (ranging from 4000–600 cm^{-1}) gives absorbance in the function of wavelength, and all the spectra and the second derivative and peak deconvolution analysis were processed using Origin 2021b.

3.2.2.5 Swelling

The swelling ratio is an important parameter for biomaterials as it represents the water uptake ability and the interaction of the material with the physiological environment [187]. Based on preliminary attempts, the swelling tests were conducted only on crosslinked scaffolds in phosphate-buffered saline (PBS) at room temperature with the submersion time being 1 hour. The samples (N=5) were weighed before and after hydration and the weights were recorded as m_0 and m_1 respectively, and the water uptake ratio (Q_m) was defined as the ratio of the mass difference (m_1-m_0) to the dry mass m_0 (Equation 3.5). The filter paper was used to absorb the extra water after hydration to give more accurate results with the absorbing time being about 10 seconds.

$$Q_m\ (\%) = \frac{m_1 - m_0}{m_0} \times 100\% \qquad \text{Equation 3.5}$$

Some preliminary swelling tests were conducted on some non-crosslinked collagen-only samples at 4 ºC, room temperature (estimated to be 20–25 ºC), and 37 ºC within the timeframe of 24 hours, aiming to probe the effect of the ambient temperature and swelling

duration time on the water absorption. The temperatures are chosen as 4 ºC is the common storage temperature for biological samples, room temperature is the operation temperature, and 37 ºC is the physiological temperature. Samples (N=5) were weighed before PBS immersion and the dry mass was recorded. The hydrated mass was recorded after the samples were put into the prepared PBS at different temperatures after 1 h, 2 h, 4 h, 8 h, 12 h, and 24 h, and filter paper was used to drain excessive water.

3.2.2.6 Degradation

A non-enzymatic degradation test was performed to investigate the viability of future *in vitro* work potential. The duration of the degradation test was 12 weeks, which aligns with the duration of a wide range of *in vitro* tests, and the test was conducted under physiological temperature (37 ºC) with gentle shaking, and the weight of the samples was measured weekly at the same time. Six types of collagen-based single-layer scaffolds and the elastin-only scaffolds (N=5) were cut into pieces of approximately 5 mm * 5 mm and were immersed in 2 ml of PBS with 0.04 g sodium azide (Merck Life Science UK Limited) in falcon tubes overnight at 37 ºC in the water bath with the revolutions per minute being 100. The original mass ($mass_0$) was recorded the following morning by removing the samples from the PBS and leaving them to drain on a metal mash for 1 minute before weighing, and the weekly mass ($mass_n$, n=1–12) was measured the same way, with the PBS solution changed every week for better sample preserving. The degradation extent is recorded as the mass loss each week compared to the original mass using Equation 3.6.

$$mass\ loss\ (\%) = \frac{mass_0 - mass_n}{mass_0} \times 100\%, n = 1,2, \dots ,12 \qquad \text{Equation 3.6}$$

3.2.2.7 Statistics

All data was presented as average, with the standard deviations as the error. The Student t-test was used when comparing two data groups, and the one-way analysis of variance (ANOVA) followed by the Tukey HSD post hoc test was employed when comparing three or more data groups. The probability value of 95 % ($p < 0.05$) as the statistical significance criterion.

3.3 Result

3.3.1 SDS-PAGE

The interpretation of the SDS-PAGE results is focused on the purity of the collagen extracted instead of its molecular weight due to the unique shape of the collagen molecules, i.e., the normally used molecular weight standards in the migration radius determination are aimed at globular proteins; with collagen molecules having extended helical structures and thus a different migration pattern, the standards are no longer good indications of the true molecular weight. Therefore, a middle ground was found to run the extracted atelocollagen sample against the commercial collagen with known purity as a standard comparison. It is noted that the commercial collagen molecular weight distribution is usually characterised by gel permeation chromatography (GPC).

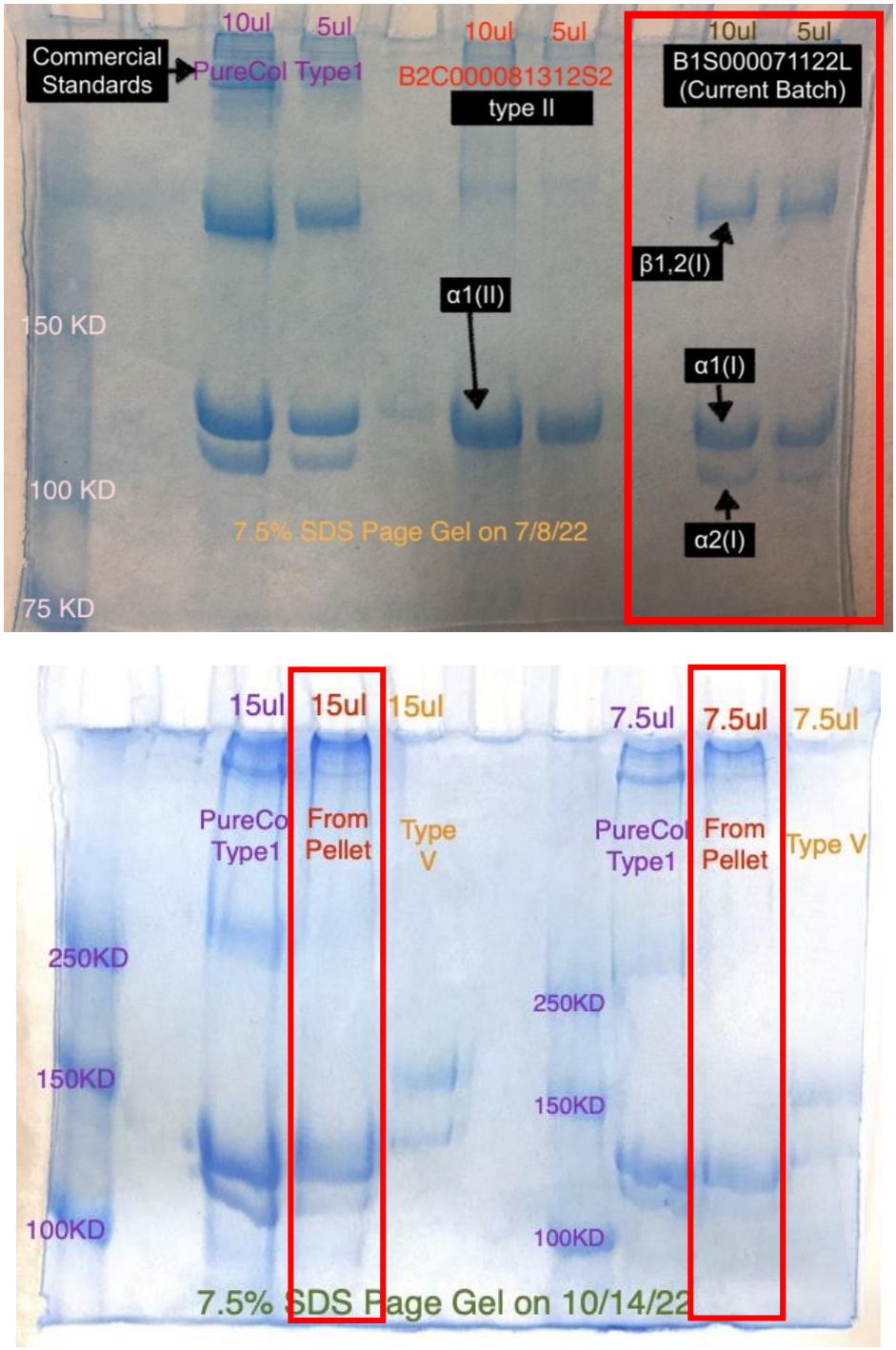


Figure 3.1 The SDS-PAGE results of the extracted skin collagen (above, labelled Current Batch) and amnion* collagen (below, labelled From Pellet). Pure commercial type I collagen (Commercial Standards/PureCo Type1) is the standard column. α1(I) and α2(I) represent the two types of α-chains composing type I collagen molecule, and β1,2(I) denotes partially dissociated dimer α1(I) + α2(I).

It can be seen from Figure 3.1 that both gels presented the two distinctive bands at about 110 kDa and 120 kDa, which corresponds to α1(I) and α2(I) chains respectively [188,189].

The intensity of α1(I) is roughly twice that of α2(I), confirming the typical [2α1(I) + 1α2(I)] type I collagen structure [190]. The amnion* collagen is shown to be more prone to degradation at 45 ºC in the Laemmli buffer, which potentially indicates a lesser extent of pre-crosslinking. Overall, it can be concluded that the extracted collagen received are type I collagen with high purity.

3.3.2 Fibrillogenesis

The fibrillogenesis is a characteristic fibre-formation process where the collagen fibrils self-assemble into fibre bundles. For better structural integrity, the monomeric collagen fibrils are preferred to be constructed into their polymeric counterpart first. Therefore, successfully proving the fibrillogenesis occurrence is the first step towards further scaffold manufacturing. In this thesis, both macroscopic and microscopic evidence are provided in support of the fibre formation.

During the collagen suspension production, the texture and appearance were observed to go through obvious changes. As can be seen in Figure 3.2, the afibrillar collagen suspension displayed a moderate level of transparency with less viscosity while its fibrillar counterpart exhibited opaque turbidity and oscillatory motion akin to jelly.

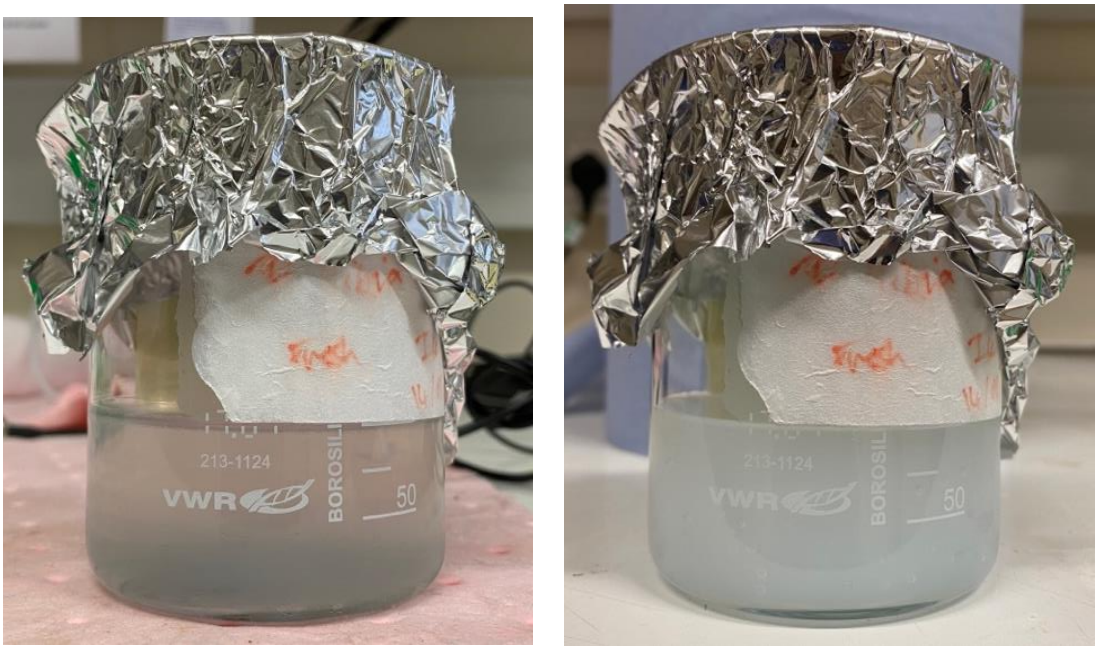


Figure 3.2 The collagen suspension before (left) and after (right) incubation.

Microscopically, the characteristic repeating D-bending pattern of collagen is chosen as the fibrillogenesis indicator, which is frequently investigated using either transmission electron microscopy [191,192] or atomic force microscopy [193–195]. With the help of Robin Scale, a colleague within the department, the D-banding feature of the reconstructed bovine collagen was able to be imaged using SEM for the first time, further visualising the process of fibrillogenesis more simply. Figure 3.3 demonstrates the distinct contrast between afibrillar and fibrillar collagen ultrastructure, namely, no discernible fibrous structure was observed in the afibrillar sample whereas evident randomly oriented spaghetti-resembling fibres were observed in the fibrillar sample. The distinctive D-banding pattern of the collagen fibre self-assembly was prominently displayed, with the measured spacing being 69.3 nm (measured across 43 bands on a singular fibre), which agrees with various literature [60,196,197]. It is worth noting that the precise percentage of the fibrillogenesis portion was unable to be characterised, more discussion on future improvement will be given in the future work section.

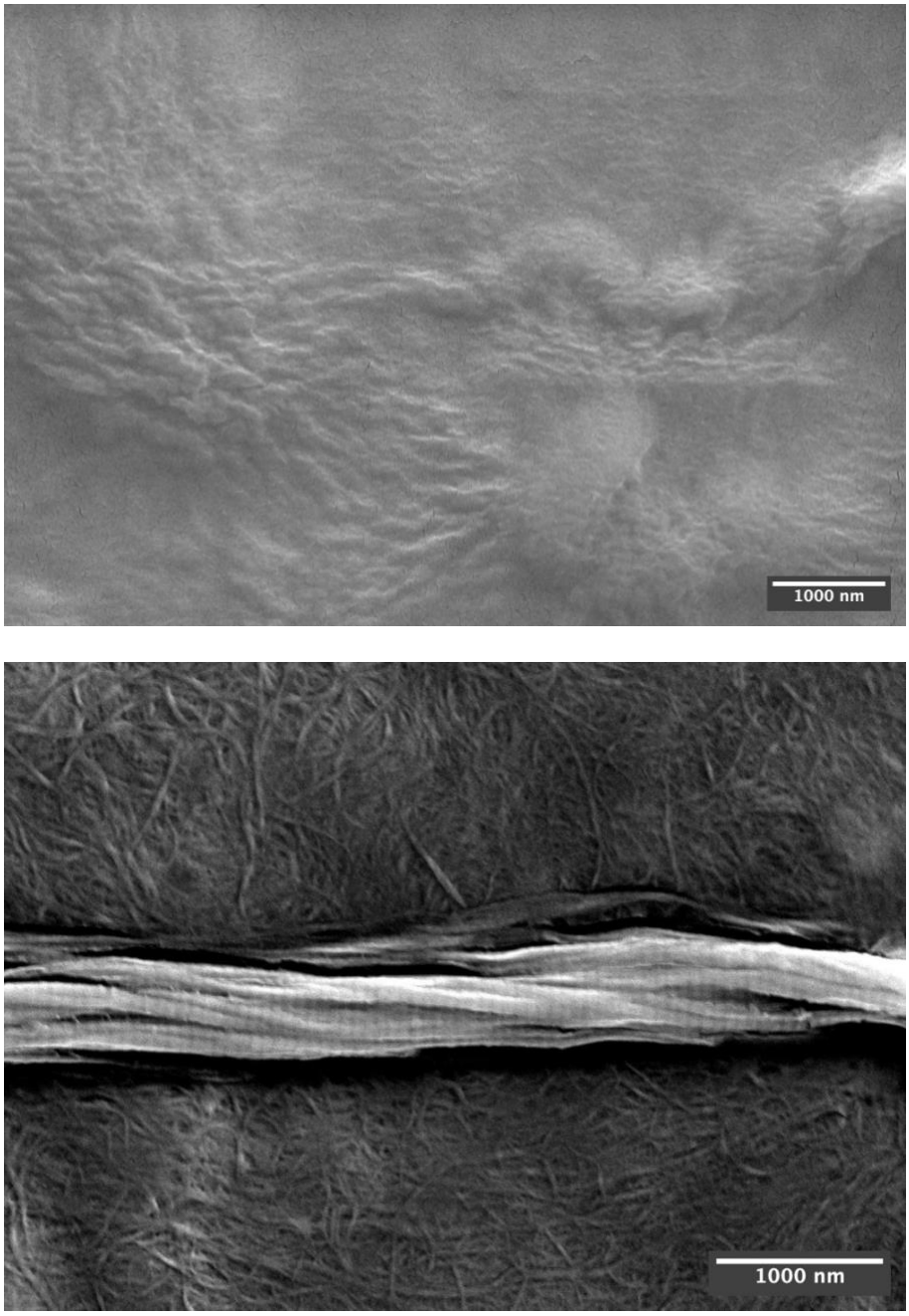


Figure 3.3 The SEM images of the collagen suspension before (above) and after (below) fibrillogenesis. No fibrillar feature was shown in the afibrillar image, forming a distinct contrast with the established fibrous structure observed in the fibrillar sample. The characteristic D-banding pattern can be easily spotted in the fibrillar sample.

3.3.3 Rheology

Figure 3.4 presents the flow curves showing the viscosity of all the sample solutions tested, revealing the correlation between the static viscosity and the shear rate. A decreasing

viscosity trend with a continuously increasing shear rate can be observed for all sample types, reflecting the expected shear-thinning behaviour of pseudoplastic fluids [198]. Based on the data obtained, the curves were compared with the theoretical Ostwald de Waele model shown in Equation 3.7, where η is the viscosity (mPa·s), γ is the shear rate (s^{-1}), K is the consistency coefficient (mPa·s^n), and n is the flow behaviour index [199]. The parameters of the fitted lines are organised in Table 3.2, which shows that the experimental results fitted well with the power law model except for the amnion*-HA mixture ($R^2 > 0.99$).

$$\eta = K\gamma^{n-1} \qquad \text{Equation 3.7}$$

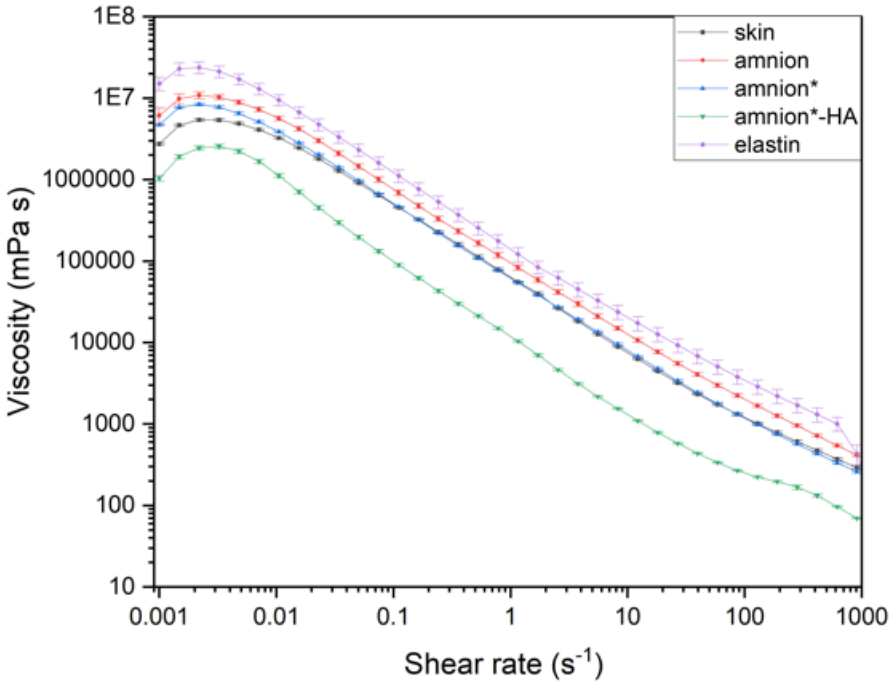
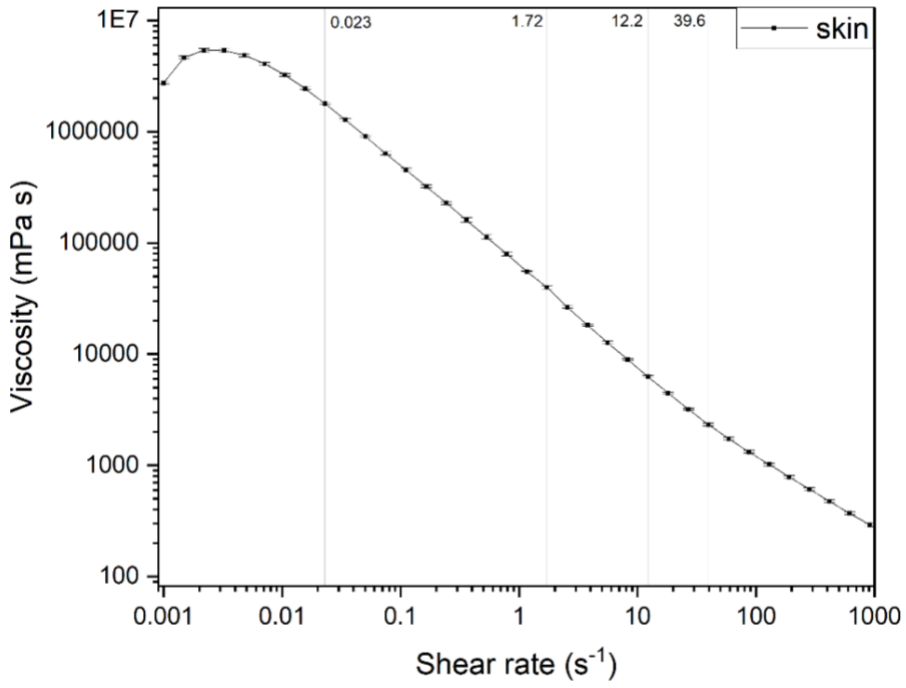


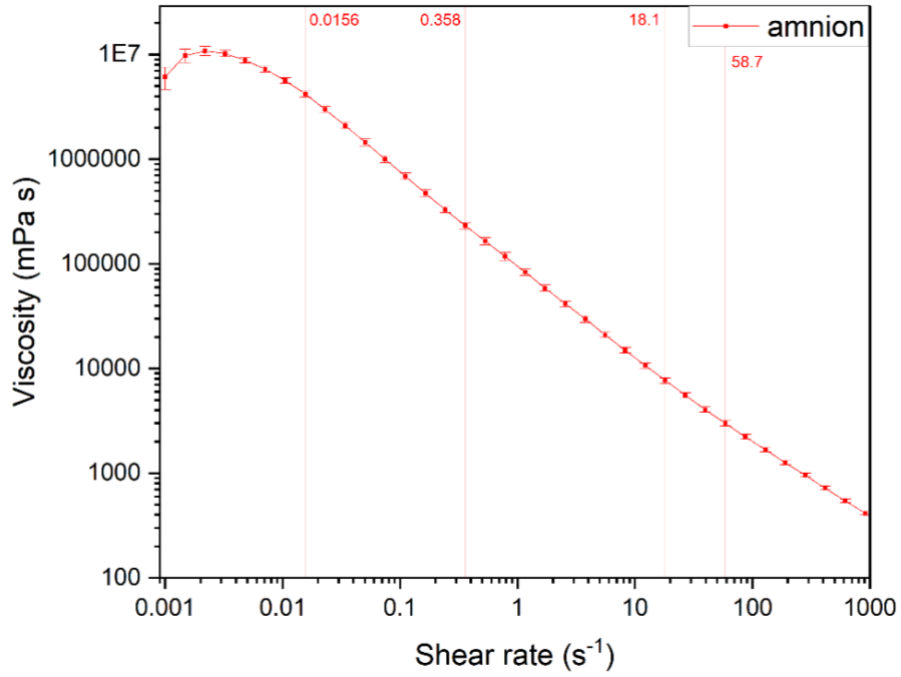
Figure 3.4 The flow curves of the various crosslinked collagen-based suspension and non-crosslinked FEG samples, plotted under the logarithm scale. *The first four data points are excluded when fitting into the linear model as the equipment sensitivity has hindered true value measurement but are preserved for data completion.

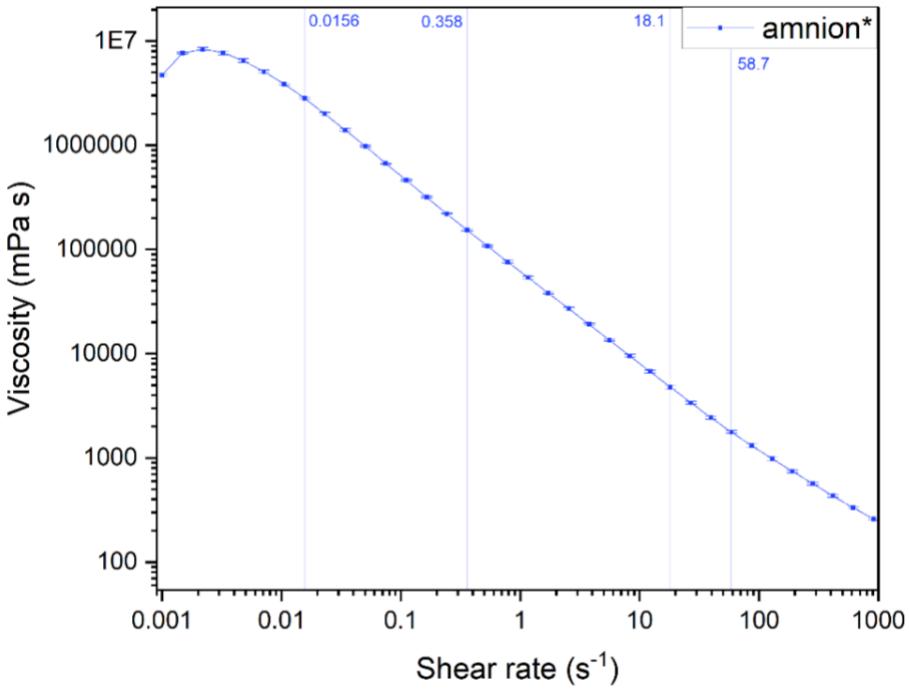
	intercept	K (Pa·s^n)	n	R^2
skin	4.79 ± 0.01	62.0	0.142 ± 0.008	0.997
amnion	5.02 ± 0.01	104	0.158 ± 0.006	0.998
amnion*	4.824 ± 0.009	66.7	0.133 ± 0.006	0.998
amnion*-HA	4.06 ± 0.04	11.6	0.18 ± 0.02	0.981
elastin	5.23 ± 0.01	169	0.145 ± 0.007	0.998

Table 3.2 The fitted parameters of the Ostwald-de-Waele-model fitting of the various samples under the shear rate ranging from 0.0048 to 913 s^{-1}.

Among the five types of samples tested, the FEG exhibited the highest viscosity overall, whereas the collagen-HA mixture showed a notably lower viscosity in comparison. The three collagen-only crosslinked suspension samples displayed a similar viscosity, comparable with the literature (about 100 Pa·s at 1 s^{-1} and about 10 Pa·s at 10 s^{-1}) [200], with the flow curves of the skin and amnion* collagen largely overlapping. Despite the satisfactory data-theory alignment marked by good R^2 values, it can be noticed that there exist several slight slope-changing points in all the curves as shown in Figure 3.5. Further Ostwald model fitting was performed with the parameters organised in Table 3.3. It can be summarised that generally, the suspensions exhibit reducing pseudoplastic behaviours when the shear rate increases and the significant decline in the consistency coefficient K only appears when the shear rate reaches a higher range. Compared to the more regularly sectioned FEG and collagen-only suspensions, HA seemed to have introduced a less linear correlation between the viscosity and the shear rate, but the aforementioned trend stands.




0.0156
0.358
18.1
58.7
amnion
1E7
1000000
100000
10000
1000
100
Viscosity (mPa s)
0.001
0.01
0.1
1
10
100
1000
Shear rate (s-1)


0.0156
0.358
18.1
58.7
amnion*
1E7
1000000
100000
10000
1000
100
Viscosity (mPa s)
0.001
0.01
0.1
1
10
100
1000
Shear rate (s-1)

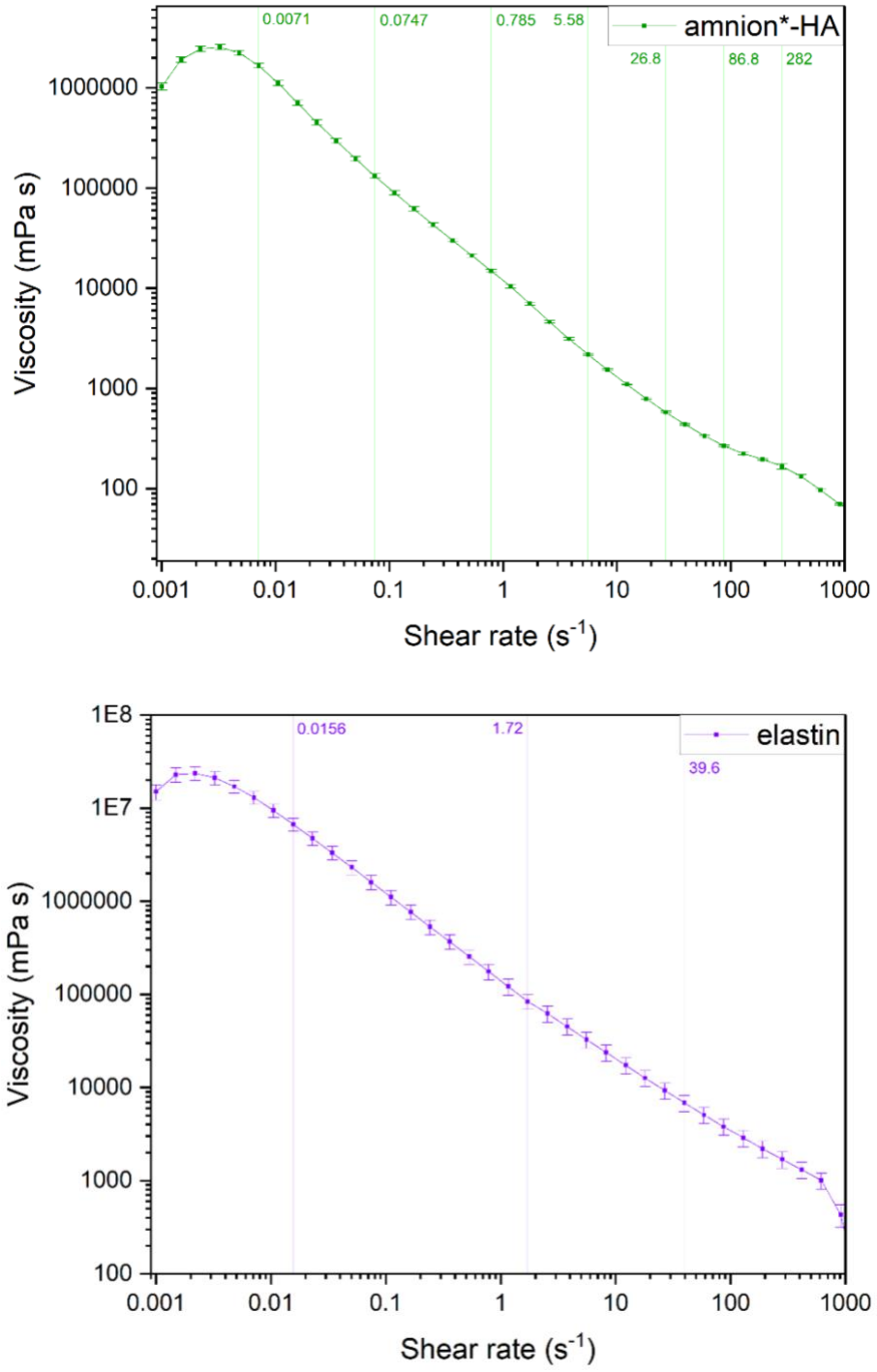


Figure 3.5 The flow curves of crosslinked skin collagen, crosslinked amnion collagen, crosslinked amnion* collagen, crosslinked amnion* collagen-HA mixture, and FEG in order, with points of slope change labelled.

skin collagen				
	intercept	K (Pa·s^n)	n	R^2
low shear rate	4.804 ± 0.002	63.7	0.111 ± 0.002	1.000
lower middle	4.803 ± 0.009	63.5	0.07 ± 0.01	0.999
upper middle	4.71 ± 0.01	51.2	0.157 ± 0.009	1.000
high shear rate	4.41 ± 0.01	25.7	0.339 ± 0.006	0.999

amnion collagen				
	intercept	K (Pa·s^n)	n	R^2
low shear rate	4.949 ± 0.005	89.0	0.069 ± 0.004	1.000
lower middle	4.976 ± 0.001	94.6	0.128 ± 0.002	1.000
upper middle	4.89 ± 0.01	77.8	0.198 ± 0.008	1.000
high shear rate	4.743 ± 0.006	55.3	0.281 ± 0.002	0.999
amnion* collagen				
	intercept	K (Pa·s^n)	n	R^2
low shear rate	4.767 ± 0.003	58.4	0.062 ± 0.003	1.000
lower middle	4.79 ± 0.01	61.6	0.116 ± 0.001	1.000
upper middle	4.73 ± 0.02	54.2	0.16 ± 0.01	1.000
high shear rate	4.47 ± 0.02	29.4	0.303 ± 0.008	0.999
fibrillar elastin gel				
	intercept	K (Pa·s^n)	n	R^2
low shear rate	5.149 ± 0.002	141	0.066 ± 0.002	1.000
mid shear rate	5.117 ± 0.003	131	0.195 ± 0.003	1.000
high shear rate	4.93 ± 0.01	85.5	0.306 ± 0.007	0.999

Table 3.3 The fitted parameters of the Ostwald-de-Waele-model fitting of the various samples sectioned into different shear rate ranges.

Under the oscillating frequency sweep conditions, all suspensions still exhibited the shear thinning behaviour, which is consistent with the previous results from the static tests as well as the literature [201]. Within the tested frequency range (0.1–10 Hz), the complex viscosity and the frequency displayed a near-perfect linear correlation with a similar sensitivity to frequency increment among all five sample types. FEG exhibited a slightly more sensitive response to a higher frequency, which could be attributed to its elastic nature. Meanwhile, the collagen-HA(mix) suspension underwent a dampened shear-thinning, proving that the HA addition effectively introduced an impact-absorbing mechanism. The curves were once again fitted with the Ostwald model with the parameters organised in Table 3.4, and the K-value is observed to be roughly the same as the complex viscosity value at 1 Hz (denoted in Figure 3.6).

	intercept	K (Pa·s^n)	n	R^2
skin	1.681 ± 0.004	48.0	0.088 ± 0.008	0.999
amnion	1.919 ± 0.002	82.9	0.111 ± 0.003	1.000

amnion*	1.846 ± 0.002	70.1	0.108 ± 0.003	1.000
amnion*-HA	1.315 ± 0.003	20.7	0.185 ± 0.005	1.000
elastin	2.299 ± 0.002	199	0.062 ± 0.002	1.000

Table 3.4 The fitted parameters of the Ostwald-de-Waele-model fitting of the various samples under the testing frequency ranging from 0.1 to 10 Hz.

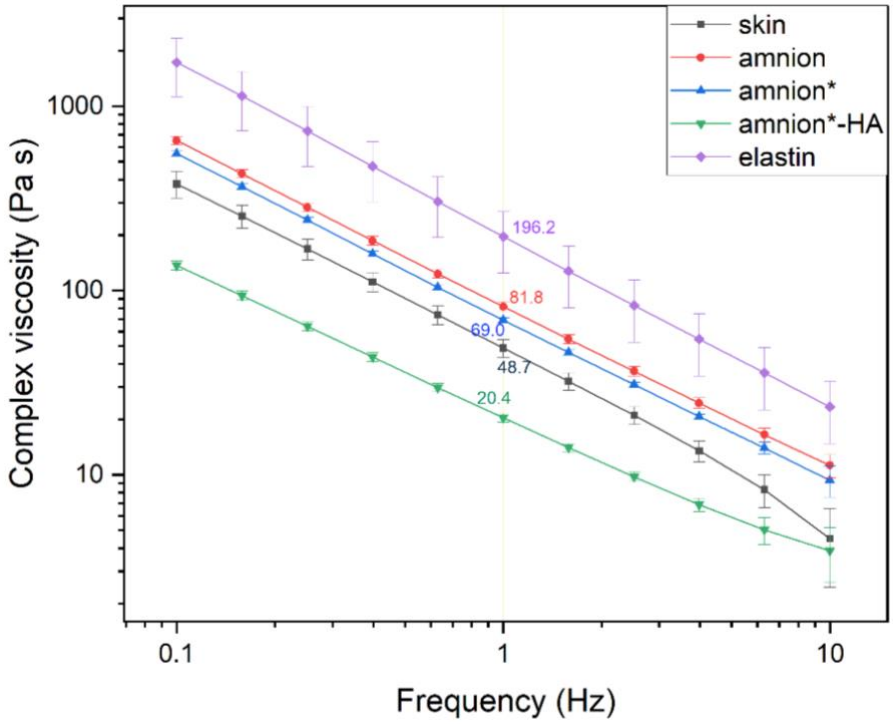


Figure 3.6 The complex viscosity at different testing frequencies of different suspensions.

3.3.4 FTIR

The typical pure collagen FTIR spectrum contains five characteristic peaks: amide A, amide B, amide I, amide II, and amide III as shown in Figure 3.7. Among these peaks, amide A (~ 3300 cm^{-1}) and amide B (~ 3075 cm^{-1}) are associated with N–H stretching. Amide I (~ 1633 cm^{-1}) results from C=O stretching coupling with N–H bending and C–N stretching while Amide II (~ 1546 cm^{-1}) is determined by N–H bending coupling with C–N stretching, and amide III (~ 1280 cm^{-1}, ~ 1240 cm^{-1}, ~1202 cm^{-1}) is a three-peak complex resulting from the combined influence from C–N stretching, N–H bending, C–C stretching, and C–H bending. Ester band (~1164 cm^{-1}), which mainly originates from the C–O stretch in the

carbonyl group, serves as a crosslinking extent indicator together with amide II, representing ester bond and amide bond formation respectively [202–206].

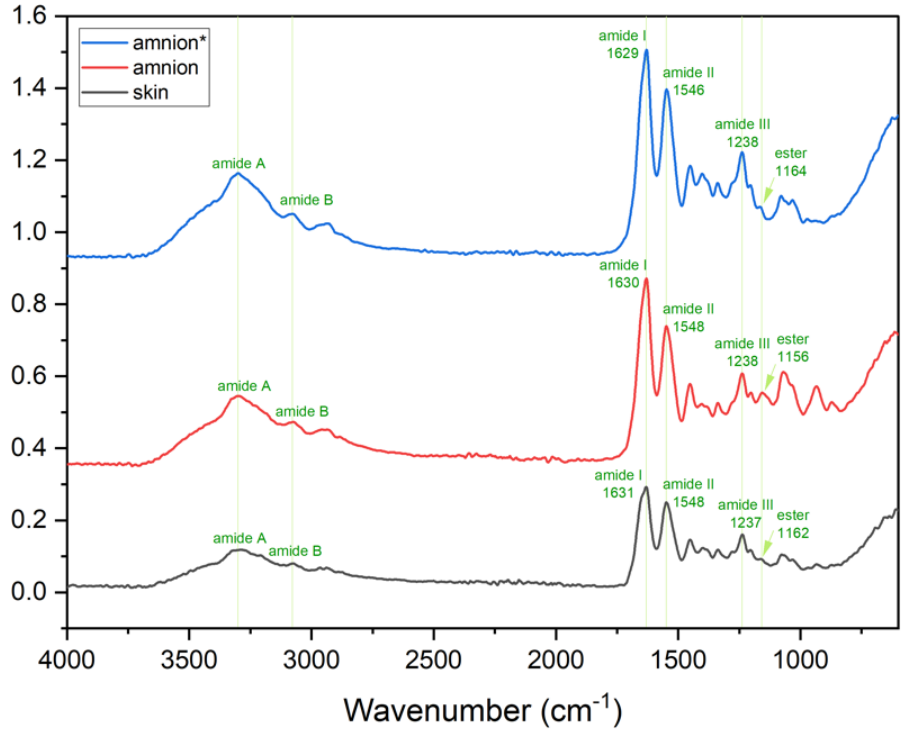


Figure 3.7 The characteristic collagen peaks (amide A, amide B, amide I, amide II, and amide III) demonstrated by the FTIR spectra of the skin, amnion, and amnion* collagen as received.

Traditionally, the amide I band is further deconvoluted in search of overlapping peaks indicating different protein secondary structures due to its sensitivity to secondary structure changes. However, the strong water interference limits the accuracy of this method. The amide III band, on the other hand, is also subject to protein secondary structure change and is easily resolved and better defined, rendering it a more suitable resource in protein secondary structure analysis [207]. Both second derivative analysis and peak deconvolution were performed on the collagen spectra to reveal the overlapping peaks and to conduct quantitive analysis, with an example of the latter shown in Figure 3.8. The peak assignment is organised in Table 3.5. In type I collagen, ~ 1285–1270 cm^{-1} is typically assigned to α-helix, ~ 1255–1230 cm^{-1} is assigned to random coils, and ~ 1220–1200 cm^{-1} is assigned to β-sheets [202,207,208]. The peak area was also integrated to give an estimation of the composition of the

different secondary structures, and the results were organised into Table 3.6. It can be observed that the collagen obtained from three different sources all showed consistent compositions, with the undefined structure (random coil) being the majority and a slightly higher percentage of α-helix than β-sheet. Moreover, comparing the results of amide I deconvolution with that of the amide III deconvolution, it can be confirmed that the amide III band is better for peak quantitive analysis for its better precision.

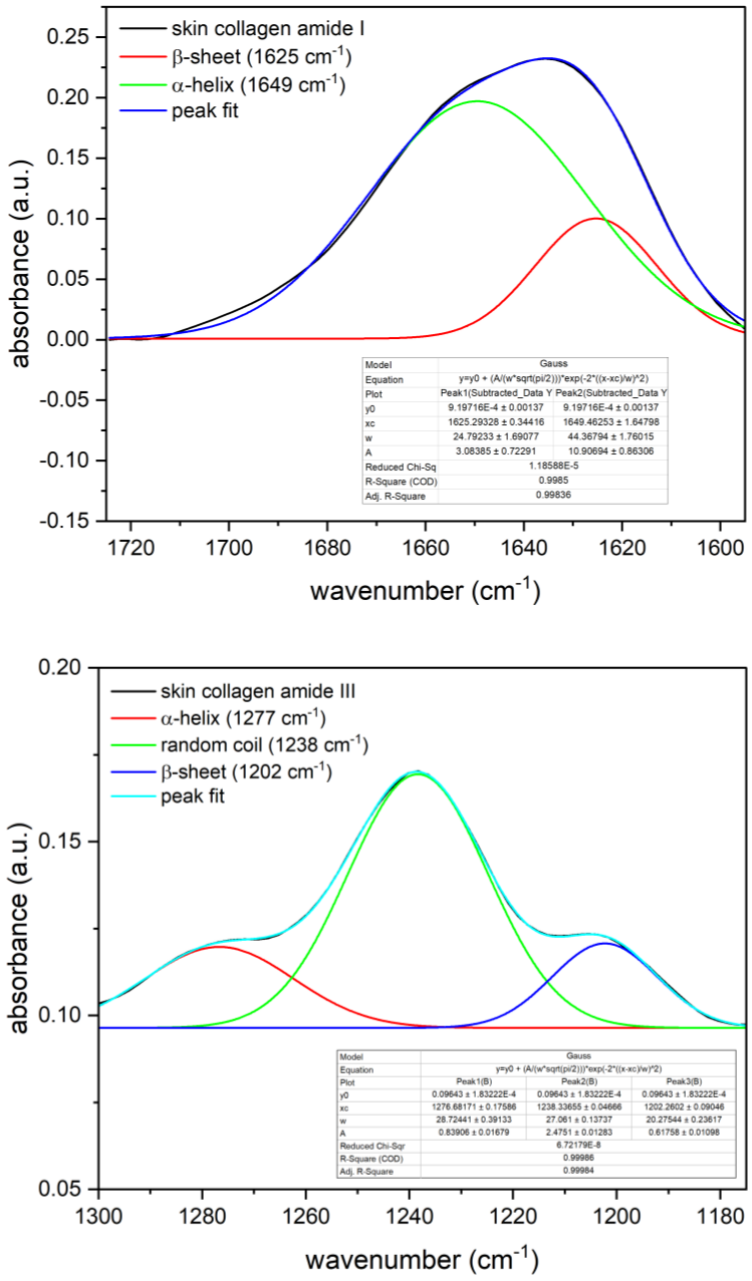


Figure 3.8 The peak deconvolution of the amide I (above) and amide III (below) of skin collagen as an example.

	α-helix	β-sheet	α-helix	random coil	β-sheet

skin	1649	1625	1277	1238	1202
amnion	1649	1625	1274	1239	1202
amnion*	1649	1625	1274	1239	1202

Table 3.5 The band assignments of the amide I (green) and amide III (blue) bands from the FTIR spectra of the skin, amnion, and amnion* collagen tested.

	α-helix	β-sheet	α-helix	random coil	β-sheet
skin	78	22	21	64	15
amnion	66	34	23	64	13
amnion*	69	31	21	63	16

Table 3.6 Estimated composition (%) of the secondary structure of the skin, amnion, and amnion* collagen derived from the peak areas of the deconvoluted amide I (green) and amide III (blue) peaks.

Similar peak analysis was performed on the skin and amnion* collagen scaffolds before and after crosslinking to investigate the effect of the fabrication and crosslinking methods on the secondary structure of collagen, with the peak assignment and the estimated composition in percentage organised in Table 3.7 and Table 3.8. It can be seen that after freeze-drying, the β-turn signal (~ 1700–1660 cm^{-1}) appeared and the wavenumber is relatively consistent apart from a major shift from the crosslinked skin collagen scaffolds. The collagen-only scaffolds fabricated are observed to exhibit no major shifts in peak numbers, indicating that the fabrication method chosen can preserve the secondary structure of the collagen. Crosslinking, on the other hand, has seen a major shift in β-turn structure in skin collagen scaffolds and the composition percentage change across all the samples, which is within expectation as amide I is expected to shift being the major target to the EDC/NHS chemistry. However, the amide III/1450cm^{-1} (assigned to CH_2) intensity ratio of all the collagen scaffolds remained at about 1, which indicates that the triple helical structure of monomeric collagen was preserved throughout sample production [209,210].

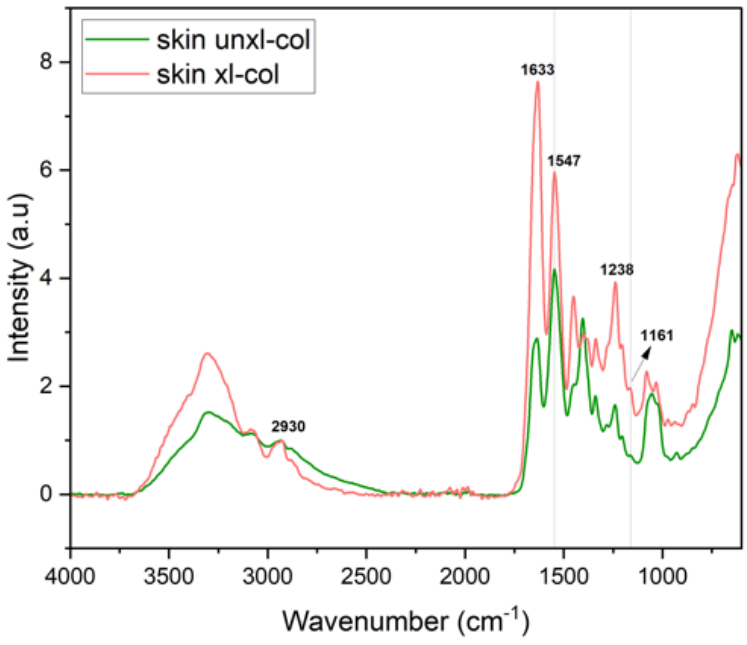
	β-turn	α-helix	β-sheet	α-helix	random coil	β-sheet
skin unxl-col	1692	1653	1627	1272	1239	1203
skin xl-col	1667	1658	1629	1269	1237	1203
amnion* unxl-col	1692	1654	1628	1276	1240	1202
amnion* xl-col	1691	1655	1627	1272	1237	1202

Table 3.7 The band assignments of the amide I (green) and amide III (blue) bands from the FTIR spectra of the skin and amnion* collagen scaffolds tested.

	β-turn	α-helix	β-sheet	α-helix	random coil	β-sheet
skin unxl-col	7	70	23	20	64	16
skin xl-col	37	14	49	26	56	18
amnion* unxl-col	6	73	21	21	64	15
amnion* xl-col	5	56	39	20	65	15

Table 3.8 Estimated composition (%) of the secondary structure of the skin and amnion* collagen scaffolds derived from the peak areas of the deconvoluted amide I (green) and amide III (blue) peaks.

FTIR spectra of the non-crosslinked and crosslinked scaffolds made of skin and amnion* collagen (Figure 3.9) were further normalised against 2930 cm^{-1}, which is assigned to CH_2 stretching and remains unaffected by the process of crosslinking [141,211]. It can be seen that amide peaks and ester band intensified, indicating effective crosslinking had occurred. Amide I at 1633 cm^{-1} is chosen as the indicator for amide formation [212], of which the relative intensity together with that of the ester band at 1161 cm^{-1} were shown in Figure 3.10. The relative crosslinking extent was calculated and summarised in Table 3.9, with both amide I and ester band intensities more than doubled for both types of collagen. It is worth noticing that the amide I/II ratio of non-crosslinked scaffolds was reduced to <0.70, but the crosslinking process restored the ratio to the level of raw material.



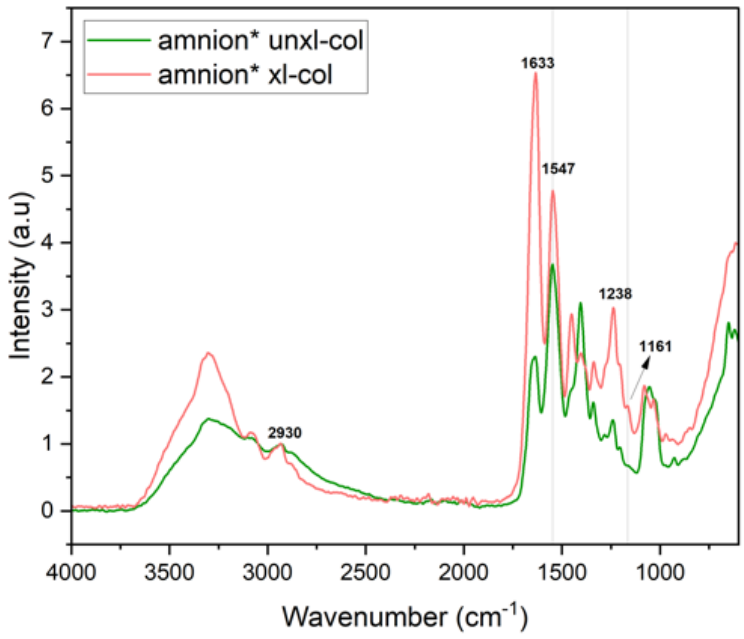


Figure 3.9 FTIR spectra of the non-crosslinked and crosslinked scaffolds made from skin collagen (above) and the non-crosslinked and crosslinked scaffolds made from amnion* collagen (below).

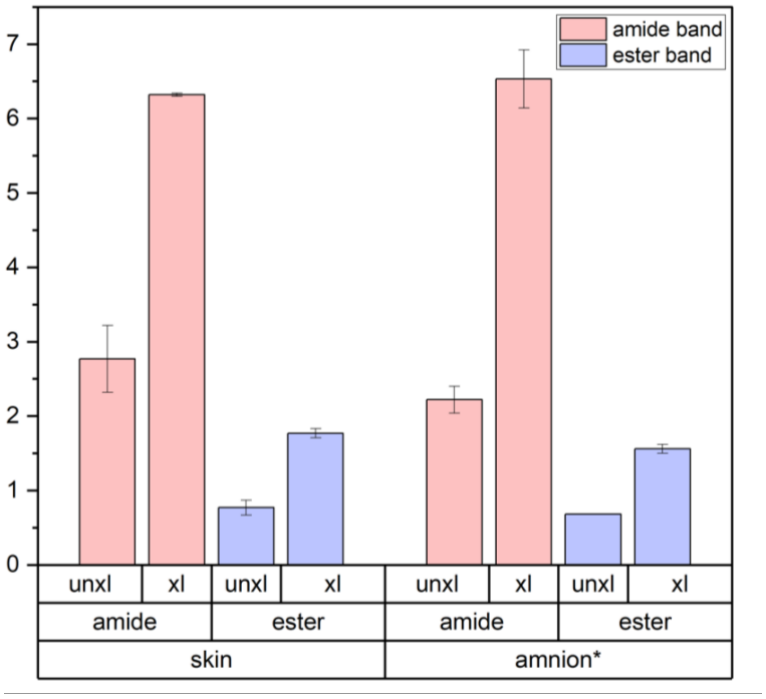


Figure 3.10 The relative crosslinking extent of amide I (1633 cm^{-1}/2930 cm^{-1}) and ester band (1161 cm^{-1}/2930 cm^{-1}) before and after crosslinking for skin and amnion* collagen.

	amide bond	ester bond
	1633 cm^{-1}/2930 cm^{-1}	1161 cm^{-1}/2930 cm^{-1}
skin	2.28	2.30
amnion*	2.94	2.29

Table 3.9 The relative crosslinking extent based on the relative intensity of amide I and ester bands of scaffolds made from skin and amnion* collagen.

A polysaccharide-specific peak at 1036 cm^{-1} resulting from C-O-C stretching in the glycosidic ring structure in HA is appointed to be the indicator of HA incorporation [213,214]. It can be seen from Figure 3.11 that, compared with the crosslinked collagen scaffold without HA, both HA incorporating methods investigated showed successful HA addition. The relative intensity of the cyclic ether band at 1036 cm^{-1} was calculated against 2930 cm^{-1}, and it can be seen that the mixing HA and collagen suspension introduces more HA than infiltrating already crosslinked scaffold in HA solution with significant differences ($p < 0.001$) (Figure 3.12).

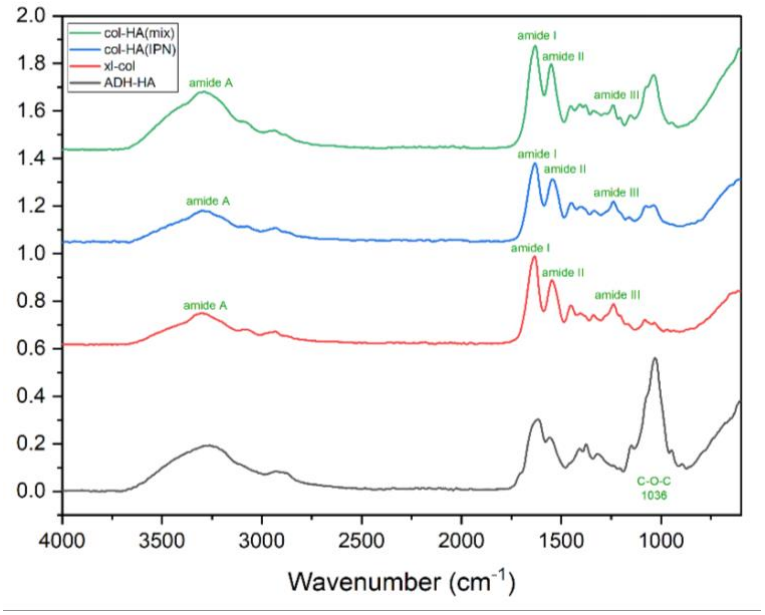


Figure 3.11 FTIR spectra of ADH-modified HA and scaffolds made from amnion* collagen before and after different methods of HA incorporation.

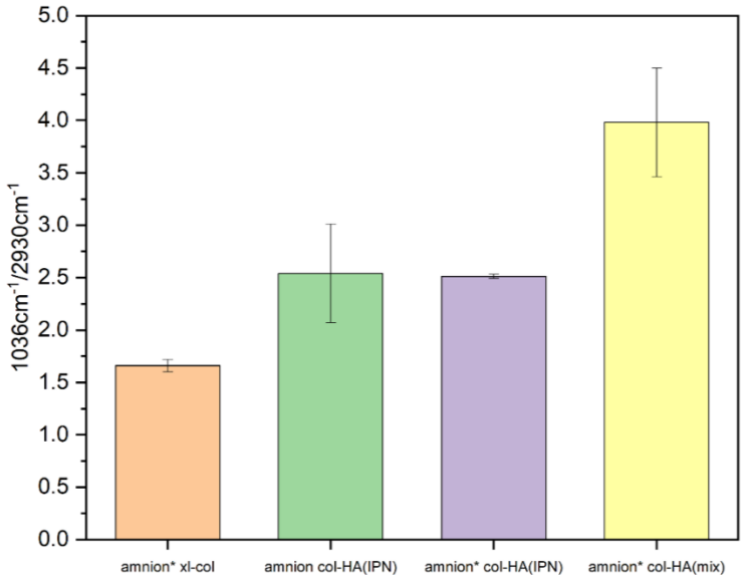


Figure 3.12 The relative intensity (1036 cm^{-1}/2930 cm^{-1}) is calculated as an indication of the HA incorporation efficiency.

3.3.5 Microstructure

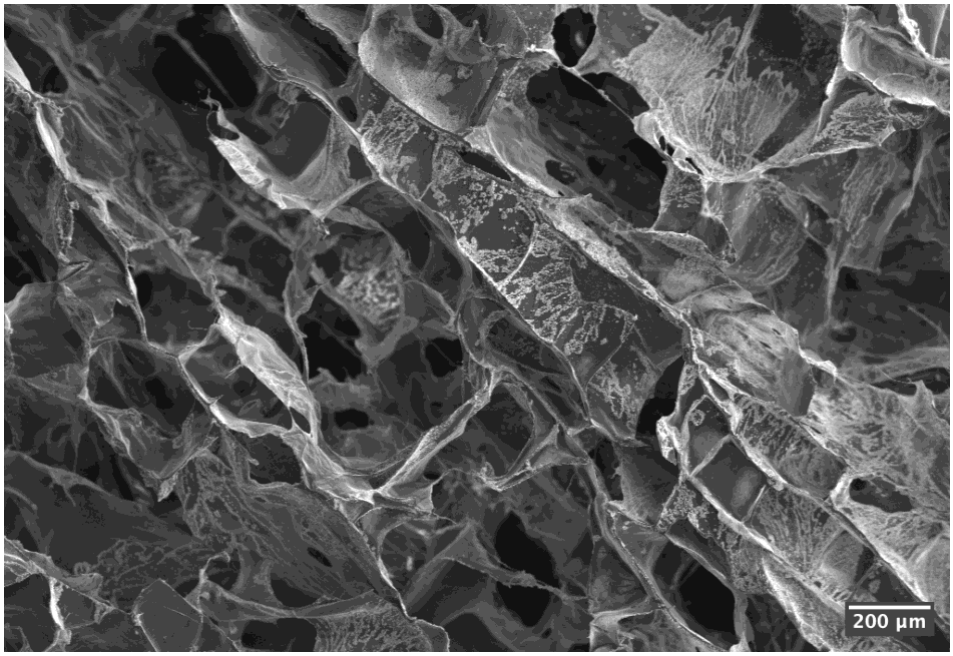
The porosities of the scaffolds (with grouping code from i to vii) are organised in Table 3.10. Generally speaking, the porosities of all the scaffolds reached over 97 %, meeting the porosity requirement for cell population and nutrition/waste exchange [215]. From scaffold groups {i and iii}, it can be observed that collagen sourced from different regions, i.e., bovine amnion and bovine skin, yielded scaffolds with different porosity; from scaffold groups {v and vi} it can be concluded that the trace amount of other collagen types in the amnion* collagen had no significant influence on the porosity value ($p > 0.35$). Scaffold groups {iii and iv} showed that the partial EDC/NHS crosslinking influenced the scaffold porosity positively ($p < 0.01$). HA, and different incorporating methods were also shown to affect the scaffold porosities. HA infiltration decreased the porosity value judging by groups {iv and vi} while HA mixing increased the porosity according to groups {iv and vii}. All $p < 0.001$ if not stated otherwise.

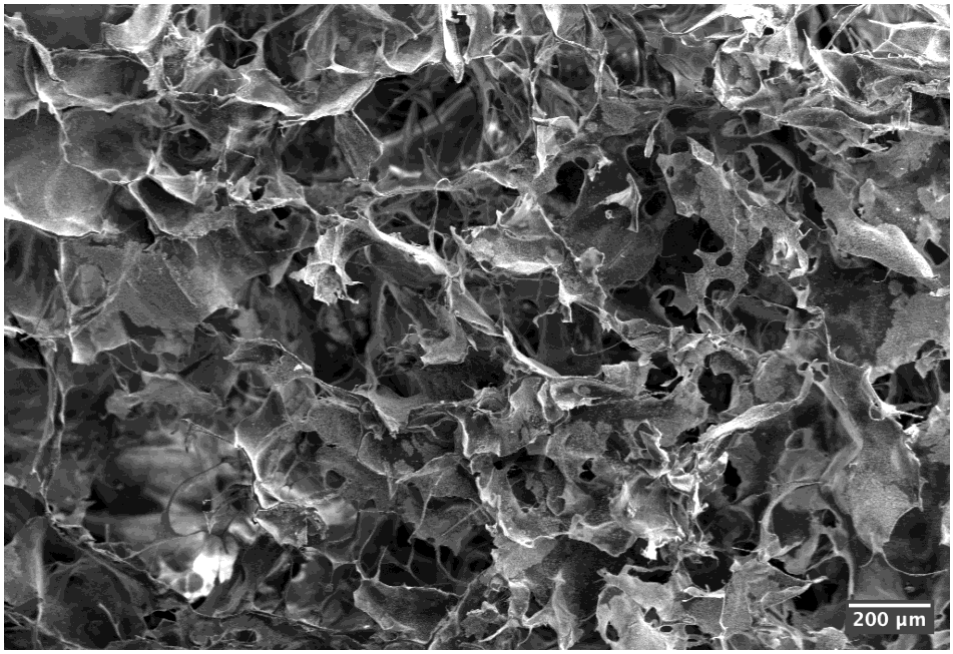
	average porosity	standard deviation

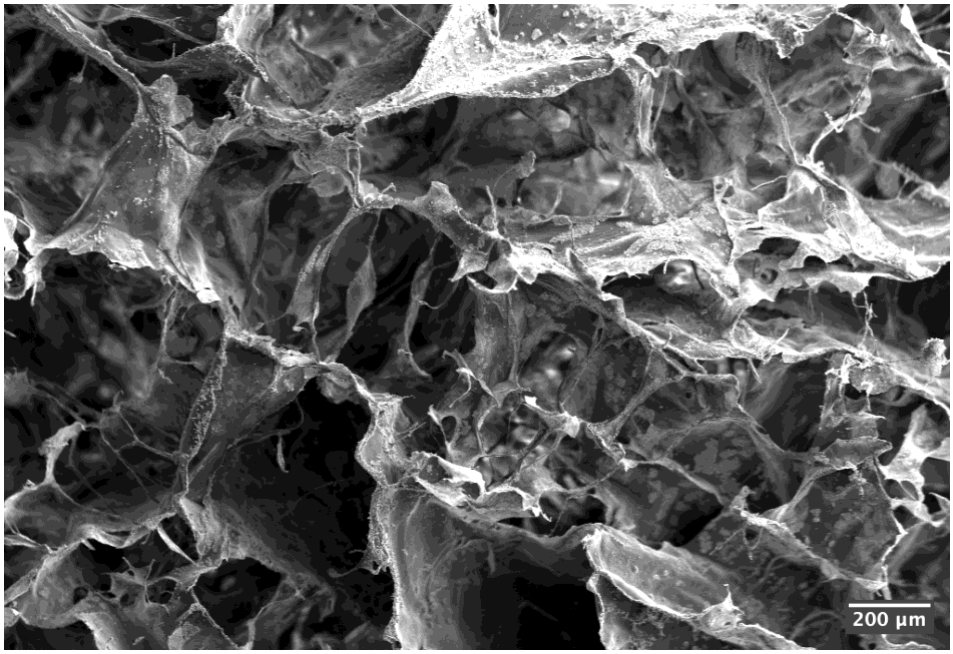
skin unxl-col (i)	97.77 %	0.02 %
skin xl-col (ii)	98.13 %	0.05 %
amnion* unxl-col (iii)	98.40 %	0.05 %
amnion* xl-col (iv)	98.55 %	0.05 %
amnion col-HA(IPN) (v)	97.7 %	0.4 %
amnion* col-HA(IPN) (vi)	97.9 %	0.1 %
amnion* col-HA(mix) (vii)	99.04 %	0.04 %

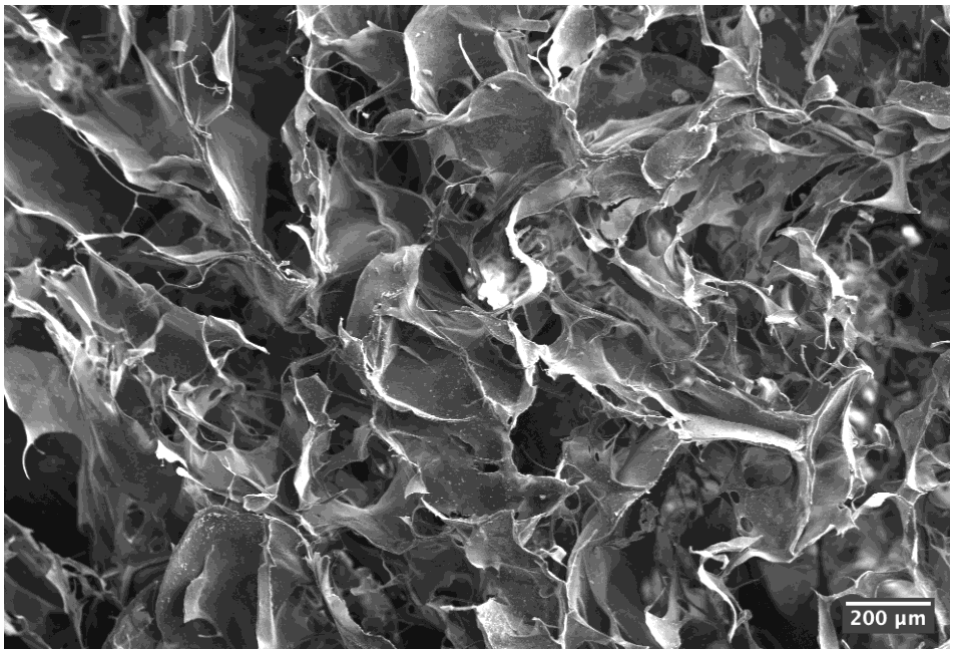
Table 3.10 The porosities of various scaffolds grouped from i to vii, shown by average and standard deviation.

Figure 3.13 presents representative SEM images of the following scaffold types in order: skin unxl-col, skin xl-col, amnion* xl-col, amnion col-HA(IPN), amnion* col-HA(IPN), and amnion* col-HA(mix). All scaffolds showed an interconnective pore morphology and were structurally intact, proving that the fabrication methods, i.e., the freeze-drying and the EDC/NHS partial crosslinking, successfully produced scaffolds with the desired microstructure. Scaffolds made of skin collagen exhibited a more integrated structure and a better-oriented pore alignment without crosslinking, and the pore walls became less intact with the pores being yet more evenly distributed after crosslinking. The crosslinked amnion* collagen scaffolds, on the other hand, exhibited a well-balanced combination of pore size homogeneity and pore structure integrity. The non-crosslinked amnion* samples, however, were not rigid enough for the sectioning and, therefore were not able to be characterised. The HA-containing scaffolds shared the basic features with the collagen-only scaffolds with a noticeable emergence of secondary pores in the IPN samples and HA threads.


200 µm


200 µm


200 µm


200 µm

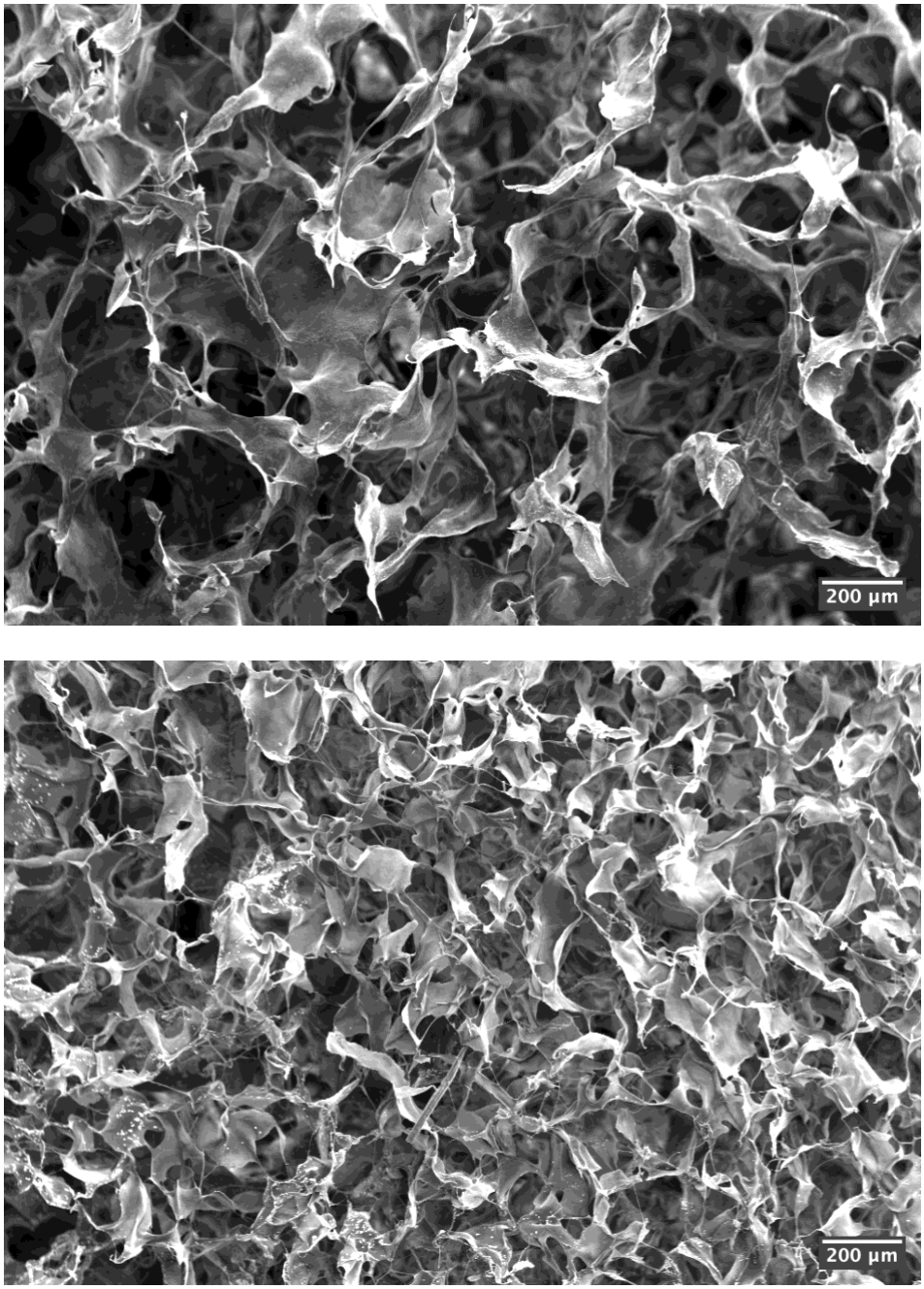
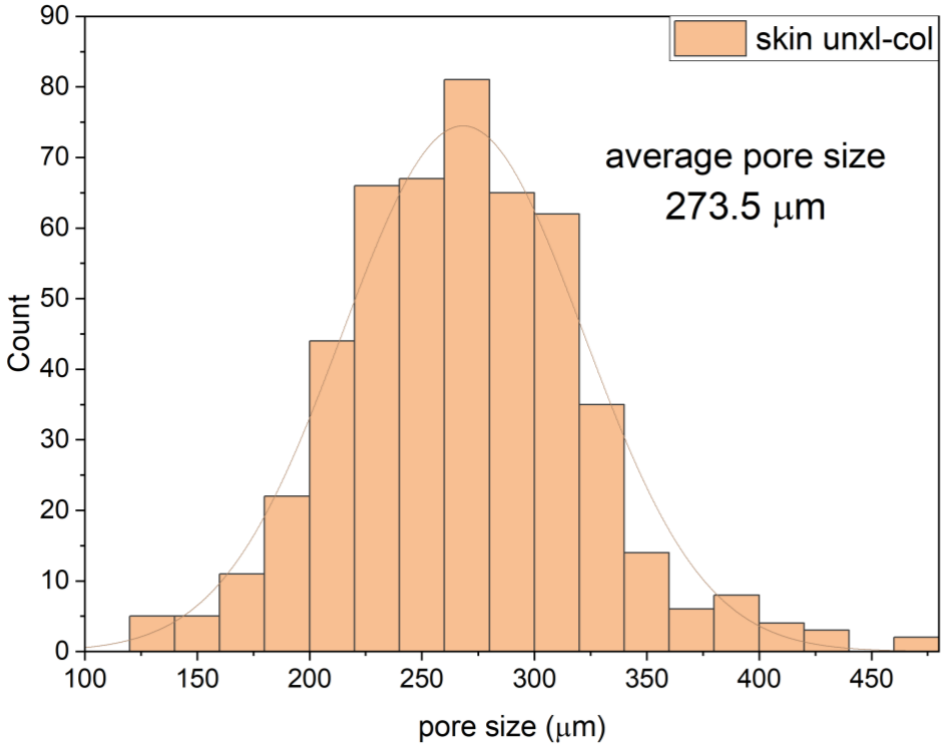
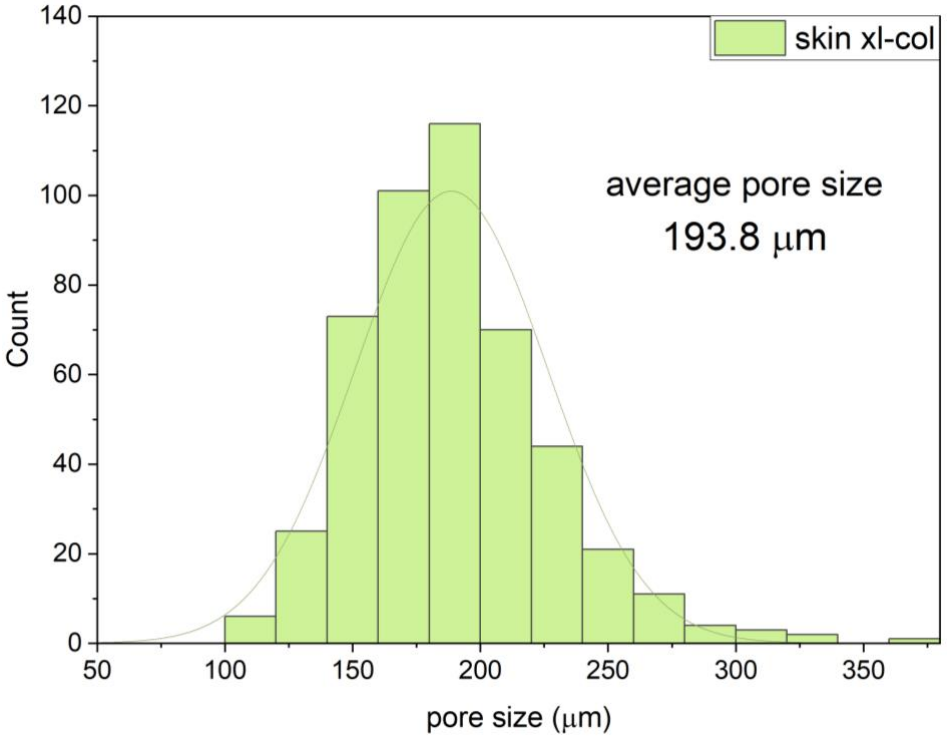


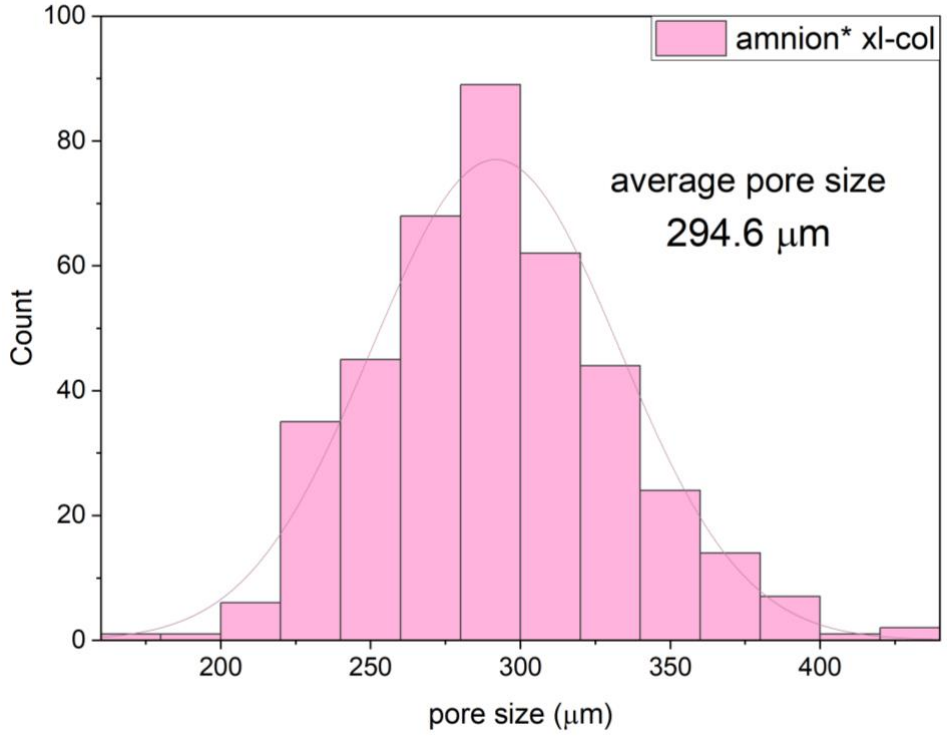
Figure 3.13 The representative SEM images of a) skin unxl-col, b) skin xl-col, c) amnion* xl-col, d) amnion col-HA(IPN), e) amnion* col-HA(IPN), and f) amnion* col-HA(mix) scaffolds (in order), imaged at the magnification of 50 times (50x).

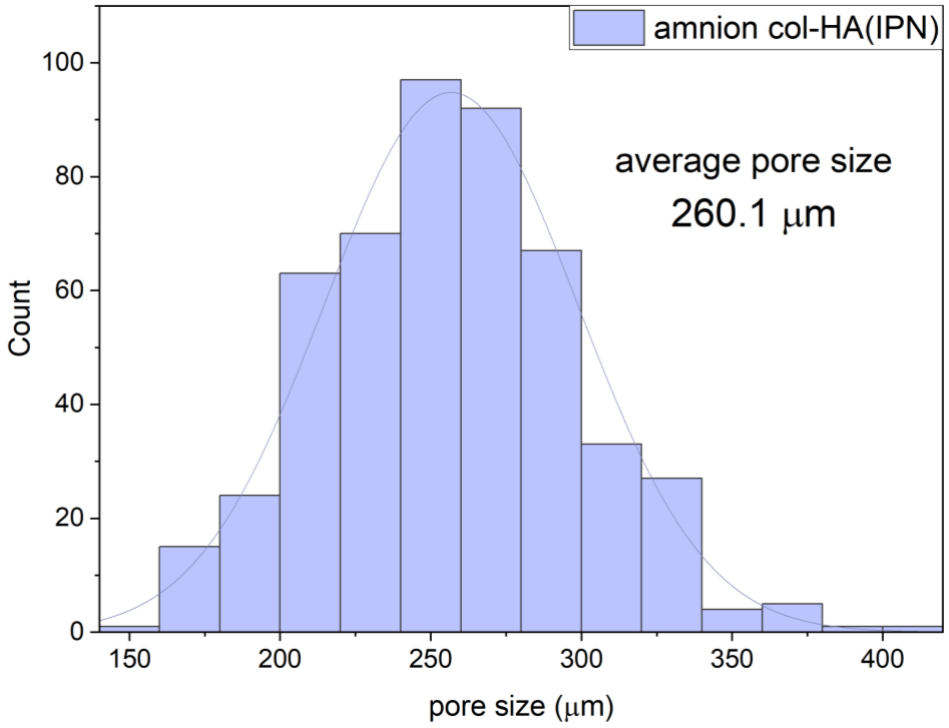
Figure 3.14 further visualised the pore size distribution of each sample type using average circularised pore size. The partial EDC/NHS crosslinking was shown to reduce the pore diameter by almost 30 % (from 273.5 µm to 193.8 µm), and HA infiltration was shown to further diminish the pore size of the crosslinked amnion* scaffolds by nearly 20 % (from

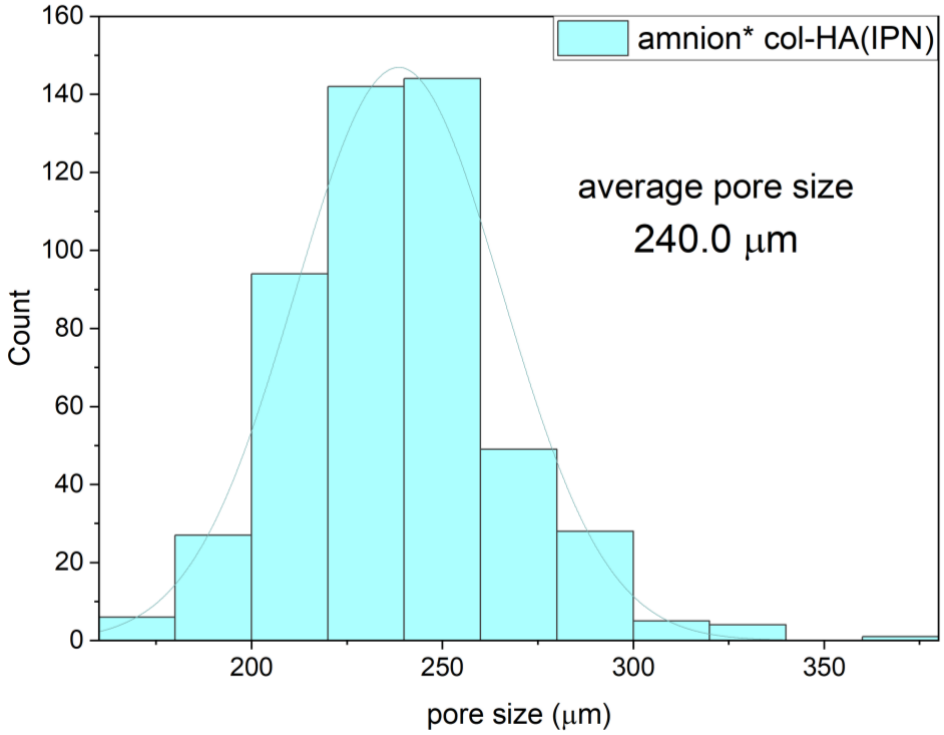
294.6 μm to 240.0 μm). Different HA incorporation methods were observed to show obvious contrast in the pore size, with the mixing method yielding significantly smaller pores than the infiltrating method (179.3 μm compared to 240.0 μm). Different collagen types were deemed to have an impact on the pore size as well, with the amnion collagen resulting in the largest pores and the skin collagen the smallest. The optimal pore size of individual applications varies based on the seeded cell type and the focused cell activities, there, therefore, exists no "golden standard" in the pore size quality assessment without further biological work and downstream applications. Nevertheless, based on empirical evidence from others' research and the wide range of different-sized pores (Figure 3.15), the scaffolds produced in this thesis are reckoned to have met the requirements for future *in vitro* and *in vivo* work [216].




skin xl-col
average pore size
193.8 μm
Count
pore size (μm)
0
20
40
60
80
100
120
140
50
100
150
200
250
300
350


amnion* xl-col
average pore size
294.6 μm
Count
pore size (μm)
0
20
40
60
80
100
200
250
300
350
400


amnion col-HA(IPN)
average pore size
260.1 μm
Count
pore size (μm)
0
20
40
60
80
100
150
200
250
300
350
400


amnion* col-HA(IPN)
average pore size
240.0 μm
Count
pore size (μm)
0
20
40
60
80
100
120
140
160
200
250
300
350

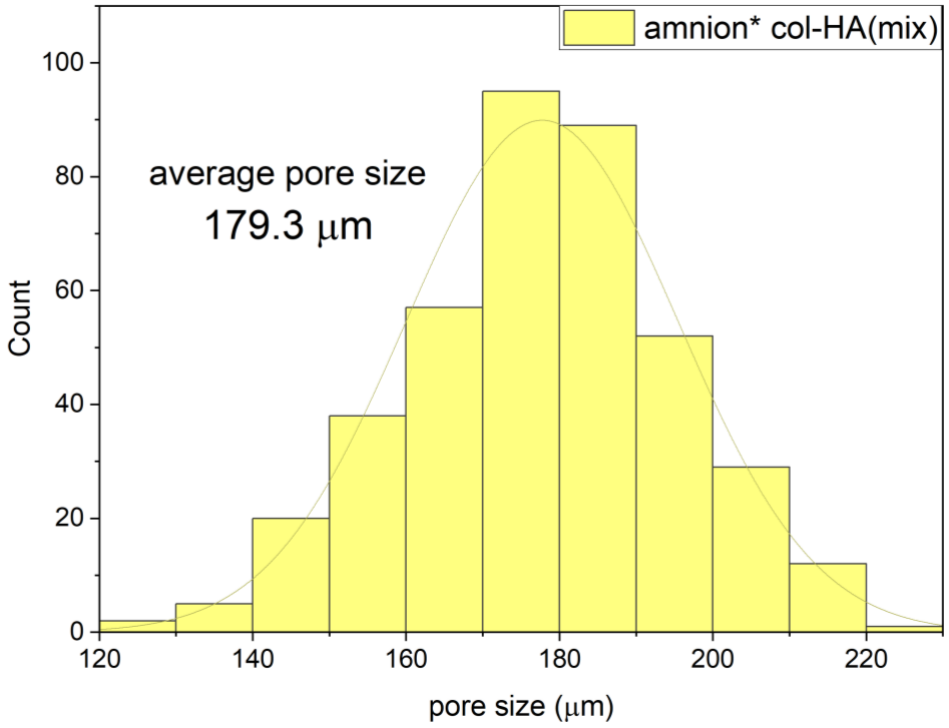


Figure 3.14 The distributions of pore sizes based on circularised average pore size of a) skin unxl-col, b) skin xl-col, c) amnion* xl-col, d) amnion col-HA(IPN), e) amnion* col-HA(IPN), and f) amnion* col-HA(mix) scaffolds (in order).

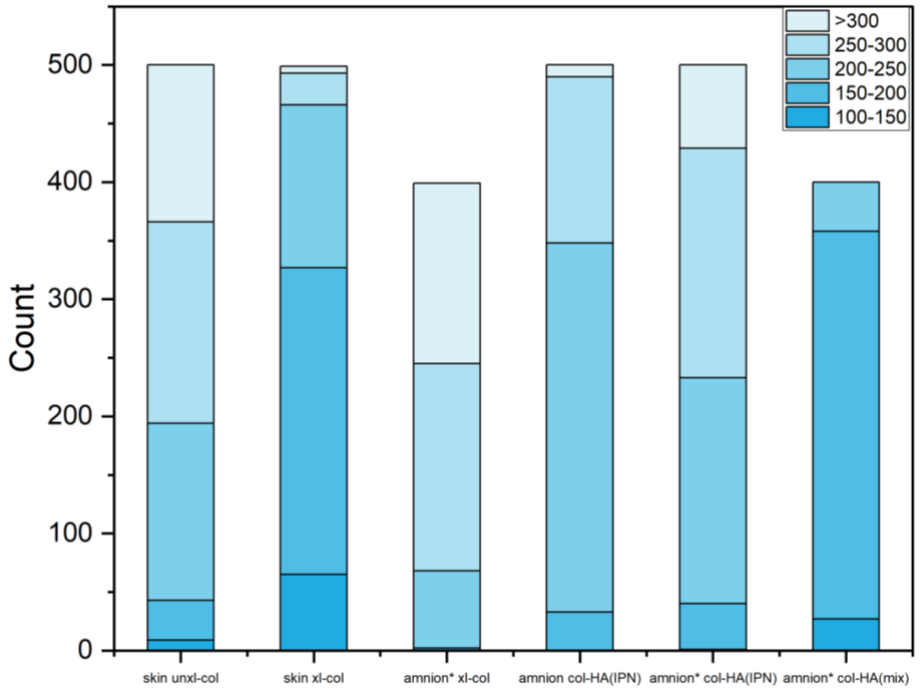


Figure 3.15 The pore size counts of different scaffolds in the form of stacked bar charts.

3.3.6 Swelling ratio

The results of the preliminary tests are shown in Figure 3.16. The existing data shows that, for non-crosslinked collagen-only scaffolds, the maximum water uptake ratio is reached within one hour, and that 37 ºC is the optimal swelling temperature as the scaffolds can retain structure integrity. The water uptake of the samples decreased gradually with incrementing time immersed in PBS, which might be the result of degradation or damage in structure integrity. The data could also conclude that the non-crosslinked collagen-only scaffolds absorb more water at a lower temperature, to the extent that samples tested at 4 ºC absorbed excessive amounts of water and disintegrated. Moreover, it was observed that the scaffolds left at 4 ºC visibly started dissolving while the samples at room temperature were solely gradually loosening up, which is a potential indicator that the scaffolds experience a higher rate of degradation at lower temperatures. It is worth mentioning that with filter paper, the results serve more as a lower-end threshold marker, and the scaffolds are expected to be fully immersed in body fluid in their applications.

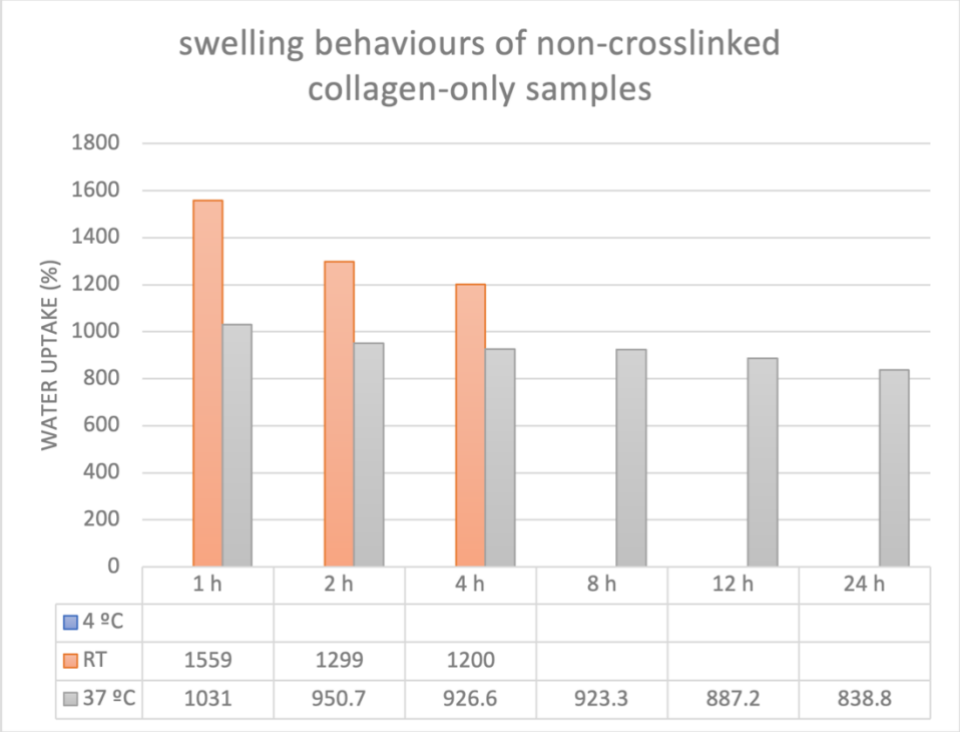


Figure 3.16 The results of the preliminary swelling test on the non-crosslinked collagen-only samples at 4 ºC, room temperature, and 37 ºC in PBS. The data obtained at 4 ºC and room temperature after 8 hours was not shown as the scaffolds reached maximum swelling and disintegrated before the data could be recorded.

The effect of the EDC/NHS crosslinking, the source of collagen, and the addition of HA on the swelling ratio is shown in Figure 3.17. The EDC/NHS partial crosslinking appeared to have slightly reduced the swelling ratio of the skin collagen samples, yet the impact was trivial ($p > 0.9$). The amnion* collagen samples exhibited more than 40 % higher water uptake than that of the skin collagen samples, yet swelling remained roughly the same before and after HA infiltration. The HA-infiltrated amnion collagen samples displayed noticeably lower water uptake than that of its amnion* counterpart with a decrease of approximately 40 %. On the contrary, pre-mixing HA with collagen was shown to have significantly elevated the water uptake by another 40 % compared to the crosslinked and HA-infiltrated samples. It is worth mentioning that the apparent swelling ratio is not an accurate reflection of the swelling ability of the scaffold material due to the porosity impact, which will be further discussed in the discussion section.

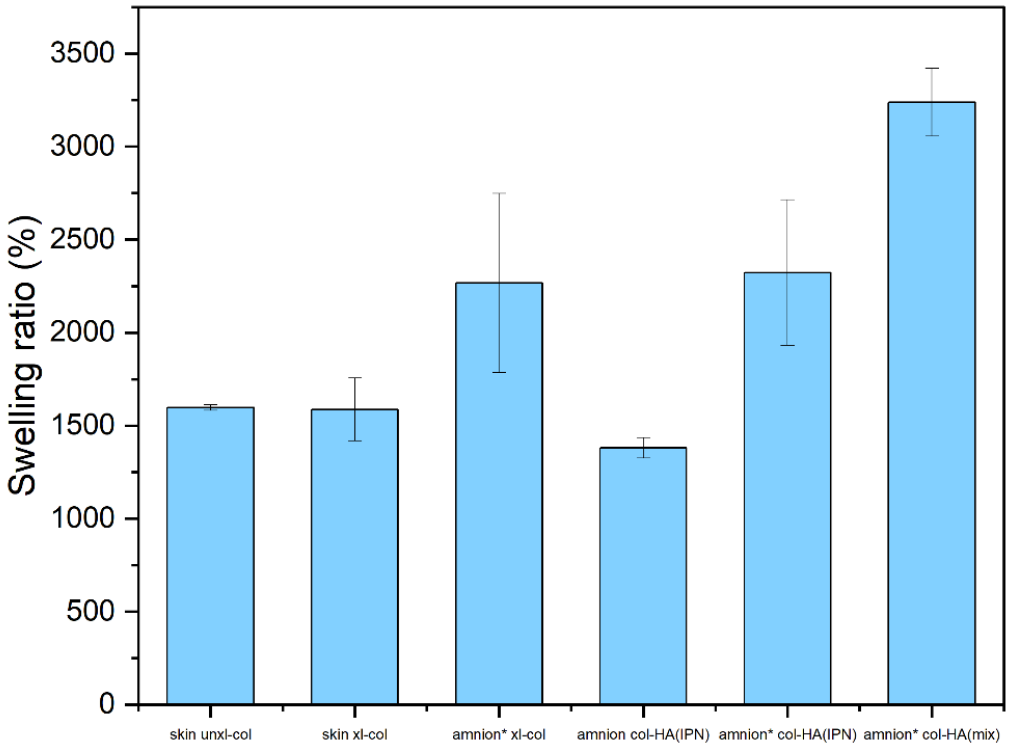
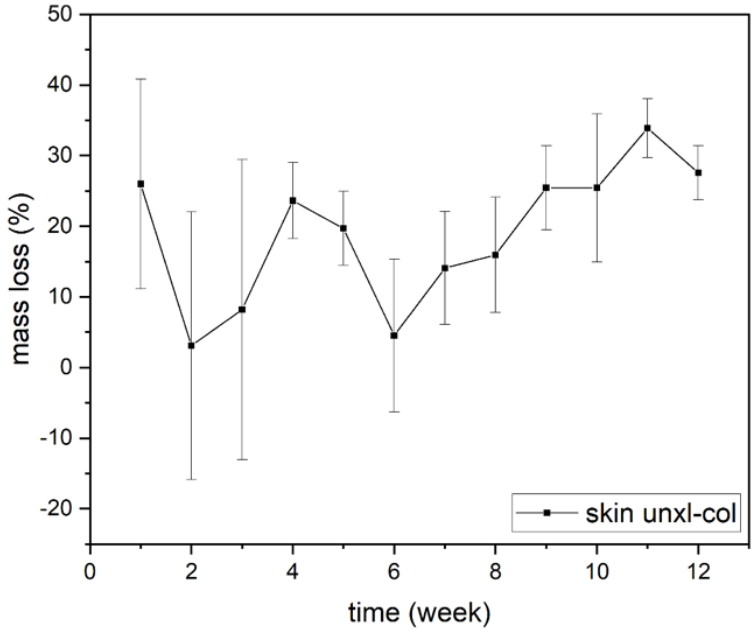
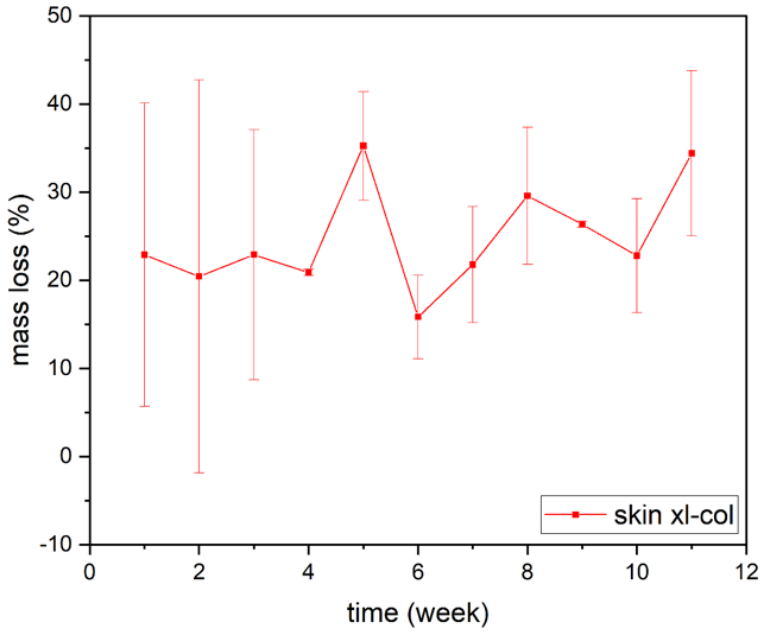


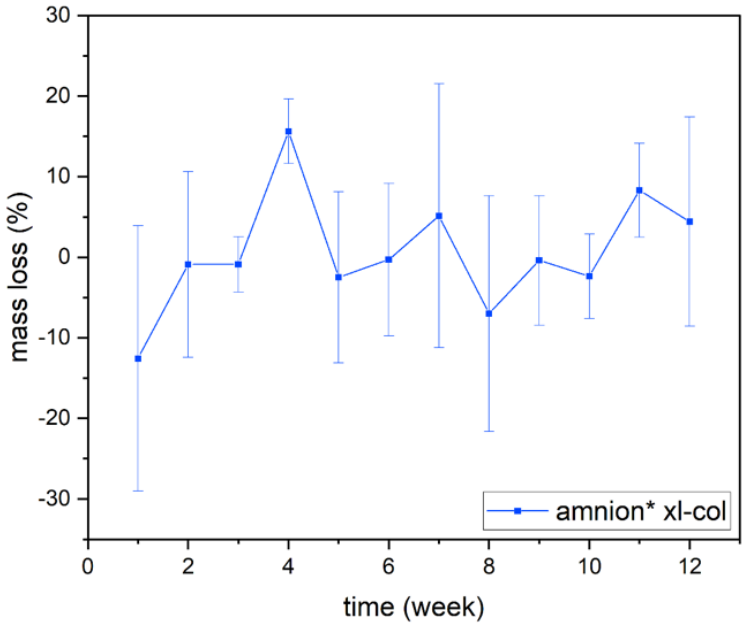
Figure 3.17 The calculated apparent swelling ratio of the samples, tested in PBS at room temperature for 1 hour.

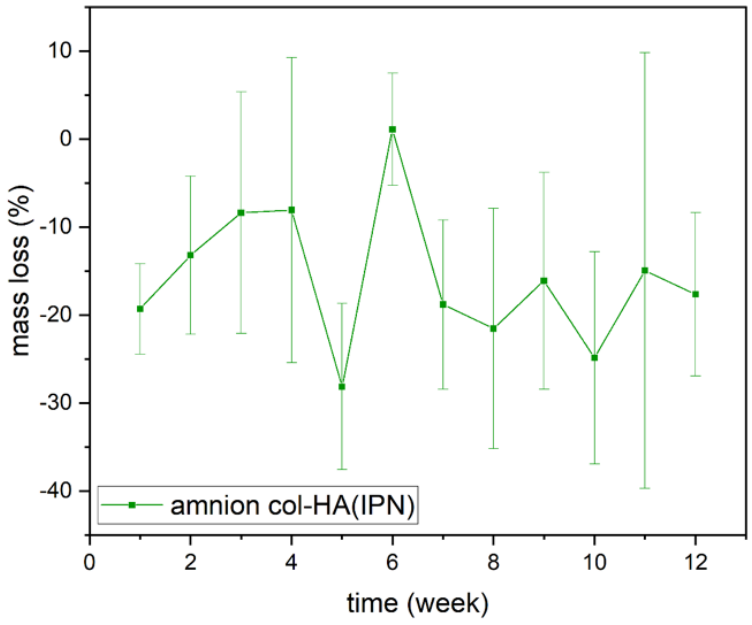
3.3.7 Degradation

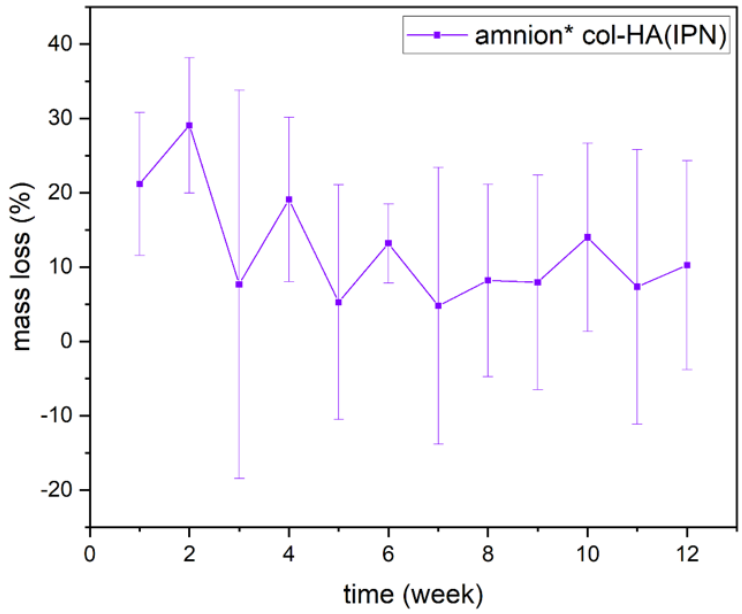
All the single-layer scaffold designs survived the 12-week non-enzymatic degradation process, with the crosslinked skin collagen scaffolds appearing to display the highest mass loss (34.40 ± 9.39 % by the 12th week). No distinctive continuously decreasing trend was shown regarding the mass of the scaffolds, and it was noticed that the ambient temperature and pressure had significant impacts on the recorded mass. This could effectively provide the reason behind the unexpected highest mass loss of crosslinked skin collagen samples, i.e., they are the most crosslinked samples with the highest resistance towards water absorption, which is proven by the low swelling ratio characterised. Therefore, the seemingly high mass loss is considered to be closer to the true value. Furthermore, the HA-infiltrated amnion collagen scaffolds and the elastin scaffolds experienced "negative mass loss", reflecting a certain level of inaccuracy in the method used, which was attributed to the inconsistent water absorption due to temperature and pressure, as well as human operating errors. Overall, the test results were less efficient in describing the accurate degradation rate; however, it sufficiently showcased that all the scaffold designs were viable in *in vitro* studies, i.e., the scaffolds can withhold the long cell culture period.

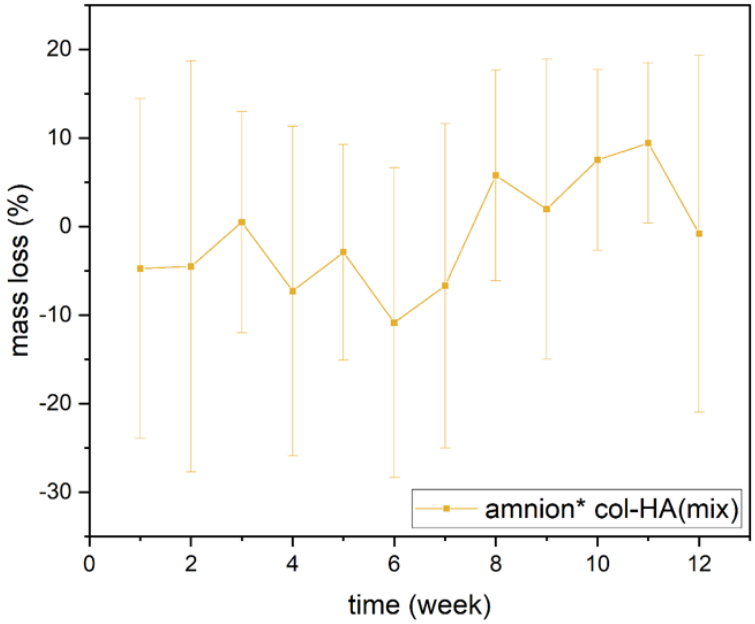

mass loss (%)
time (week)
skin unxl-col


mass loss (%)
time (week)
skin xl-col


mass loss (%)
time (week)
amnion* xl-col


mass loss (%)
time (week)
amnion col-HA(IPN)


amnion* col-HA(IPN)
mass loss (%)
time (week)
40
30
20
10
0
-10
-20
0
2
4
6
8
10
12


amnion* col-HA(mix)
mass loss (%)
time (week)
20
10
0
-10
-20
-30
0
2
4
6
8
10
12

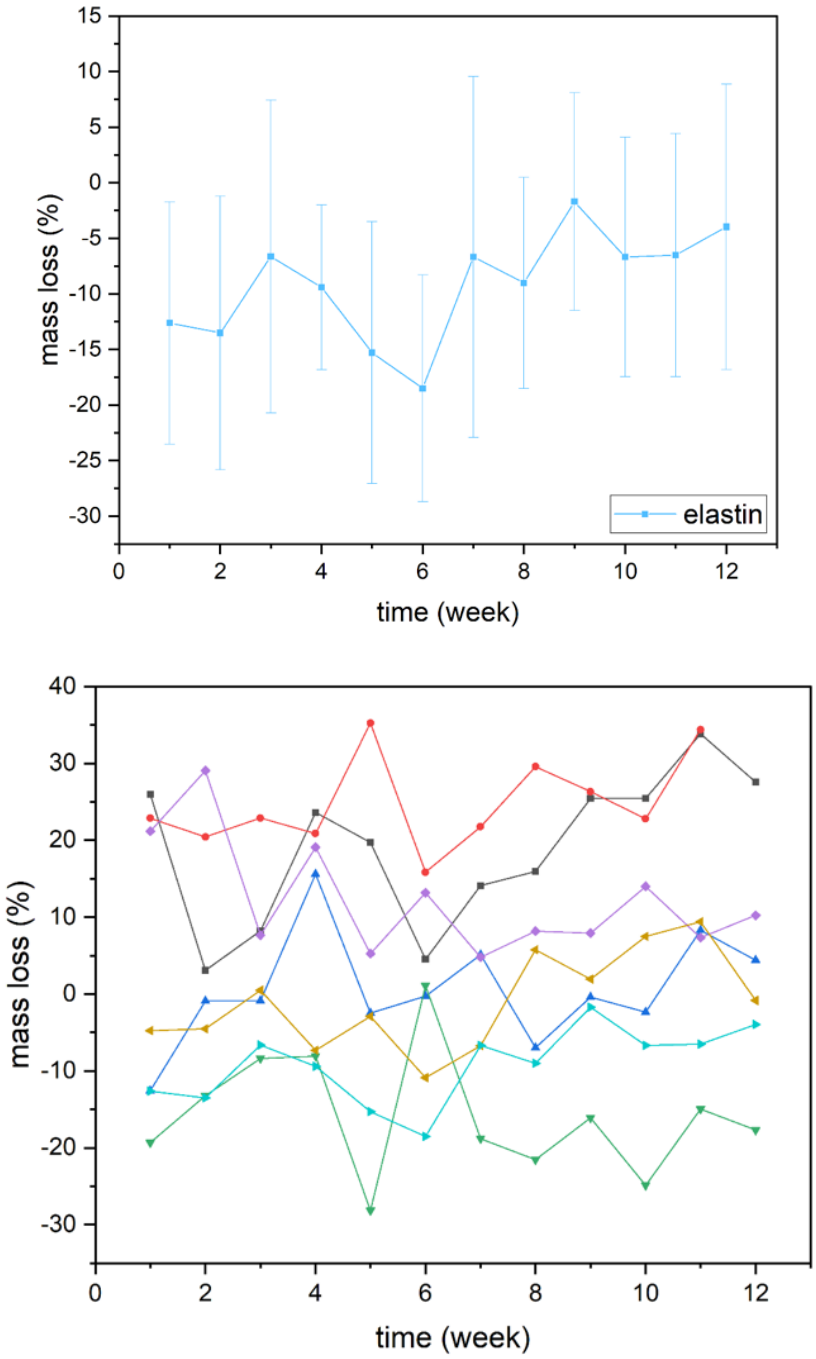


Figure 3.18 The non-enzymatic degradation trends of the samples tested over the 12-week testing period.

3.4. Discussion

3.4.1 Collagen-Elastin Layer

To mimic the ventricularis layer of the aortic valve leaflets structurally and functionally, a collagen-elastin composite layer was experimented with first instead of the current elastin-

only design. Various attempts at fabricating the collagen-elastin composition were successfully carried out using different techniques with polymeric collagen [191,217]. Yet, the preliminary attempts with the type I atelocollagen used in this thesis have proven that the traditional method, i.e., blending collagen and elastin, did not apply to monomeric collagen as it did polymeric collagen. The complication was introduced by the slight difference in the fabrication protocol, which compared to the polymeric collagen scaffold fabrication includes the additional step of fibrillogenesis. Preliminary attempts of mixing collagen and elastin in different stages of the fabrication and the corresponding results are organised in Table 3.11.

collagen solution/scaffold fabrication step	**corresponding elastin addition point**	**result (all unsuccessful)**
lyophilised collagen in deionised water (pH 3.2)	lyophilised collagen and FEG in deionised water (pH 2.7)	collagen and FEG separation after centrifuge
the addition of TBS and pH adjustment to neutral for fibrillogenesis (pH 7.2)	lyophilised FEG dissolve in deionised water (pH 2.7), pH to 7.2 to mix with collagen	FEG less swollen and separation existed, absence of collagen fibrillogenesis
fibrillar collagen suspension after fibrillogenesis (pH 7.2)	lyophilised FEG dissolve in deionised water (pH 2.7), pH to 7.2 to mix with collagen	FEG formed small globular lumps, separation from collagen
collagen scaffold	immerse in 1 %wt elastin solution to form IPN	FEG failed to infiltrate the collagen structure

Table 3.11 The various preliminary attempts exploring the possibility of the fabrication of a collagen-elastin composite layer with type I atelocollagen and FEG.

The failed attempts at mixing collagen and FEG in the liquid phase can be attributed to the following three reasons: the separation of the mixture, the reduced FEG swelling level, and the prevention of collagen fibrillogenesis imposed by FEG. The mixing of collagen and FEG can be considered differently as the dissolving of collagen into either acidic (pH 2.7) or neutral (pH 7.2) FEG solution or vice versa, simplifying the problem down to the solubility of the components. Various factors are reported to have an impact on protein solubility, including intrinsic properties such as the amino acid composition, the molecular weight, the amino acid polarity and conformation, and environmental conditions such as the ionic

strength, the solvent type, the pH, and the temperature [218]. In this thesis, the amino acid polarity and the electrostatic forces are hypothesised as the likely deterministic factors affecting the collagen and FEG interactions in the liquid phase.

Elastin represents a group of peptides and protein sequences that show elasticity, and there exist various compositions and lengths instead of one strictly defined molecular structure. Nonetheless, a shared feature is observed across different elastin types: being affluent in glycine, proline, and lysine [219]. A sequence of valine-proline-glycine-Xaa-glycine was reported to be reappearing, with Xaa frequently being valine [80,220]. Among the amino acids mentioned above, all are non-polar except for lysine, resulting in a highly non-polar and hydrophobic nature of the native elastin molecules. The reoccurrence of lysine in the peptide sequence does contribute to the hydrophilic part of elastin in its soluble precursor tropoelastin [221], yet the amount drastically reduces when the structure undergoes oxidative deamination and sequential condensation, which forms hydrophobic desmosine and isodemosine crosslinks [222,223]. Collagen, on the other hand, was reported to contain mostly polar molecules [224]. Therefore, it is reasonable to assume that this difference in polarity is potentially preventing the mixing of collagen and FEG, yet the level of effect remains unknown without further experiments.

Besides polarity, protein solubility also depends on the electrostatic forces in the hydrophobic reactions [218]. When the repulsive force emerges from the electrostatic effect and exceeds the attractive force posed by hydrophobicity, the protein molecules would prefer to disperse into solution. The isoelectric point (pI) refers to the pH where the charge carried by the molecule reaches “net zero”. Therefore, a protein solution at pH = pI is at the lowest electrostatic repulsion point where the hydrophobic interaction prevails, leaving the protein less likely to dissolve. The reported pI of collagen and elastin are about 7.2 and 5.6 (plateau between 4–8) respectively [184,225,226], which can explain the volume shrinkage, the formation

of small globular elastin lumps when the pH was adjusted to physiological, and the separation of elastin. In an acidic environment, both collagen and elastin are positively charged; therefore, the repulsive electrostatic force combined with the molecular conformation prevents further homogenising of the two proteins. It is worth mentioning that the zeta potential of the protein suspensions was not characterised in this thesis and the above hypothesis was formed based on literature research and reasoning.

An absence of collagen fibrillogenesis was observed with the presence of FEG. Collagen fibrillogenesis is a self-assembly process based on the intrinsic properties of the collagen molecules, and its mechanism is not well studied due to the extreme size, the heterogeneous composition, and the complicated hydroxylation and crosslinking of collagen molecules [227–230]. Among the few understandings of the topic, the precursor peptide chains with one amino end and one carboxyl end are characterised and understood to align either in a unipolar (C–to–N to C–to–N) or a bipolar (C–to–N to N–to–C) manner, which possibly explains the effect of FEG on collagen fibrillogenesis [231]. There exist two popular theories on the formation of such regular alignment: by precipitation resembling liquid crystalline and by the formation and propagation of nuclei [232,233], with evidence endowing both claims [234,235]. Elastin is also made of peptides that inevitably contain the same type of amino and carboxyl ends, which could be included in the C–N arrangements at first; however, the different structure and conformation of elastin chains can interrupt both the liquid crystalline precipitation and the nucleation and propagation, which further disrupts the collagen fibrillogenesis process.

3.4.2 Viscosity and Shear Thinning

Shear thinning is a phenomenon that explicitly describes a non-Newtonian fluid behaviour where the solution/suspension viscosity dwindles under an ascending shear strain rate, and it

is commonly observed in polymer solutions. Among the various viscosity models such as the Cross model and the Carreau model [236,237], the Ostwald de Waele model was chosen as the curve-fitting model as the involvement of the zero-shear viscosity and the infinite viscosity can be eliminated. When the non-Newtonian index n is less than 1, it pinpoints the shear-thinning behaviour of a solution/suspension, and as the n-value diverges from 1, the solution/suspension demonstrates an increased level of pseudoplasticity. Furthermore, the consistency coefficient K can be considered as a viscosity criterion, as a higher K-value denotes a higher viscosity value [238]. Overall, these fitted parameters also serve as benchmarking points for the future reproduction of the designs in this thesis.

The detailed shear-thinning mechanism of the collagen suspension still lacks investigation; however, this section presents a possible mechanism based on experimental data and corresponding analysis. In the pre-test crosslinked collagen suspension, there exist the covalent bonds resulting from crosslinking, the inter- and intra-molecular hydrogen bonds, the Van der Waals force, the chain entanglement provided by the steric hindrance effect, and the possible electrostatic interactions in between the positively charged collagen fibres, leading to the formation of an entangled complex. At a relatively low shear rate (about 0.01 to 1 s^{-1}), a minimum shear force is applied, therefore the rheological response ought to still be within the elastic region, where fibre alignment and elongation commence but are still limited by the strong covalent crosslinks. At the lower middle range (around 1 to 15 s^{-1}), a certain degree of disentanglement is initiated, disrupting the weaker intermolecular interactions, and causing a partial reduction in the steric hindrance effect within the suspension. At the upper middle range (approximately 15 to 50 s^{-1}), the disentangled chains undergo additional stretching and alignment in the direction of the applied shear stress. At this stage, a greater number of non-chemical bonds are broken, while the covalent bonds and the relative positioning of the collagen molecules remain intact. At a relatively high shear rate

(50 to 1000 s^{-1}), the chains experience some uncoiling, leading to a significant increment in chain motion. The suspension is now exposed under a substantial reduction of intermolecular forces, allowing for relative movement between the adjacent collagen chains; consequently, a continuous decrease in viscosity is observed.

In the low and lower middle shear rate regions of the tested samples, the initially present non-chemical interactions gradually weakened while the covalent bonds were unaffected, resulting in less variation in the n-value and the maintaining of a high pseudoplasticity degree. In the upper middle section, the noticeable decrease in the K-value in the experimental data can be attributed to the increased disentanglement of the collagen molecules which allowed chains to align and elongate. Nevertheless, the presence of strong chemical crosslinks continued to restrict extensive and further chain movements, leaving the n-value slightly increased. As the shear rate entered the high region, the significant disruption of physical bonds together with the potential partial breakage of the covalent bonds occurred, resulting in a large-scale chain uncoiling and sliding, which is reflected by the substantial decrease in K-value and the pronounced increase in the n-value from the experimental data.

As for FEG, the dominance of the globular tertiary structure originated from the hydrophobicity led to a reduced or even eliminated entanglement, which consequently undermined the distinctiveness between the lower and the upper middle regions. In the case of the amnion* collagen and HA mixture, the HA molecules served as a lubricant by infiltrating into the collagen entanglement, dwarfing the physical interactions between the collagen chains and, at the same time forming hydrogen bonds with the collagen molecules for further stabilisation. Therefore, the apparent viscosity of the collagen-HA mixture is lower than that of the pure collagen suspension; however, the decrease is less drastic than reported [236], possibly because the steric hindrance effect is still dominant [198].

3.4.3 FTIR

EDC/NHS chemistry prevails in collagen crosslinking for its zero-length mechanism, where EDC reacts with collagen carboxyl group and forms an activated intermediate which in turn reacts with amino groups on adjacent collagen. Therefore, amide formation dominates the crosslinking mechanism, with a coexistent ester bond introduced by NHS, stabilising the reactive intermediate and increasing nucleophilicity [150]. Given the 4h reaction time, the produced scaffolds are assumed to be partially crosslinked, hence the substantial amount of intermediate ester bond existence. The relative amide crosslinking extent is higher among amnion* samples than that of skin samples, which can be attributed to the higher intrinsic crosslinking extent in skin collagen for structural purposes compared with less developed collagen from bovine amnion. From the second derivative and peak deconvolution analysis, it could be seen that both the fabrication and crosslinking methods had no impact on the collagen secondary structure derived from the amide III bands; however, in the amide I band, crosslinking was shown to reduce the amount of α-helix and increase the amount of β-sheet. This effect was reported in another study, with the reason explained to be the disruption of hydrogen bonds stabilising the α-helix and the rearrangement of the side chains [239].

An anomalous change of the amide I and II band intensity ratio was observed, wherein the amide II intensity surpassed that of amide I. This phenomenon has been previously recorded in other studies [240,241], but further explanation was absent. It was reported that fibre orientation has a potential effect on the amide I/II ratio if most of the fibres are aligned perpendicularly to the light source [242], but the microstructure and compressive properties discussed in the next chapter are not sufficiently evident to support this hypothesis. Another study indicated that a lower water content might lead to stronger amide II intensity [243], but the neglectable bounded water residue is deemed unlikely to account for the significant disparity. Amide I is recognised to be highly sensitive to collagen secondary

structure, and amide II is accepted to be more subject to hydrogen bonds and hydration levels [244]. Therefore, it is proposed that the higher amide II intensity originated potentially from the side chain secondary and tertiary amine structure, while the low amide I absorption resulted from a large portion of unreacted carboxylic acid groups.

Quantitive analysis of the HA incorporation percentage is carried out based on the peak intensity analysis, and the peak area data is organised in Table 3.12. It can be seen that compared to collagen-only scaffolds, HA infiltration is effective in introducing HA content, however not as much as the mixing method. When collagen and HA solutions are mixed, chemical linkages, as well as entanglement, hydrogen bonds and other physical interactions, take place, resulting in a more intertwined mixture. On the other hand, the established porous collagen network imposed spatial constraints for HA molecules to navigate and react with collagen amino groups, obstructing further HA infiltration.

sample	peak area
amnion* xl-col	11.9
amnion col-HA(IPN)	16.7
amnion* col-HA(IPN)	19.0
amnion* col-HA(mix)	34.1

Table 3.12 Peak area analysis on the amnion* collagen-only scaffolds and the HA-incorporated scaffolds to investigate the HA incorporation extent.

3.4.4 Porosity and Pore Size

The EDC/NHS partial crosslinking was shown to increase the porosity, which aligns with the conclusion from one study where a beneficial impact on porosity was seen with increasing EDC concentration, yet the EDC-based crosslinking still resulted in porosity reduction compared to non-crosslinked samples [245]. Another study reported a similar porosity before and after the EDC/NHS crosslinking, with the post-crosslinking porosity being slightly higher, which better complies with the result of this thesis [147]. The author proposes that the additional crosslinking and the resultant wash-up steps might have removed some non-

crosslinked collagen content, leading to a density decrease and consequently resulting in increased porosity. For the HA-infiltrated samples, the HA part introduced more density into the collagen network, prompting a corresponding porosity reduction. Similarly, HA would replace a portion of collagen content volume-wise when mixed in, thereby reducing the density of the composite (HA density was reported to be 1.23 g/cm^3 [246], lower than that of pure collagen which is 1.35 g/cm^3), resulting in scaffolds with higher porosity.

The pores formed by the freeze-drying methods are negative replicas of the sublimated ice crystals in essence [247]. In other words, the pore morphology of the freeze-dried scaffolds is dependent on ice crystal nucleation and growth. It is assumed that the swollen collagen fibres are homogenously distributed before freezing, and are rejected by the moving ice front as the freezing process progresses [248]. A rapid and uncontrolled freezing process was reported to result in non-uniformed crystal nucleation and growth while a slow and controlled cooling process is fundamental for isotropic pore formation [249,250], which is related to the magnitude of supercooling [251]. In this thesis, the cooling rate was not precisely controlled due to equipment limitations, resulting in the pore size exhibiting an approximately normal distribution with a slightly broader range. Nevertheless, this broad distribution of pores can be advantageous as it expands the potential application range to other branches of tissue engineering adapting to various cell types, each of which possesses different optimal proliferation and differentiation pore sizes.

In the absence of chemical crosslinking, the collagen fibres experience a reduced constraint, which facilitates the relative movements between adjacent fibres, consequently decreasing the resistance to the ice front advancing, leading to the formation of an intact and aligned microstructure and larger pore sizes. Upon the introduction of chemical crosslink units, the collagen fibres acquire elevated rigidity and hence become less prone to tighter packing, which results in the emergence of smaller pore sizes and a relatively homogeneous

pore size distribution with a compromised pore wall integrity. The noticeably larger pore size characterised in the amnion* samples provides additional evidence supporting the hypothesis that the skin collagen is intrinsically more extensively crosslinked compared to the collagen obtained from the bovine amnion. HA infiltration introduced a secondary HA network, occupying a volumetric portion within the structure, further reducing the pore size consequently compared to the parent crosslinked collagen network. Mixing HA with collagen, on the other hand, partially compromises the scaffold integrity due to the reduced collagen content. As a result, the mixed samples were observed to be more subjected to volume shrinkage during freeze-drying, leading to a significant reduction in pore size.

3.4.5 Swelling

To study the actual effect of the EDC/NHS crosslinking, the source of collagen, and the addition of HA on the swelling ratio, it is important to normalise the data against the porosities of different sample types. For regular polymer samples, the swelling ratio reflects only the swelling ability of the polymer itself; however, in porous materials, the pores allow extra water to be absorbed, rendering the swelling ratio tested higher than the true value. Assuming the water (in this case, PBS) absorbed is independent of all factors but the pore volume, the amount of liquid mass absorbed can be calculated using the pore volume (V_{pore}) and the density of the liquid absorbed (ρ_{liquid}). The pore volume can be obtained knowing the volume of the sample and the sample porosity, and therefore, the adjusted swelling ratio normalised against sample porosity (Q_m') can be defined using the equation below:

$$Q'_m = \frac{m_1 - m_0 - m_{pore}}{m_0} \times 100\% = Q_m - \frac{\rho_{liquid} \cdot V_{sample} \cdot porosity}{m_0} \times 100\%$$

Due to the lack of the length data, the adjusted swelling ratio is unable to be quantified. Nonetheless, this section will give a qualitative analysis based on the swelling ratio and the porosity. As observed before, the EDC/NHS partial crosslinking has no

significant impact on the skin collagen sample swelling ratio; however, the crosslinked skin collagen samples have a significantly higher porosity, therefore, it is concluded that the partial EDC/NHS crosslinking might affect the swelling ratio negatively. Similarly, the higher water uptake exhibited by the amnion* collagen samples can to a certain extent be attributed to their higher porosities. The swelling ability seemingly remained roughly the same before and after HA infiltration, yet the reduced porosity of the HA-infiltrated samples can be evidence that the HA infiltration effectively improved the sample swelling ability. The pre-mixed collagen-HA samples have the largest porosity, which is very likely to have contributed partly to the 40 % swelling increase. Despite sharing similar levels of porosity, amnion collagen samples showed a reduced water uptake ability. It is considered that this difference might be attributed to the ability of type IX and XI collagen to form proteoglycans with HA, which would boost the water uptake amount due to superior hydrophilicity [252]. Yet with the trace amount and the lack of further experimental data, there exists insufficient evidence to support this hypothesis.

It was reported in various studies that crosslinking effectively decreased the swelling ratio, which was previously adopted as the method to characterise the crosslink density within the author's research group [167,253–255]. However, crosslinking density among other factors such as the collagen concentration [256], the solvent type [257], the fabrication method and fibre alignment [258], the pore morphology [259], and ambient temperature and pressure all contribute partially to the swelling behaviour. Therefore, the crosslink density was not characterised using this method in this thesis. However, it is recommended that either free amino acid analysis [260] or 2,4,6-trinitrobenzene sulfonic acid (TNBS) assay [148] should be employed in the characterisation of crosslink density.

The swelling ratio calculated from this study has seen no obvious decrease with partial crosslinks. Apart from the porosity, the intrinsic nature of the EDC/NHS chemistry is

deemed another possible explanation. EDC/NHS chemistry introduces fewer crosslinks into the system than the traditional crosslinking agents such as glutaraldehyde and genipin, at the same time creating a more hydrophilic surface that promotes water uptake [261]. This hypothesis is supported by data from the preliminary attempts of the author using polymeric collagen and unpublished data within the research group. The uncontrollable systematic error brought in by using the filter paper could potentially have an impact as well, as it can absorb more water from the looser non-crosslinked structure than from the more interlinked crosslinked samples.

Between the crosslinked skin and amnion* samples, the greater water uptake of the latter can be attributed to the less matured nature of the bovine embryo membrane and the more crosslinked network of the bovine skin tissue, which is supported by the FTIR results. The addition of HA is expected to benefit the water uptake due to the high hydrophilicity of the polysaccharide structure, which was further consolidated by the mixed collagen-HA samples having a further 43 % increment of swelling [262]. The non-significant change in swelling after HA infiltration can also be explained by a lesser HA incorporation extent and a greater collagen/HA interaction brought in by the ADH modification apart from the impact of porosity [263].

3.5 Conclusion

In this chapter, we have walked through the benchmarking of collagen purity, the examination of fibrillogenesis occurrence, and the synthesis of base suspension/solution for single-layer scaffolds, as well as the characterisations of fabricated scaffolds including microstructure (SEM), chemical structure (FTIR), water absorption and non-enzymatic degradation.

With the aim being probing the viability of the proposed fabrication methods, it is to be concluded that:

- With the fibrillogenesis protocol adopted, monomeric collagen has been proven to be a potential tissue engineering heart valve starting material.
- Lyophilisation as a scaffold production method for monomeric collagen imposes no change in the collagen backbone chemical structure and can yield desirable microstructure, therefore is deemed effective.
- The proposed crosslinking and HA-incorporating methods were proven to have successfully introduced chemical modifications to the monomeric collagen structure.

When analysing the results from various characterisations, three different aspects were focused on: the effect of collagen difference, the effect of crosslinking, and the effect of HA incorporation and different HA incorporation methods. These focuses highlight the other goal of this investigation, exploring different materials and modifications in order to provide options for different applications.

On the front of the collagen source, it can be concluded that:

- The trace amount of impurity in amnion* collagen has no negative impact on the successful scaffold fabrication, therefore is recommended to be prioritised in materials selection due to the easy extraction process and better yield.
- All three types of collagen have met the standard for tissue engineering scaffold, with amnion* collagen slightly superior in pore morphology and water absorption.
- Skin collagen is inherently more crosslinked than collagen sourced from amnion.
- Each type of collagen yields a different range of porosity and pore size, providing ample choices for different cell types.

Partial crosslinking with 30 mM EDC/15 mM NHS has been showed to:

- Slightly increase porosity.

- Drastically decrease pore size by 30 %.
- Have no significant influence on water uptake and degradation resistance.

HA incorporation has shown a concrete effect on scaffold properties, with infiltration and pre-mixing possessing individual impacts:

- Both methods have slight alterations to porosity but meet the > 90 % criterion.
- Pre-mixing HA with collagen introduces significantly more HA into the network, therefore able to uplift the water absorption ability by 40 %; however, this method yields scaffolds with a much smaller pore size (179.3 μm).
- HA-infiltration reduces pore size by 20 % to 240.0 μm compared to crosslinked scaffolds; however, the negative effect on the water storage room available is counteracted by the hydrophilicity of HA, leaving the water absorption ability unchanged.

Chapter 4 Mechanical properties of collagen-based scaffolds

4.1 Introduction

With the promising outcome of the collagen-based single-layer scaffold fabrication, the next step from a materials science point of view is to investigate the mechanical properties of these structures. The mechanical properties are of great importance in biological work too, as both the cells themselves and their activities can be subject to and even be regulated by the mechanical strength of their local environment. For example, the effect of Young's modulus and the compressive strength was extensively studied on the cell-mediated contraction of a collagen-glycosaminoglycan scaffold, and the fibroblasts were shown to bend and buckle individual struts within the structure [264]. The four pillars of this chapter are the dynamic tensile properties, the compressive properties, the tensile properties, and the bending properties, covering the essential mechanical responses required in the practical application of the scaffolds fabricated. Firstly, the viscoelasticity of the suspensions was measured in the hope of providing insights into the intra- and inter-molecular interactions. Secondly, the scaffold viscoelasticity was investigated to further understand the behaviours of the scaffolds under an oscillating load as the target organ, the heart, would experience. Moreover, mechanical responses under both compression and tension were studied in the form of stress-strain curves, continuing the pursuit of understanding the mechanical responses of the structure designed under various loading modes. Lastly, the bending behaviours in the hydrated state have been examined to reveal the scaffolds' responses in a physiological-like environment as well as the suitability for further cell activities. Different from Chapter 3, this chapter lays out the aforementioned mechanical properties separately. Nonetheless, the mechanical properties themselves are interconnected through the microstructure and deformation mechanisms. Furthermore, the effect of the crosslinking and the HA modification on the properties tested will be evaluated as well.

4.2 Materials and Methods

4.2.1 Viscoelasticity

Viscoelastic materials exhibit both viscous and elastic behaviours under deformation; therefore, the viscoelastic behaviour is crucial for biomaterial development as it plays a major part in biological tissue biomechanics. The viscoelastic properties invested in this thesis include the storage modulus (G'), the loss modulus (G") and the loss factor (tanδ). When a sinusoidal oscillating strain (γ_0) and an oscillatory frequency (ω) are applied, a solely in-phase stress response manifests pure elasticity while a fully π/2 out-of-phase stress response demonstrates perfect viscous behaviour. However, a phase difference (δ) between 0 and π/2 is mostly commonly observed, leaving the material tested displaying viscoelasticity. The storage modulus G' is determined by the in-phase elastic portion of the complex shear modulus (G^*), while the loss modulus G" can be derived from the out-of-phase viscous component of G^*. The loss factor is defined as the ratio of G" and G' [265].

$$\gamma(t) = \gamma_0 \cos \omega t$$

$$\sigma(t) = G^* \sigma_0 \cos(\omega t + \delta)$$

$$G' = G^* \cos \delta$$

$$G'' = G^* \sin \delta$$

$$\tan \delta = \frac{G''}{G'}$$

The viscoelasticity of different samples was tested using an Anton Paar MCR702 Rheometer at the Department of Engineering Science, University of Oxford. A 25mm stainless steel parallel plate geometry with sandpaper attached was chosen, with the pre-trimming gap set at 1 mm. Samples (N=5) were freshly prepared and tested under a constant temperature of 4 ºC controlled by a Peltier temperature control (Deben, UK). The constant maximum shear strain was set at 0.3 % to ensure the deformation did not surpass the elastic region of the samples, and the oscillatory frequency was set from 0.628 to 62.8 rad/s. Each

test was repeated once on the same sample and the results were taken from the second run to ensure any preexisting slack was rid of. The viscoelasticity of scaffolds produced was characterised using a TA Instruments DMA Q800 dynamic mechanical analysis at the Department of Engineering Science, University of Oxford. Scaffolds in the non-hydrated state (N=5) were put under tension with a 0.3 N preload and a 0.1 % constant strain, and the testing frequency oscillated at 0.1, 0.3, 1.0, 3.0, and 10.0 Hz. All tests were repeated once and the results were taken from the second run, and the data obtained was plotted on a logarithm scale using OriginLab 2021.

4.2.2 Static Uniaxial Compression and Tension

Static uniaxial compression tests were carried out on the non-hydrated cylindrical samples at room temperature using the DMA Q800. Samples (N=5) were subjected to a 0.01 N preload to ensure full contact and a 0.3 N/min force rate until the force applied reached 3 N. 3 N was chosen because preliminary tests showed that the samples reached the densification region at this point, and given the main focus of this thesis is in the elastic region and the stress plateau, 3 N was considered to be a time-sufficient point to terminate the test. The test conditions were kept identical for tensile tests, with the rectangular samples (N=5) subjected to a 0.3 N/min tensile force until failure. For compression, the properties of interest include Young's moduli (E_{comp}) of both the upper and lower linear regions and the stress and strain value at 3 N. The stress and strain values at 3 N act as checkpoints across samples as a way to assess the strength of the scaffolds in the densification region. The tensile behaviours of interest include the tensile modulus (E_{ten}), the ultimate tensile strength (UTS), and the failure strain. Furthermore, the bending modulus of the non-hydrated scaffolds was calculated using the equation below [266]:

$$E_{bend} = \frac{4}{\left(\frac{1}{\sqrt{E_{ten}}} + \frac{1}{\sqrt{E_{comp}}}\right)^2}$$

4.2.3 Self-deflection

The bending behaviour of all the single-layer collagen-based scaffolds was investigated in the hydrated state to gain insight into the mechanical response in physiological conditions as well as to investigate the effect of hydration on the structure. An improved version of a self-deflection test developed by former group members was adopted as the test method [266], which centres around the idea of using the weight of the water absorbed as a universally distributed weight that causes scaffold deflection. By combining the measured deflection and water mass with beam theory, the bending modulus can be calculated.

The samples (N=5) were weighed before hydration with the dry mass recorded as m_{dry}. The samples were then immersed in PBS for an hour based on a preliminary test investigating the optimal submersion time mentioned in Chapter 3. After an hour, the samples were taken out of the PBS with the excessive liquid eliminated by filter paper. The samples were weighed again, and the hydrated mass was recorded as m_{wet}. The weight of the water is proportional to water uptake, which is calculated as Q_m. The samples were then carefully placed on a U-shaped metal plate with a span of 20 mm and sandpaper on each end and let deflect freely, with the equilibrium state being recorded by a Canon G7X Mark III camera. The maximum height from the centre (h) and scaffold thickness (t) were measured from the images taken using ImageJ for deflection (d) calculation, and the bending modulus was calculated using beam theory, assuming the beam cross-section is rectangular when calculating the second moment of inertia (I) [266].

$$Q_m = \frac{m_{wet} - m_{dry}}{m_{dry}}$$

$$d = h - \frac{t}{2}$$

$$E_{bend,wet} = \frac{5Q_m m_{dry} g l^3}{384 d I}$$

$$I = \frac{w t^3}{12}$$

4.2.4 Statistics

The test results obtained on the DMA Q800 were analysed using the built-in software, TA Universal Analysis, with all data being presented as mean ± standard deviation. The Student t-test and the one-way analysis of variance (ANOVA) coupled with the Tukey HSD post hoc test were both adopted to compare groups of data, with a probability value of 95 % ($p < 0.05$) as the statistical significance criterion.

4.3 Results

4.3.1 Rheology

The suspensions tested are listed in Table 4.1. The representative G'–ω and G"–ω correlations of the various partially crosslinked collagen suspensions are shown in Figure 4.1. All collagen suspensions exhibited no crossover points between the storage and loss moduli and no characteristic three-zone behaviour of the viscoelastic fluid [267]. However, a plateau region was observed where G' largely exceeded G", demonstrating the gel-like rheological properties of the crosslinked collagen suspensions [265]. Both the storage and loss moduli were shown to increase with the gradually increasing angular frequency, with G' overweighing G" to a great extent.

crosslinked skin collagen suspension	skin
crosslinked amnion collagen suspension	amnion
crosslinked amnion* collagen suspension	amnion*
amnion* collagen and HA mixture	amnion*-HA

fibrillar elastin gel	elastin

Table 4.1 A summary of the suspension nomenclature.

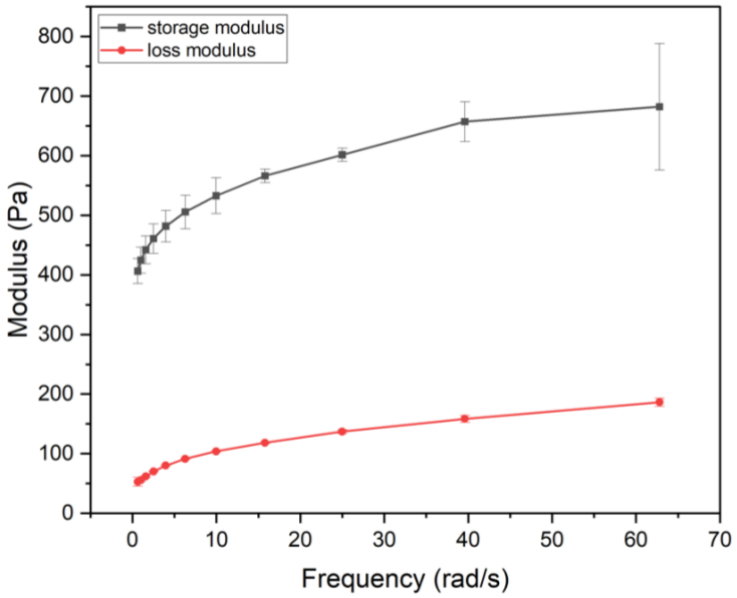


Figure 4.1 The representative G'–ω and G"–ω curves of the EDC/NHS partial-crosslinked collagen suspensions obtained from the frequency sweep test with the angular frequency increasing from 0.628 to 62.8 rad/s.

The HA-incorporated suspension, compared to its collagen-only counterparts, showed drastically reduced storage and loss moduli; fibrillar elastin gel, on the other hand, exhibited prominently greater G' and G" values. Nevertheless, the patterns that the dynamic moduli increase with increasing angular frequency remained unaltered as shown in Figure 4.2. It is worth noting that when plotted under the logarithm scale, the storage modulus against frequency (G'–ω) plots of all the collagen-only suspensions showed a similar numerical value of the slope of around 0.1, while the numerical slope value of the collagen-HA mixture increased to 0.18 and that of the elastin gel dropped to 0.07. The gradient of the loss modulus against frequency (G"–ω) logarithm scale plot deviates more, with the five samples ranging from 0.16 to 0.31. Fibrillar elastin displayed more elasticity than the collagen-only suspension, while HA effectively increased the viscosity. It is worth pointing out that the loss modulus of elastin decreased first and then increased with increasing frequency. This

interesting and different behaviour is likely to be caused by the globular structure of the elastin molecules, which will be discussed later.

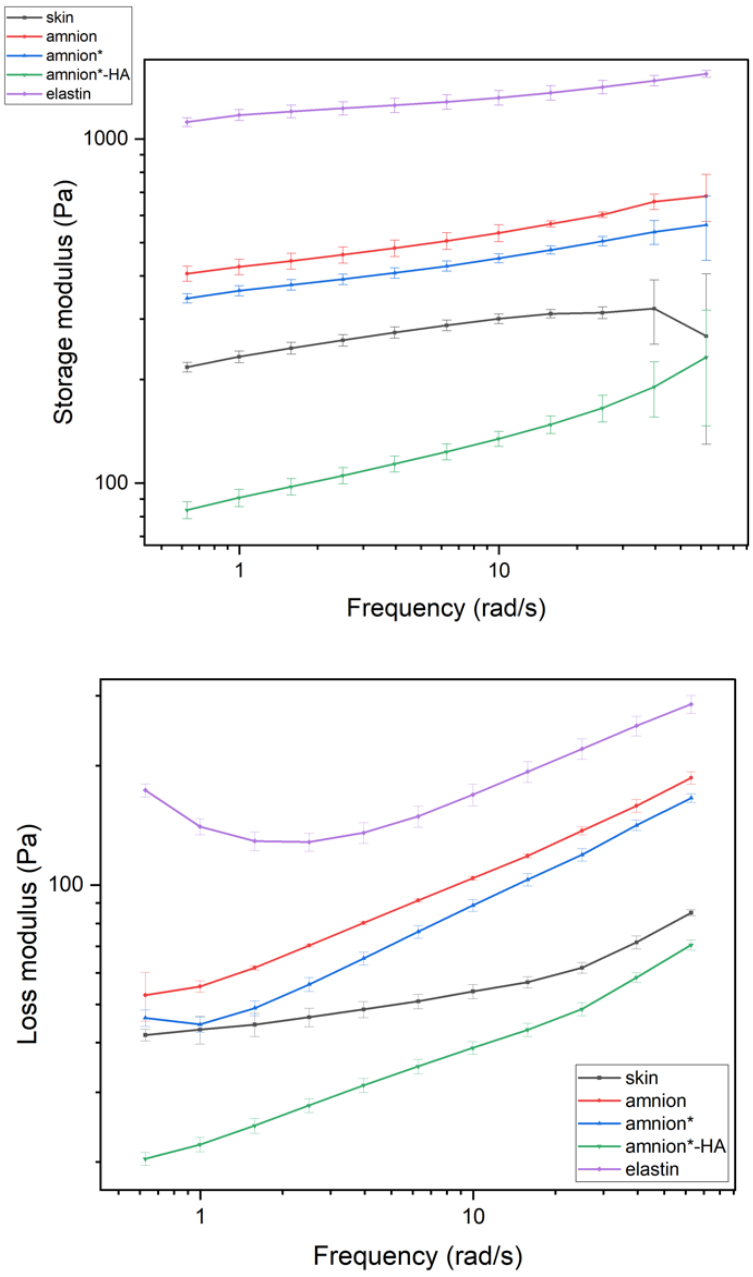


Figure 4.2 The progression of the storage modulus (above) and the loss modulus (below) of all the suspensions tested under increasing frequency. The progression was plotted under logarithmic scales.

The ratio of loss modulus to storage modulus, i.e. the loss factor (tanδ), was also characterised, and the results were converted to phase angle (δ) for a more direct interpretation of the lag in immediate elastic response as shown in Figure 4.3. Overall, the phase angle increased with increasing frequency for all samples, exhibiting higher viscous

response at higher frequencies. However, the highest phase angle remained below 25 °, confirming the elasticity dominance. Amnion* collagen and HA mixture showed the highest dampening effect effectively introduced by HA, while elastin displayed high elasticity due to its globular structure and non-crosslinked nature [184].

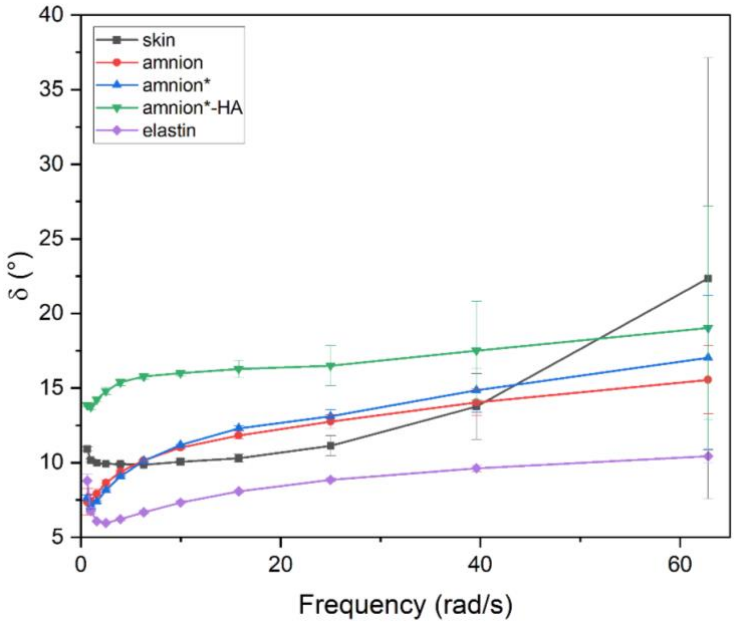


Figure 4.3 The progression of the loss factor in the form of phase angle of all suspensions tested under increasing frequency.

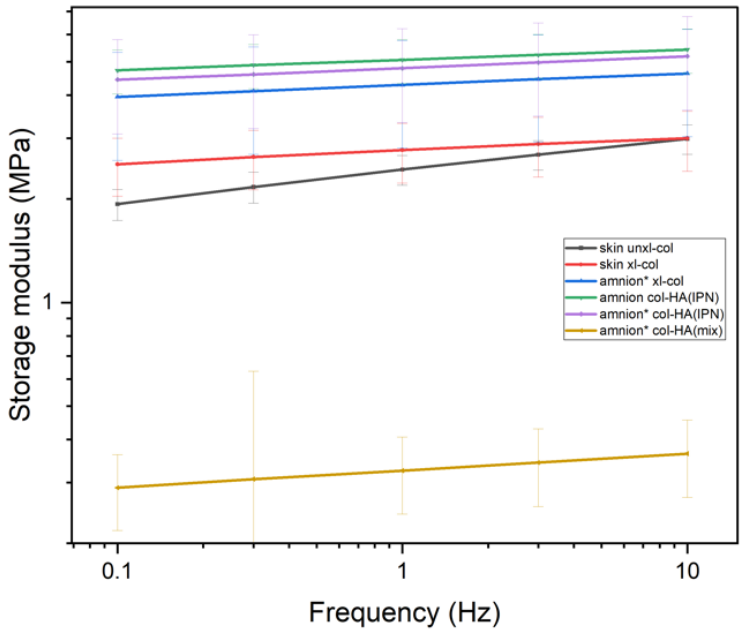
	E (Pa)	G' (Pa)	G" (Pa)	tanδ
skin xl	689	287 ± 10	51 ± 2	0.17
amnion xl	1214	506 ± 28	91.4 ± 0.9	0.18
amnion* xl	1025	427 ± 14	76 ± 3	0.18
amnion*-HA	295	123 ± 7	35 ± 1	0.28
elastin	3072	1280 ± 63	149 ± 9	0.12

Table 4.2 The summary of the viscoelasticity properties of the various suspensions tested at 1 Hz. The estimated Young's modulus (E) is calculated from the equation $E = 2G'(1 + \upsilon)$, with υ being 0.2 for gel-like suspensions, which is applicable in this thesis [268]. Please note that both Young's modulus and the loss factor were calculated values therefore the standard deviation was omitted.

4.3.2 Scaffold viscoelasticity

Dynamic frequency sweep was performed on all the scaffold designs under tension mode to investigate the viscoelasticity progression with increasing frequency, and the results were

plotted on the logarithm scale for direct depiction and further gradient study as shown in Figure 4.4. For all scaffold designs, the storage modulus (in the form of log G') increased linearly with frequency (in the form of log f) with the coefficient of determination $R^2 > 0.999$. The non-crosslinked samples exhibited the highest numerical slope value of 0.09 while the crosslinked samples showed a much lower numerical slope value of about 0.03. HA infiltration imposed no alteration to the slope value compared to the crosslinked parent network; HA premixing, on the other hand, slightly increased the numerical slope value to 0.05. The loss modulus, however, showed less linear correlation except for amnion HA-infiltrated and skin non-crosslinked samples (R^2 being 0.991 and 0.975 respectively), with the slope of log G"–log f curves having similar numerical values to those of log G'–log f curves.



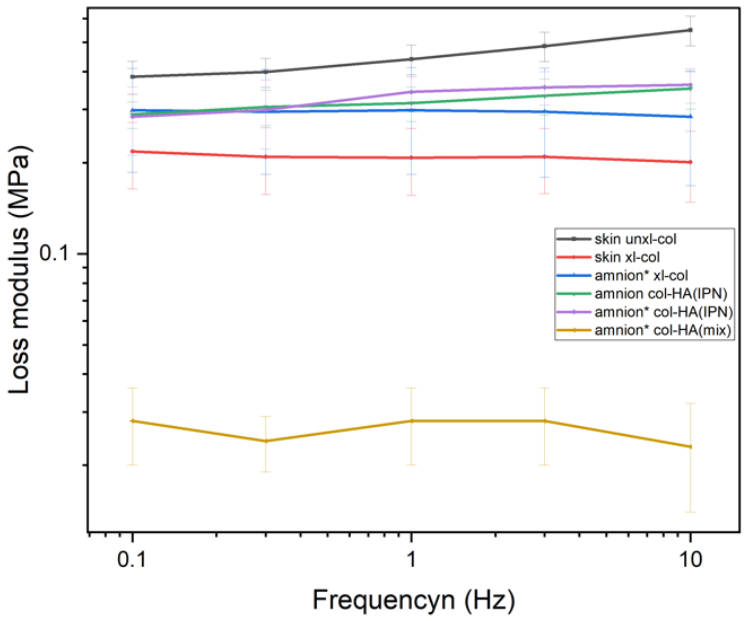


Figure 4.4 The progression of the storage modulus (above) and the loss modulus (below) with increasing frequency on the logarithm scale obtained by the tensile frequency sweep test.

All the scaffold designs displayed strong elasticity dominance (G' >> G" with no crossover point), aligning with the behaviours of the dehydrated lightly crosslinked polymeric structure. The effect of crosslinking was investigated by comparing the modulus-frequency curves of the non-crosslinked and crosslinked skin collagen scaffolds. Besides the slope reduction in log G'–log f curves introduced by crosslinking network formation, an opposite effect on loss modulus with progressing frequency was observed, with increasing G" shown among the non-crosslinked samples and diminishing G" displayed by the crosslinked scaffolds. For the non-crosslinked samples, the log G'–log f and log G"–log f curves are observed to be parallel to each other, resulting in a relatively unchanged loss factor. The phase angle experienced a gradual decline over growing frequency, marking a more significant elastic response.

The dynamic properties of the collagen-based single-layer scaffolds at 1 Hz are summarised and listed in Table 4.3. It can be seen that the partial crosslinking effectively increased the elasticity reflected by an increased G' and a decreased G". Compared to the skin collagen, the amnion* collagen provided even more elasticity while maintaining a

similar level of loss factor. In the non-hydrated state, the inclusion of HA showed no visible impact on the loss factor, i.e., HA incorporation introduced no dampening effect to the system, which is understandable given hydration is crucial for the exhibition of dampening. The difference in the storage and loss moduli values is proposed to have a close affiliation with the microstructure of different samples, and the trend should be similar to the results in tensile tests therefore will be discussed in the same section later. HA infiltration has slightly improved the shear stiffness and has pivoted the dwindling trend of G" against frequency to a positive correlation, yielding a lower loss factor at low frequency and a higher loss factor when frequency reached 2 Hz when compared to that of the parent collagen network. Premixing collagen suspension with HA, on the contrary, drastically decreased both the storage and loss moduli of the produced scaffolds. Nevertheless, HA premixing has proved to be the better method to incorporate the characteristic dampening effect of HA into crosslinked samples, demonstrated by the highest phase angle shown in Figure 4.5.

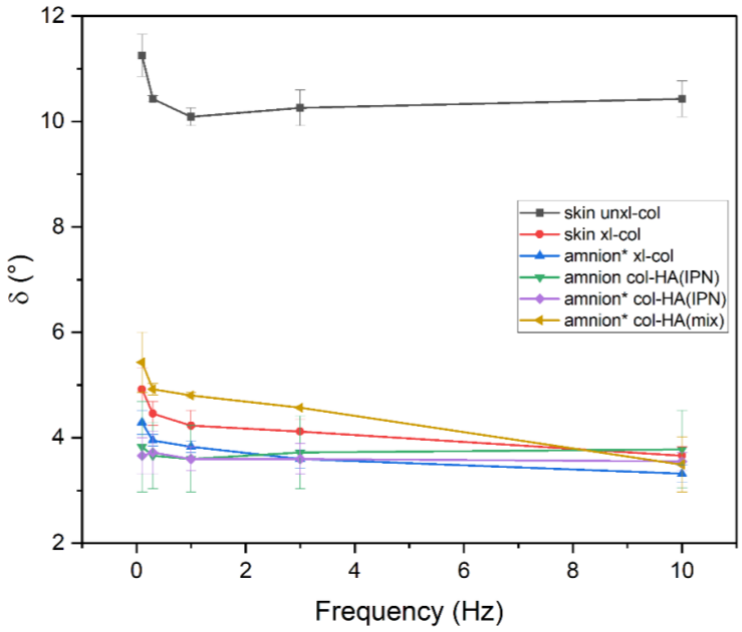


Figure 4.5 The progression of the loss factor of the scaffolds in the form of phase angle tested by frequency sweeping under tensile mode.

	G' (MPa)	G" (MPa)	tanδ
skin unxl-col	2.4 ± 0.2	0.44 ± 0.05	0.18

skin xl-col	2.8 ± 0.6	0.21 ± 0.05	0.07
amnion* xl-col	4.3 ± 1.5	0.3 ± 0.1	0.07
amnion col-HA(IPN)	5.1 ± 0.7	0.32 ± 0.04	0.06
amnion* col-HA(IPN)	5 ± 1	0.34 ± 0.04	0.06
amnion* col-HA(mix)	0.33 ± 0.08	0.03 ± 0.01	0.08

Table 4.3 The summary of viscoelasticity properties of the various scaffold designs tested at 1 Hz. Please note that 1 Hz is chosen as it represents the normal resting heart rate of 60 bpm.

4.3.3 Compression

The non-crosslinked scaffolds possess irregular pores throughout, introducing a bending-dominated foam mechanical response [269]. As illustrated in Figure 4.6, the characteristic stress-strain curve of the non-crosslinked collagen scaffolds under compression consists of three sections: the linear region, the stress plateau region and the densification region. The linear elastic region is attributed to pore edge bending and is expected to emerge from approximately 5 % strain for structures with less than 30 % relative density, which coincides with the measured linear region of the non-crosslinked scaffolds (about 4–20 %). When the pore wall buckling and the slight pore collapsing start to be the dominant deformation mechanism, the stress-strain curve enters a plateau region where the stress gains limitedly with largely increasing strain. The final stage of densification resulting from complete pore collapsing commences at about 50 % strain and gains obviosity when the strain reaches 60 %, aligning with evidence from the literature [270].

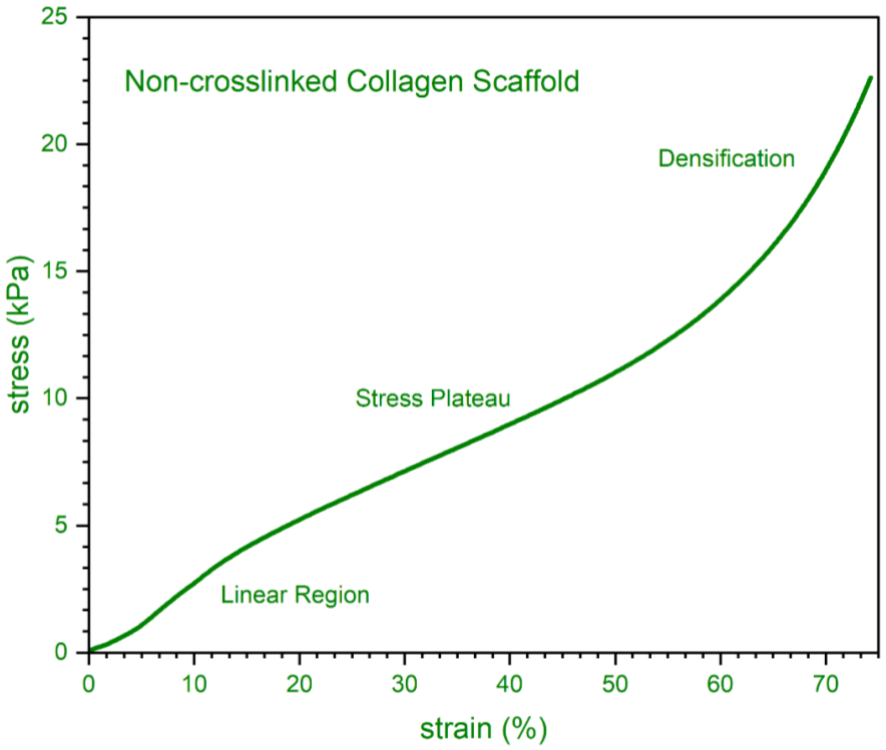


Figure 4.6 The representative compressive stress-strain curve of the non-crosslinked collagen scaffolds, with the force rate applied to be 0.3 N/min.

Despite both being partially crosslinked with 30 mM/15 mM EDC/NHS, samples made of skin and amnion* collagen demonstrated variance against each other and the non-crosslinked samples as shown in Figure 4.7. Crosslinking has seen the skin collagen samples with a less defined stress-strain curve due to the more aggressive incline in the plateau region, together with an upward shift of the linear region. The amnion* scaffolds, on the other hand, have kept the characteristic regions clear, with the onset of densification commencing at a lower strain compared to non-crosslinked samples. It is hypothesised that with further crosslinking, the amnion* samples will display a similar stress-strain response more adjacent to that of the skin samples, as the skin collagen was proved to be intrinsically more crosslinked in the previous chapter.

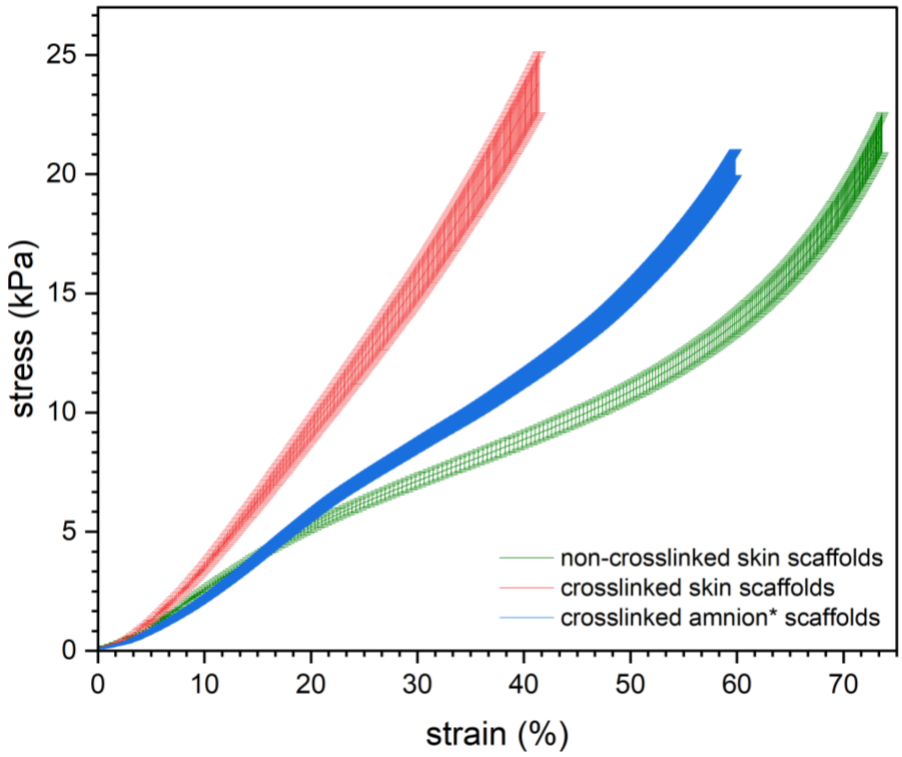


Figure 4.7 The compressive stress-strain curves of the non-crosslinked skin collagen, the crosslinked skin collagen, and the crosslinked amnion* collagen scaffolds, with the results presented as mean and error bars.

Generally speaking, HA infiltration is considered to have preserved the linear region, the stress plateau, and the densification feature as shown in Figure 4.8. At the same time, due to the random fashion of the secondary HA network introduction, inconsistency started to appear in the supposedly linear region, and the standard deviation saw an obvious jump compared with the collagen-only scaffolds. On the contrary, pre-mixing HA and collagen suspension exhibited great curve repeatability. However, the compressive deformation response displayed has a vast difference in shape, with a compliable initial linear stage followed by a stiffening region resembling the characteristic J-curve of biomaterials as shown in Figure 4.9.

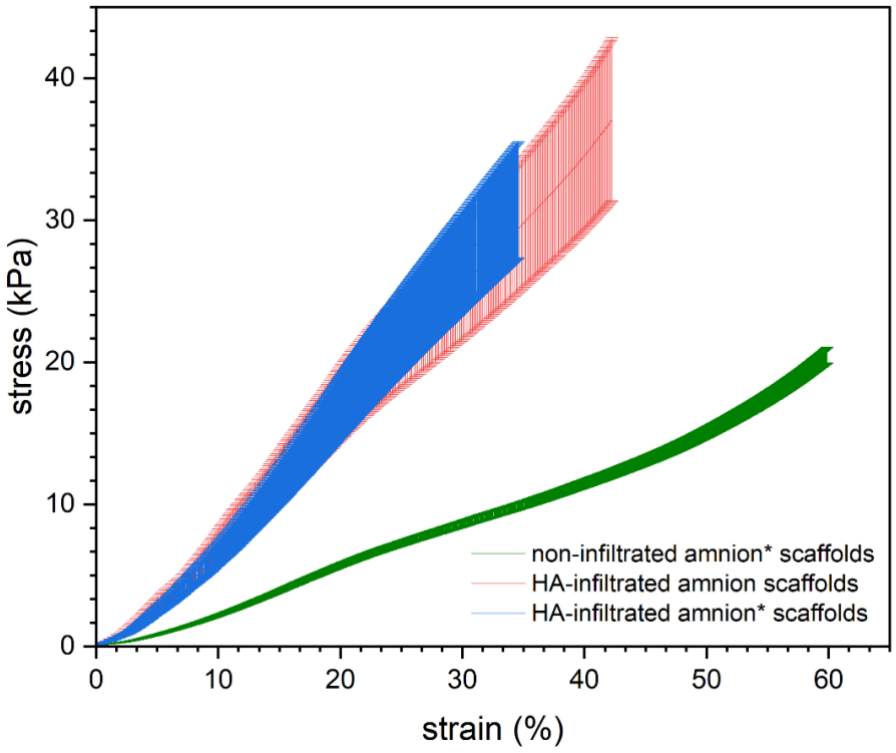


Figure 4.8 The compressive stress-strain curves of the non-infiltrated amnion* collagen, the HA-infiltrated amnion collagen, and the amnion* collagen scaffolds, with the results presented as mean and error bars.

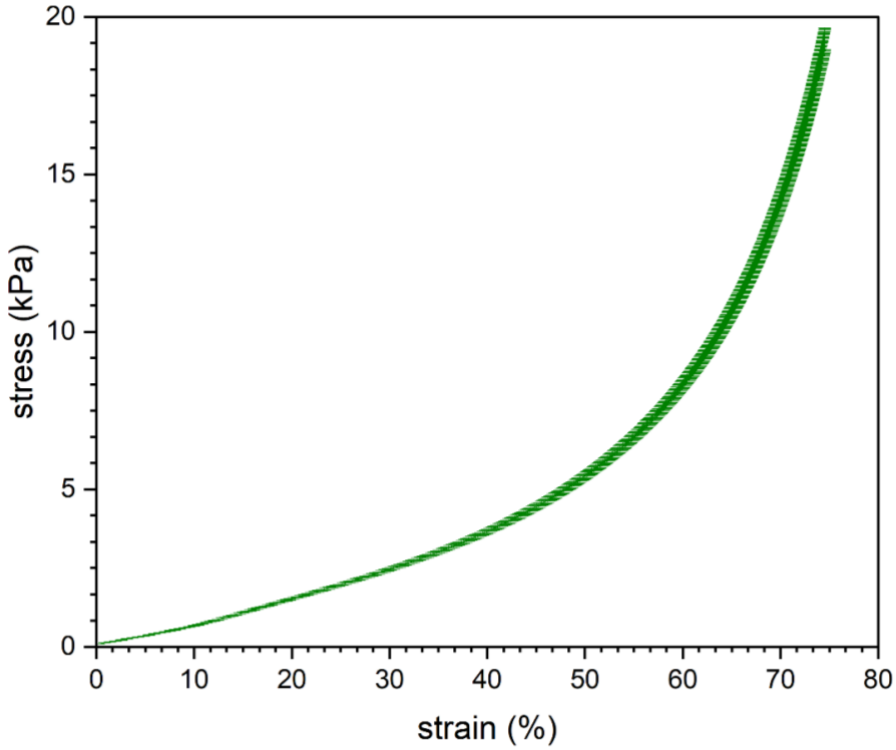


Figure 4.9 The representative compressive stress-strain curve of the pre-mixed amnion* collagen-HA scaffolds, with the force rate applied to be 0.3 N/min and the results presented as mean and error bars.

The lower region compressive Young's modulus (E_{comp}) is taken from the slope value of the linear elastic part of the stress-strain curve, while the upper region modulus (E_{csp}) describes the inclination of the plateau region. The stress and strain values at 3 N were recorded as the checkpoint for the deformation extent, and all the results are summarised in Table 4.4. Partial crosslinking demonstrated a significantly positive impact on the compressive stiffness of collagen scaffolds by achieving a 1.4-fold improvement in the compressive modulus from 29 ± 4 kPa to 40 ± 2 kPa. On top of that, HA infiltration further improved the compressive stiffness by 1.5 times from 42 ± 1 kPa to 63 ± 3 kPa. By partially replacing the collagen structure with the less stiff HA, the pre-mixed collagen-HA composite scaffolds showed a much lower compressive stiffness and compliance level than that of the non-crosslinked samples. The compliance resistance of the other samples that underwent various modifications all displayed reduced elongation, with the more stiffed HA-infiltrated samples being the least compliant.

	modulus (kPa)		3 N point	
sample ID	lower	upper	strain (%)	stress (kPa)
skin unxl-col	29 ± 4	18 ± 2	74.3 ± 0.5	21.7 ± 0.8
skin xl-col	40 ± 2	54 ± 9	43 ± 3	24 ± 1
amnion* xl-col	42 ± 1	27 ± 3	59 ± 1	20.5 ± 0.6
amnion col-HA(IPN)	80 ± 29		42 ± 13	35 ± 3
amnion* col-HA(IPN)	63 ± 3	104 ± 24	35 ± 2	29.5 ± 0.6
amnion* col-HA(mix)	6 ± 2	8.6 ± 0.8	76 ± 1	19.2 ± 0.2

Table 4.4 A summary of the compressive properties of interest for the various types of scaffolds being tested in the non-hydrated state at a fixed force rate of 0.3 N/min.

4.3.4 Tension

Figure 4.10 presents the representative stress-strain curve of the non-crosslinked collagen scaffolds under tension, demonstrating the characteristic brittle plastic foam polymer mechanical response, aligning with preliminary DSC results. The curve can be divided into two regions: a short linear elastic region at extremely low strain (~ 0–1.2 %) followed by a

plastic deformation region until the fracture is reached at ~ 20 %*. For the crosslinked samples shown in Figure 4.11, the linear elastic region is slightly shortened while the extensibility is significantly diminished, leaving the scaffolds more brittle with the fracture strain being at ~ 5 %* [271,272]. Similar to the results from the compression tests, HA infiltration has no impact on the characteristic stress-strain curve features other than Young's modulus as shown in Figure 4.12. The previously manifested inconsistency and batch-to-batch difference in compression are less noticeable when tested under tension, which can be attributed to different deformation mechanisms of compressive and tensile tests. Akin to the compressive response, the pre-mixed collagen-HA scaffolds exhibited a "toe region" before entering the linear elastic region as shown in Figure 4.13.

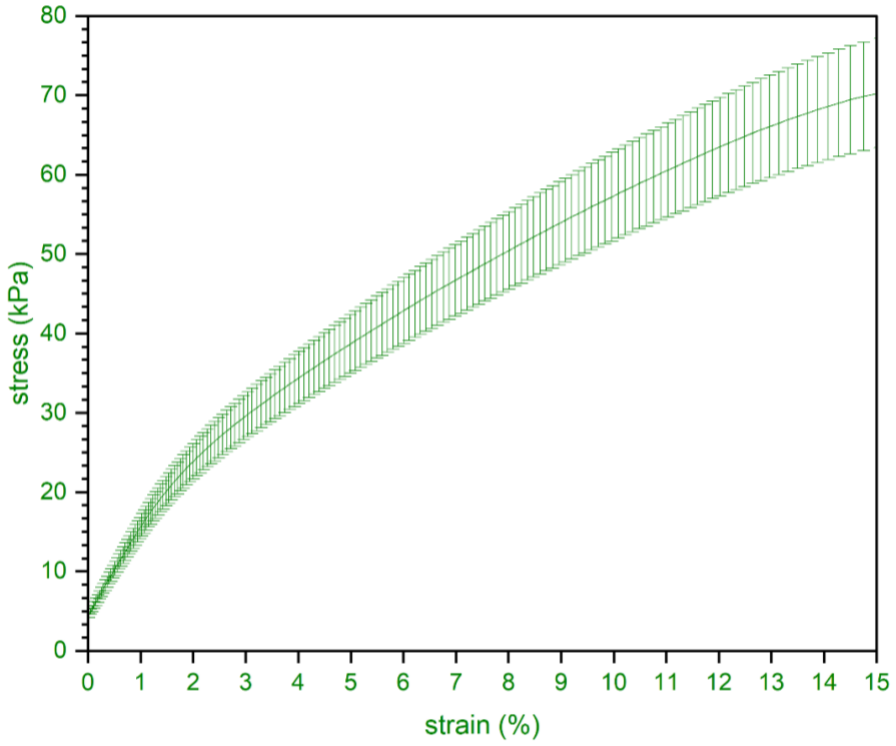


Figure 4.10 The representative tensile stress-strain curve of the non-crosslinked collagen scaffolds, with the force rate applied to be 0.3 N/min. *15 % strain is taken from the least extensible sample for curve averaging.

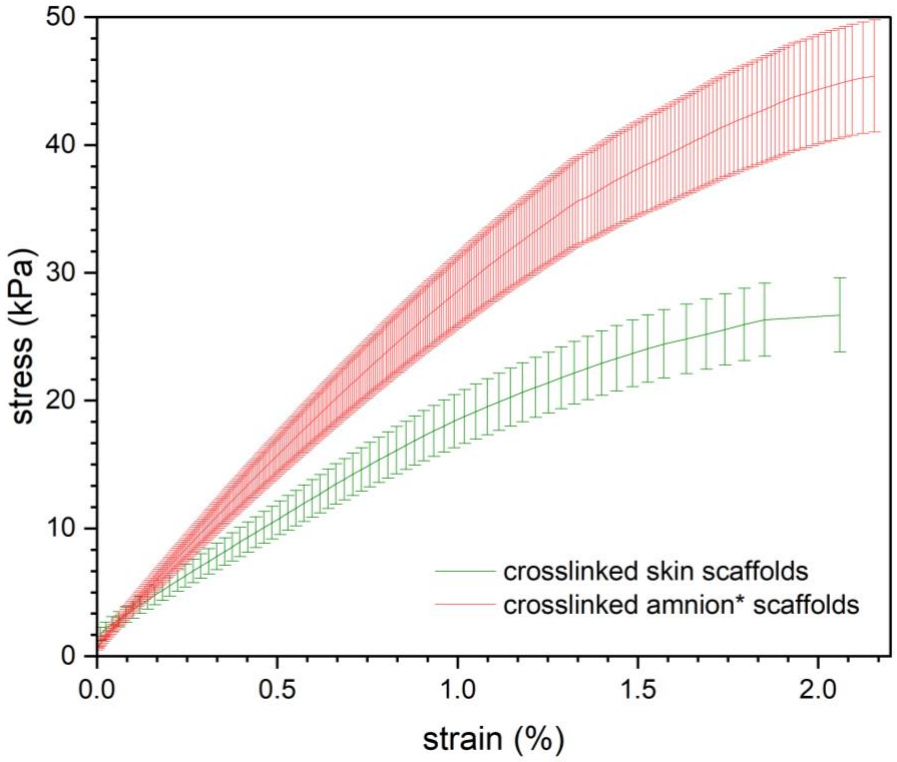


Figure 4.11 The tensile stress-strain curves of the crosslinked skin collagen and amnion* collagen scaffolds tested under the same conditions. *Same as Figure 4.10, the data were averaged according to the least extensible samples.

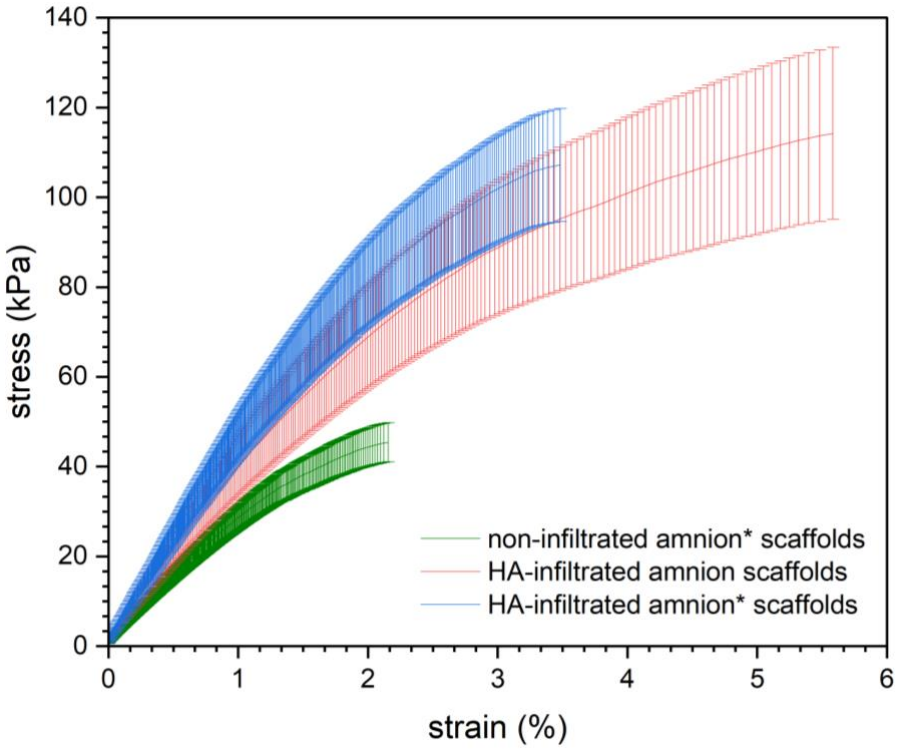


Figure 4.12 The tensile stress-strain curves of the non-infiltrated amnion* collagen, the HA-infiltrated amnion collagen, and the amnion* collagen scaffolds.

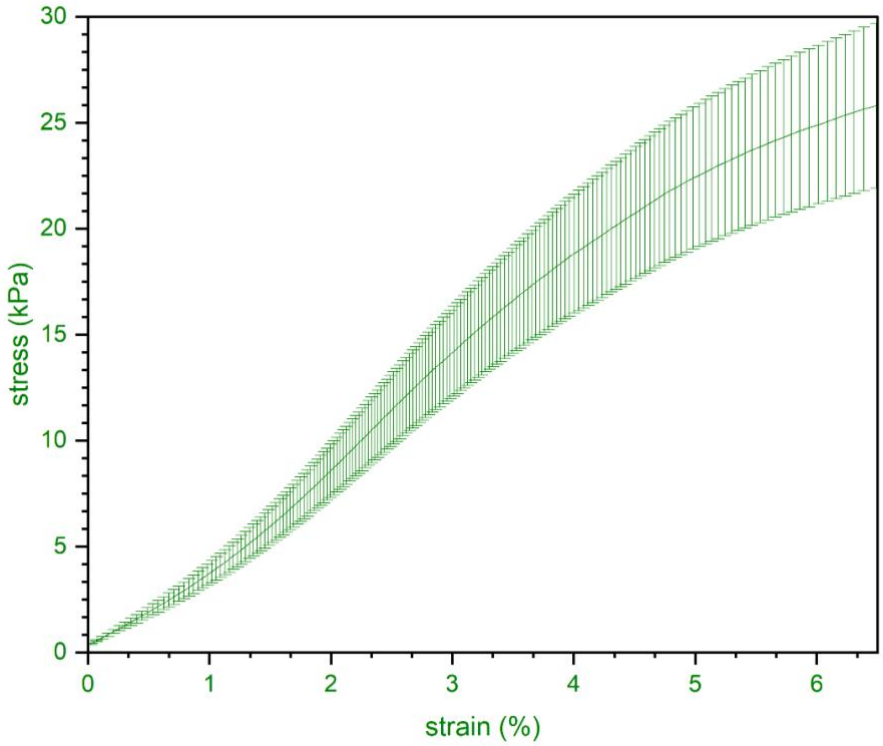


Figure 4.13 The representative tensile stress-strain curve of the pre-mixed amnion* collagen-HA scaffolds, with the force rate applied to be 0.3 N/min.

The tensile Young's modulus (E_{ten}) is calculated from the short linear elastic region of the stress-strain curve, and the UTS and the failure strain were directly obtained from the endpoint of the curve. All the data are organised in Table 4.5. Lacking chemical crosslinks, the non-crosslinked scaffolds showed greater compliance with the UTS and elongation-at-break being 82.3 kPa and 20.9 % respectively, while the partially crosslinked collagen scaffolds underwent a drastic decrease in failure strain. Partial crosslinking was proved to have significantly improved the tensile modulus by 1.6 times from 1.14 MPa to 1.77 MPa, and E_{ten} of the less intrinsically crosslinked amnion* collagen reached 3.29 MPa.

After being infiltrated with the secondary HA network, the tensile stiffness remained at a similar level compared to the increase under compression, pointing to a different dominant deformation mechanism. Nonetheless, the introduction of HA recovered the linear

elastic region to the level of non-crosslinked samples and significantly improved tensile strength, demonstrating the beneficial effect of HA incorporation in mechanical property enhancement. On the other hand, the brittle polymeric foam and J-curve combined pre-mixed collagen-HA samples experienced a significantly negative impact on tensile modulus (0.55 MPa), however, the extensibility increased to 7.88 %.

	E_{ten} (MPa)	UTS (kPa)	failure strain (%)
skin unxl-col	1.1 ± 0.1	82 ± 16	21 ± 3
skin xl-col	1.8 ± 0.4	40 ± 7	4.6 ± 0.5
amnion* xl-col	3 ± 1	66 ± 21	5.1 ± 0.3
amnion col-HA(IPN)	4.0 ± 0.8	127 ± 18	6 ± 1
amnion* col-HA(IPN)	4 ± 1	128 ± 32	6 ± 1
amnion* col-HA(mix)	0.55 ± 0.08	27 ± 8	7.88 ± 0.03

Table 4.5 A summary of the tensile properties of interest for various types of scaffolds being tested in the non-hydrated state under a fixed force rate of 0.3 N/min.

4.3.5 Bending

The setup and a schematic illustration of the measurement of the height (h) is shown in Figure 4.14, with it being measured from the centre of the sample without deflection to the lowest point of the scaffold after self-deflection. The non-crosslinked samples were not stiff enough to carry out the test after an hour of submersion in PBS at room temperature, therefore the data were not collected. Both the experimentally collected data on the hydrated samples (Figure 4.15) and the theoretically calculated data from the compressive and tensile results (Figure 4.16) are listed for comparison, and the values are organised in Table 4.6. Generally speaking, hydration has drastically diminished the stiffness of the scaffolds except for the pre-mixed collagen-HA samples, of which the bending modulus had only halved after hydration (20.7 kPa to 9.24 kPa). Both HA incorporation methods demonstrated significant enhancement in the structural bending stiffness, with the infiltrating method possessing more

benefits. It is worth noticing that the differences among groups are akin to those shown in compressive tests, foreshadowing a compression-dominating bending response.

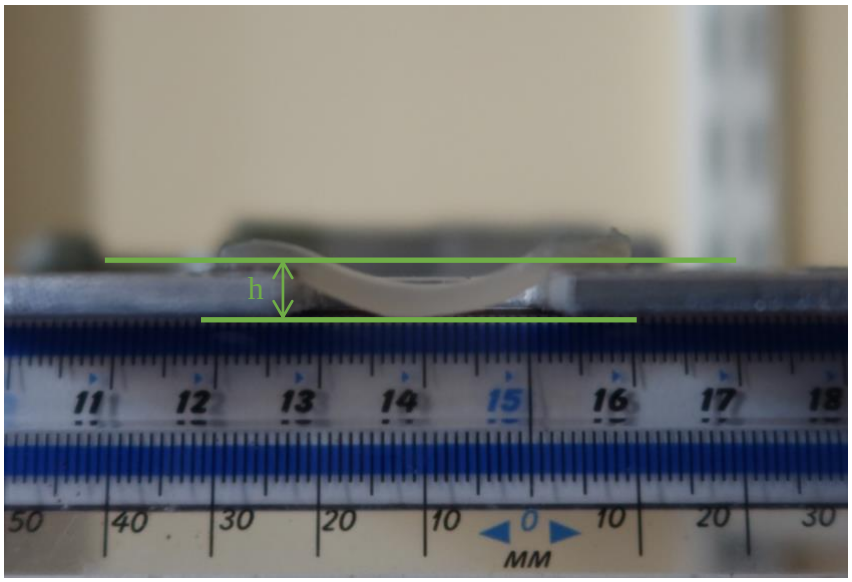


Figure 4.14 The representative illustration of the self-deflection test on the hydrated collagen-based scaffold, with the span being set as 20 mm.

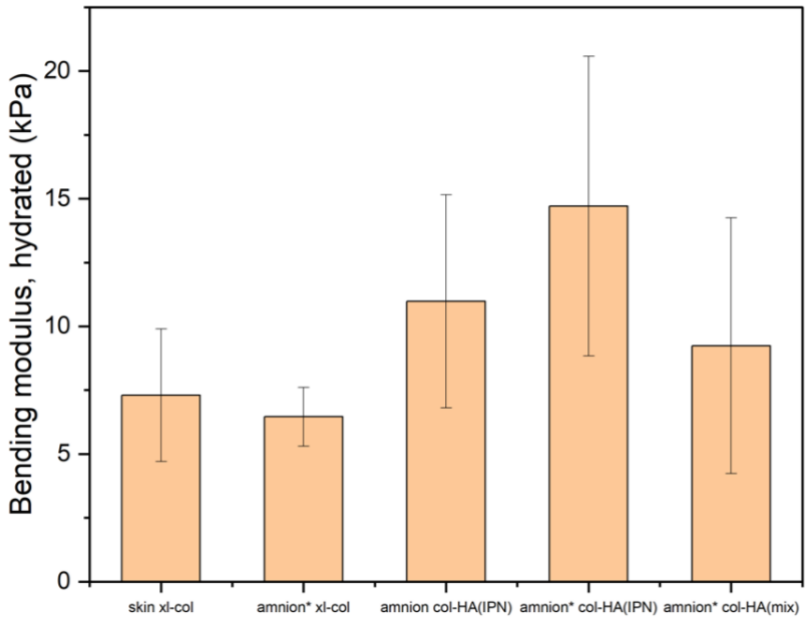


Figure 4.15 The bending moduli of the hydrated scaffolds.

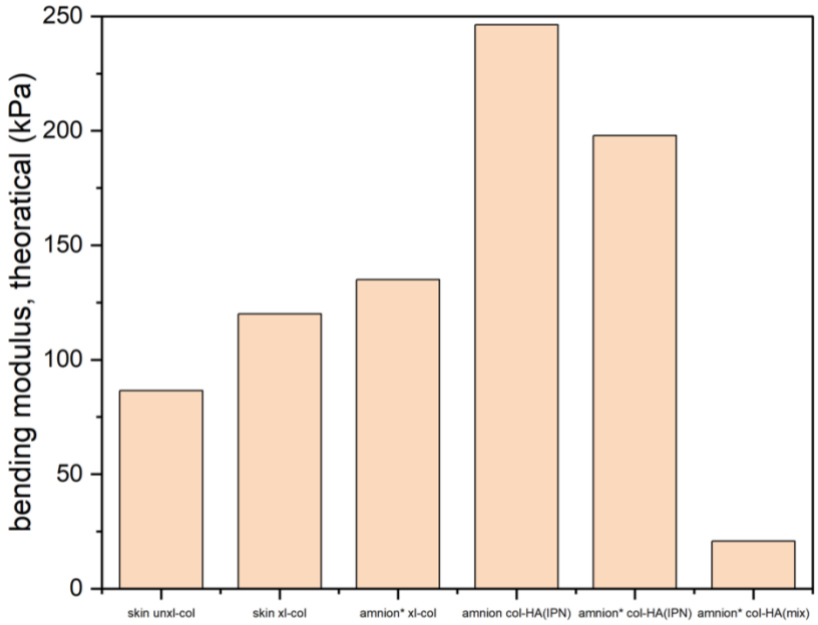


Figure 4.16 The calculated bending moduli of the non-hydrated samples based on experimental compressive and tensile property data, therefore is presented with error bars.

	$E_{bend,\ dry}$ (kPa)	$E_{bend,\ wet}$ (kPa)
skin unxl-col	86	
skin xl-col	120	7 ± 3
amnion* xl-col	135	6 ± 1
amnion col-HA(IPN)	246	11 ± 4
amnion* col-HA(IPN)	198	15 ± 6
amnion* col-HA(mix)	20.7	9 ± 5

Table 4.6 A summary of the theoretical bending moduli in the non-hydrated state and the experimental bending moduli in the hydrated state of the samples tested.

4.4 Discussion

4.4.1 Suspension Viscoelasticity

Storage modulus indicates the elastic energy-storing ability, and with the elevating angular frequency introducing increasing shear rate, the energy available for storage hence increases, leading to the positive effect of frequency on storage modulus [273]. The dominance of storage modulus over loss modulus reflects a strong dominance of the elastic portion of the collagen suspension viscoelasticity, and the influence of the viscous portion dropped (reduced tanδ),

coinciding with the previously mentioned shearing thinning behaviour [274]. The reduction of both G' and G" with HA addition can be attributed to the rule of mixing, as HA has significantly lower G' and G" values compared to collagen [275]).

The Maxwell (spring and dashpot in series) and the Voigt (spring and dashpot in parallel) models shown in Figure 4.17 are the starting point leading to a more complicated polymer viscoelasticity discussion, and a more complicated version, the 4-element model as shown in Figure 4.20, which combines the features of both models can offer a more accurate explanation [276]. In the Maxwell model, the stress applied in the system is the same for the spring component and the dashpot component, whereas the total strain equals the Hookean strain of the spring and strain of the viscous component dashpot:

$$\sigma_{system} = \sigma_{spring} = \sigma_{dashpot}$$

$$\sigma_{spring} = E_{spring}\gamma_{spring}$$

$$\sigma_{dashpot} = \eta_{dashpot}\frac{\gamma_{dashpot}}{t}$$

$$\gamma_{system} = \gamma_{spring} + \gamma_{dashpot} = \frac{\sigma_{system}}{E_{spring}} + \frac{\sigma_{system}}{\gamma_{dashpot}}t = \sigma_{system}\left(\frac{1}{E} + \frac{t}{\eta}\right)$$

Meanwhile, in the Voigt model, the elongation development is limited to the strain of the dashpot while the strain reached is constrained by the extent of spring extending. The spring and dashpot share the applied stress, giving similar system strain:

$$\gamma_{system} = \gamma_{spring} = \gamma_{dashpot}$$

$$\sigma_{system} = \sigma_{spring} + \sigma_{dashpot} = E_{spring}\gamma_{spring} + \eta_{dashpot}\frac{\gamma_{dashpot}}{t}$$

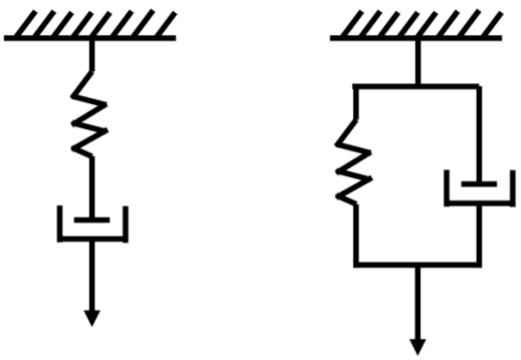


Figure 4.17 The illustration of the Maxwell (left) and the Voigt (right) models describing polymer viscoelastic behaviours.

It was reported that the equations below linked the storage modulus, the loss modulus, and the frequency (Hz) with the spring modulus E and the dashpot viscosity η under the assumptions of the two models [277]. For the classic Maxwell model, the equations are:

$$G' = \frac{E(\eta\omega)^2}{E^2 + (\eta\omega)^2}$$

$$G'' = \frac{E^2\eta\omega}{E^2 + (\eta\omega)^2}$$

With the spring modulus E and the dashpot viscosity η as the unknown variables, the above equations can be solved as:

$$E = \frac{(G')^2 + (G'')^2}{G'}$$

$$\eta = \frac{(G')^2 + (G'')^2}{G''\omega}$$

For the Kelvin-Voigt model,

$$G' = E$$

$$G'' = \eta\omega$$

Which can be written as:

$$E = G'$$

$$\eta = \frac{G''}{\omega}$$

To gain insight into the modulus of the elastic spring proportion and the viscosity of the viscous dashpot component, experimental storage and loss moduli data were substituted into the equations above, and the theoretical spring modulus and dashpot viscosity were calculated and plotted. Figure 4.18 gives the comparison between the calculated spring modulus (E) based on the Maxwell model and the actual storage modulus (G') of the suspension. On the basis that the suspensions presented a highly elasticity-dominant nature, the theoretical spring modulus (E) is expected to be close to the storage modulus (G'), which is the case as shown in Figure 4.18, with the discrepancy broadening with increasing frequency, indicating that at lower frequency, the Maxwell model is sufficient to represent the elastic component of the suspensions. Figure 4.19 displays comparisons among the experimental complex viscosity, the Maxwell viscosity, and the Voigt viscosity of the five suspension types. It can be seen from the figures that the Voigt model is more suitable for representing the suspensions' viscoelastic behaviours regarding the viscosity portion.

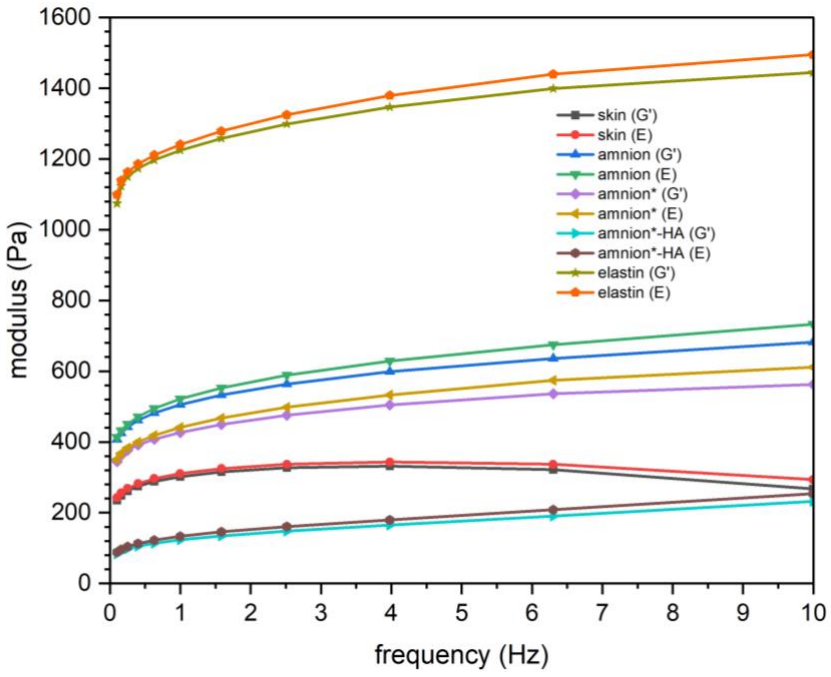


Figure 4.18 The comparison between the calculated spring modulus (E) based on the Maxwell model and the experimental storage modulus (G') of different samples.

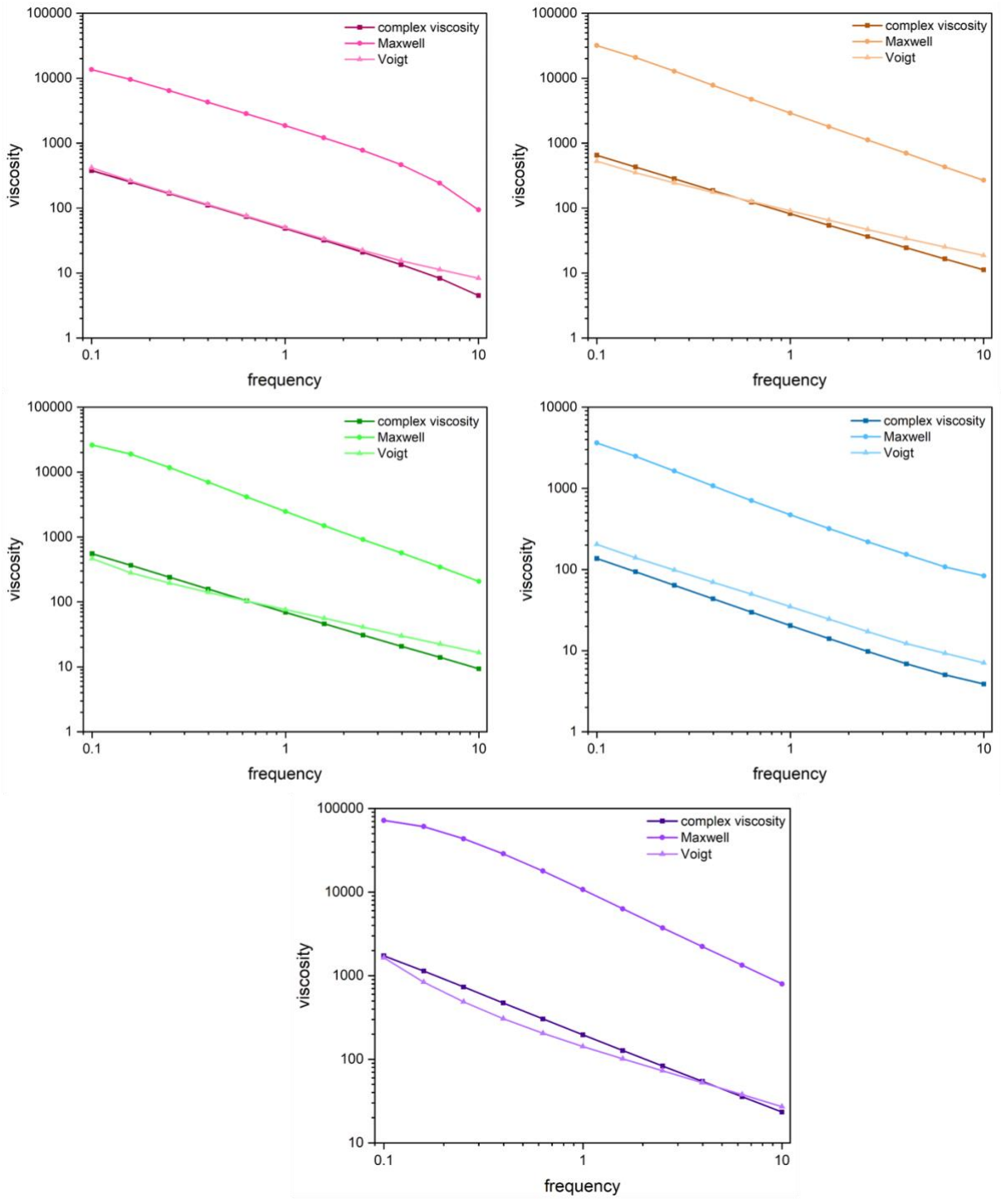


Figure 4.19 The experimental complex viscosity, the Maxwell viscosity, and the Voigt viscosity of in sequence the skin collagen suspension, the amnion collagen suspension, the amnion* collagen suspension, the amnion*-HA suspension, and the elastin fibrillar gel.

In the attempt to further understand the dynamic mechanical response, the acquired data of G' or G'' was plotted against ω to fit into the commonly adopted correlation

$$G'^{(\prime)}(\omega) \sim \omega^{n}$$

where ω is the angular frequency (rad/s). More visualised, the modulus-frequency curve was plotted on a logarithm scale for gradient study. For materials exhibiting Maxwellian behaviours (entanglement network), n=2 for G' and n=1 for G'' [278]. On the other hand, for crosslinked networks exhibiting no entanglement effect, the n-value for both G' and G'' is expected to be 0. The n-value calculated for the results obtained is ~ 0.10 for crosslinked collagen suspensions, confirming the partially crosslinked nature of the gel and the dominant effect of chemical crosslinks over physical entanglements on viscoelasticity. G'' of skin collagen is noticeably lower than that of amnion and amnion* collagen gel (0.16 versus 0.29 and 0.31), which can be attributed to the intrinsically more crosslinked nature of skin collagen. It is worth mentioning that as a nature-derived polymer, collagen has prominent differences with synthetic polymers regarding its rheological and viscoelastic properties, which might be under the influence of peptide chain length, helical structure and the high molecular weight [201].

For the collagen-HA mixture, the n-value for G' increased to 0.18 while maintained at the same level for G'' (0.26). A possible explanation lies behind the inclusion of HA, which dampened the relative percentage of crosslinks to entanglement between HA and collagen molecules, subsequently increasing the frequency dependency of storage modulus. As for the level n-value of G'' before and after HA incorporation, due to the elasticity prevalence over viscosity, the number of entanglements introduced was less impactful. For elastin gel, despite the absence of a chemical crosslinking step, it nevertheless displayed frequency dependence akin to crosslinked gel (n=0.06 for G', comparable to the original work on elastin gel). The hydrolysed rod-like fibres replaced the globular ones in insoluble powder form, thereby largely hindering the contribution from entanglements. The n-value of G'' of elastin gel is also approximately of the same level, similarly due to minimal contribution from the viscosity portion to viscoelasticity response.

It was mentioned briefly in the Result section that the loss modulus of the fibrillar gel elastin decreased first with the increasing frequency then increased again. Different from the triple helical structure of the collagen molecules, elastin molecules are hydrophobic and globular. Therefore, increasing from a low frequency, instead of slowly starting to slide past each other, the molecules first unfold, rendering the whole system more subjective to intramolecular chain movement and therefore elastic deformation. This extra step compared to the collagen suspensions is assumed to have introduced the initial loss factor decrease with increasing frequency. After the chain extension, the elastin gel started behaving similarly to the collagen suspensions, i.e., experiencing increasing loss modulus again with increasing frequency. The existence of this critical point of the elastin loss factor gives insight into the frequency under which elastin experiences the least energy dissipation, which is more desirable for heart valve leaflet designs. The critical frequency is about 0.4 Hz for fibrillar gel elastin, which is lower than the physiological condition of the heart activity (about 1 Hz), therefore, further studies should focus on the modification of the elastin to ensure it preserves the most energy.

4.4.2 Scaffold Viscoelasticity

In tensile frequency sweep tests conducted on scaffolds, the shear strain was controlled as a constant of 0.3 %, and with increasing frequency, the system experienced a shorter time within each cycle. In the Maxwell model, when strain is held as constant, the initial immediate strain response from the spring component would reduce over time, accompanied by a gradually increased strain from the dashpot component. With increasing frequency, the time allowed for dashpot development shortens, resulting in a larger portion of elastic over viscous response. In the Voigt model, the dashpot acts as the limitation to elongation extent, and to reach the same shear strain, larger stress would need to be applied with shortened

cyclic time, which is supported by increasing shear stress detected by the system while testing.

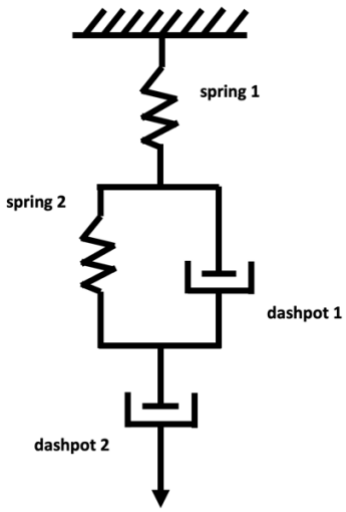


Figure 4.20 An illustration of the 4-element model combining the Maxwell model and Voigt model describing more complicated viscoelastic systems.

A similar gradient study has been done on scaffolds tested in the non-hydrated state as well. In general, G' was observed to have increased with higher frequency for all sample types. As mentioned above, the Voigt part requires incremental shear stress to maintain constant strain, and with the $\frac{t}{\eta}$ value being roughly unchanged, the maintenance of similar strain would result in slightly increased G'. G", however, has seen three different trends, respectively gradually increasing for the HA-infiltrated collagen and the non-crosslinked skin collagen scaffolds, level for the crosslinked collagen scaffolds, and fluctuating and non-linear behaviour from the collagen-HA mixed samples. For the crosslinked samples, the fibre aligning ability is drastically reduced, resulting in an almost entirely crosslinked network ($n \approx 0$). For the collagen-HA mixed samples, the fluctuation can potentially be attributed to the uneven distribution of collagen and HA fibres, which is hypothesised to be eliminated once the optimal fabrication method is developed.

The non-crosslinked skin collagen scaffolds exhibited almost parallel log(G')–log(f) and log(G")–log(f) plots with slopes of 0.09 and 0.08 respectively, while the crosslinked

counterparts showed markedly weakened G'–f correlation (n-value around 0.035), marking the shift to a more crosslinked network. HA infiltration had no impact on the n-value, which is expected as the dampening effect of the HA is only significant when the samples are hydrated. Parallel log(G')–log(f) and log(G")–log(f) relationships were also found in the HA-infiltrated samples, which coincides with the finding of a different study investigating a collagen-chitosan system [210].

4.4.3 Deformation Mechanism

It is within the expectation that forms of modification will impact the compressive mechanism thus altering the stress-strain curve shape. Crosslinking is shown to shorten or eliminate the plateau region originating from the pore wall buckling and the small-scale pore collapsing while HA infiltration inevitably introduces noticeable batch-to-bath differences, and the explanation for these variances lies in the microstructures. As elaborated in Chapter 3, the crosslinked skin collagen scaffolds possess less extent of intact pore walls and, therefore cannot resist the stress exerted by creating more deformation. The amnion* collagen, similarly, displays a moderate level of integrity and homogeneity, hence the curve obtained. Other than different HA secondary network configurations, the differences between the amnion and the amnion* samples can be attributed to the smaller pore size and narrower pore size distribution of the amnion* samples, which reportedly has a positive impact on resistance to compressive deformation [279].

The J-curve behaviour is frequently observed and most of the time required in the application of biomaterials as it grants the device both a free range of motion at a small amount of stress and high resistance when the stress goes beyond the desired level. It is in favour because of its concave shape and the resulting under-curve area, which represents the energy released at failure compared to Hookean materials, achieving minimised crack

propagation. It is, nevertheless, less commonly seen when the structure is tested in the non-hydrated state. Here, the HA dispersion is reckoned to be responsible based on the composite theory, as both preliminary test results on HA-only samples and literature on HA mechanical properties support that the stronger stiffness provided by collagen can be drastically reduced by forming a composite with HA.

For the mechanical behaviours of fabricated scaffolds under compression, tension and bending, further discussion is carried out based on the deformation mechanism mentioned in section 4.3.3. Firstly, in the elastomeric foam, the slopes of the linear region of both the compressive and tensile stress-strain curves (E_{comp} and E_{ten}, respectively) are expected to be equal due to the same governing deformation mechanism. However, E_{ten} measured in this thesis are constantly two orders of magnitude higher than that of E_{comp}. The explanation can be developed upon the cubic cell model proposed by Gibson [280] and standard beam theory [281]. As Figure 4.21 illustrates, when considered as a closed cell, the deformation is composed of three parts: the pore wall bending, the pore edge bending, and the pore wall stretching or buckling under tension or compression. It has been proposed that

$$\frac{E_{ten}}{E_s} = 2\left(\frac{1-\Phi}{3}\frac{\rho}{\rho_s}\right)^3 + 4\left(\frac{\Phi}{3}\frac{\rho}{\rho_s}\right)^2 + \frac{1-\Phi}{3}\frac{\rho}{\rho_s}$$

$$\frac{E_{comp}}{E_s} = 2\left(\frac{1-\Phi}{3}\frac{\rho}{\rho_s}\right)^3 + 4\left(\frac{\Phi}{3}\frac{\rho}{\rho_s}\right)^2$$

where E_s is Young's modulus of pure material, and Φ is the pure material fraction contained in the pore edges, with the terms in sequence attributed to the pore wall bending, the pore edge bending, and the pore wall stretching. Pore wall buckling under compression is negligible, therefore while the pore wall stretching is the determinant component in tensile deformation, the pore edge bending dominates compressive response. The relative density of all samples produced is extremely low (0.02 or below), therefore creating the two orders of magnitude difference in compressive and tensile moduli.

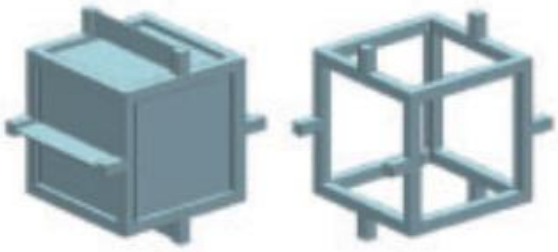


Figure 4.21 The cubic cell model with the closed cell model on the left and the open cell model on the right [279].

4.4.4 Effects of Modification

The influence of crosslinking is investigated by including the knowledge of rubber elasticity. According to the rubber elasticity theory [282], the effective crosslink density (v_e) can be calculated using the equation:

$$v_e = \frac{E\Phi^{-\frac{1}{3}}}{3RT}$$

where E is Young's modulus, Φ is the volume fraction, R is the gas constant, and T is the temperature. It can be interpreted that under the same testing temperature with the same volume fraction, the effective crosslink density is linearly related to Young's modulus. After partially crosslinking with EDC/NHS, the compressive and tensile moduli increased to 1.4 and 1.6 times respectively, corresponding to the relative crosslink density increment. It can be combined with FTIR data and concluded that not the entirety of amide and ester bonds have contributed to effective crosslink density. It is also worth noticing that crosslinking appeared to have more impact on the compressive response, which can be attributed to the pore edge bending dominance under compression. The crosslinks would increase the stiffness of the pore edges, introducing more bending resistance. Meanwhile, the strengthening effect is reduced under tension because the pore wall fibre aligning mechanism is less affected by crosslinks.

HA was discovered to have a significantly positive effect on compressive stiffness and imposed a 1.5-fold increase on compressive modulus (from 41.8 kPa to 62.8 kPa). Similar to crosslinks, the infiltrated HA served to strengthen pore edge stiffness but based on the stiffness of the HA network itself, the effect is relatively limited. However, as concluded in Chapter 3, the porosity of HA-infiltrated scaffolds is significantly lower than that of the parental collagen network (97.9 % compared to 98.6 %), leaving the relative density of HA-infiltrated samples 1.5 times higher (0.0212 versus 0.0145). Associating with the cubic cell deformation model, the difference in relative density contributes compressive deformation with the power of 2, resulting in a theoretically 2.1-fold increase in compressive modulus if relative density were to be the only effective factor. This combined with the aforementioned pore edge strengthening, coupled with reduced pore size, serves as a potential explanation for the compressive stiffness. The same explanation can also be applied to tensile stiffness.

Mixing HA and collagen solution before moulding, however, has brought in fundamental changes to scaffold mechanical properties in the non-hydrated state. Firstly, both compressive and tensile moduli have seen drastic drops to 15 % and 16 % of those of the crosslinked collagen-only samples which cannot be explained by the decreased relative density or the shrunk pore size. Interestingly, a study pointed out that with no ionic strength altering salt presenting, the positively charged collagen molecules and negatively charged HA chains form a polyion complex (PIC) structure in an aqueous environment that hinders diffusion during the solidification process at freezing temperature, magnifying structure heterogeneity and resulting in poor mechanical properties [283].

The formation of PIC can also explain the other distinct difference, which is the appearance of the “toe region” in the stress-strain curve under both tension and compression, in other words, the “J-curve” behaviour that is only expected in the hydrated state. With collagen and HA being compactly complexed, the initial stress applied under tension is

hypothesised to act on breaking the physical complexation first, aiding the fibre alignment along the axial direction, therefore causing a derivation of the tensile stress-strain curve. As for compression, the missing plateau signifies the omission of pore wall buckling and small-scale pore collapsing, potentially being a consequence of the coiled complex offering more compression resistance, prolonging the linear region. Once the structure started to yield, full-scale pore collapses ensued.

4.4.5 Bending

Combining the compressive and tensile responses, the bending behaviours can be deduced accordingly. In the standard beam theory, the compressive and tensile properties contribute equally, and the neutral axis is located in the centre of the beam. However, with vastly different moduli, it is worth investigating the main factor affecting the bending stiffness of the scaffolds. When bent, the bending moment initiates compressive stress in the region above the neutral axis and tensile stress below. The forces can be expressed in equations:

$$F_{ten} = \int_0^{h_2} \sigma_{ten} b \, dy = \int_0^{h_2} \kappa E_{ten} y b \, dy = \kappa E_{ten} \frac{b {h_2}^2}{2}$$

$$F_{comp} = \int_0^{h_1} \sigma_{comp} b \, dy = \int_0^{h_1} \kappa E_{comp} y b \, dy = \kappa E_{comp} \frac{b {h_1}^2}{2}$$

$$\sigma = \frac{My}{I} = \frac{\kappa E_{ten} I y}{I} = \kappa E_{ten} y$$

where M is the bending moment, h_1 and h_2 are the distance from the upper and lower surface to the neutral axis, κ is the curvature, b is the width of the cross-section, and I is the second moment of inertia. For a continuous transition from compressive region to tensile region, F_{ten} and F_{comp} should be of equal values, which gives the location of the neutral axis:

$$\frac{h_1}{h_2} = \frac{\sqrt{E_{ten}}}{\sqrt{E_{comp}}} = N$$

For the non-crosslinked and the crosslinked scaffolds, the neutral axis location value N is calculated to be 6.3 and 6.7 respectively, both exhibiting a strong compression dominance in bending behaviours. After partial crosslinking, the theoretical bending modulus in the non-hydrated state saw a 1.4-fold increase, corresponding with the increase in the dominant compressive stiffness. The non-crosslinked samples in the hydrated state were not up to the self-deflection test mechanical standards, therefore no comparison could be done to indicate the quantitive bending strength. However, it is assumed that the performed crosslink modification improved the hydrated bending strength based on the fact that the crosslinked samples could indeed withstand the bending test.

Hydration was tested to have drastically reduced the bending stiffness by a magnitude, which is attributed largely to the different deformation mechanisms as well as the interaction with water, which will be further discussed with stress-strain curves in Chapter 5. For now, quantitive analysis is performed on the data obtained to further understand the effect of different HA incorporation methods as well as the effect of different collagen sources. In previous analyses of the non-hydrated samples, different factors played a noticeable part in altering the mechanical properties. However, consistency in general exists across different properties within the same sample type. The amnion* collagen is reported to yield approximately 1.5 times stiffer scaffolds apart from under compression, which could be explained by the fact that the amnion* collagen suspension is 1.5 times stiffer than the skin collagen suspension and that both the viscoelasticity and tensile tests shared the tensile mechanism. This difference, however, was not spotted in the hydrated state, which could potentially be due to that the amnion* collagen has a better water uptake ability, leading to further interaction with water stretching the structure in addition to the load.

HA infiltration, on the other hand, appeared to improve mostly the compressive stiffness while maintaining the viscoelasticity and tensile properties. It was explained earlier

that HA infiltration strengthens pore edge stiffness by possessing a slightly denser structure and that the relative density has a more significant effect on compression than on tension. In the hydrated state, as developed earlier, the compression-dominate bending stiffness saw a 2.3-fold increase, which is even higher than compression (1.5-fold increase). The extra boosting could have originated from the hydrogen bonding introduced by HA, which could also explain the similar level of bending stiffness of the pre-mixed collagen-HA samples compared to their inferior performance in the non-hydrated state.

4.5 Conclusion

In this chapter, the viscoelastic, compressive, tensile, and bending properties were investigated for all the collagen-based single-layer samples, revealing further information on the deformation mechanism and effect of different factors. First of all, it was brought to light that for both suspensions and scaffolds, elasticity dominates over viscosity, and because of that, simple viscoelasticity models such as the Maxwell and the Kelvin-Voigt models can predict the suspension viscoelastic behaviours in different aspects within the tested frequency range relatively accurately. Within the same property tested, it can be concluded that different types of collagen had more impact on tensile than compressive stiffness, providing preliminary guidance on which type of collagen to choose for different loading applications. At the same time, it revealed that scaffold compressing and stretching are regulated by different deformation mechanisms, and after further discussion, it was concluded that the pore wall stretching dominates deformation under tension while the pore edge bending contributes the most to compression. Bending was later studied to be compression-dominate due to the neutral axis shift as a response to the imbalanced compressive and tensile moduli.

Crosslinking was proven to uplift the mechanical potential in both the non-hydrated and the hydrated states, with Young's modulus under compression and tension experiencing a

1.4-fold and 1.6-fold increase respectively. However, such improvements are at the expense of reduced extensibility, with the endpoint or breakpoint strain dropping to 58 % and 22 % of the non-crosslinked sample values. HA infiltration, contrary to collagen source, was shown to have more impact on the strengthening of the compression and bending stiffness over viscoelasticity or tensile properties, and relative density and hydrogen bonding were determined to be the reasons. Pre-mixing collagen suspension with HA resulted in a structure with far inferior non-hydrated properties, yet further bending tests in the hydrated state reinstated the viability of this design under the application physiological conditions. At last, the first glance at the behaviours of the hydrated samples revealed that hydration plummets the stiffness.

Chapter 5 Fabrication and characterisation of tri-layer scaffolds

5.1 Introduction

With the success of the collagen-based single-layer scaffold fabrication and further investigations into their mechanical properties, tri-layer scaffolds are to be assembled and characterised. Two different designs marked by different middle layers and fabrication routes were materialised and examined in aspects of the microstructure, the mechanical properties in both the non-hydrated and hydrated states, and the degradation resistance in a non-enzymatic environment. The microstructure was revealed by SEM, looking at the interface transitions as well as potential structural changes when the single-layered are stacked up. A similar set of mechanical tests was performed on the tri-layer scaffolds under the same test conditions for direct comparisons, with the addition of the three-point bending test investigating the bending properties and the bending anisotropy in the non-hydrated state in both the With Curvature (WC) and the Against Curvature (AC) directions. On the hydrated front, the self-deflection tests were conducted in both WC and AC directions as well, characterising the bending anisotropy in physiological conditions. Besides that, compression tests were done in submersion mode to gain insights into the stress-strain response in physiological conditions. To complete the full evaluation of whether the designs are potentially viable for future *in vitro* and *in vivo* works and even possible clinical applications, a 12-week non-enzymatic degradation study was conducted to shed some light on the degradation resistance required for cell culture in the media.

5.2 Materials and Methods

5.2.1 Fabrication

The crosslinked amnion* collagen and the fibrillar elastin gel were selected to be the component of the fibrosa- and the ventricularis-mimicking layer respectively, with the

spongiosa-imitating layer being either amnion* collagen-HA(IPN) or amnion* collagen-HA(mix). The former is labelled as tri-layer(ipn), and the latter as tri-layer(mix).

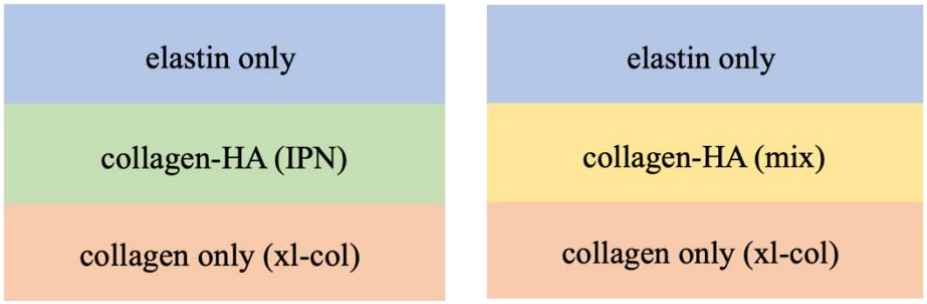


Figure 5.1 The schematics of the two tri-layer scaffold designs: tri-layer(ipn) on the left and tri-layer(mix) on the right.

Similar to the single-layer scaffolds, the tri-layer designs were fabricated by casting the suspension into the moulds and freezing, followed by freeze-drying. The same moulds were used with the thickness of each layer being as close as possible to one-third of the thickness of the moulds. For the tri-layer(ipn) scaffolds, the collagen-only layer was laid down first and flattened to about one-third length of the mould height. Subsequently, the HA-infiltrated collagen scaffolds ready after the two washing steps were gently placed on top of the collagen layer, with the thickness being made sure to be one-third of the height when the collagen parent network was being fabricated beforehand. Excessive water was absorbed for closer contact between layers and consistent concentration of the suspensions, and it was achieved by tapping the surface gently with filter paper. Finally, the fibrillar gel elastin was added on top of the collagen-HA(IPN) layer and carefully flattened without pressing down into the bottom two layers. The samples were then placed into the -20 ºC freezer overnight, awaiting further freeze-drying.

For the tri-layer(mix) design, the general idea of layer-by-layer moulding still applies. However, due to the lack of a solid supporting middle layer keeping the suspensions from being mixed, a multistep alteration has been made to the original method. After the bottom collagen-only layer had been laid down and flattened, the samples were placed into the -20 ºC

freezer briefly to let the suspension slightly solidify. Once it was taken out of the freezer again, the consecutive premixed collagen and HA layer was added on top and flattened. The same procedure was repeated until the final successful addition of the top fibrillar gel elastin layer. Eventually, the whole structure was transferred back into the freezer overnight and for further freeze-drying.

5.2.2 SEM

Zeiss EVO SEM was employed to observe the microstructure of the tri-layer designs. Instead of perpendicularly to the axis, the samples were sectioned into thin slices of 1–2 mm along the axial direction using a sharp surgical scalpel, including the topology of all three layers. The cut slices were then placed on aluminium pin stubs with carbon tapes and coated with 5 mm of either platinum or chrome (Leica EM ACE600), and a thin layer of silver dag (Agar Scientific Ltd, UK) was applied on the side creating a conductive path for the secondary electrons. The accelerating voltage was set to be 10 kV, and the probe current was 200 pA. The morphology information was analysed using ImageJ (National Institutes of Health, US) for further comparison with the single-layer scaffolds.

5.2.3 Mechanical Properties (Non-hydrated)

The same set of mechanical tests was conducted with the addition of the three-point bending test for the bending properties in the non-hydrated state of the tri-layer scaffolds. The viscoelasticity in the non-hydrated state was tested under tension before the tensile test using TA Instruments DMA Q800, with samples (N=5) being subjected to a 0.3 N preload and a 0.1 % constant strain and the testing frequency oscillating at 0.1, 0.3, 1.0, 3.0, and 10.0 Hz, which was selected to represent the low, moderate, and high frequency, which correspond to the long-timescale and short-timescale deformation modes. On top of that, the frequency

range selection covers the overtime fatigue (low frequencies), the resting (about 1 Hz), and under-impact (high frequencies) scenarios related to the heart valve activities. For the static compressive and tensile tests, the test conditions were set to be the same as those of the single-layer scaffolds for cross-examination, with the preload being 0.01 N and the force rate being 0.3 N/min. The theoretical bending modulus was calculated from the compressive and tensile moduli measured, serving as a comparison with the bending modulus tested empirically by three-point bending.

The three-point bending test is widely employed in testing the bending properties due to its simple procedure and accurate results. It is based on the beam theory that involves a beam subjected to a concentrated load at its centre with two roller supports at the two ends as shown in Figure 5.2, and the convex side of the sample is under tension and the concave side is under compression. In the case of the tri-layer designs in this study, the collagen-only and the fibrillar elastin gel layers have different tensile and compressive stiffness. Therefore, the placement (i.e., which side faces up) will inevitably determine the final results. Given the scaffolds are aimed to be applied as part of the heart valve leaflets, which regulate blood flow direction, it is of great importance to investigate the bending properties both in the With Curvature direction (WC, the collagen-only layer facing up) and the Against Curvature direction (AC, the fibrillar elastin gel layer facing up). The test was conducted on samples (N=5) in both directions with the same geometry as the tensile test samples with a 0.01 N preload and 0.3 N/min force rate until 3 N on the DMA Q800.

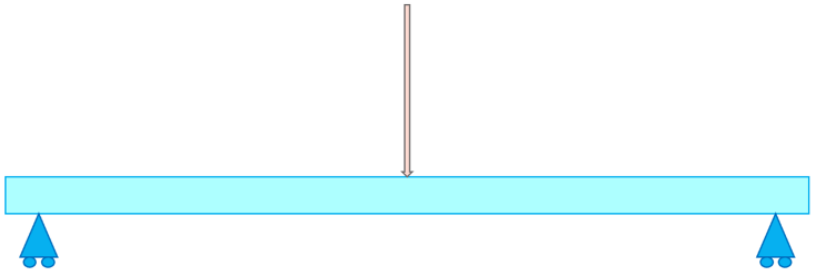


Figure 5.2 A schematic illustration of the three-point bending test.

5.2.4 Mechanical Properties (Hydrated)

Like single-layer samples, the self-deflection test was employed to obtain the bending modulus of hydrated samples. Samples (N=5) were weighed before and after one hour of hydration in PBS, and the mass values were recorded accordingly for water uptake calculation. After excessive water was absorbed by filter paper and the hydrated weight was recorded, the samples were gently placed onto the U-shaped metal plate with a span of 20 mm and let deflect freely in both the WC and AC directions. After equilibrium was reached, the final extent of deflection was imaged by a Canon G7X Mark III camera for further data measurement and analysis using ImageJ, and the bending modulus was calculated using the beam theory.

Compression tests were carried out under the submersion mode of DMA Q800 to reveal the compressive behaviours of the tri-layered scaffolds in the hydrated state. The preload was changed to 0.001 N instead of 0.01 N due to the less stiff nature of the samples, but the force rate was kept the same at 0.3 N/min for comparison purposes. Samples (N=5) were placed at the centre of the bottom container, and the top clamp was brought down to secure the samples from moving. PBS was subsequently poured into the container and the samples were left submerged for 10 min ensuring full hydration. Once the samples were ready, the same protocol as the compression test in the non-hydrated state was put in place. The data was viewed and analysed using the software connected to the machine.

5.2.5 Degradation

A non-enzymatic degradation test was performed to verify the feasibility of the potential future *in vitro* work predicted from the results of single-layer scaffolds as well as to study the integrity of the layered structure under physiological conditions. The experiment was carried

out for 12 weeks at 37 ºC with gentle shaking, with the sample weight being measured weekly at the same time. The 5 mm x 5 mm samples (N=5) were immersed in ~ 2 ml of PBS with 0.04 g sodium azide, and the tests were conducted in the same manner as the single-layer designs. The degradation progress is manifested by mass loss, which can be calculated from Equation 3.6.

5.2.6 Statistics

All data were presented in the form of average ± standard deviation. Both the Student t-test and the ANOVA followed by the Tukey HSD post hoc test were used to compare groups of data when deemed appropriate, with a probability value of 95 % ($p < 0.05$) as the statistical significance criterion.

5.3 Results

5.3.1 Pore Morphology

The pore morphology of any three-dimensional scaffold holds a critical effect on cell morphology, attachment, and function [284], therefore, a few images were taken in adjacent areas on the same sample of both tri-layer scaffold designs and were stitched together for pore morphology features under magnification and overview. Figures 5.3 and 5.4 both presented three distinctive layers and seamless interface transitions, with the morphology features of each layer coherent with the findings of its single-layer components, proving the proposed tri-layer scaffold fabrication method to be effective. Besides, the demonstrated open pore structure with well-interconnected pores provided the foundation for potential future biological work.

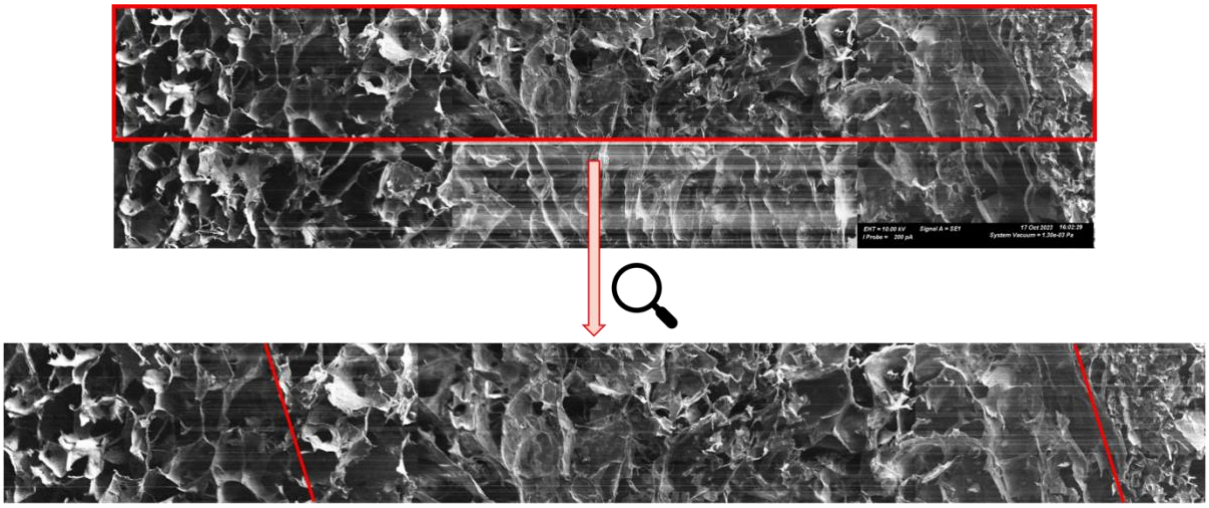


Figure 5.3 SEM images of a tri-layer(ipn) scaffold sample under the magnification of x50.

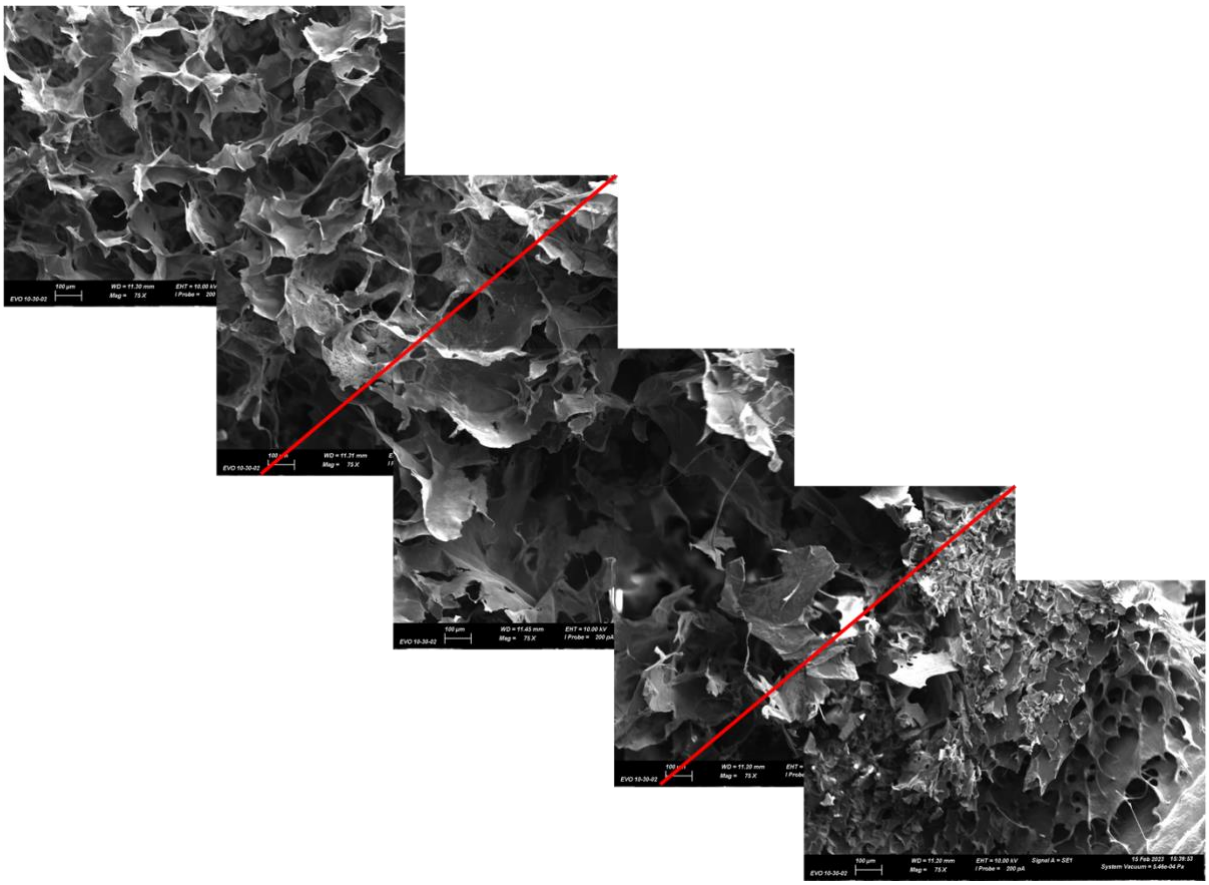


Figure 5.4 SEM images of a tri-layer(mix) scaffold sample under the magnification of x75.

The average pore size was further measured and calculated, and the results are listed in Table 5.1. Between the two tri-layer designs, the average pore sizes of the collagen-only layer are consistent with each other; when compared with the crosslinked collagen scaffolds, however, a roughly 40 % decrease in pore size was observed. The HA-infiltrated layer within

the tri-layer(ipn) sample showed a similar average pore size as expected, yet the pre-mixed collagen-HA layer within the tri-layer(mix) sample had undergone an 18 % decrease in pore size.

tri-layer(ipn)		tr-layer(mix)	
collagen-only	187 ± 83	collagen-only	178 ± 88
collagen-HA(IPN)	220 ± 142	collagen-HA(mix)	147 ± 61

Table 5.1 The average pore size (μm) of the collagen-based layers within the two types of tri-layer scaffold designs.

5.3.2 Viscoelasticity

Similar to the single-layer samples, the tensile frequency sweep test was performed on both types of tri-layer designs before the tensile force ramp static test, and the curves were plotted logarithmically along with relevant single-layer components for gradient study and comparison. It can be seen from Figure 5.5 that both types of tri-layer scaffolds showed linearly increasing storage modulus with frequency ($R^2 > 0.999$), with tri-layer(ipn) displaying a higher slope value of 0.043 compared to 0.028 of tri-layer(mix), meaning that the elasticity of the tri-layer(ipn) is more dependent on frequency. For the loss modulus shown in Figure 5.6, the tri-layer(ipn) samples presented a reduced ability to dissipate energy as heat while the tri-layer(mix) showed the opposite, with the loss modulus increasing as frequency went up.

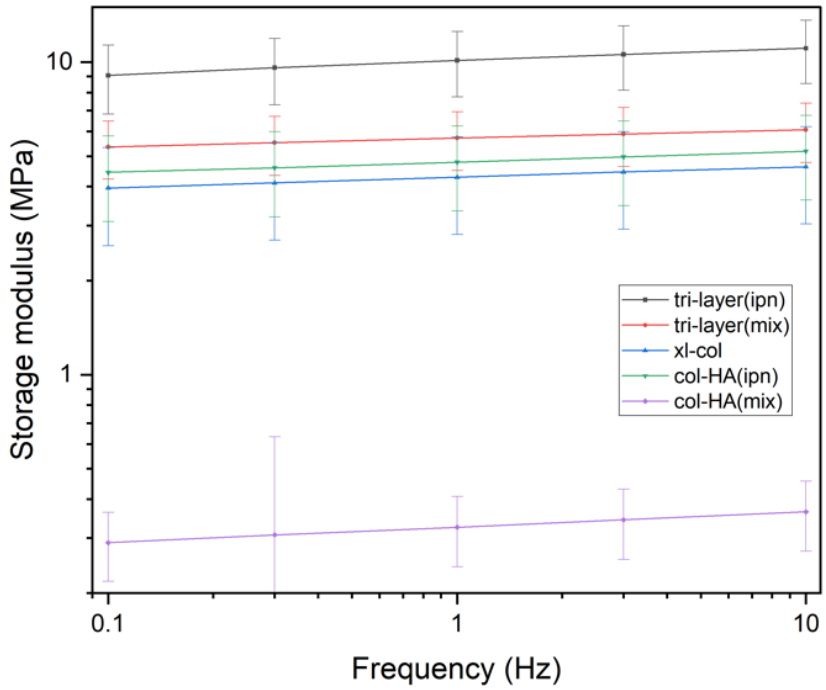


Figure 5.5 The progression of the storage moduli of the tri-layer scaffolds and their composing individual layers with increasing frequency on the logarithm scale obtained with tensile frequency sweep.

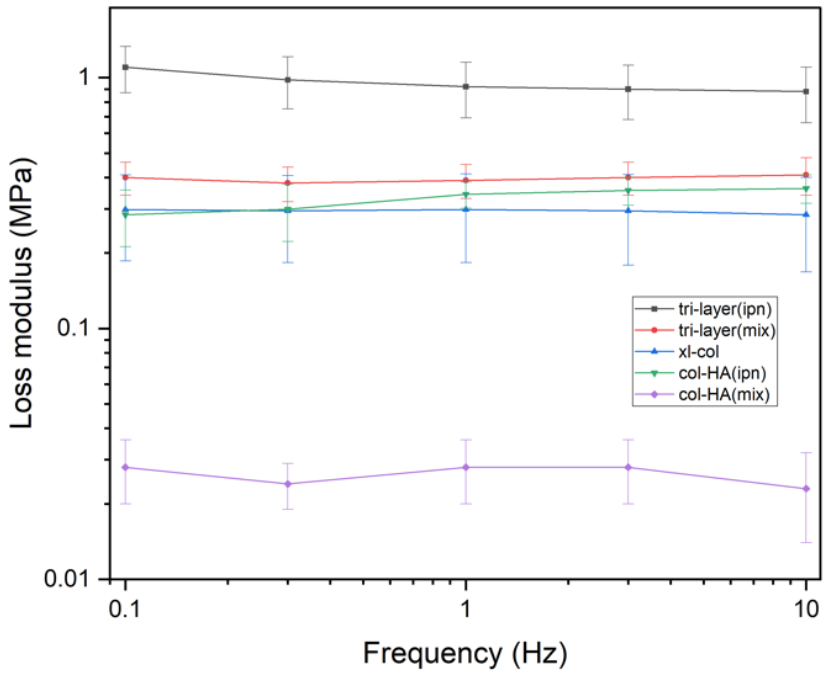


Figure 5.6 The progression of the loss moduli of the tri-layer scaffolds and their composing individual layers with increasing frequency on the logarithm scale obtained with tensile frequency sweep.

Composition-wise, based on pre-existing data, the elastin-only layer is assumed to further improve the elastic energy storage ability, which was experimentally proven as the tri-

layer(ipn) scaffolds showed significantly greater storage modulus than that of both collagen-only and collagen-HA layer. The same influence can be spotted in the improvement in the storage modulus of tri-layer(mix) samples from the collagen-only layer despite the collagen-HA layer exhibiting a vastly lower energy storage ability. It can be concluded that elastin also has a positive effect on loss modulus for both designs; however, the progression trend of loss modulus is more controlled by the HA-incorporated layers. The obtained data is concluded to support the hypothesis of the different functions and properties each layer brings into the whole structure: collagen to increase stiffness, elastin to increase elasticity, and HA to increase the dampening effect.

	storage modulus (MPa)	loss modulus (MPa)	loss factor
tri-layer(ipn)	10 ± 2	0.9 ± 0.2	0.09
tri-layer(mix)	6 ± 1	0.36 ± 0.06	0.07
amnion* xl-col	4 ± 1	0.3 ± 0.1	0.07
amnion* col-HA(IPN)	5 ± 1	0.34 ± 0.04	0.06
amnion* col-HA(mix)	0.33 ± 0.08	0.03 ± 0.01	0.08

Table 5.2 The summary of viscoelasticity properties of the two designs and relevant single-layer components at 1 Hz, consistent with single-layer components, both designs exhibited elasticity-dominance, with the tri-layer(ipn) design being more prone to elasticity influence.

5.3.3 Compression

The representative compressive stress-strain curves of both designs tested in the non-hydrated state are presented in Figure 5.7. It can be interpreted that the tri-layer designs have retained the characteristic stress-strain curve of non-crosslinked samples, i.e., the linear region (lower linear region), the stress plateau (upper linear region), and the densification region. Both designs share similar linear elastic regions from just after complete contact had been made to ~ 12 % strain, which is approximately in line with the linear regions of all single-layer components. However, the design containing the pre-mixed collagen-HA layer exhibited a broader and mild stress plateau region followed by a more defined densification progress

compared to its HA-infiltrated counterpart. The compressive properties of interest are organised in Table 5.3, and it can be concluded and within the expectation that the design with infiltrated HA exhibited greater compression stiffness and less compliance, with the compressive modulus and 3 N strain being 112 kPa and 30.1 % respectively compared to 27.0 kPa and 54.2 % of the other design.

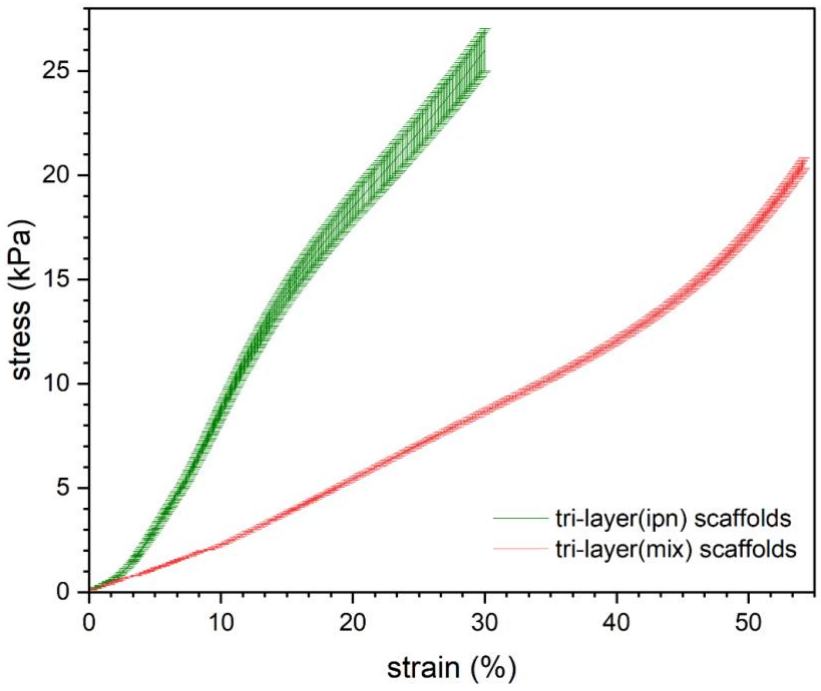


Figure 5.7 The representative non-hydrated compressive stress-strain curves of tri-layer scaffolds, with the force rate applied to be 0.3 N/min.

	modulus (kPa)		3 N point	
sample ID	lower	upper	strain (%)	stress (kPa)
tri-layer(ipn)	112 ± 33	72 ± 10	30 ± 5	26 ± 1
tri-layer(mix)	27 ± 11	32 ± 5	54 ± 2	20.6 ± 0.2

Table 5.3 The summary of the compressive properties of interest for the two tri-layer scaffold designs tested in the non-hydrated state under a fixed force rate of 0.3 N/min.

The compressive moduli of both tri-layer designs were compared with the compressive moduli of the individual layers to further investigate the contribution of each layer to the compression deformation mechanism. Figure 5.8 displays that the compressive modulus of the tri-layer(ipn) scaffold has surpassed that of both collagen-only and collagen-

HA layers, indicating a dominating influence from the elastin-only layer; however, with similar collagen-only and elastin-only layers, the middle collagen-HA layer appears to be the limiting factor for the tri-layer(mix) design. Nonetheless, the patterns in both designs align with the composite/laminate theory, which will be further investigated in the discussion section.

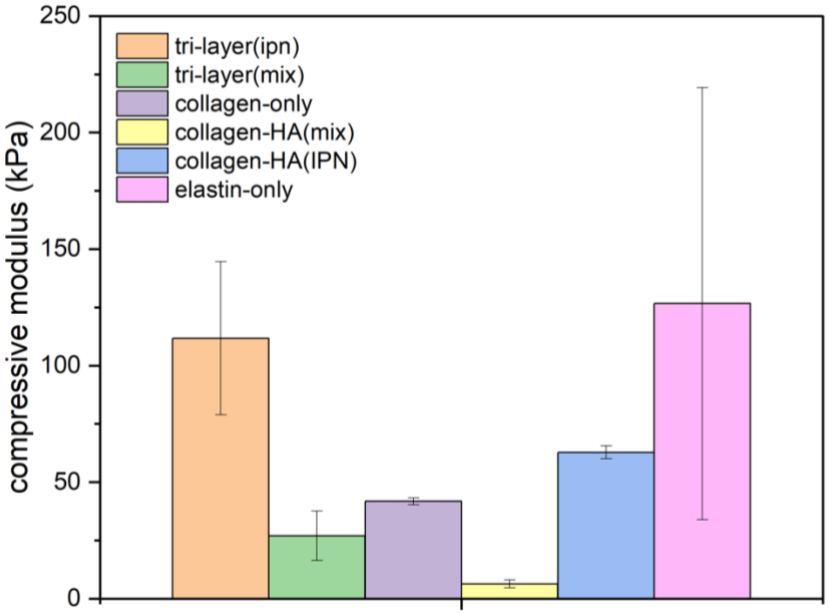


Figure 5.8 A direct comparison of compressive moduli across the single-layer components and the tri-layer designs.

Both tri-layer scaffold designs were tested in the hydrated state as well to investigate their behaviour in physiological conditions, and the resultant representative compression stress-strain curves are shown in Figure 5.9. Completely different from the previous results obtained in the non-hydrated state, the stress-strain curves exhibit the desired J-curve for biomedical applications, i.e., the toe region, the linear region, and the densification region. Due to the limitation imposed by equipment sensitivity, the toe region signal was omitted. Hydration has effectively extended the linear region of both designs, with the tri-layer(ipn) displaying a slightly longer linear response until ~ 45 % strain compared to ~ 40 % of the tri-layer(mix) structure. The compressive properties of interest are listed in Table 5.3, and

contrary to what was observed from non-hydrated samples, the tri-layer(mix) exhibited better stiffness under physiological conditions, with the compressive modulus being 1.44 kPa compared to 0.907 kPa of the tri-layer(ipn) samples. However, the tri-layer(ipn) design showed a better strengthening effect at 3 N despite being more compliant, reaching the stress value of 24.0 kPa at 86.1 % strain.

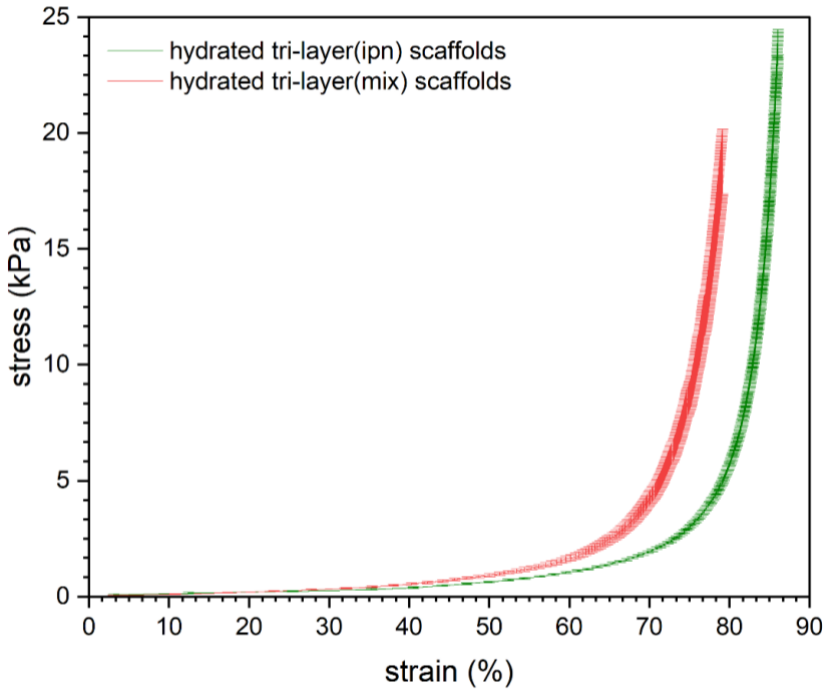


Figure 5.9 The hydrated compressive stress-strain curve of tri-layer scaffolds, with the force rate applied to be 0.3 N/min.

sample ID	modulus (kPa)	3 N point	
		strain (%)	stress (kPa)
tri-layer(ipn)	0.91 ± 0.04	86 ± 1	24.0 ± 0.6
tri-layer(mix)	1.44 ± 0.09	79 ± 2	19 ± 1

Table 5.3 A summary of the compressive properties of interest for the two tri-layer scaffold designs tested in the hydrated state under a fixed force rate of 0.3 N/min.

5.3.4 Tension

Figure 5.10 compares the tensile stress-strain curves of both tri-layer designs. It can be seen that, despite the tri-layer(ipn) sample being slightly stiffer, the shape of both curves falls in

line with the brittle polymer foam nature of the structure, which is also consistent with the results of the collagen-based scaffolds. The linear region where the modulus was measured is even shorter than that of the collagen-based samples (~ 0.5 % versus ~ 1.0 %), with the stiffness decreasing with increasing load, demonstrating the initial behaviour of the S-curve. After the scaffolds entered the plastic deformation region, the failure stress was met going into the plateau region, without reaching the fibre alignment strengthening region of the second half of the S-curve. Compared with the collagen-based scaffolds tested in Chapter 4, both designs displayed greater stiffness at a similar level, with the tri-layer(ipn) being slightly stiffer (Table 5.4). The less mechanically sufficient pre-mixed collagen-HA as the middle layer had a significantly less negative effect on the tensile stiffness than on compressive stiffness, in other words, the soft middle layer imposed neglectable limitation on tensile properties, indicating a distinctively different deformation mechanism. Moreover, the tri-layer designs exhibited improved extensibility as well as ultimate strength.

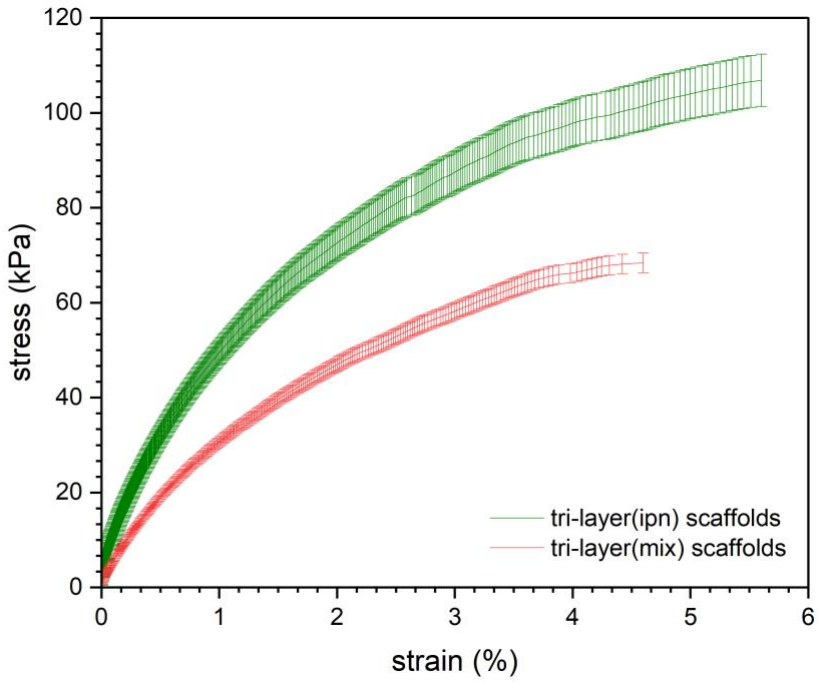


Figure 5.10 The non-hydrated tensile stress-strain curves of the tri-layer scaffolds, with the applied force rate being 0.3 N/min.

sample ID	modulus (MPa)	failure strain (%)	UTS (kPa)

tri-layer(ipn)	4.3 ± 0.4	10 ± 2	146 ± 50
tri-layer(mix)	4.0 ± 0.6	7 ± 1	77 ± 9

Table 5.4 A summary of the tensile properties of interest for the two tri-layer scaffold designs tested in the non-hydrated state under a fixed force rate of 0.3 N/min.

5.3.5 Bending

Consistent with the results from the compressive and tensile tests, the stress-strain curves of both tri-layer designs when subjected to three-point bending under both the WC and AC directions exhibited similar features: the linear region, the stress plateau, and the densification region (Figure 5.11). It can be observed that all samples displayed distinctly defined linear regions, with that of the tri-layer(ipn) samples shorter than that of the tri-layer(mix) samples, and that of the samples in the AC direction shorter than that of the samples in the WC direction. Except for the tri-layer(ipn) tested in the AC direction, all other three curves have well-defined stress plateaus unlike the strain-hardened curves obtained in compression and tension. Further into the densification region, there appeared to be multiple steps in the stress-strain progression for most samples, which will be discussed later together with the deformation mechanism.

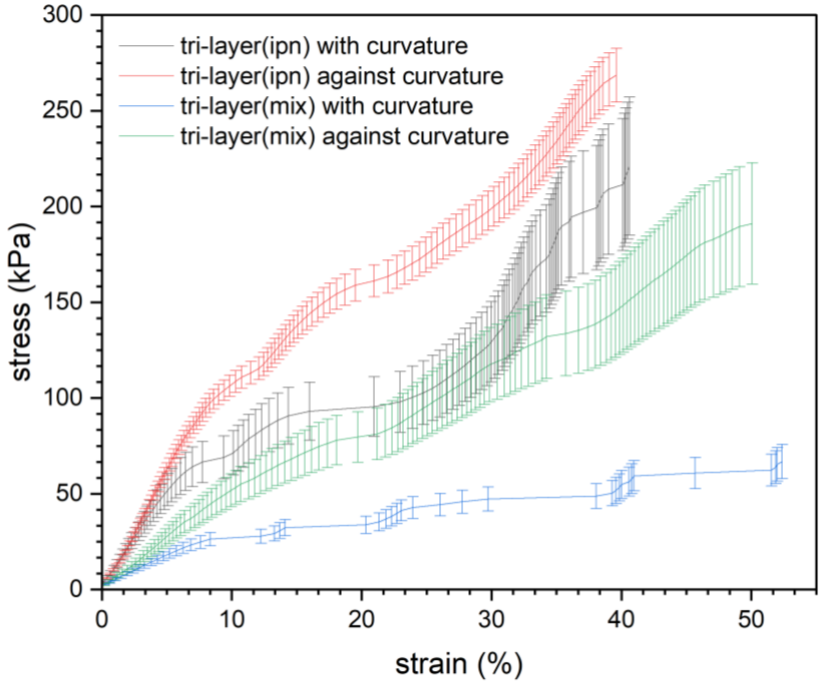


Figure 5.11 The stress-strain curves of the tri-layer scaffolds obtained from the three-point bending test in both with-curvature and against-curvature directions, with the applied force rate being 0.3 N/min.

The bending stiffness represented by Young's modulus of both tri-layer designs tested in both the WC and AC directions in the non-hydrated and hydrated states is measured and summarised in Table 5.4. First of all, the data indicated that the tri-layer(ipn) scaffolds are significantly stronger than the tri-layer(mix) samples before hydration in both directions, coinciding with the results from the compression test and the compression-dominant bending mechanism mentioned in Chapter 4. However, the distinct difference was eliminated once put into the physiological conditions, showing that both designs are equally capable of withholding stress under flexion. Secondly, the scaffolds are consistently stiffer when tested in the AC direction, i.e., when the elastin side is placed on top, manifesting the desired anisotropic nature of the scaffolds intended to mimic similar bending anisotropicity discovered in native heart valve leaflets [183]. Hydration, as predicted from previous results, has dropped the bending stiffness drastically, with the bending modulus of the tri-layer(ipn) and the tri-layer(mix) scaffolds being a mere ~ 0.5 % and ~ 1.2 % respectively of that of the non-hydrated samples. Lastly, the non-hydrated theoretical bending modulus of both designs was

calculated from the data obtained from the compressive and tensile tests to be 332 kPa and 92.1 kPa, with the tri-layer(ipn) design being the stiffer one. Given the assumption of material isotropicity, the quantitive comparison is deemed meaningless; nevertheless, the experimental bending modulus is half a magnitude higher, requiring further qualitative analysis of the deformation mechanism.

three-point bending (the non-hydrated samples)		
	bending modulus, WC (kPa)	bending modulus, AC (kPa)
tri-layer(ipn)	1208 ± 178	1452 ± 392
tri-layer(mix)	290 ± 48	571 ± 169
self-deflection (the hydrated samples)		
	bending modulus, WC (kPa)	bending modulus, AC (kPa)
tri-layer(ipn)	5 ± 1	8 ± 2
tri-layer(mix)	4 ± 2	6 ± 3

Table 5.5 A summary of the tri-layer scaffold bending modulus tested in both the with-curvature (WC) and the against-curvature (AC) directions in the non-hydrated state by three-point bending at 0.3 N/min force rate and in the hydrated state by self-deflection.

5.3.6 Degradation

Both tri-layer designs survived the 12-week non-enzymatic degradation, with the tri-layer(mix) one exhibiting better degradation resistance. The mass loss of the tri-layer samples is attributed to the separation between the elastin-only layer and the rest two layers, which is deemed to result from the small sample size and the sample damage by sample cutting. Tri-layer(mix) scaffolds are expected to be more hydrophilic due to the greater HA percentage, therefore the absorbed water can also reflect in less mass loss. Similar to single-layer scaffolds, the results alone are not sufficient to conclude that the tri-layer designs are degradation-resistant. However, it is vital in determining whether it is feasible to carry out further in vitro and in vivo work and in designing the optimal sample preparation for biological experiments.

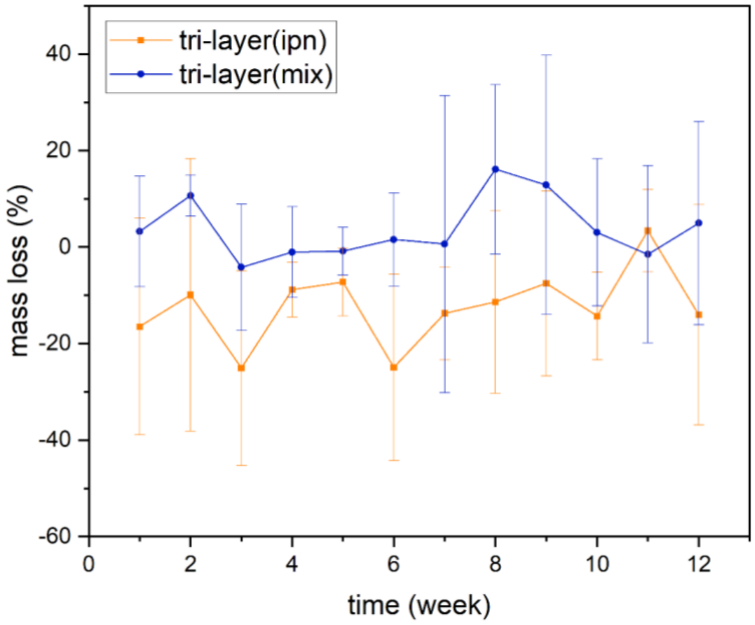


Figure 5.12 The progression of mass loss (%) of the tri-layer scaffolds over a testing time of 12 weeks without enzymes, at 37 ºC in PBS with gentle shaking.

5.4 Discussion

5.4.1 Pore Morphology

A few possible explanations were proposed to explain the discrepancy in the average pore size between the crosslinked collagen layer and the collagen-only layer within the tri-layer scaffolds. Batch-to-batch differences and the slight compression of the bottom layer during sample sectioning can partially contribute to the problem yet are deemed trivial. The compression of the bottom layer during the moulding process is hypothesised to be one reason behind the reduced pore size. The flattening technique involves gently tapping the loaded moulds on a flat surface to allow an even distribution of the highly viscous suspension inside, which is less of a problem in producing single-layer scaffolds with a homogenous constituent. However, with the subsequently added layers especially elastin having a much greater density (~ 0.083 g/cm^3 for fibrillar elastin gel versus ~ 0.006 g/cm^3 for collagen suspension), the weight of the elastin layer itself together with any movement imposing a

downward facing force will inevitably cause the bottom collagen layer with less structure stiffness (Young's modulus calculated to be 1.03 kPa) and a shear-thinning nature. Moulding the elastin layer first was experimented with, yet the extremely high viscosity was proved to be an obstacle towards obtaining a flat surface for subsequent layer addition.

The most likely reason behind this discrepancy, however, is attributed to the impact of thermal gradient on the ice crystal formation process. According to Fourier's law of thermal conduction:

$$Q = -kA\frac{dT}{dx}$$

the heat transfer (Q) is proportional to the negative thermal gradient and the area (A, perpendicular to the gradient) of the surface through which the heat flows. In this case, the thermal gradient drives the heat exchange rate, therefore affects the velocity of the ice front and is likely to impact the pore size. It was reported that with the gradual decrease in the cooling rate in the regions farther away from the cooling surface, i.e., the edge of the mould, displacement is more likely to be the ice crystal formation mechanism, whereas entrapment, on the other hand, dominates the ice crystal formation closer to the cooling surface [285]. The displacement-dominant pore formation was reported to yield larger pores than the entrapment-leading pore formation, which coincides with the pore size distribution within the tri-layer scaffolds. Moreover, the single-layer scaffolds share the same height as the tri-layer scaffolds, therefore, the overall average pore size of the collagen-only single-layer scaffolds would be higher than the collagen-only layer in the tri-layer scaffold closest to the cooling surface, which also aligns with the result from this study. Therefore, the thermal gradient is likely to explain the reduction in the pore size of the collagen layer compared to the collagen-only scaffold. It is also worth mentioning that the low thermal conductivity of the PTFE moulds used hindered the volumetric freezing process, and the expanding surface layer exerted an extra compressive force towards the bottom collagen layer.

It can be seen from the SEM images that the pores are rather asymmetrical due to the constant freezing temperature [284], but both the valvular endothelial cells residing on the surface and the valvular interstitial cells embedded throughout the matrix [286] are reported to be able to change shape and size in response to the flow pattern, valve curvature, shear stress distribution and so on [287], hence the microstructure is still deemed to be in favour of cell activities due to its interconnective nature. Apart from the in vivo cells, HPSCs (including human embryonic stem cells and iPSCs) are commonly employed in *in vitro* studies due to their potential to differentiate into VECs and VICs [288], therefore it is worthwhile to investigate the optimal pore size range of these cells and their activities.

Discrepancy exists where the optimal pore size range is discussed regarding porous structure and cell activities, as it varies with different cell types, matrix materials, cell activities, and application focuses [289]. Studies reported that most cells including endothelial cells failed to colonise porous structures with pore size > 300 μm due to the limitation in bridging and forming a network with adjacent cells [290,291]. However, another study on endothelial cell attachment and proliferation on a semi-porous segmented polyurethane structure with an average pore size of ~ 300 μm indicated improved cell activities [292]. For the majority of mature cells, a communal "optimal range" was reported to be 100–150 μm, with pore size lower than 80 μm proven to negatively impact cell viability [293]. The pore size range of the two tri-layer designs treads slightly above that range, however, several studies have reported successful cell attachment, proliferation, differentiation, and gene expression on a broader range from approximately 80 μm to 400 μm [294–296].

5.4.2 Compression

Similar to the single-layer scaffolds, the stress-strain response of tri-layer designs commences with a lower elastic linear region, followed by an upper linear region and a densification

region. The upper linear region is normally presented as a plateau where an almost constant stress is accompanied by an increasing strain, however, the continuous increase of stress as well as strain in a linear manner provokes further investigation into the deformation mechanism. This behaviour is attributed to the various pore sizes and wall thicknesses. There exists a linear dependence of plateau strain on pore dimensions and a cubic dependence on wall thickness and given the observed spread in both values (wall thickness measured to be 15 ± 4 μm), the non-ideal compression response can be easily explained. It was reported that the non-plateau behaviour is caused by strain hardening [297] and that the slope value is defined as the strain hardening coefficient, which varies with the strain rate applied [298]. As a consequence of plastic deformation, strain hardening often originates from an increasing amount of elastically active chains or non-Gaussian stretching [299], the latter of which is commonly seen in the less mobile amorphous networks such as the scaffolds in this study [300], being a characteristic feature of porous materials [301]. However, based on the above observations and explanations, it is highly unlikely that strain hardening could be a mechanism for this thesis.

To understand the contribution of each layer to the total stiffness of the tri-layer structure, the idea of the effective area is introduced.

$$E = \frac{\sigma}{\varepsilon} = \frac{F}{A\varepsilon}$$

When the whole tri-layer structure is subjected to a constant load (F), to achieve equal strain across the layers, we could get:

$$\frac{E_1}{E_2} = \frac{A_2}{A_1}$$

For the tri-layer(ipn) scaffolds, the moduli of the three layers are 42 kPa, 63 kPa, and 127 kPa; for the tri-layer(mix) scaffolds, the moduli are 42 kPa, 27 kPa, and 127 kPa. Upon calculation, the updated schematic scaffold illustrations implementing the effective area

theory assuming equal strain are shown in Figure 5.13 as follows. In reality, all three layers are of the same cross-section area (A), therefore different deformation strains reacting to the load are expected and were observed.

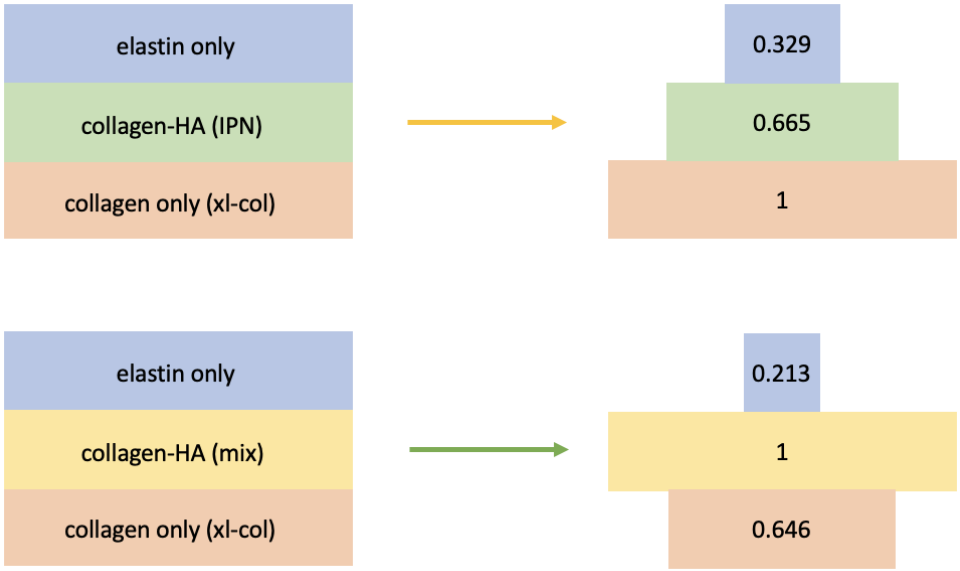


Figure 5.13 Schematic illustrations of the two tri-layer designs implementing the effective area theory assuming equal strain.

With the compressive behaviours of the tri-layer structure and corresponding individual layers being studied, it would be intriguing to investigate the relationship between the two. With compressive modulus being the first focus, the effective compressive stiffness of the layered structure is calculated based on the superposition principle with the layered being considered parallel to each other. Assuming the mechanical response of individual layers is independent when the whole structure is subjected to an evenly distributed compressive force, the stress throughout the system is considered equal, and the total deformation is a sum of the deformation of each layer, as indicated in the equation below:

$$\varepsilon_{total} = \varepsilon_{col} + \varepsilon_{col-HA} + \varepsilon_{ela}$$

Within the linear region, the effective compressive modulus can be calculated using Hooke's Law, with the whole system and individual layers sharing the same stress value:

$$\frac{1}{E_{total}} = \frac{1}{E_{col}} + \frac{1}{E_{col-HA}} + \frac{1}{E_{ela}}$$

The effective compressive modulus of the tri-layer(ipn) design is thus calculated to be 20.9 kPa and that of the tri-layer(mix) design is calculated to be 5.29 kPa, which by comparing with the data obtained from experiments, are both only ~ 20 % of the tested values (18.8 % and 19.6 % respectively).

The discrepancy between the theoretical and experimental compressive modulus is hypothesised to potentially be a result of various effects, including non-axial deformation, microstructure, layer thickness etc. First of all, the simplified model assumes the layers maintain the same dimensions while being compressed, which is compliable with rigid materials such as metals and ceramics. However, with soft especially porous materials, the factor of non-axial deformation must be considered. Looking at the post-test samples, the least stiff layers, i.e., the collagen-only layer for the tri-layer(ipn) samples and the collagen-HA(mix) layer for the tri-layer(mix) samples, exhibited a necking-like inward contraction. This subtle inward shrinkage inevitably led to an intensification of the stress due to reduced effective area, which subsequently resulted in a mild potential strain hardening, strengthening the structure stiffness as a whole. Secondly, from the SEM images of the tri-layer samples, the pore wall network is more intact than that in the single-layer scaffolds, which can be attributed to a more controlled freezing process due to a reduced thickness/volume. A more intact pore wall structure coupled with the aforementioned reduction in pore size effectively upgraded the structural compressive stiffness.

For the contribution of individual layers, the stress and strain data (organised in Table 5.6) when the force loaded reached 3 N is being concentrated on. The endpoint deformation of the tri-layer scaffolds is a complicated combination of the deformation of each layer, therefore only qualitative analysis will be provided. Experiencing the same load, the stiffer elastin layer undergoes significantly less deformation (estimated to be about 20 %) than the

less compression-resistant collagen layer (over 60 %) within the tri-layer(ipn) design when the stress within the system reaches 26.0 kPa, this combining with the ~ 30 % strain of the middle HA-infiltrated layer and provided that all layers are of the same thickness, would yield a ~ 37 % deformation instead of the tested 30.1%, indicating an uneven contribution from each layer to the overall compression resistance. Similarly in the tri-layer(mix) design, the resultant strain at 3 N assuming equal contribution among layers is calculated to be slightly lower than the experimental data (~ 51 % compared to 54.2 %).

	E_{comp} (kPa)	strain at 3N (%)	stress at 3N (kPa)
collagen-HA(ipn)	63 ± 3	35 ± 2	29.5 ± 0.6
tri-layer(ipn)	112 ± 33	30 ± 5	26.0 ± 1.0
collagen-only	42 ± 1	59 ± 1	20.5 ± 0.6
elastin-only	127 ± 93	19 ± 5	20.1 ± 0.3
tri-layer(mix)	27 ± 11	54 ± 2	20.6 ± 0.3
collagen-HA(mix)	6 ± 2	75.8 ± 1.0	19.2 ± 0.2

Table 5.6 A summary of the compressive data of the non-hydrated tri-layer samples and the corresponding individual layers.

For both designs, elastin is deemed as a constant element and therefore is excluded from this part of the discussion. The relative stiffness of the collagen and the collagen-HA layers, however, is focused on instead. With both tri-layer designs, the collagen-HA layer is observed to deform the first and the most despite the relative stiffness, followed by the collagen-only layer, with the elastin-only layer being the last one to respond visibly to the load. Furthermore, it was observed that despite the attempts at a seamless fit during sample moulding, elastin seemed to have experienced the least volume shrinkage. The resultant slight reduction in the load-bearing area consequently led to increased stress in the middle layer, which could potentially contribute to the deformation pattern. In the tri-layer(ipn) design, the collagen-HA layer is stiffer than the collagen layer and, therefore is more resistant to the slightly increased stress, leading to the lower-than-expected strain at 3 N. On the contrary, the

collagen-HA layer in the tri-layer(mix) design is the softest layer of all, the stress inclination hence elevated the level of elongation at 3 N.

Once hydrated, the compressive response of the samples experienced distinctive changes, with the most obvious one being the shape of the stress-strain curve. Being a lightly crosslinked polymer network in the non-hydrated state, the scaffolds exhibited a rubber-akin deformation pattern; however, the hydration and the ensuing lubrication and molecular interaction effect completely changed the deformation mechanism, generating the characteristic J-shaped stress-strain curve. The J-curve displays three distinctive regions: the "toe" region, the linear region, and the densification region. The "toe" region is a macroscopic manifestation of the unfolding and aligning of the naturally crimped collagen fibres, which requires minimum energy, therefore the structure is able to reach about 2-5% strain with minimal stress [302]. Entering the linear region, the collagen molecules begin to uncoil and slide against each other similar to the non-hydrated sample; however, the free and intermediate water serves as a lubricant and facilitates the reversible chain movement [303], resulting in a much more extended linear region. This unique mechanism allows extreme structure flexibility in physiological conditions where the device is often placed in a dynamic flow. Once the force exceeds the environmental standards, the structure toughens up and enters the densification region as a response, with the collagen fibre itself being subjective to the load enhanced by the further restriction on chain elasticity imposed by hydrogen bond formation [304].

Except for the change in stress-strain curve shape, the compressive modulus has seen a drastic drop since hydrated, which was reported in various studies [147,305–307]. The Flory-Rehner model is widely applied to predict the hydrated structural stiffness of polymer networks knowing the non-hydrated stiffness and the volume fraction of the water absorbed [308]. However, when the experimental data is substituted into the equation, the water content

for both designs is abnormally close to 1. In other words, the experimental compressive modulus when hydrated is lower than the theoretical value due to the limitation imposed by the assumption of entropic elasticity [309]. A study has proposed a scaling law theory where in the direction of gain water content, the hydrated elastic modulus has a 2.3 power law relationship with the starting elastic modulus (i.e., the non-hydrated elastic modulus) instead of the original 1/3 proposed by Flory, which fits better with the experimental data of this thesis (scaffold material volume fraction calculated to be 12 % and 28 % respectively for both tri-layer scaffold designs) [310].

Furthermore, it is noticed that contrary to the result of non-hydrated scaffolds, the tri-layer(mix) design is 1.6 times stiffer than the tri-layer(ipn) design. It was reported in one study that the pore size contributed more to the stiffness when the scaffold was swollen and that a smaller average pore size would result in an increased compressive resistance [311]. The much smaller pore size of the pre-mixed collagen-HA layer combined with the central location of the layer is deemed to be one potential explanation towards the higher compressive modulus of the tri-layer(mix) samples. The collagen-HA polyion complex structure mentioned in Chapter 4 is hypothesised to be another possible explanation. As previously mentioned, in an aqueous environment, the PIC structure promotes a compact interaction between collagen and HA molecules, which only to a large extent exist in the pre-mixed collagen-HA structure. When placed under compression, such a compact structure provides more resistance to deformation and, therefore may lead to better stiffness [312].

The compressive properties of the non-hydrated scaffolds are comparable with a similar tri-layer structure with hydroxyapatite [313], demonstrating a competitive compression stiffness level. Compared to another tri-layer bone tissue engineering scaffold, the hydrated compressive modulus of the two designs in this study has largely exceeded the reported value of ~ 3.5 Pa [314], further confirming the mechanical superiority of the tri-layer designs in this

thesis over the existing similar structures. However, the human heart valve leaflet has Young's modulus in the magnitude of MPa instead of kPa [315], rendering the collagen-based TEHV designs less an ideal substitute for mechanical valves and bioprosthetic valves. Nonetheless, it is still considered a big step towards the advancement of the more mechanically capable natural polymer-based tissue engineering scaffold designs.

5.4.3 Tension

Due to the brittle nature of the samples, tensile tests were not able to be performed on the non-hydrated elastin-only scaffolds, therefore limiting the comparison of tensile stiffness between the tri-layer and single-layer scaffolds. However, preliminary compressive properties measured from elastin samples indicated that the non-hydrated elastin scaffolds are stiffer than collagen-based samples with less linear extensibility. Assuming the elastin-only scaffolds behave similarly under compressive and tensile deformation, the improved stiffness and shortened linear region compared to the single-layer collagen-based samples could be attributed to the elastin layer. Moreover, the less distinctive linear region potentially originated from a continuous extension from crimped fibres in each layer at separate timings [316]. It is worth noting that no visible delamination was observed during the tensile tests conducted, indicating a high interlayer delamination resistance, which was reported to enhance tension stiffness as well [317].

As previously mentioned in Chapter 4, pore wall stretching dominates the deformation mechanism under tension instead of pore edge bending. Therefore, different from compression where the stiffness of the middle collagen-HA determines the overall non-hydrated sample stiffness, the stiffest outer layer can further extend until the tensile stress within the layer develops and the external force applied reaches the limit [318]. As a result, the two tri-layer designs appeared to exhibit similar levels of tension resistance (4.3 MPa and 4.0

MPa). The tri-layer scaffolds fabricated in this thesis are considered to be highly tension-resistant compared to the published data of various studies using natural polymers as scaffold materials [319–322] and even exhibited comparable or better tensile properties than scaffolds made of synthetic polymers such as PCL [323], PA-collagen [324], PLGA [325]. Nevertheless, it is important to bear in mind that after hydration, a drastic drop in tensile modulus up to ~ 95 % is expected to occur [305] due to the swelling and lubricating effects.

5.4.4 Bending and the "ideal design"

Three-point bending is widely used for its simplicity in sample preparation and testing conditions, and the minimum contact between the support and the sample excels at eliminating the effects of clamp constraint in tensile tests and uneven surface in compression tests; however, it measures a combined effect of tensile, compressive, and shear properties of the sample instead of the fundamental properties of the materials themselves [326]. Therefore, the stress-strain curves obtained from the three-point bend test are expected to exhibit similar characteristic features, which in general aligns with the results plotted in Figure 5.12, with a few deviations to be discussed. First of all, the bending stress-strain curves all displayed a highly distinctive linear region, contrary to the S-curve lightly crosslinked polymer feature under tension and compression. Secondly, the previously observed elevating stress plateau is replaced by the characteristic plastic deformation of minimum stress increase accompanied by a substantial strain development. Lastly, the densification region where the stiffness rapidly goes up was less smooth and stable but appeared to display multiple "mini-plateau" before eventually falling back into the expected pattern.

Three potential aspects are considered to be responsible: the more evenly distributed stress state in the three-point bending set-up [327], the anisotropic nature of the structure, and different mechanism and microstructure responses under deformation. Tensile tests were

conducted along the direction of the length (the longer side), which aligns with the tension direction in three-point bending; however, compressive tests were performed along the axis while the top layers when bent are compressed perpendicular to the axial direction. It is hypothesised that the stiffest layer in this case will bear more load and regulate the compression resistance and the whole structure acts closely to a single-component structure than a layered one, therefore more prone to yield a simple linear response in the linear region. Moreover, the uniaxial load under tension and compression compared to the biaxial or even triaxial stress distribution is more influential on the defect (in this case, the pores), rendering a tendency of strain hardening, while the more complicated pore response to multi-directional stress can to some level counteract each other and lower the tendency of strain hardening, resulting in an almost-flat stress plateau region [328]. The step-like densification is attributed to the layered structure responding to the shear stress at play in the bending mode, allowing non-axial movement of the pores before the complete pore collapsing.

Knowing the compressive and tensile moduli of the tri-layer scaffolds, the position of the neutral axis when the samples are subjected to flexure can be theoretically predicted using this equation deduced in Chapter 4:

$$\frac{h_t}{h_b} = \frac{\sqrt{E_{ten}}}{\sqrt{E_{comp}}} = N$$

For the tri-layer(ipn) scaffolds, the neutral axis position is similar to that calculated in collagen-based scaffolds with an N-value of 6.2, meaning that when placed in the with-curvature direction, the top collagen-only and the middle collagen-HA layer are entirely subjected to compression, while the bottom elastin-only layer is subjected to both tension and compression (42:58). On the contrary, when tested in the against-curvature direction, the elastin-only layer and the collagen-HA layer experience compression, while the collagen-only layer at the bottom goes through both tension and compression. For the tri-layer(mix) scaffolds, the N-value almost doubled to 12.2, demonstrating a remarkable compression

dominance. When tested in the with-curvature direction, most of the structure experiences compression except for a thin layer of elastin at the bottom; and when tested against-curvature, only a thin layer of collagen at the bottom is theoretically subjected to tension.

From the results of compression tests on single-layer scaffolds, it was experimentally proved that the elastin-only scaffolds exhibited a stiffer nature compared with the collagen-based scaffolds. Therefore, it is to be assumed that when the flexion is in the against-curvature direction, the tri-layer scaffolds display higher bending resistance, coinciding with experimental data. Such bending anisotropy is desired as it has been demonstrated in the biomechanics of the native aortic heart valve. During a cardiac cycle, the ventricle contraction (systole) pumps the blood from the left ventricle into the aorta, forcing the heart valve to open; then while the left ventricle experiences a relaxation process (diastole), the valve closes to prevent the blood from backflowing [329]. To let the blood flow through while effectively preventing the backflow, the valves possess greater bending stiffness in the opposite direction of the blood flow, which is when the aorta-facing fibrosa side is under tension. In other words, the native valves are more resistant to bending in the against-curvature direction [330].

The theoretical bending modulus calculated using Equation 4.6 (332 kPa for tri-layer(ipn) and 92.1 kPa for try-layer(mix)) is significantly lower than experimental values, and attempts have been carried out with limited data available for further investigation. Being a layered structure, take the against-curvature direction as an example and combine the neutral axis location, when subjected to flexure, the entire elastin-only and collagen-HA layers are compressed, and the collagen-only layer is subjected to both tension and compression. Therefore, an attempt to calculate the bending modulus using the tensile and compressive data of individual layers under the assumptions that the compressive stiffness is

determined by either the least stiff or the stiffest layer was carried out, using another form of the equation:

$$E_{bend} = \frac{b}{3}\left(h_b{}^3 E_{ten} + h_t{}^3 E_{comp}\right)$$

where *b* is the width of the sample, h_b is the distance from the bottom of the sample to the neutral axis, h_t is the distance from the sample top to the neutral axis, and *I* is the second moment of inertia of the rectangular beam [331]. The theoretical bending modulus of the tri-layer(ipn) and the tri-layer(mix) samples calculated were still significantly lower than the experimental data. Tri-layer structure has been reported to have a positive impact on bending stiffness [332], yet to fully understand the bending mechanism of the fabricated layered structure, the effect of the interlayer interaction and the shear stress distribution needs to be further reviewed on top of more experimental data collection.

The bending anisotropy was observed in hydrated scaffolds as well, marking the potential of the tri-layer scaffolds designed for physiological applications with cell affinity to be tested. The bending modulus values have shown less difference between the two samples contrary to the results obtained from the hydrated compression test where the tri-layer(mix) was determined to be stiffer. Due to equipment limitation, the tensile modulus in the hydrated state was not measured, but the tensile modulus of the two designs is expected to be of similar level, as different from compression where a middle layer with smaller pore size enhances the deformation resistance, the stiffest layer under tension is dominantly supporting the composite structure when force is applied parallelly to the interfaces. A discrepancy was observed between the single-layer scaffolds and the tri-layer ones, with the former appearing to be stiffer. It was reported in a previous study on the hydrated mechanical properties of fibrillar elastin gel scaffold that elastin had less stiffness under tension than collagen-based structures [184], which could explain the decrease in bending stiffness. It is at the same time worth noting that the compression tests were conducted in full submersion, which eliminates

the water loss and incomplete swelling, while the self-deflection tests were carried out with water absorbed as the distributed weights, leading to reduced accuracy in swelling extent, which could in turn manifest as discrepant data.

The bending stiffness of native porcine or human aortic heart valve leaflets was repeatedly characterised under various conditions and all data reported are about a magnitude higher than the bending modulus of the tri-layer fabricated in this study [333,334]. However, cells were reported to regulate the mechanical properties of the scaffolds and to enhance the flexure resistance by 2–6 times [114]. Therefore, the designed tri-layer scaffolds are deemed to have the potential to be brought forward to further in vitro and in vivo experiments to characterise the mechanical response in a more physiology-adjacent environment.

Table 2.4 shows that the total thickness of the aortic valve leaflets is under 1 mm, with the distribution of the three layers varying from evenly distributed to major dominance of one of the layers (often the fibrosa or the spongiosa). The diameter of the aortic valve is reported to be 20 mm and the area of each leaflet is roughly 2.5–3.5 cm^2 [335]. That is to say, the "ideal design" should be thinner and half-moon-shaped with the diameter being ~ 21 mm to fit its physiological environment better, as shown in Figure 5.14. Based on the current dimensions of the rectangular samples (4 cm x 1 cm x 0.3 cm), reducing the length, width, and height by half each would give the required dimension without changing the mechanical properties due to the unchanged aspect ratio.

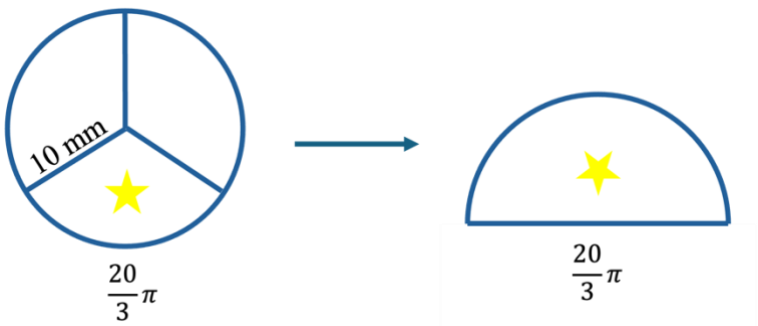


Figure 5.14 Simplified schematics of the top view of the aortic heart valve (left) and one flattened leaflet (right).

It was discussed in the bending deformation mechanism section that the neutral axis is towards the bottom of the structure. In the WC direction, the collagen-only and collagen-HA layers are entirely subjected to compression while the elastin layer is partially subjected to tension. In the tri-layer(ipn) design, the collagen-HA(IPN) layer is stiffer than the collagen-only layer, therefore, reducing the thickness proportion of either the collagen-only layer or the elastin layer is favourable for bending resistance. For the tri-layer(mix) design, however, increasing the collagen-only layer proportion is preferred. In the AC direction for the tri-layer(ipn) design, the stronger compression-resistant layers, i.e., the elastin and the collagen-HA(IPN) layers, are subjected to compression, while the collagen-only layer is partially under tension. It was developed before that all the scaffolds were more tension-resistant, therefore, the tri-layer(ipn) structure would benefit the most if the collagen-only layer was entirely under tension while the other two layers were subjected to compression entirely. Combining this with the situation in the WC direction, it is assumed that for the tri-layer(ipn) scaffolds, the "ideal" design requires 14 % of the thickness to be collagen-only, 14 % to be elastin, and the rest 66 % to be the collagen-HA(IPN) layer. Similarly, under the same principle, the "ideal" design requires less collagen-HA(mix) proportion. The analysis is based on data obtained from the non-hydrated samples under the assumption that the reduction in the mechanical properties of hydration is proportional to the non-hydrated data.

It was developed before that smaller pore size was beneficial to the scaffold stiffness. The optimal cell activity pore size for the VICs and the VECs is about 100–150 μm as mentioned previously, therefore, there exists room for the scaffolds fabricated to have smaller pore size to improve their mechanical properties while maintaining a cell-favourable environment. To achieve that, the "ideal" design should be frozen at a lower temperature than -20 ºC for smaller pore formation and with a controlled cooling rate to ensure a narrow pore size distribution around the optimal range. Moreover, a higher concentration of the collagen

suspension can to some extent increase the structural strength according to preliminary experiments.

5.5 Conclusion

In this chapter, the fabrication of the two tri-layer designs together with the mechanical property-heavy characterisation was elaborated on, with the analysis focusing on the potential of future work down the biological and clinical lines. Microstructurally speaking, the tri-layer scaffolds possess the desired structure with interconnected and integrated pores and smooth transitions between layers. The pore size has seen a reduction in the collagen-only layers positioned at the bottom during the moulding process, but the diversity and distribution of the pores are deemed sufficient to meet the standard of cell activities for both designs. The mechanical tests in the non-hydrated state shed light on the mechanical response of the layer structure as well as the individual components in a composite environment, revealing the different deformation mechanisms under different modes the load is applied. The tri-layer scaffolds were reported to share similar characteristic features to the individual layers, with a positive enhancement in the stiffness due to the layered structure. Moreover, the designed bending anisotropy essential to the application as heart valve replacement was observed in the three-point bending tests. To further explore the response of the designs in a more physiological-adjacent environment, compression and bending properties were examined in the hydrated state. Both designs exhibited the desired “J-curve” stress-strain response vital to devices aimed at medical applications, and the bending anisotropy observed when hydrated aligns with the extent of the native valves (AC direction bending modulus is 1.5 times stronger than that in WC direction for the tri-layer(ipn) structure and 1.6 times for the tri-layer(mix) design). The two designs are deemed to be equally suitable for TEHV applications, however, the lack of mechanical strength remains a major issue. Nevertheless,

further cell seeding is predicted to regulate the mechanical properties positively, and both designs have shown promising conditions for cells to populate and modify the mechanical properties.

Chapter 6 Conclusions

This thesis aims to successfully develop

- Tri-layer porous scaffolds mimicking the structure of native heart valve leaflets with each layer sharing similar compositions as the collagen-rich fibrosa, GAGs-involving spongiosa, and elastin-incorporated ventricularis.
- Methods to make atelocollagen experience fibrillogenesis and therefore a viable starting material in tissue engineering scaffold construction in general.
- Fabrication procedures including chemical crosslinking and HA modification to improve the mechanical responses and tailor the structure to be more mechanically matching to the native heart valve leaflets.

Along the way to achieve the goals above, gradual steps were taken. Firstly, after benchmarking the purity of the collagen received, fibrillogenesis was induced and its occurrence was proved in a visualised way in both macroscopic (increased suspension turbidity) and microscopic (D-banding pattern captured by SEM) ways. The precursing collagen-based suspensions were then produced with their flow properties being measured, capturing the shear-thinning nature of the suspensions while providing benchmarking viscosity to minimise the commonly occurring batch-to-batch differences in collagen-involving production. It is worth mentioning that due to altered protocol catering to atelocollagen, a homogeneous collagen-elastin mixture suitable for freeze-casting was unable to be produced, therefore the ventricularis-mimicking layer consisted of only the fibrillar gel elastin developed by a previous group member, Dr Iftekhar.

Subsequently, the well-developed freeze-drying method and EDC/NHS crosslinking chemistry were employed in the fabrication of single-layer porous scaffolds suitable for cell attachment and proliferation, with the microstructure examined using SEM, and the backbone intactness, crosslinking efficiency as well as HA modification effectiveness manifested by FTIR. Two routes for incorporating HA into the collagen network for the middle layer were

proposed, and various characterisations have shown the viability for both. Further water uptake and non-enzymatic degradation studies shed light on how the structures interact with water and the degradation resistance, laying the foundation for future biological work in the physiological environment. All single-layer scaffolds fabricated were deemed to be suitable for further *in vitro* study as they all exhibited a high porosity (over 97 %), suitable pore size (179.3 to 294.6 μm), and sufficient degradation resistance over at least 12 weeks, which is longer than the usual in vitro study period.

Once the fabrication was deemed successful, one of the most important aspects of heart valve replacement application, the mechanical properties, were extensively studied. By characterising the viscoelastic behaviours of both the suspensions and the resultant scaffolds, the elasticity-dominating nature of the collagen was revealed. The compressive modulus of all the single-layer scaffolds ranged from 29 kPa to 80 kPa, and the tensile modulus ranged from 0.55 MPa to 4 MPa in the non-hydrated state. The magnitude difference was attributed to the different deformation mechanisms the scaffolds experience, with the pore wall stretching dominating tensile deformation while the pore edge bending governing compression responses. The bending modulus was measured by a "homemade" self-deflection test in the hydrated state and hydration was shown to drastically reduce the structure stiffness by introducing expansion caused by swelling (modulus ranging from 7 kPa to 15 kPa), however, the existence of HA alleviated the reduction by the strengthening effect provided by the hydrogen bonds.

With the single-layer scaffolds being successfully synthesised and proven promising mechanically and structurally, the thesis proceeded to the assembly of the tri-layer designs. Both tri-layer scaffolds featuring slightly different mid-layers were successfully assembled with interconnected and integrated pores and smooth transitions between layers without signs of delamination (demonstrated by SEM images). The pore size saw a reduction in the

collagen-only layers due to its positioning during the moulding process, however, it was not deemed as problematic as it brought in the diversity and distribution of pores positive for cell activities. Apart from similar sets of mechanical tests as single-layer scaffolds, the three-point bend test in the non-hydrated state was introduced in both With Curvature and Against Curvature directions and clear bending anisotropy was observed in both designs (WC: 1208 ± 178 kPa, AC: 1452 ± 392 kPa for tri-layer(ipn) and WC: 290 ± 48 kPa, AC: 571 ± 169 kPa for tri-layer(mix)). After hydration to the full extent, the anisotropic bending behaviour was preserved (WC: 5 ± 1 kPa, AC: 8 ± 2 kPa for tri-layer(ipn) and WC: 4 ± 2 kPa, AC: 6 ± 3 kPa for tri-layer(mix)). Moreover, the compression test in the hydrated state exhibited the desired J-curve stress-strain behaviour for biomaterials.

Throughout the whole thesis, the effects of three factors were investigated, including the collagen source, the crosslinks, and the modification of HA and how it was incorporated into the system, providing rough guidance on the tailoring of the scaffolds targeting slightly different applications. Intrinsically, collagen sourced from bovine skin is more crosslinked than collagen extracted from the bovine amnion due to its maturity. Therefore, chemical crosslinks have less effect on skin collagen and scaffolds produced from skin collagen have smaller pore sizes. As a result, the suspension made of amnion* collagen is 1.5 times stiffer and further manifests in an accordingly improved tensile stiffness. Due to different deformation mechanisms, the compression and bending properties were less affected, and the better water interaction ability in reverse slightly reduced the bending modulus when in the hydrated state. Crosslinks had a significant influence on the microstructure and therefore the mechanical properties as well, yet it had no noticeable effect on the water uptake ability and the degradation resistance. Partial crosslinking decreased the pore size by 30 %, resulting in a significant increase in both compressive modulus (from 29 kPa to 40 kPa) and tensile modulus (from 1.1 MPa to 1.8 MPa), however, the increase was at the expense of

extensibility. HA infiltration and premixing HA with collagen suspension resulted in completely different scaffold microstructure and mechanical properties, however, both produced scaffolds with highly porous structures still, with the premixed scaffolds having a much smaller pore size (179.3 μm versus 240.0 μm). Additionally, the infiltrated secondary HA network strengthened the compression hence bending stiffness due to the strengthening of the pore edge, whereas the collagen-HA homogeneous structure struggles mechanically due to the nature of HA. Nevertheless, once hydrated, the differences disappeared under the influence of hydrogen bonds, making both designs viable and worthwhile for further development and biological work.

Chapter 7 Future Work

This thesis has successfully served as proof-of-concept research on the application of atelocollagen in the tri-layer scaffold context together with HA and fibrillar elastin gel as a potential aortic heart valve leaflet replacement. Nevertheless, further investigations and characterisations are recommended for future studies that this thesis could not cover.

Firstly, it was intended for the ventricularis-mimicking layer to comprise both collagen and elastin chemically, yet the attempt was unsuccessful due to difficulties in mixing the collagen and elastin components. In the discussion, it was mentioned that after centrifugation, the pre-mixed collagen and elastin separated into layers. It is recommended for future studies to use a homogeniser to gently blend the mixture to avoid the air bubbles introduced by the hand-held blender, and to use a vacuum in a controlled temperature environment (~ 4 ºC) to de-bubble the solution. This method is speculated to effectively reduce the separation of the two components and therefore can produce an atelocollagen-elastin blend for the ventricularis layer.

As mentioned before, freeze-drying is often chosen as a scaffold fabrication method because of its relatively simple protocol and the ability to tune the pore morphology. A lower freezing temperature is reported to lead to smaller pore sizes by various studies, and a controlled cooling rate also impacts the pore size and its distribution [336]. Therefore, it is recommended by the author that a more comprehensive study on the influence of the freezing temperature and the cooling rate on the pore morphology of these atelocollagen-based scaffolds would be useful in mapping out the desired fabricating parameters aiming at different applications as different cell types and activities require slightly different pore sizes.

FTIR is a powerful analytical method for studying the chemical structure of the natural polymers characterised in this thesis, however, more information is needed to gain insight into the HA inclusion percentage. It is recommended that histology studies be done for future studies to visualise the successful incorporation of the HA and that if resources

allow, solution nuclear magnetic resonance (NMR) should be adopted in quantifying the HA amount as supplementary data for the FTIR peak area analysis. To perform solution NMR, TBS/PBS can be used to dissolve the scaffolds at 4 ºC with gentle stirring for at least 72 hours, and the saccharide ring is recommended to be the structure to differentiate HA content from the collagen network.

EDC/NHS partial crosslinking with the concentration being 30 mM/15 mM was chosen for this thesis based on preliminary results assuming the collagen scaffolds achieved fully crosslinked at a concentration of 60 mM/30 mM. This crosslinking method has proven to be effective, and it is also reported that the cell activities weaken when the crosslinking density is high [337]. Therefore, it is important to find the balance between improved structural stiffness and minimum extensibility and cell attaching sites required. It is recommended for future studies to further investigate the effect of EDC/NHS concentrations as well as the crosslinking time on the scaffold crosslinking density and the consequent mechanical properties. To measure the crosslinking density more accurately, chemical analysis such as the free amino acid analysis should be conducted [150].

Furthermore, it was reported that despite being non-cytotoxic, EDC/NHS can still have some impact on cell behaviours compared to novel nature-derived crosslinking chemicals such as dialdehyde alginate and procyanidins, which showed promising potential in replacing EDC/NHS in the crosslinking of monomeric collagen [338–341]. Preliminary experiments were conducted by the author, and both dialdehyde alginate and procyanidins were proven to effectively crosslink the scaffold from the FTIR data. However, due to limited material supply, more research on the mechanical properties was not able to be done despite the scaffolds fabricated being stiff by observation. Therefore, similar crosslinking studies and their impact on scaffold mechanical properties as well as the follow-up biocompatibility research are encouraged for future research in this area.

Despite not being suitable for estimating scaffold crosslinking density in this research, a full-round swelling test on all sample types at different temperatures (4 ºC, 25 ºC, and 37 ºC) and after different saturation times (ranging from 1 to 12 hours) should be carried out to gain a better understanding of how the scaffolds behave in storage temperature (4 ºC), in between implantation (25 ºC as room temperature representative), and physiological conditions (37 ºC). Additionally, enzymatic degradation with collagenase, hyaluronidase, and elastase individually and with different combinations is suggested to be done to further understand how the structure would behave once implanted. The different combination also serves as a way to indirectly measure the percentage of a certain component.

Regarding the mechanical properties, a must-do first step should be characterising the tensile properties of the tri-layer scaffolds in the hydrated state as the supplementary dataset to the compression and bending data for a better understanding of the deformation patterns. Bi-layer scaffolds, i.e., collagen/collagen-HA scaffolds and collagen-HA/elastin scaffolds, should be fabricated and tested in the hydrated states for their tensile, compressive, and bending properties (in both the WC and AC directions) to complement the single-layer and tri-layer scaffold data to understand further each layer's contribution to the total structure mechanical properties. Moreover, to better mimic the native heart valve leaflet, any form of dynamic biaxial flexure test and biplanar tension test in the hydrated state should be performed. It is proposed that, if possible, a device with a closed chamber and a water-pumping mechanism can be designed to specialise in dynamic flexure characterisations of membrane materials. The samples can be clamped in the middle of the chamber full of physiological liquid, which can be pumped in both directions to simulate the "normal flow" and the "backflow" of the blood. The stress sensor and motion detector can pick up the instant stress-strain signal for a real-time dynamic reading of the mechanical properties. It is also worth characterising the time-dependent properties such as stress relaxation, creep

deformation, and fatigue to understand the long-term mechanical properties after implantation. Mechanical properties of the scaffolds seeded with cells should also be characterised using the same method, equipment, and parameters, as the cell embedment was reported to regulate and reinforce the mechanical properties [342].

One of the gaps between the current designs and the applicable design in clinics is the thickness. According to the data in Table 2.4, the thickness of the native heart valve leaflets is no greater than 1 mm, whereas the tri-layer scaffold designs are 2–3 mm in thickness. Moreover, the design in this thesis assumes equal thickness of each layer in the tri-layer scaffold based on the same data, yet there might be a different thickness allocation to maximise the mechanical efficiency. After a comprehensive data set is collected, finite element analysis (FEA) can be applied. ANSYS or ABAQUS is suggested as the software and if former, the SOLID185 and the 1st order OGDEN HYPERFOAM are the recommended element type and material type.

Last but not least, more work could be done on the fibrillar gel elastin. It was first discovered by a previous group member, and this thesis is only the third-ever research adopting the material. First off, the modification of the elastin is to be looked at, as despite being compression resistant, the brittle nature imposes challenges for structure handling when in the non-hydrated states. Mixing collagen and elastin as one of the layers as mentioned before should alleviate this issue, however, the elastin itself can be useful in other applications, for example, temperature- or pH-controlled drug delivery systems; therefore, it is worth searching for plasticiser for the fibrillar elastin gel to improve its handling properties.

Overall, the majority of the research on tissue engineering scaffolds still focuses on their biocompatibility, leaving the equally important mechanical properties rather overlooked. Therefore, future research on this design would benefit from a comprehensive mechanical

property characterisation both experimentally and theoretically, alongside with other physical, chemical, and biological property characterisations.

References

1. Liu P, Zhang T, Huang Y. Three-dimensional model of normal human dermal tissue using serial tissue sections. *Front Bioeng Biotechnol*. 2024;12:1347159. doi:10.3389/fbioe.2024.1347159
2. Schoen FJ. Cardiac valves and valvular pathology: update on function, disease, repair, and replacement. *Cardiovasc Pathol*. 2005;14(4):189-194.
3. Schoen FJ. Mechanisms of function and disease of natural and replacement heart valves. *Annu Rev Pathol Mech Dis*. 2012;7:161-183. doi:10.1146/annurev-pathol-011110-130257
4. D'Arcy JL, Coffey S, Loudon MA, et al. Large-scale community echocardiographic screening reveals a major burden of undiagnosed valvular heart disease in older people: The OxVALVE Population Cohort Study. *Eur Heart J*. 2016;37(47):3515-3522a. doi:10.1093/eurheartj/ehw229
5. Nkomo VT, Gardin JM, Skelton TN, Gottdiener JS, Scott CG, Enriquez-Sarano M. Burden of valvular heart diseases: a population-based study. *Lancet*. 2006;368(9540):1005-1011. doi:10.1016/S0140-6736(06)69208-8
6. Saurav A. Outcomes of mitral valve repair compared with replacement in patients undergoing concomitant aortic valve surgery: a meta-analysis of observational studies. *Eur J Cardiothorac Surg*. 2015;48(3):347-353.
7. Kheradvar A, Groves EM, Dasi LP, et al. Emerging Trends in Heart Valve Engineering: Part I. Solutions for Future. *Ann Biomed Eng*. 2015;43(4):833-843. doi:10.1007/s10439-014-1209-z
8. Fioretta ES, Dijkman PE, Emmert MY, Hoerstrup SP. The future of heart valve replacement: recent developments and translational challenges for heart valve tissue engineering. *J Tissue Eng Regen Med*. 2018;12(1):e323-e335. doi:10.1002/term.2326

9. Barili F, Dainese L, Topkara VK, Biglioli P, Polvani G. The future of human valve allografts: Bioengineering and stem cells. *Artif Organs*. 2005;29(11):923. doi:10.1111/j.1525-1594.2005.00158.x

10. Cooley DA, Liotta D, Cromie HW, Hall CW, Wieting DW, Bloodwell RD. Aortic valve prosthesis incorporating lightweight titanium ball, Dacron velour-covered cage and seat. *ASAIO J*. 1967;13(1). https://journals.lww.com/asaiojournal/fulltext/1967/04000/aortic_valve_prosthesis_incorporating_lightweight.24.aspx

11. Kay EB, Suzuki A, Demaney M, Zimmerman HA. Comparison of ball and disc valves for mitral valve replacement. *Am J Cardiol*. 1966;18(4):504-514. doi:10.1016/0002-9149(66)90002-6

12. Carrel T, Dembitsky WP, de Mol B, et al. Non-physiologic closing of bi-leaflet mechanical heart prostheses requires a new tri-leaflet valve design. *Int J Cardiol*. 2020;304:125-127. doi:https://doi.org/10.1016/j.ijcard.2020.01.056

13. DONOVAN TJ, HUFNAGEL CA, EASTCOTT HH. Techniques of endocardial anastomosis for circumventing the pulmonic valve. *J Thorac Surg*. 1952;23(4):348-359. doi:10.1016/s0096-5588(20)31130-2

14. Hufnagel CA. Experiences with new types of aortic valvular prostheses. *Ann Surg*. 1958;147(5):636-644.

15. Zilla P. Prosthetic heart valves: Catering for the few. *Biomaterials*. 2008;29(4):385-406.

16. Lakier JB. Porcine xenograft valves. Long-term (60-89-month) follow-up. *Circulation*. 1980;62(2):313-318. Accessed January 19, 2021. http://ahajournals.org

17. Iaizzo PA, Bianco RW, Hill AJ, St. Louis JD. *Heart Valves: From Design to Clinical Implantation*. (Louis PAIWBJHD St., ed.). Springer; 2013. doi:10.1007/978-1-4614-

6144-9

18. Chambers JC. Pulmonary autograft procedure for aortic valve disease: long-term results of the pioneer series. *Circulation*. 1997;96(7):2206-2214.

19. Dvir D, Webb J, Brecker S, et al. Transcatheter aortic valve replacement for degenerative bioprosthetic surgical valves: Results from the global valve-in-valve registry. *Circulation*. 2012;126(19):2335-2344. doi:10.1161/CIRCULATIONAHA.112.104505

20. Chhatriwalla AK, Allen KB, Saxon JT, et al. Bioprosthetic Valve Fracture Improves the Hemodynamic Results of Valve-in-Valve Transcatheter Aortic Valve Replacement. *Circ Cardiovasc Interv*. 2017;10(7). doi:10.1161/CIRCINTERVENTIONS.117.005216

21. Edelman JJ, Khan JM, Rogers T, et al. Valve-in-Valve TAVR: State-of-the-Art Review. *Innov Technol Tech Cardiothorac Vasc Surg*. 2019;14(4):299-310. doi:10.1177/1556984519858020

22. Alperi A, Garcia S, Rodés-Cabau J. Transcatheter valve-in-valve implantation in degenerated surgical aortic and mitral bioprosthesis: Current state and future perspectives. *Prog Cardiovasc Dis*. 2022;72:54-65. doi:10.1016/j.pcad.2021.10.001

23. Tomášek A, Maňoušek J, Kuta J, et al. Metals and Trace Elements in Calcified Valves in Patients with Acquired Severe Aortic Valve Stenosis: Is There a Connection with the Degeneration Process? *J Pers Med*. 2023;13(2):320. doi:10.3390/jpm13020320

24. BARNARD CN, SCHRIRE V, GOOSEN CC, HOLMGREN L V. Complete replacement of the mitral valve. *S Afr Med J*. 1963;37(1):97-100. doi:10.1016/s0022-5223(19)32638-8

25. Rezvova MA, Klyshnikov KY, Gritskevich AA, Ovcharenko EA. Polymeric Heart Valves Will Displace Mechanical and Tissue Heart Valves: A New Era for the

Medical Devices. *Int J Mol Sci*. 2023;24(4). doi:10.3390/ijms24043963

26. Rezvova MA, Ovcharenko EA, Nikishev PA, et al. The use of SIBS triblock copolymers in cardiac surgery: In vitro and in vivo studies in comparison with ePTFE. *Vestn Transplantologii i Iskusstv Organov*. 2019;21(4):67-80. doi:10.15825/1995-1191-2019-4-67-80
27. Ghanbari H, Viatge H, Kidane AG, Burriesci G, Tavakoli M, Seifalian AM. Polymeric heart valves: new materials, emerging hopes. *Trends Biotechnol*. 2009;27(6):359-367. doi:10.1016/j.tibtech.2009.03.002
28. Oveissi F, Naficy S, Lee A, Winlaw DS, Dehghani F. Materials and manufacturing perspectives in engineering heart valves: a review. *Mater Today Bio*. 2020;5:100038. doi:10.1016/j.mtbio.2019.100038
29. Bloomfield P. Choice of heart valve prosthesis. *Heart*. 2002;87(6):583-589.
30. Besanko J, Beltrame J, Edwards J, et al. Bioprosthetic Versus Mechanical Prostheses in Patients Aged 50 to 70 Years Undergoing Aortic Valve Replacement Surgery: Outcomes Analysis From Propensity Score Matching. *Hear Lung Circ*. 2024;33:S231-S232. doi:10.1016/J.HLC.2024.06.221
31. Shao Z, Tao T, Xu H, et al. Recent progress in biomaterials for heart valve replacement: Structure, function, and biomimetic design. *View*. 2021;2(6):1-17. doi:10.1002/VIW.20200142
32. Puri R, Auffret V, Rodés-Cabau J. Bioprosthetic Valve Thrombosis. *J Am Coll Cardiol*. 2017;69(17):2193-2211. doi:10.1016/j.jacc.2017.02.051
33. Head SJ, Çelik M, Kappetein AP. Mechanical versus bioprosthetic aortic valve replacement. *Eur Heart J*. 2017;38(28):2183-2191. doi:10.1093/eurheartj/ehx141
34. Kidane AG, Burriesci G, Edirisinghe M, Ghanbari H, Bonhoeffer P, Seifalian AM. A novel nanocomposite polymer for development of synthetic heart valve leaflets. *Acta*

Biomater. 2009;5(7):2409-2417. doi:10.1016/j.actbio.2009.02.025

35. Dhandayuthapani B, Yoshida Y, Maekawa T, Kumar DS. Polymeric scaffolds in tissue engineering application: A review. *Int J Polym Sci*. 2011;2011. doi:10.1155/2011/290602

36. Ulery BD, Nair LS, Laurencin CT. Biomedical Applications of Biodegradable Polymers. *J Polym Sci B Polym Phys*. 2011;49(12):832-864.

37. Ibrahim DM, Kakarougkas A, Allam NK. Recent advances on electrospun scaffolds as matrices for tissue-engineered heart valves. *Mater Today Chem*. 2017;5:11-23. doi:10.1016/j.mtchem.2017.05.001

38. Merryman WD, Huang H-YS, Schoen FJ, Sacks MS. The effects of cellular contraction on aortic valve leaflet flexural stiffness. *J Biomech*. 2006;39(1):88-96. doi:10.1016/j.jbiomech.2004.11.008

39. Qiu Q, Dunmore-Buyze J, Boughner DR, Lacefield JC. Evaluation of an Algorithm for Semiautomated Segmentation of Thin Tissue Layers in High-Frequency Ultrasound Images. *IEEE Trans Ultrason Ferroelectr Freq Control*. 2006;53(2):324-334. doi:10.1109/TUFFC.2006.1593371

40. Lu X, Senda S, Mizushige K, et al. Evaluation of progression in nonrheumatic aortic valvular stenosis by scanning acoustic microscopy. *Ultrasound Med Biol*. 2000;26(4):563-569. doi:10.1016/S0301-5629(99)00149-0

41. Khan Z, Boughner DR, Lacefield JC. Reconsidering the layer thickness distribution in aortic valve cusps using high-frequency ultrasound. In: *2007 4th IEEE International Symposium on Biomedical Imaging: From Nano to Macro - Proceedings*. ; 2007:868-871. doi:10.1109/ISBI.2007.356990

42. Stella JA, Sacks MS. On the biaxial mechanical properties of the layers of the aortic valve leaflet. *J Biomech Eng*. 2007;129(5):757-766. doi:10.1115/1.2768111

43. Vesely I, Lozon A. Natural preload of aortic valve leaflet components during glutaraldehyde fixation: Effects on tissue mechanics. *J Biomech*. 1993;26(2):121-131. doi:10.1016/0021-9290(93)90043-E

44. Vesely I, Noseworthy R. Micromechanics of the fibrosa and the ventricularis in aortic valve leaflets. *J Biomech*. 1992;25(1):101,111-109,113. doi:10.1016/0021-9290(92)90249-Z

45. Vesely I. Analysis of the Medtronic Intact bioprosthetic valve. Effects of "zero-pressure" fixation. *J Thorac Cardiovasc Surg*. 1991;101(1):90-99.

46. Lee JM, Boughner DR, Courtman DW. The glutaraldehyde-stabilized porcine aortic valve xenograft. II. Effect of fixation with or without pressure on the tensile viscoelastic properties of the leaflet material. *J Biomed Mater Res*. 1984;18(1):79-98. doi:10.1002/jbm.820180109

47. Gross L, Kugel MA. Topographic Anatomy and Histology of the Valves in the Human Heart. *Am J Pathol*. 1931;7(5):445-474.7. Accessed February 18, 2021. http://www.ncbi.nlm.nih.gov/pubmed/19969978

48. Lincoln J, Lange AW, Yutzey KE. Hearts and bones: Shared regulatory mechanisms in heart valve, cartilage, tendon, and bone development. *Dev Biol*. 2006;294(2):292-302. doi:10.1016/j.ydbio.2006.03.027

49. Sacks MS, David Merryman W, Schmidt DE. On the biomechanics of heart valve function. *J Biomech*. 2009;42(12):1804-1824. doi:10.1016/j.jbiomech.2009.05.015

50. Culav EM, Clark CH, Merrilees MJ. Connective tissues: Matrix composition and its relevance to physical therapy. *Phys Ther*. 1999;79(3):308-319. doi:10.1093/ptj/79.3.308

51. Vyavahare N, Ogle M, Schoen FJ, et al. Mechanisms of bioprosthetic heart valve failure: Fatigue causes collagen denaturation and glycosaminoglycan loss. *J Biomed*

Mater Res. 1999;46(1):44-50. doi:10.1002/(SICI)1097-4636(199907)46:1<44::AID-JBM5>3.0.CO;2-D

52. Talman EA, Boughner DR. Effect of altered hydration on the internal shear properties of porcine aortic valve cusps. *Ann Thorac Surg*. 2001;71(5):S375-S378. doi:10.1016/S0003-4975(01)02546-2

53. Eckert CE, Fan R, Mikulis B, et al. On the biomechanical role of glycosaminoglycans in the aortic heart valve leaflet. *Acta Biomater*. 2013;9(1):4653-4660. doi:10.1016/j.actbio.2012.09.031

54. Butcher JT, Simmons CA, Warnock JN. Review: Mechanobiology of the aortic heart valve. *J Heart Valve Dis*. 2008;17(1):62-73.

55. Hardingham T. Proteoglycans and Glycosaminoglycans. In: *Dynamics of Bone and Cartilage Metabolism: Principles and Clinical Applications*. Cold Spring Harbor Laboratory Press; 2006:85-98. doi:10.1016/B978-012088562-6/50006-6

56. Rego B V, Sacks MS. A functionally graded material model for the transmural stress distribution of the aortic valve leaflet. *J Biomech*. 2017;54:88-95. doi:10.1016/j.jbiomech.2017.01.039

57. Bashey RI, Torii S, Angrist A. Age-related collagen and elastin content of human heart valves. *J Gerontol*. 1967;22(2):203-208. doi:10.1093/geronj/22.2.203

58. Ricard-Blum S, Ruggiero F. The collagen superfamily: From the extracellular matrix to the cell membrane. *Pathol Biol*. 2005;53(7):430-442. doi:10.1016/j.patbio.2004.12.024

59. Taylor PM. Biological matrices and bionanotechnology. *Philos Trans R Soc Lond B Biol Sci*. 2007;362(1484):1313-1320.

60. Baer E, Cassidy JJ, Hiltner A. Hierarchical Structure of Collagen Composite Systems. In: *Viscoelasticity of Biomaterials*. American Chemical Society; 1992:2-23.

doi:10.1021/bk-1992-0489.ch001

61. Schwarcz HP, Abueidda D, Jasiuk I. The Ultrastructure of Bone and Its Relevance to Mechanical Properties. *Front Phys*. 2017;5(SEP):39. doi:10.3389/fphy.2017.00039

62. Holmes R, Kirk S, Tronci G, Yang X, Wood D. Influence of telopeptides on the structural and physical properties of polymeric and monomeric acid-soluble type I collagen. *Mater Sci Eng C*. 2017;77:823-827. doi:10.1016/j.msec.2017.03.267

63. Einbinder J, Schubert M. Binding of mucopolysaccharides and dyes by collagen. *J Biol Chem*. 1951;188(1):335-341. doi:10.1016/s0021-9258(18)56175-5

64. Steven FS, Jackson DS. Purification and amino acid composition of monomeric and polymeric collagens. *Biochem J*. 1967;104(2):534-536. doi:10.1042/bj1040534

65. Gross J, Kirk D. The heat precipitation of collagen from neutral salt solutions: some rate-regulating factors. *J Biol Chem*. 1958;233(2):355-360. doi:10.1016/s0021-9258(18)64764-7

66. Steven FS, Tristram GR. The presence of non-protein nitrogen in acetic acid-soluble calf-skin collagen. *Biochem J*. 1962;83(2):240-244. doi:10.1042/bj0830240

67. Gale M, Pollanen MS, Markiewicz P, Goh MC. Sequential assembly of collagen revealed by atomic force microscopy. *Biophys J*. 1995;68(5):2124-2128. doi:10.1016/S0006-3495(95)80393-0

68. Kadler KE, Hojima Y, Prockop DJ. Assembly of collagen fibrils de novo by cleavage of the type I pC-collagen with procollagen C-proteinase. Assay of critical concentration demonstrates that collagen self-assembly is a classical example of an entropy-driven process. *J Biol Chem*. 1987;262(32):15696-15701. doi:10.1016/s0021-9258(18)47783-6

69. Miyamoto Y, Ishikawa K, Takechi M, et al. Basic properties of calcium phosphate cement containing atelocollagen in its liquid or powder phases. *Biomaterials*.

1998;19(7-9):707-715. doi:10.1016/S0142-9612(97)00186-5

70. Orgel JPRO, San Antonio JD, Antipova O. Molecular and structural mapping of collagen fibril interactions. *Connect Tissue Res*. 2011;52(1):2-17. doi:10.3109/03008207.2010.511353

71. Timpl R, Furthmayr H, Beil W. Maturation of the immune response to soluble rat collagen: late appearance of antibodies directed to N-terminal sites of the 2-chain. *J Immunol*. 1972;108(1):119-125.

72. Morimoto K, Kunii S, Hamano K, Tonomura B. Preparation and structural analysis of actinidain-processed atelocollagen of yellowfin tuna (Thunnus albacares). *Biosci Biotechnol Biochem*. 2004;68(4):861-867. doi:10.1271/bbb.68.861

73. Parenteau-Bareil R, Gauvin R, Berthod F. Collagen-based biomaterials for tissue engineering applications. *Materials (Basel)*. 2010;3(3):1863-1887. doi:10.3390/ma3031863

74. Hanai K, Kojima T, Ota M, Onodera J, Sawada N. Effects of Atelocollagen Formulation Containing Oligonucleotide on Endothelial Permeability. *J Drug Deliv*. 2012;2012:1-9. doi:10.1155/2012/245835

75. George J, Onodera J, Miyata T. Biodegradable honeycomb collagen scaffold for dermal tissue engineering. *J Biomed Mater Res - Part A*. 2008;87(4):1103-1111. doi:10.1002/jbm.a.32277

76. Yadavalli VK, Svintradze D V., Pidaparti RM. Nanoscale measurements of the assembly of collagen to fibrils. *Int J Biol Macromol*. 2010;46(4):458-464. doi:10.1016/j.ijbiomac.2010.02.012

77. Zhang J, Zou M, Zhang M, et al. Impact of Telopeptides on Self-Assembly Properties of Snakehead (Channa argus) Skin Collagen. *Food Biophys*. 2016;11(4):380-387. doi:10.1007/s11483-016-9452-5

78. Miyata T, Taira T, Noishiki Y. Collagen engineering for biomaterial use. *Clin Mater*. 1992;9(3-4):139-148. doi:10.1016/0267-6605(92)90093-9

79. Giro MG, Davidson JM. Elastin. *Methods Enzymol*. 1988;163:656-673.

80. Sandberg LB, Soskel NT, Leslie JG. Elastin Structure, Biosynthesis, and Relation to Disease States. *N Engl J Med*. 1981;304(10):566-579. doi:10.1056/nejm198103053041004

81. Cleary EG, Gibson MA. Elastin-associated microfibrils and microfibrillar proteins. *Int Rev Connect Tissue Res*. 1983;10:97-209. doi:10.1016/b978-0-12-363710-9.50009-5

82. Moore J, Thibeault S. Insights into the role of elastin in vocal fold health and disease. *J Voice*. 2012;26(3):269-275. doi:10.1016/j.jvoice.2011.05.003

83. Gray WR, Sandberg LB, Foster JA. Molecular model for elastin structure and function. *Nature*. 1973;246(5434):461-466. doi:10.1038/246461a0

84. Debelle L, Alix AJP, Wei SM, et al. The secondary structure and architecture of human elastin. *Eur J Biochem*. 1998;258(2):533-539. doi:10.1046/j.1432-1327.1998.2580533.x

85. Daamen WF, Veerkamp JH, van Hest JCM, van Kuppevelt TH. Elastin as a biomaterial for tissue engineering. *Biomaterials*. 2007;28(30):4378-4398. doi:10.1016/j.biomaterials.2007.06.025

86. Karamanos NK, Hjerpe A, Tsegenidis T, Engfeldt B, Antonopoulos CA. Determination of iduronic acid and glucuronic acid in glycosaminoglycans after stoichiometric reduction and depolymerization using high-performance liquid chromatography and ultraviolet detection. *Anal Biochem*. 1988;172(2):410-419. doi:10.1016/0003-2697(88)90463-0

87. Fraser JRE, Laurent TC, Laurent UBG. Hyaluronan: Its nature, distribution, functions and turnover. In: *Journal of Internal Medicine*. Vol 242. Blackwell Publishing Ltd;

1997:27-33. doi:10.1046/j.1365-2796.1997.00170.x

88. Murata K. Acidic glycosaminoglycans in human heart valves. *J Mol Cell Cardiol*. 1981;13(3):281-292. doi:10.1016/0022-2828(81)90316-3

89. Boström H, Moretti A, Whitehouse M. Studies on the biochemistry of heart valves I. On the biosynthesis of mucopolysaccharides in bovine heart valves. *BBA - Biochim Biophys Acta*. 1963;74(C):213-221. doi:10.1016/0006-3002(63)91360-X

90. Liu L, Liu Y, Li J, Du G, Chen J. Microbial production of hyaluronic acid: current state, challenges, and perspectives. *Microb Cell Fact*. 2011;10(1):99. doi:10.1186/1475-2859-10-99

91. Chakrabarti B, Park JW, Stevens ES. Glycosaminoglycans: Structure and interactio. *Crit Rev Biochem Mol Biol*. 1980;8(3):225-313. doi:10.3109/10409238009102572

92. Toole BP. Hyaluronan: From extracellular glue to pericellular cue. *Nat Rev Cancer*. 2004;4(7):528-539. doi:10.1038/nrc1391

93. Rossvoll O, Samstad S, Torp HG, et al. The Velocity Distribution in the Aortic Anulus in Normal Subjects: A Quantitative Analysis of Two-dimensional Doppler Flow Maps. *J Am Soc Echocardiogr*. 1991;4(4):367-378. doi:10.1016/S0894-7317(14)80447-1

94. Sacks MS, Smith DB, Hiester ED. The aortic valve microstructure: Effects of transvalvular pressure. *J Biomed Mater Res*. 1998;41(1):131-141. doi:10.1002/(SICI)1097-4636(199807)41:1<131::AID-JBM16>3.0.CO;2-Q

95. Yoganathan AP, He Z, Jones SC. Fluid mechanics of heart valves. *Annu Rev Biomed Eng*. 2004;6:331-362. doi:10.1146/annurev.bioeng.6.040803.140111

96. Hasan A, Ragaert K, Swieszkowski W, et al. Biomechanical properties of native and tissue engineered heart valve constructs. *J Biomech*. 2014;47(9):1949-1963. doi:10.1016/j.jbiomech.2013.09.023

97. Thubrikar MJ, Aouad J, Nolan SP. Comparison of the in vivo and in vitro mechanical

properties of aortic valve leaflets. *J Thorac Cardiovasc Surg*. 1986;92(1):29-36. doi:10.1016/s0022-5223(19)35928-8

98. Thubrikar M, Piepgrass WC, Bosher LP, Nolan SP. The elastic modulus of canine aortic valve leaflets in vivo and in vitro. *Circ Res*. 1980;47(5):792-800. doi:10.1161/01.RES.47.5.792

99. Clark RE. Stress strain characteristics of fresh and frozen human aortic and mitral leaflets and chordae tendineae: implications for clinical use. *J Thorac Cardiovasc Surg*. 1973;66(2):202-208. doi:10.1016/s0022-5223(19)40619-3

100. Sacks MS, Yoganathan AP. Heart valve function: A biomechanical perspective. *Philos Trans R Soc B Biol Sci*. 2007;362(1484):1369-1391. doi:10.1098/rstb.2007.2122

101. Jiang H, Campbell G, Boughner D, Wan WK, Quantz M. Design and manufacture of a polyvinyl alcohol (PVA) cryogel tri-leaflet heart valve prosthesis. *Med Eng Phys*. 2004;26(4):269-277. doi:10.1016/j.medengphy.2003.10.007

102. Stella JA, Liao J, Sacks MS. Time-dependent biaxial mechanical behavior of the aortic heart valve leaflet. *J Biomech*. 2007;40(14):3169-3177. doi:10.1016/j.jbiomech.2007.04.001

103. Saidy NT, Wolf F, Bas O, et al. Biologically Inspired Scaffolds for Heart Valve Tissue Engineering via Melt Electrowriting. *Small*. 2019;15(24):1900873. doi:10.1002/smll.201900873

104. Mol A, Bouten CVC, Baaijens FPT, Zünd G, Turina MI, Hoerstrup SP. Tissue engineering of semilunar heart valves: Current status and future developments. *J Heart Valve Dis*. 2004;13(2):272-280. Accessed February 22, 2021. https://pubmed.ncbi.nlm.nih.gov/15086267/

105. Missirlis YF, Chong M. Aortic valve mechanics--Part I: material properties of natural porcine aortic valves. *J Bioeng*. 1978;2(3-4):287-300.

106. Rousseau EPM, Sauren AAHJ, van Hout MC, van Steenhoven AA. Elastic and viscoelastic material behaviour of fresh and glutaraldehyde-treated porcine aortic valve tissue. *J Biomech*. 1983;16(5):339-348. doi:10.1016/0021-9290(83)90017-9

107. Broom ND, Thomson FJ. Influence of fixation conditions on the performance of glutaraldehyde-treated porcine aortic valves: towards a more scientific basis. *Thorax*. 1979;34(2):166-176. doi:10.1136/thx.34.2.166

108. Sauren AAHJ, van Hout MC, van Steenhoven AA, Veldpaus FE, Janssen JD. The mechanical properties of porcine aortic valve tissues. *J Biomech*. 1983;16(5):327-337. doi:10.1016/0021-9290(83)90016-7

109. Balguid A, Rubbens MP, Mol A, et al. The role of collagen cross-links in biomechanical behavior of human aortic heart valve leaflets - Relevance for tissue engineering. *Tissue Eng*. 2007;13(7):1501-1511. doi:10.1089/ten.2006.0279

110. Peteris Stradins, Romans Lacis, Iveta Ozolanta, et al. Comparison of biomechanical and structural properties between human aortic and pulmonary valve. *Eur J Cardio-Thoracic Surg*. 2004;26(3):634-639. doi:10.1016/j.ejcts.2004.05.043

111. Merryman WD, Engelmayr GC, Liao J, Sacks MS. Defining biomechanical endpoints for tissue engineered heart valve leaflets from native leaflet properties. *Prog Pediatr Cardiol*. 2006;21(2):153-160. doi:10.1016/j.ppedcard.2005.11.001

112. Billiar KL, Sacks MS. Biaxial mechanical properties of the natural and glutaraldehyde treated aortic valve cusp - Part I: Experimental results. *J Biomech Eng*. 2000;122(1):23-30. doi:10.1115/1.429624

113. Mirnajafi A, Raymer JM, Mcclure LR, Sacks MS. The flexural rigidity of the aortic valve leaflet in the commissural region. *J Biomech*. 2006;39:2966-2973. doi:10.1016/j.jbiomech.2005.10.026

114. Nazir R, Bruyneel A, Carr C, Czernuszka J. Collagen type I and hyaluronic acid based

hybrid scaffolds for heart valve tissue engineering. *Biopolymers*. 2019;110(8). doi:10.1002/bip.23278

115. Wieckiewicz M, Opitz V, Richter G, Boening KW. Physical properties of polyamide-12 versus PMMA denture base material. *Biomed Res Int*. 2014;2014:150298. doi:10.1155/2014/150298

116. Gloeckner DG, Bihir KL, Sacks MS. Effects of Mechanical Fatigue on the Bending Properties of the Porcine Bioprosthetic Heart Valve. *ASAIO J*. 1999;45(1):59-63. https://journals.lww.com/asaiojournal/Fulltext/1999/01000/Effects_of_Mechanical_Fatigue_on_the_Bending.14.aspx

117. Engelmayr GC, Hildebrand DK, Sutherland FWH, Mayer JE, Sacks MS. A novel bioreactor for the dynamic flexural stimulation of tissue engineered heart valve biomaterials. *Biomaterials*. 2003;24(14):2523-2532. doi:10.1016/S0142-9612(03)00051-6

118. Sauvage JB, Aufray M, Jeandrau JP, Chalandon P, Poquillon D, Nardin M. Using the 3-point bending method to study failure initiation in epoxide-aluminum joints. *Int J Adhes Adhes*. 2017;75:181-189. doi:10.1016/j.ijadhadh.2017.03.011

119. Jiao T, Clifton RJ, Converse GL, Hopkins RA. Measurements of the effects of decellularization on viscoelastic properties of tissues in ovine, baboon, and human heart valves. *Tissue Eng - Part A*. 2012;18(3-4):423-431. doi:10.1089/ten.tea.2010.0677

120. Grashow JS, Sacks MS, Liao J, Yoganathan AP. Planar biaxial creep and stress relaxation of the mitral valve anterior leaflet. *Ann Biomed Eng*. 2006;34(10):1509-1518. doi:10.1007/s10439-006-9183-8

121. Grashow J, Yoganathan A, Sacks M. Biaixal stress–stretch behavior of the mitral valve anterior leaflet at physiologic strain rates. *Ann Biomed Eng*. 2006;34(2):315-325.

Accessed February 24, 2021. https://link.springer.com/content/pdf/10.1007/s10439-005-9027-y.pdf

122. Anssari-Benam A, Bader DL, Screen HRC. A combined experimental and modelling approach to aortic valve viscoelasticity in tensile deformation. *J Mater Sci Mater Med*. 2011;22(2):253-262. doi:10.1007/s10856-010-4210-6

123. Sell SA, McClure MJ, Garg K, Wolfe PS, Bowlin GL. Electrospinning of collagen/biopolymers for regenerative medicine and cardiovascular tissue engineering. *Adv Drug Deliv Rev*. 2009;61(12):1007-1019. doi:10.1016/j.addr.2009.07.012

124. Matthews JA, Wnek GE, Simpson DG, Bowlin GL. Articles Electrospinning of Collagen Nanofibers. *Biomacromolecules*. 2002;3(2):232-238. doi:10.1021/bm015533u

125. Wegst UGK, Schecter M, Donius AE, Hunger PM. Biomaterials by freeze casting. *Philos Trans R Soc A Math Phys Eng Sci*. 2010;368(1917):2099-2121. doi:10.1098/rsta.2010.0014

126. Noble C, Maxson EL, Lerman A, Young MD. Mechanical and finite element evaluation of a bioprinted scaffold following recellularization in a rat subcutaneous model. *J Mech Behav Biomed Mater*. 2020;102:103519. doi:10.1016/j.jmbbm.2019.103519

127. Maxson EL, Young MD, Noble C, et al. In vivo remodeling of a 3D-Bioprinted tissue engineered heart valve scaffold. *Bioprinting*. 2019;16:e00059. doi:10.1016/j.bprint.2019.e00059

128. Sell SA, Wolfe PS, Garg K, McCool JM, Rodriguez IA, Bowlin GL. The Use of Natural Polymers in Tissue Engineering: A Focus on Electrospun Extracellular Matrix Analogues. *Polymers (Basel)*. 2010;2(4):522-553. doi:10.3390/polym2040522

129. Pham QP, Sharma U, Mikos AG. Electrospinning of polymeric nanofibers for tissue

engineering applications: A review. *Tissue Eng*. 2006;12(5):1197-1211. doi:10.1089/ten.2006.12.1197

130. Nam J, Huang Y, Agarwal S, Lannutti J. Materials selection and residual solvent retention in biodegradable electrospun fibers. *J Appl Polym Sci*. 2008;107(3):1547-1554. doi:10.1002/app.27063

131. Deville S. Freeze-Casting of Porous Biomaterials: Structure, Properties and Opportunities. *Materials (Basel)*. 2010;3(3):1913-1927. doi:10.3390/ma3031913

132. Beachley V, Wen X. Fabrication of nanofiber reinforced protein structures for tissue engineering. *Mater Sci Eng C*. 2009;29(8):2448-2453. doi:10.1016/j.msec.2009.07.008

133. Stratton S, Manoukian OS, Patel R, Wentworth A, Rudraiah S, Kumbar SG. Polymeric 3D printed structures for soft-tissue engineering. *J Appl Polym Sci*. 2018;135(24):45569. doi:10.1002/app.45569

134. An J, Teoh JEM, Suntornnond R, Chua CK. Design and 3D Printing of Scaffolds and Tissues. *Engineering*. 2015;1(2):261-268. doi:10.15302/J-ENG-2015061

135. Weadock KS, Miller EJ, Bellincampi LD, Zawadsky JP, Dunn MG. Physical crosslinking of collagen fibers: Comparison of ultraviolet irradiation and dehydrothermal treatment. *J Biomed Mater Res*. 1995;29(11):1373-1379. doi:10.1002/jbm.820291108

136. Davidenko N, Bax D V., Schuster CF, et al. Optimisation of UV irradiation as a binding site conserving method for crosslinking collagen-based scaffolds. *J Mater Sci Mater Med*. 2016;27(1):1-17. doi:10.1007/s10856-015-5627-8

137. Lee JE, Park JC, Hwang YS, Kim JK, Kim JG, Sub H. Characterization of UV-irradiated dense/porous collagen membranes: morphology, enzymatic degradation, and mechanical properties. *Yonsei Med J*. 2001;42(2):172-179. doi:10.3349/ymj.2001.42.2.172

138. Harriger MD, Supp AP, Warden GD, Boyce ST. Glutaraldehyde crosslinking of collagen substrates inhibits degradation in skin substitutes grafted to athymic mice. *J Biomed Mater Res*. 1997;35(2):137-145. doi:10.1002/(SICI)1097-4636(199705)35:2<137::AID-JBM1>3.0.CO;2-O

139. Wu X, Black L, Santacana-Laffitte G, Patrick CW. Preparation and assessment of glutaraldehyde-crosslinked collagen-chitosan hydrogels for adipose tissue engineering. *J Biomed Mater Res - Part A*. 2007;81(1):59-65. doi:10.1002/jbm.a.31003

140. Zeeman R, Dijkstra PJ, Van Wachem PB, et al. Successive epoxy and carbodiimide cross-linking of dermal sheep collagen. *Biomaterials*. 1999;20(10):921-931. doi:10.1016/S0142-9612(98)00242-7

141. Everaerts F, Torrianni M, Hendriks M, Feijen J. Biomechanical properties of carbodiimide crosslinked collagen: Influence of the formation of ester crosslinks. *J Biomed Mater Res Part A*. 2008;85A(2):547-555. doi:10.1002/jbm.a.31524

142. Zeugolis DI, Paul GR, Attenburrow G. Cross-linking of extruded collagen fibers-A biomimetic three-dimensional scaffold for tissue engineering applications. *J Biomed Mater Res Part A*. 2009;89A(4):895-908. doi:10.1002/jbm.a.32031

143. Sundararaghavan HG, Monteiro GA, Lapin NA, Chabal YJ, Miksan JR, Shreiber DI. Genipin-induced changes in collagen gels: Correlation of mechanical properties to fluorescence. *J Biomed Mater Res - Part A*. 2008;87(2):308-320. doi:10.1002/jbm.a.31715

144. Ryan AJ, Ryan EJ, Cameron AR, O'Brien FJ. Hierarchical biofabrication of biomimetic collagen-elastin vascular grafts with controllable properties via lyophilisation. *Acta Biomater*. 2020;112:52-61. doi:10.1016/j.actbio.2020.06.002

145. McManamon C, Cameron A, de Silva JP, Daly R, O'Brien FJ, Cross GLW. Effect of cross-linking and hydration on microscale flat punch indentation contact to collagen-

hyaluronic acid films in the viscoelastic limit. *Acta Biomater*. 2020;111:279-289. doi:10.1016/j.actbio.2020.04.043

146. Luo X, Guo Z, He P, et al. Study on structure, mechanical property and cell cytocompatibility of electrospun collagen nanofibers crosslinked by common agents. *Int J Biol Macromol*. 2018;113:476-486. doi:10.1016/j.ijbiomac.2018.01.179

147. Davidenko N, Schuster CF, Bax D V., et al. Control of crosslinking for tailoring collagen-based scaffolds stability and mechanics. *Acta Biomater*. 2015;25:131-142. doi:10.1016/j.actbio.2015.07.034

148. Madaghiele M, Calò E, Salvatore L, et al. Assessment of collagen crosslinking and denaturation for the design of regenerative scaffolds. *J Biomed Mater Res - Part A*. 2016;104(1):186-194. doi:10.1002/jbm.a.35554

149. Cheng Z (Annie). Biological Multi-Functionalization and Surface Nanopatterning of Biomaterials. *Thèse l'université Bordeaux 1*. Published online December 12, 2013. Accessed August 23, 2024. https://theses.hal.science/tel-01016695

150. Yang C. Enhanced physicochemical properties of collagen by using EDC/NHS-crosslinking. *Bull Mater Sci*. 2012;35(5):913-918. doi:10.1007/s12034-012-0376-5

151. Weadock KS, Miller EJ, Keuffel EL, Dunn MG. Effect of physical crosslinking methods on collagen-fiber durability in proteolytic solutions. *J Biomed Mater Res*. 1996;32(2):221-226. doi:10.1002/(SICI)1097-4636(199610)32:2<221::AID-JBM11>3.0.CO;2-M

152. Hafemann B, Ghofrani K, Gattner HG, Stieve H, Pallua N. Cross-linking by 1-ethyl-3-(3-dimethylaminopropyl)-carbodiimide (EDC) of a collagen/elastin membrane meant to be used as a dermal substitute: Effects on physical, biochemical and biological features in vitro. *J Mater Sci Mater Med*. 2001;12(5):437-446. doi:10.1023/A:1011205221972

153. Shepherd JH, Ghose S, Kew SJ, Moavenian A, Best SM, Cameron RE. Effect of fiber crosslinking on collagen-fiber reinforced collagen-chondroitin-6-sulfate materials for regenerating load-bearing soft tissues. *J Biomed Mater Res - Part A*. 2013;101 A(1):176-184. doi:10.1002/jbm.a.34317

154. Vrana NE, Builles N, Kocak H, et al. EDC/NHS cross-linked collagen foams as scaffolds for artificial corneal stroma. *J Biomater Sci Polym Ed*. 2007;18(12):1527-1545. doi:10.1163/156856207794761961

155. Weadock K, Olson RM, Silver FH. Evaluation of collagen crosslinking techniques. *Biomater Med Devices Artif Organs*. 1983;11(4):293-318. doi:10.3109/10731198309118815

156. Anastase-Ravion S, Carreno MP, Blondin C, et al. Synergistic effects of glucose and ultraviolet irradiation on the physical properties of collagen. *J Biomed Mater Res*. 2002;60(3):384-391. doi:10.1002/jbm.10111

157. Haugh MG, Jaasma MJ, O'Brien FJ. The effect of dehydrothermal treatment on the mechanical and structural properties of collagen-GAG scaffolds. *J Biomed Mater Res - Part A*. 2009;89(2):363-369. doi:10.1002/jbm.a.31955

158. Olde Damink LHH, Dijkstra PJ, Van Luyn MJA, Van Wachem PB, Nieuwenhuis P, Feijen J. Glutaraldehyde as a crosslinking agent for collagen-based biomaterials. *J Mater Sci Mater Med*. 1995;6(8):460-472. doi:10.1007/BF00123371

159. Nguyen T-H, Lee B-T. Fabrication and characterization of cross-linked gelatin electro-spun nano-fibers. *J Biomed Sci Eng*. 2010;03(12):1117-1124. doi:10.4236/jbise.2010.312145

160. Ko CS, Huang JP, Huang CW, Chu IM. Type II collagen-chondroitin sulfate-hyaluronan scaffold cross-linked by genipin for cartilage tissue engineering. *J Biosci Bioeng*. 2009;107(2):177-182. doi:10.1016/j.jbiosc.2008.09.020

161. Yan LP, Wang YJ, Ren L, et al. Genipin-cross-linked collagen/chitosan biomimetic scaffolds for articular cartilage tissue engineering applications. *J Biomed Mater Res - Part A*. 2010;95 A(2):465-475. doi:10.1002/jbm.a.32869

162. Muzzarelli RAA, El Mehtedi M, Bottegoni C, Aquili A, Gigante A. Genipin-crosslinked chitosan gels and scaffolds for tissue engineering and regeneration of cartilage and bone. *Mar Drugs*. 2015;13(12):7314-7338. doi:10.3390/md13127068

163. Calderon L, Collin E, Velasco-Bayon D, Murphy M, O'Halloran D, Pandit A. Type II Collagen-Hyaluronan Hydrogel - A Step Towards A Scaffold For Intervertebral Disc Tissue Engineering. *Eur Cells Mater*. 2010;20:134-148. doi:10.22203/eCM.v020a12

164. Divakar P, Moodie KL, Demidenko E, Jack Hoopes P, Wegst UGK. Quantitative evaluation of the in vivo biocompatibility and performance of freeze-cast tissue scaffolds. *Biomed Mater*. 2020;15(5):055003. doi:10.1088/1748-605X/ab316a

165. Li Q, Mu L, Zhang F, et al. A novel fish collagen scaffold as dural substitute. *Mater Sci Eng C*. 2017;80:346-351. doi:10.1016/j.msec.2017.05.102

166. Grabska-Zielińska S, Sionkowska A, Carvalho Â, Monteiro FJ. Biomaterials with potential use in bone tissue regeneration-collagen/chitosan/silk fibroin scaffolds cross-linked by EDC/NHS. *Materials (Basel)*. 2021;14(5):1-21. doi:10.3390/ma14051105

167. Nong LM, Zhou D, Zheng D, et al. The effect of different cross-linking conditions of EDC/NHS on type II collagen scaffolds: an in vitro evaluation. *Cell Tissue Bank*. 2019;20(4):557-568. doi:10.1007/s10561-019-09790-7

168. Kaczmarek B, Sionkowska A, Kozlowska J, Osyczka AM. New composite materials prepared by calcium phosphate precipitation in chitosan/collagen/hyaluronic acid sponge cross-linked by EDC/NHS. *Int J Biol Macromol*. 2018;107(PartA):247-253. doi:10.1016/j.ijbiomac.2017.08.173

169. Colazzo F, Sarathchandra P, Smolenski RT, et al. Extracellular matrix production by

adipose-derived stem cells: Implications for heart valve tissue engineering. *Biomaterials*. 2011;32(1):119-127. doi:10.1016/j.biomaterials.2010.09.003

170. Taylor PM, Sachlos E, Dreger SA, Chester AH, Czernuszka JT, Yacoub MH. Interaction of human valve interstitial cells with collagen matrices manufactured using rapid prototyping. *Biomaterials*. 2006;27(13):2733-2737. doi:10.1016/j.biomaterials.2005.12.003

171. Dreger SA, Thomas P, Sachlos E, et al. Potential for synthesis and degradation of extracellular matrix proteins by valve interstitial cells seeded onto collagen scaffolds. *Tissue Eng*. 2006;12(9):2533-2540. doi:10.1089/ten.2006.12.2533

172. Antipova CG, Lukanina KI, Krasheninnikov S V., et al. Study of highly porous poly-l-lactide-based composites with chitosan and collagen. *Polym Adv Technol*. 2021;32(2):853-860. doi:10.1002/pat.5136

173. Kozlowska J, Sionkowska A, Osyczka AM, Dubiel M. Stabilizing effect of carbodiimide and dehydrothermal treatment crosslinking on the properties of collagen/hydroxyapatite scaffolds. *Polym Int*. 2017;66(8):1164-1172. doi:10.1002/pi.5371

174. Newman K, Clark K, Gurumurthy B, Pal P, Janorkar A V. Elastin-collagen based hydrogels as model scaffolds to induce three-dimensional adipocyte culture from adipose derived stem cells. *Bioengineering*. 2020;7(3):1-12. doi:10.3390/bioengineering7030110

175. Khajavi M, Hajimoradloo A, Zandi M, Pezeshki-Modaress M, Bonakdar S, Zamani A. Fish cartilage: A promising source of biomaterial for biological scaffold fabrication in cartilage tissue engineering. *J Biomed Mater Res - Part A*. Published online March 18, 2021. doi:10.1002/jbm.a.37169

176. Sionkowska A, Michalska M, Walczak M, Śmiechowski K, Grabska S. Preparation

and characterization of silk fibroin/collagen sponge modified by chemical cross-linking. *Mol Cryst Liq Cryst*. 2016;640(1):180-190. doi:10.1080/15421406.2016.1261433

177. Kaczmarek B, Sionkowska A, Łukowicz K, Osyczka AM. Characterization of scaffolds based on chitosan and collagen with glycosaminoglycans. *Int J Polym Anal Charact*. 2019;24(4):374-380. doi:10.1080/1023666X.2019.1598639

178. Liu Y, Gu J, Fan D. Fabrication of high-strength and porous hybrid scaffolds based on nano-hydroxyapatite and human-like collagen for bone tissue regeneration. *Polymers (Basel)*. 2020;12(1):61. doi:10.3390/polym12010061

179. Chen Q, Bruyneel A, Clarke K, Carr C, Czernuszka J. Collagen-based scaffolds for potential application of heart valve tissue engineering. *J Tissue Sci Eng*. 2012;3.

180. Gurumurthy B, Griggs JA, Janorkar A V. Optimization of collagen-elastin-like polypeptide composite tissue engineering scaffolds using response surface methodology. *J Mech Behav Biomed Mater*. 2018;84:116-125. doi:10.1016/j.jmbbm.2018.04.019

181. Nazir R, Bruyneel A, Carr C, Czernuszka J. Mechanical and Degradation Properties of Hybrid Scaffolds for Tissue Engineered Heart Valve (TEHV). *J Funct Biomater*. 2021;12(1):20. doi:10.3390/jfb12010020

182. Chen Q, Bruyneel A, Carr C, Czernuszka J. Bio-mechanical properties of novel bi-layer collagen-elastin scaffolds for heart valve tissue engineering. In: *Procedia Engineering*. Vol 59. Elsevier Ltd; 2013:247-254. doi:10.1016/j.proeng.2013.05.118

183. Chen Q, Bruyneel A, Carr C, Czernuszka J. Trilayer scaffold with cardiosphere-derived cells for heart valve tissue engineering. *J Biomed Mater Res Part B Appl Biomater*. 2020;108(3):729-737. doi:10.1002/jbm.b.34427

184. Iftekhar S. Isolation of Fibrillar Elastin Gel (FEG) and its application in heart valve

tissue engineering. Published online 2020.

185. Gezmis H. The Influence of Collagen-Based Scaffolds on Cardiac Differentiation and Endothelial Growth. Published online 2023.

186. Yu X, Xia Z, Wang L, et al. Controlling the structural organization of regenerated bone by tailoring tissue engineering scaffold architecture. *J Mater Chem*. 2012;22(19):9721-9730. doi:10.1039/c2jm30332a

187. Perez-Puyana V, Jiménez-Rosado M, Romero A, Guerrero A. Crosslinking of hybrid scaffolds produced from collagen and chitosan. *Int J Biol Macromol*. 2019;139:262-269. doi:10.1016/j.ijbiomac.2019.07.198

188. Benjakul S, Thiansilakul Y, Visessanguan W, et al. Extraction and characterisation of pepsin-solubilised collagens from the skin of bigeye snapper (Priacanthus tayenus and Priacanthus macracanthus). *J Sci Food Agric*. 2010;90(1):132-138. doi:10.1002/jsfa.3795

189. Kittiphattanabawon P, Benjakul S, Visessanguan W, Nagai T, Tanaka M. Characterisation of acid-soluble collagen from skin and bone of bigeye snapper (Priacanthus tayenus). *Food Chem*. 2005;89(3):363-372. doi:10.1016/j.foodchem.2004.02.042

190. Chi CF, Cao ZH, Wang B, Hu FY, Li ZR, Zhang B. Antioxidant and functional properties of collagen hydrolysates from Spanish mackerel skin as influenced by average molecular weight. *Molecules*. 2014;19(8):11211-11230. doi:10.3390/molecules190811211

191. Vazquez-Portalatin N, Alfonso-Garcia A, Liu JC, Marcu L, Panitch A. Physical, Biomechanical, and Optical Characterization of Collagen and Elastin Blend Hydrogels. *Ann Biomed Eng*. 2020;48(12):2924-2935. doi:10.1007/s10439-020-02605-x

192. Harris JR, Soliakov A, Lewis RJ. In vitro fibrillogenesis of collagen type I in varying ionic and pH conditions. *Micron*. 2013;49:60-68. doi:10.1016/j.micron.2013.03.004

193. Asgari M, Latifi N, Heris HK, Vali H, Mongeau L. In vitro fibrillogenesis of tropocollagen type III in collagen type i affects its relative fibrillar topology and mechanics. *Sci Rep*. 2017;7(1):1-10. doi:10.1038/s41598-017-01476-y

194. Bozec L, Odlyha M. Thermal denaturation studies of collagen by microthermal analysis and atomic force microscopy. *Biophys J*. 2011;101(1):228-236. doi:10.1016/j.bpj.2011.04.033

195. Baselt DR, Revel JP, Baldeschwieler JD. Subfibrillar structure of type I collagen observed by atomic force microscopy. *Biophys J*. 1993;65(6):2644-2655. doi:10.1016/S0006-3495(93)81329-8

196. Bozec L, Van Der Heijden G, Horton M. Collagen fibrils: Nanoscale ropes. *Biophys J*. 2007;92(1):70-75. doi:10.1529/biophysj.106.085704

197. Borrego-González S, Rico-Llanos G, Becerra J, Díaz-Cuenca A, Visser R. Sponge-like processed D-periodic self-assembled atelocollagen supports bone formation in vivo. *Mater Sci Eng C*. 2021;120:111679. doi:10.1016/j.msec.2020.111679

198. Vulpe R, Le Cerf D, Dulong V, et al. Rheological study of in-situ crosslinkable hydrogels based on hyaluronanic acid, collagen and sericin. *Mater Sci Eng C*. 2016;69:388-397. doi:10.1016/j.msec.2016.07.003

199. Muller FL, Davidson JF. Rheology of Shear Thinning Polymer Solutions. *Ind Eng Chem Res*. 1994;33(10):2364-2367. doi:10.1021/ie00034a016

200. Suo H, Zhang J, Xu M, Wang L. Low-temperature 3D printing of collagen and chitosan composite for tissue engineering. *Mater Sci Eng C*. 2021;123:111963. doi:10.1016/j.msec.2021.111963

201. Lai G, Li Y, Li G. Effect of concentration and temperature on the rheological behavior

of collagen solution. *Int J Biol Macromol*. 2008;42(3):285-291. doi:10.1016/j.ijbiomac.2007.12.010

202. Stani C, Vaccari L, Mitri E, Birarda G. FTIR investigation of the secondary structure of type I collagen: New insight into the amide III band. *Spectrochim Acta - Part A Mol Biomol Spectrosc*. 2020;229. doi:10.1016/j.saa.2019.118006

203. Wang XH, Li DP, Wang WJ, et al. Crosslinked collagen/chitosan matrix for artificial livers. *Biomaterials*. 2003;24(19):3213-3220. doi:10.1016/S0142-9612(03)00170-4

204. Ji Y, Yang X, Ji Z, et al. DFT-Calculated IR Spectrum Amide I, II, and III Band Contributions of N-Methylacetamide Fine Components. *ACS Omega*. 2020;5(15):8572-8578. doi:10.1021/acsomega.9b04421

205. Belbachir K, Noreen R, Gouspillou G, Petibois C. Collagen types analysis and differentiation by FTIR spectroscopy. *Anal Bioanal Chem*. 2009;395(3):829-837. doi:10.1007/s00216-009-3019-y

206. Bonnier F, Rubin S, Ventéo L, et al. In-vitro analysis of normal and aneurismal human ascending aortic tissues using FT-IR microspectroscopy. *Biochim Biophys Acta - Biomembr*. 2006;1758(7):968-973. doi:10.1016/j.bbamem.2006.05.018

207. Cai S, Singh BR. Identification of β-turn and random coil amide III infrared bands for secondary structure estimation of proteins. *Biophys Chem*. 1999;80(1):7-20. doi:10.1016/S0301-4622(99)00060-5

208. Anastasiadis K, Eliades G. Dentine Conditioners: Effect on Collagen Probed By Amide-III Peak Analysis. *Dent Mater*. 2022;38:e5. doi:10.1016/j.dental.2021.12.038

209. De Guzzi Plepis AM, Goissis G, Das-Gupta DK. Dielectric and pyroelectric characterization of anionic and native collagen. *Polym Eng Sci*. 1996;36(24):2932-2938. doi:10.1002/pen.10694

210. Machado AAS, Martins VCA, Plepis AMG. Thermal and rheological behavior of

collagen: Chitosan blends. *J Therm Anal Calorim*. 2002;67(2):491-498. doi:10.1023/A:1013953316829

211. Lee YC, Chiang CC, Huang PY, et al. Evidence of preserved collagen in an Early Jurassic sauropodomorph dinosaur revealed by synchrotron FTIR microspectroscopy. *Nat Commun*. 2017;8. doi:10.1038/ncomms14220

212. Schmidt FN, Zimmermann EA, Campbell GM, et al. Assessment of collagen quality associated with non-enzymatic cross-links in human bone using Fourier-transform infrared imaging. *Bone*. 2017;97:243-251. doi:10.1016/j.bone.2017.01.015

213. Paşcalău V, Popescu V, Popescu GL, et al. Obtaining and characterizing alginate/k-carrageenan hydrogel cross-linked with adipic dihydrazide. *Adv Mater Sci Eng*. 2013;2013. doi:10.1155/2013/380716

214. Sinyayev VA, Toxeitova GA, Batyrbayeva AA, Sassykova LR, Azhigulova RN, Sakhipov YN. A comparative investigtion of the IR spectra of a carbohydrate series. *J Chem Technol Metall*. 2020;55(4):724-729.

215. Wu YC, Lee TM, Chiu KH, Shaw SY, Yang CY. A comparative study of the physical and mechanical properties of three natural corals based on the criteria for bone-tissue engineering scaffolds. *J Mater Sci Mater Med*. 2009;20(6):1273-1280. doi:10.1007/s10856-009-3695-3

216. Karageorgiou V, Kaplan D. Porosity of 3D biomaterial scaffolds and osteogenesis. *Biomaterials*. 2005;26(27):5474-5491. doi:10.1016/j.biomaterials.2005.02.002

217. Buttafoco L, Kolkman NG, Engbers-Buijtenhuijs P, et al. Electrospinning of collagen and elastin for tissue engineering applications. *Biomaterials*. 2006;27(5):724-734. doi:10.1016/j.biomaterials.2005.06.024

218. Zayas JF. Solubility of Proteins. In: *Functionality of Proteins in Food*. Springer, Berlin, Heidelberg; 1997:6-75. doi:10.1007/978-3-642-59116-7_2

219. Zhang Z, Ortiz O, Goyal R, Kohn J. Biodegradable Polymers. In: *Principles of Tissue Engineering: Fourth Edition*. Elsevier Inc.; 2013:441-473. doi:10.1016/B978-0-12-398358-9.00023-9

220. Conticello VP, Carpenter Desai HE. Elastins. In: *Polymer Science: A Comprehensive Reference, 10 Volume Set*. Vol 9. Elsevier; 2012:71-103. doi:10.1016/B978-0-444-53349-4.00248-X

221. Nasrollahzadeh M, Maham M, Nezafat Z, Shafiei N. Protein and polypeptide biopolymer chemistry. In: *Biopolymer-Based Metal Nanoparticle Chemistry for Sustainable Applications: Volume 1: Classification, Properties and Synthesis*. Elsevier; 2021:107-144. doi:10.1016/B978-0-12-822108-2.00005-3

222. Davis NR, Anwar RA. On the Mechanism of Formation of Desmosine and Isodesmosine Cross-Links of Elastin. *J Am Chem Soc*. 1970;92(12):3778-3782. doi:10.1021/ja00715a040

223. Farhat WA, Geutjes PJ. Artificial biomaterials for urological tissue engineering. In: *Biomaterials and Tissue Engineering in Urology*. Woodhead Publishing; 2009:243-254. doi:10.1533/9781845696375.3.243

224. Mirsanaye K, Golaraei A, Habach F, et al. Polar organization of collagen in human cardiac tissue revealed with polarimetric second-harmonic generation microscopy. *Biomed Opt Express*. 2019;10(10):5025. doi:10.1364/boe.10.005025

225. Yang J, Ding C, Tang L, et al. Novel Modification of Collagen: Realizing Desired Water Solubility and Thermostability in a Conflict-Free Way. *ACS Omega*. 2020;5(11):5772-5780. doi:10.1021/acsomega.9b03846

226. Morozova S, Muthukumar M. Electrostatic effects in collagen fibril formation. *J Chem Phys*. 2018;149(16). doi:10.1063/1.5036526

227. Kadler KE, Holmes DF, Trotter JA, Chapman JA. Review Artice: Collagen fibril

formation Karl. *Biochem J*. 1996;11:1-11.

228. Kadler KE. Fell Muir Lecture: Collagen fibril formation in vitro and in vivo. *Int J Exp Pathol*. 2017;98(1):4-16. doi:10.1111/iep.12224

229. Eyre DR, Paz MA, Gallop PM. Cross-linking in collagen and elastin. *Annu Rev Biochem*. 1983;VOL. 53(1):717-748. doi:10.1146/annurev.biochem.53.1.717

230. Gistelinck C, Witten PE, Huysseune A, et al. Loss of Type I Collagen Telopeptide Lysyl Hydroxylation Causes Musculoskeletal Abnormalities in a Zebrafish Model of Bruck Syndrome. *J Bone Miner Res*. 2016;31(11):1930-1942. doi:10.1002/jbmr.2977

231. Holmes DF, Lowe MP, Chapman JA. Vertebrate (chick) collagen fibrils formed in Vivo can exhibit a reversal in molecular polarity. *J Mol Biol*. 1994;235(1):80-83. doi:10.1016/S0022-2836(05)80016-6

232. Martin R, Farjanel J, Eichenberger D, et al. Liquid crystalline ordering of procollagen as a determinant of three-dimensional extracellular matrix architecture. *J Mol Biol*. 2000;301(1):11-17. doi:10.1006/jmbi.2000.3855

233. Gross J, Highberger JH, Schmitt FO. COLLAGEN STRUCTURES CONSIDERED AS STATES OF AGGREGATION OF A KINETIC UNIT. THE TROPOCOLLAGEN PARTICLE. *Proc Natl Acad Sci*. 1954;40(8):679-688. doi:10.1073/pnas.40.8.679

234. Bruns RR, Hulmes DJS, Therrien SF, Gross J. Procollagen segment-long-spacing crystallites: Their role in collagen fibrillogenesis. *Proc Natl Acad Sci U S A*. 1979;76(1):313-317. doi:10.1073/pnas.76.1.313

235. Hulmes DJ, Bruns RR, Gross J. On the state of aggregation of newly secreted procollagen. *Proc Natl Acad Sci U S A*. 1983;80(2):388-392. doi:10.1073/pnas.80.2.388

236. Zheng T, Tang P, Shen L, Bu H, Li G. Rheological behavior of collagen/chitosan

blended solutions. *J Appl Polym Sci*. 2021;138(34):50840. doi:10.1002/app.50840

237. Sionkowska A, Lewandowska K, Adamiak K. The influence of uv light on rheological properties of collagen extracted from silver carp skin. *Materials (Basel)*. 2020;13(19):1-10. doi:10.3390/ma13194453

238. Ma S, Zhu P, Wang M. Effects of konjac glucomannan on pasting and rheological properties of corn starch. *Food Hydrocoll*. 2019;89:234-240. doi:10.1016/j.foodhyd.2018.10.045

239. Usha R, Sreeram KJ, Rajaram A. Stabilization of collagen with EDC/NHS in the presence of l-lysine: A comprehensive study. *Colloids Surfaces B Biointerfaces*. 2012;90(1):83-90. doi:10.1016/j.colsurfb.2011.10.002

240. De Campos Vidal B, Mello MLS. Collagen type I amide I band infrared spectroscopy. *Micron*. 2011;42(3):283-289. doi:10.1016/j.micron.2010.09.010

241. Vidal CMP, Zhu W, Manohar S, et al. Collagen-collagen interactions mediated by plant-derived proanthocyanidins: A spectroscopic and atomic force microscopy study. *Acta Biomater*. 2016;41:110-118. doi:10.1016/j.actbio.2016.05.026

242. Bi X, Li G, Doty SB, Camacho NP. A novel method for determination of collagen orientation in cartilage by Fourier transform infrared imaging spectroscopy (FT-IRIS). *Osteoarthr Cartil*. 2005;13(12):1050-1058. doi:10.1016/j.joca.2005.07.008

243. Jackson M, Choo LP in., Watson PH, Halliday WC, Mantsch HH. Beware of connective tissue proteins: Assignment and implications of collagen absorptions in infrared spectra of human tissues. *BBA - Mol Basis Dis*. 1995;1270(1):1-6. doi:10.1016/0925-4439(94)00056-V

244. Paschalis EP, Verdelis K, Doty SB, Boskey AL, Mendelsohn R, Yamauchi M. Spectroscopic characterization of collagen cross-links in bone. *J Bone Miner Res*. 2001;16(10):1821-1828. doi:10.1359/jbmr.2001.16.10.1821

245. Arif MMA, Fauzi MB, Nordin A, Hiraoka Y, Tabata Y, Yunus MHM. Fabrication of bio-based gelatin sponge for potential use as a functional acellular skin substitute. *Polymers (Basel)*. 2020;12(11):1-19. doi:10.3390/polym12112678

246. Burdick JA, Chung C, Jia X, Randolph MA, Langer R. Controlled degradation and mechanical behavior of photopolymerized hyaluronic acid networks. *Biomacromolecules*. 2005;6(1):386-391. doi:10.1021/bm049508a

247. Deville S, Saiz E, Tomsia AP. Freeze casting of hydroxyapatite scaffolds for bone tissue engineering. *Biomaterials*. 2006;27(32):5480-5489. doi:10.1016/j.biomaterials.2006.06.028

248. Deville S, Saiz E, Nalla RK, Tomsia AP. Freezing as a path to build complex composites. *Science (80-)*. 2006;311(5760):515-518. doi:10.1126/science.1120937

249. Mandal BB, Kundu SC. Cell proliferation and migration in silk fibroin 3D scaffolds. *Biomaterials*. 2009;30(15):2956-2965. doi:10.1016/j.biomaterials.2009.02.006

250. Zhang J, Zhou A, Deng A, et al. Pore architecture and cell viability on freeze dried 3D recombinant human collagen-peptide (RHC)-chitosan scaffolds. *Mater Sci Eng C*. 2015;49:174-182. doi:10.1016/j.msec.2014.12.076

251. Hunt JD. Pattern formation in solidification. *Mater Sci Technol*. 1999;15(1):9-14. doi:10.1179/026708399773002755

252. Lee YI, Lee SG, Kim J, Choi S, Jung I, Lee JH. Proteoglycan combined with hyaluronic acid and hydrolyzed collagen restores the skin barrier in mild atopic dermatitis and dry, eczema-prone skin: A pilot study. *Int J Mol Sci*. 2021;22(19):10189. doi:10.3390/ijms221910189

253. Liu L, Liu D, Wang M, Du G, Chen J. Preparation and characterization of sponge-like composites by cross-linking hyaluronic acid and carboxymethylcellulose sodium with adipic dihydrazide. *Eur Polym J*. 2007;43(6):2672-2681.

doi:10.1016/j.eurpolymj.2007.02.045

254. Grover CN, Cameron RE, Best SM. Investigating the morphological, mechanical and degradation properties of scaffolds comprising collagen, gelatin and elastin for use in soft tissue engineering. *J Mech Behav Biomed Mater*. 2012;10:62-74. doi:10.1016/j.jmbbm.2012.02.028

255. Zheng L, Lu HQ, Fan HS, Zhang XD. Reinforcement and chemical cross-linking in collagen-based scaffolds in cartilage tissue engineering: A comparative study. *Iran Polym J (English Ed*. 2013;22(11):833-842. doi:10.1007/s13726-013-0182-y

256. Takallu S, Mirzaei E, Azadi A, Karimizade A, Tavakol S. Plate-shape carbonated hydroxyapatite/collagen nanocomposite hydrogel via in situ mineralization of hydroxyapatite concurrent with gelation of collagen at pH = 7.4 and 37°C. *J Biomed Mater Res - Part B Appl Biomater*. 2019;107(6):1920-1929. doi:10.1002/jbm.b.34284

257. Lai VK, Nedrelow DS, Lake SP, et al. Swelling of Collagen-Hyaluronic Acid Co-Gels: An In Vitro Residual Stress Model. *Ann Biomed Eng*. 2016;44(10):2984-2993. doi:10.1007/s10439-016-1636-0

258. Tonndorf R, Gossla E, Aibibu D, Lindner M, Gelinsky M, Cherif C. Wet spinning and riboflavin crosslinking of collagen type I/III filaments. *Biomed Mater*. 2019;14(1):015007. doi:10.1088/1748-605X/aaebda

259. Monfregola L, Bugatti V, Amodeo P, De Luca S, Vittoria V. Physical and water sorption properties of chemically modified pectin with an environmentally friendly process. *Biomacromolecules*. 2011;12(6):2311-2318. doi:10.1021/bm200376c

260. Grover CN, Gwynne JH, Pugh N, et al. Crosslinking and composition influence the surface properties, mechanical stiffness and cell reactivity of collagen-based films. *Acta Biomater*. 2012;8(8):3080-3090. doi:10.1016/j.actbio.2012.05.006

261. Nair M, Best SM, Cameron RE. Crosslinking collagen constructs: Achieving cellular

selectivity through modifications of physical and chemical properties. *Appl Sci*. 2020;10(19):1-14. doi:10.3390/app10196911

262. Mohammadi F, Samani SM, Tanideh N, Ahmadi F. Hybrid scaffolds of hyaluronic acid and collagen loaded with prednisolone: An interesting system for osteoarthritis. *Adv Pharm Bull*. 2018;8(1):11-19. doi:10.15171/apb.2018.002

263. Zhang L, Xiao Y, Jiang B, Fan H, Zhang X. Effect of adipic dihydrazide modification on the performance of collagen/hyaluronic acid scaffold. *J Biomed Mater Res - Part B Appl Biomater*. 2010;92(2):307-316. doi:10.1002/jbm.b.31516

264. Freyman TM, Yannas I V, Pek YS, Yokoo R, Gibson LJ. Micromechanics of fibroblast contraction of a collagen-GAG matrix. *Exp Cell Res*. 2001;269(1):140-153. doi:10.1006/excr.2001.5302

265. Ross-Murphy SB. Rheological characterisation of gels. *J Texture Stud*. 1995;26(4):391-400. doi:10.1111/j.1745-4603.1995.tb00979.x

266. Chen Q. Collagen-Based Scaffolds for Heart Valve Tissue Engineering. Published online 2013.

267. Hsieh TT, Tiu C, Simon GP, Yu Wu R. Rheology and miscibility of thermotropic liquid crystalline polymer blends. *J Nonnewton Fluid Mech*. 1999;86(1-2):15-35. doi:10.1016/S0377-0257(98)00200-6

268. Castro APG, Laity P, Shariatzadeh M, Wittkowske C, Holland C, Lacroix D. Combined numerical and experimental biomechanical characterization of soft collagen hydrogel substrate. *J Mater Sci Mater Med*. 2016;27(4):1-9. doi:10.1007/s10856-016-5688-3

269. Scheffler M, Colombo P. *Cellular Ceramics: Structure, Manufacturing, Properties and Applications*. Wiley-VCH; 2006. doi:10.1002/3527606696

270. Harley BA, Leung JH, Silva ECCM, Gibson LJ. Mechanical characterization of

collagen-glycosaminoglycan scaffolds. *Acta Biomater*. 2007;3(4):463-474. doi:10.1016/j.actbio.2006.12.009

271. Rostiashvili VG, Vilgis TA. Statistical Thermodynamics of Polymeric Networks. In: *Encyclopedia of Polymeric Nanomaterials*. ; 2014:1-18. doi:10.1007/978-3-642-36199-9_308-1

272. Yu YJ, Hearon K, Wilson TS, Maitland DJ. The effect of moisture absorption on the physical properties of polyurethane shape memory polymer foams. *Smart Mater Struct*. 2011;20(8). doi:10.1088/0964-1726/20/8/085010

273. Ansari IA, Gupta GA, Ramkumar J, Kar KK. Fly ash-mixed polymeric media for abrasive flow machining process. In: *Handbook of Fly Ash*. ; 2021:681-713. doi:10.1016/B978-0-12-817686-3.00003-7

274. Böhning M, Frasca D, Schulze D, Schartel B. Multilayer graphene/elastomer nanocomposites. In: *Carbon-Based Nanofillers and Their Rubber Nanocomposites: Fundamentals and Applications*. Elsevier; 2019:139-200. doi:10.1016/B978-0-12-817342-8.00006-8

275. Hong GW, Moon HJ, Lee HM, Kim DK, Lee KH. Deformation characteristics of hydrogel products based on cross-linked hyaluronic acid. *J Cosmet Dermatol*. Published online 2023. doi:10.1111/jocd.15801

276. Ramli H, Zainal NFA, Hess M, Chan CH. Basic principle and good practices of rheology for polymers for teachers and beginners. *Chem Teach Int*. 2022;4(4):307-326. doi:10.1515/cti-2022-0010

277. Jóźwiak B, Orczykowska M, Dziubiński M. Fractional generalizations of Maxwell and Kelvin-Voigt models for biopolymer characterization. *PLoS One*. 2015;10(11). doi:10.1371/journal.pone.0143090

278. Santinath Singh S, Aswal VK, Bohidar HB. Internal structures of agar-gelatin co-

hydrogels by light scattering, small-angle neutron scattering and rheology. *Eur Phys J E Soft Matter*. 2011;34(6):1-9. doi:10.1140/epje/i2011-11062-3

279. Hössinger-Kalteis A, Reiter M, Jerabek M, Major Z. Overview and comparison of modelling methods for foams. *J Cell Plast*. 2021;57(6):951-1001. doi:10.1177/0021955X20966329

280. Gibson LJ, Ashby MF. *Cellular Solids : Structure and Properties*. Second edi.; 1997.

281. Timoshenko S, Goodier JN. *Theory of Elasticity*. 3rd ed. McGraw-Hill; 1970.

282. Peppas NA, Merrill EW. Crosslinked poly(vinyl alcohol) hydrogels as swollen elastic networks. *J Appl Polym Sci*. 1977;21(7):1763-1770. doi:10.1002/app.1977.070210704

283. Chen S, Zhang Q, Nakamoto T, Kawazoe N, Chen G. Highly active porous scaffolds of collagen and hyaluronic acid prepared by suppression of polyion complex formation. *J Mater Chem B*. 2014;2(34):5612-5619. doi:10.1039/c4tb00780h

284. Lawrence BJ, Madihally S V. Cell colonization in degradable 3D porous matrices. *Cell Adh Migr*. 2008;2(1):9-16. doi:10.4161/cam.2.1.5884

285. Joukhdar H, Seifert A, Jüngst T, Groll J, Lord MS, Rnjak-Kovacina J. Ice Templating Soft Matter: Fundamental Principles and Fabrication Approaches to Tailor Pore Structure and Morphology and Their Biomedical Applications. *Adv Mater*. 2021;33(34). doi:10.1002/adma.202100091

286. Cheng LX, Xie MH, Qiao WH, et al. Generation and characterization of cardiac valve endothelial-like cells from human pluripotent stem cells. *Commun Biol*. 2021;4(1). doi:10.1038/s42003-021-02571-7

287. Butcher JT, Nerem RM. Valvular endothelial cells and the mechanoregulation of valvular pathology. *Philos Trans R Soc B Biol Sci*. 2007;362(1484):1445-1457. doi:10.1098/rstb.2007.2127

288. Wilson HK, Canfield SG, Shusta E V, Palecek SP. Concise Review: Tissue-Specific

Microvascular Endothelial Cells Derived From Human Pluripotent Stem Cells. *Stem Cells*. 2014;32(12):3037-3045. doi:10.1002/stem.1797

289. Teebken OE, Haverich A. Tissue Engineering of Small Diameter Vascular Grafts. *Eur J Vasc Endovasc Surg*. 2002;23(6):475-485. doi:https://doi.org/10.1053/ejvs.2002.1654

290. Zeltinger J, Sherwood JK, Graham DA, Müeller R, Griffith LG. Effect of Pore Size and Void Fraction on Cellular Adhesion, Proliferation, and Matrix Deposition. *Tissue Eng*. 2001;7(5):557-572. doi:10.1089/107632701753213183

291. Salem AK, Stevens R, Pearson RG, et al. Interactions of 3T3 fibroblasts and endothelial cells with defined pore features. *J Biomed Mater Res*. 2002;61(2):212-217. doi:10.1002/jbm.10195

292. Cho EH, Yang Y Il, Mun C-W, Kim JK. Tissue-engineered semi-microporous segmented polyetherurethane vascular prostheses. *J Biomater Sci Polym Ed*. 2005;16(6):775-790. doi:10.1163/1568562053992441

293. Yannas I V., Lee E, Orgill DP, Skrabut EM, Murphy GF. Synthesis and characterization of a model extracellular matrix that induces partial regeneration of adult mammalian skin. *Proc Natl Acad Sci U S A*. 1989;86(3):933-937. doi:10.1073/pnas.86.3.933

294. Tufan Y, Öztatlı H, Doganay D, et al. Multifunctional Silk Fibroin/Carbon Nanofiber Scaffolds for In Vitro Cardiomyogenic Differentiation of Induced Pluripotent Stem Cells and Energy Harvesting from Simulated Cardiac Motion. *ACS Appl Mater Interfaces*. 2023;15(36):42271-42283. doi:10.1021/acsami.3c08601

295. Khayyatan F, Nemati S, Kiani S, Hojjati Emami S, Baharvand H. Behaviour of human induced pluripotent stem cell-derived neural progenitors on collagen scaffolds varied in freezing temperature and laminin concentration. *Cell J*. 2014;16(1):53-62.

296. Bružauskaitė I, Bironaitė D, Bagdonas E, Bernotienė E. Scaffolds and cells for tissue regeneration: different scaffold pore sizes—different cell effects. *Cytotechnology*. 2016;68(3):355-369. doi:10.1007/s10616-015-9895-4

297. Xu Y, Šavija B. 3D auxetic cementitious-polymeric composite structure with compressive strain-hardening behavior. *Eng Struct*. 2023;294. doi:10.1016/j.engstruct.2023.116734

298. Emori K, Fushimi S, Miura T, Yonezu A. FEM simulation of polymeric foam with random pore structure: Uniaxial compression with loading rate effect. *Polym Test*. 2020;82. doi:10.1016/j.polymertesting.2019.106303

299. Xu D, Craig SL. Strain hardening and strain softening of reversibly cross-linked supramolecular polymer networks. *Macromolecules*. 2011;44(18):7478-7488. doi:10.1021/ma201386t

300. Liao T, Yang X, Zhao X, Tang Y, Jiang Z, Men Y. Gaussian and Non-Gaussian Distributions of Fracture Properties in Tensile Stretching of High-Density Polyethylene. *Macromolecules*. 2021;54(18):8860-8874. doi:10.1021/acs.macromol.1c00944

301. Zhao JH, Xie ZL, Zhong T, et al. Strain rate effects on the mechanical behavior of porous titanium with different pore sizes. *Mater Sci Eng A*. 2021;821. doi:10.1016/j.msea.2021.141593

302. Robi K, Jakob N, Matevz K, Matjaz V. The Physiology of Sports Injuries and Repair Processes. In: *Current Issues in Sports and Exercise Medicine*. IntechOpen; 2013. doi:10.5772/54234

303. Pissis P, Kyritsis A. Hydration studies in polymer hydrogels. *J Polym Sci Part B Polym Phys*. 2013;51(3):159-175. doi:10.1002/polb.23220

304. Huang Y, Li X, Lu Z, et al. Nanofiber-reinforced bulk hydrogel: Preparation and

structural, mechanical, and biological properties. *J Mater Chem B*. 2020;8(42):9794-9803. doi:10.1039/d0tb01948h

305. Suchý T, Šupová M, Bartoš M, et al. Dry versus hydrated collagen scaffolds: are dry states representative of hydrated states? *J Mater Sci Mater Med*. 2018;29(2):1-14. doi:10.1007/s10856-017-6024-2

306. Varley MC, Neelakantan S, Clyne TW, Dean J, Brooks RA, Markaki AE. Cell structure, stiffness and permeability of freeze-dried collagen scaffolds in dry and hydrated states. *Acta Biomater*. 2016;33:166-175. doi:10.1016/j.actbio.2016.01.041

307. Wang X, Li Q, Hu X, et al. Fabrication and characterization of poly(l-lactide-co-glycolide) knitted mesh-reinforced collagen-chitosan hybrid scaffolds for dermal tissue engineering. *J Mech Behav Biomed Mater*. 2012;8:204-215. doi:10.1016/j.jmbbm.2012.01.001

308. Treloar LRG, Montgomery DJ. The Physics of Rubber Elasticity. *Phys Today*. 1959;12(2):32-34. doi:10.1063/1.3060678

309. Xu S, Zhou Z, Liu Z, Sharma P. Concurrent stiffening and softening in hydrogels under dehydration. *Sci Adv*. 2023;9(1):1-11. doi:10.1126/sciadv.ade3240

310. Li Z, Liu Z, Ng TY, Sharma P. The effect of water content on the elastic modulus and fracture energy of hydrogel. *Extrem Mech Lett*. 2020;35:100617. doi:10.1016/j.eml.2019.100617

311. Gorczyca G, Tylingo R, Szweda P, Augustin E, Sadowska M, Milewski S. Preparation and characterization of genipin cross-linked porous chitosan-collagen-gelatin scaffolds using chitosan-CO2 solution. *Carbohydr Polym*. 2014;102(1):901-911. doi:10.1016/j.carbpol.2013.10.060

312. Wang H, Fu Y, Su M, Hao H. Effect of structure design on compressive properties and energy absorption behavior of ordered porous aluminum prepared by rapid casting.

Mater Des. 2019;167:107631. doi:10.1016/j.matdes.2019.107631

313. Pugliese E, Sallent I, Ribeiro S, et al. Development of three-layer collagen scaffolds to spatially direct tissue-specific cell differentiation for enthesis repair. *Mater Today Bio*. 2023;19:100584. doi:10.1016/j.mtbio.2023.100584

314. Cao R, Xu Y, Xu Y, et al. Development of Tri-Layered Biomimetic Atelocollagen Scaffolds with Interfaces for Osteochondral Tissue Engineering. *Adv Healthc Mater*. 2022;11(11). doi:10.1002/adhm.202101643

315. Li RL, Russ J, Paschalides C, et al. Mechanical considerations for polymeric heart valve development: Biomechanics, materials, design and manufacturing. *Biomaterials*. 2019;225:119493. doi:10.1016/j.biomaterials.2019.119493

316. Masoumi N, Annabi N, Assmann A, et al. Tri-layered elastomeric scaffolds for engineering heart valve leaflets. *Biomaterials*. 2014;35(27):7774-7785. doi:10.1016/j.biomaterials.2014.04.039

317. Reis PNB, Ferreira JAM, Antunes F V., Richardson MOW. Effect of interlayer delamination on mechanical behavior of carbon/epoxy laminates. *J Compos Mater*. 2009;43(22):2609-2621. doi:10.1177/0021998309344649

318. Boersma QD, Douma LANR, Bertotti G, Barnhoorn A. Mechanical controls on horizontal stresses and fracture behaviour in layered rocks: A numerical sensitivity analysis. *J Struct Geol*. 2020;130:103907. doi:10.1016/j.jsg.2019.103907

319. Caruso I, Yin K, Divakar P, Wegst UGK. Tensile properties of freeze-cast collagen scaffolds: How processing conditions affect structure and performance in the dry and fully hydrated states. *J Mech Behav Biomed Mater*. 2023;144(May):105897. doi:10.1016/j.jmbbm.2023.105897

320. Carter P, Rahman SM, Bhattarai N. Facile fabrication of aloe vera containing PCL nanofibers for barrier membrane application. *J Biomater Sci Polym Ed*.

2016;27(7):692-708. doi:10.1080/09205063.2016.1152857

321. Isfandiary A, Widiyanti P, Hikmawati D. Composite of chitosan-collagen-aloe vera for scaffolds application on skin tissue. *J Biomimetics, Biomater Biomed Eng*. 2017;32:82-89. doi:10.4028/www.scientific.net/JBBBE.32.82

322. López Angulo DE, do Amaral Sobral PJ. Characterization of gelatin/chitosan scaffold blended with aloe vera and snail mucus for biomedical purpose. *Int J Biol Macromol*. 2016;92:645-653. doi:10.1016/j.ijbiomac.2016.07.029

323. Soletti L, Hong Y, Guan J, et al. A bilayered elastomeric scaffold for tissue engineering of small diameter vascular grafts. *Acta Biomater*. 2010;6(1):110-122. doi:10.1016/j.actbio.2009.06.026

324. Hou J, Chen L, Zhou M, et al. Multi-layered polyamide/collagen scaffolds with topical sustained release of N-Acetylcysteine for promoting wound healing. *Int J Nanomedicine*. 2020;15:1349-1361. doi:10.2147/IJN.S232190

325. Garcia-Orue I, Gainza G, Gutierrez FB, et al. Novel nanofibrous dressings containing rhEGF and Aloe vera for wound healing applications. *Int J Pharm*. 2017;523(2):556-566. doi:10.1016/j.ijpharm.2016.11.006

326. Scărlătescu DD, Modrea A, Stanciu MD. Three-point Bend Test to Determine the Mechanical Behavior of the Tubes Used in Water Supply Networks. In: *Procedia Manufacturing*. Vol 32. Elsevier B.V.; 2019:179-186. doi:10.1016/j.promfg.2019.02.200

327. Jeon G, Ha D, Park Y, Jeong C. Three-Point Bending Properties of Hybrid Multi-Materials Using Adhesive Bonding Dependent on Strength Difference between Steel and Aluminum. *Materials (Basel)*. 2022;15(9). doi:10.3390/ma15093328

328. Geltmacher AB, Koss DA, Matic P, Stout MG. A modeling study of the effect of stress state on void linking during ductile fracture. *Acta Mater*. 1996;44(6):2201-2210.

doi:10.1016/1359-6454(95)00366-5

329. Pelech AN. Murmurs. In: *Nelson Pediatric Symptom-Based Diagnosis*. Elsevier; 2017:116-143.e2. doi:10.1016/B978-0-323-39956-2.00008-X

330. Calvert JW, Lefer DJ. Chapter 6 - Overview of Cardiac Muscle Physiology. In: Hill JA, Olson ENBT-M, eds. Academic Press; 2012:57-66. doi:https://doi.org/10.1016/B978-0-12-381510-1.00006-5

331. Chamis CC. Analysis of the Three-Point-Bend Test for Materials With Unequal Tension and Compression Properties. *SPI Reinf Plast Compos Inst Annu Conf Proc*. 1974;(March).

332. Hazwani F, Todo M. Deformation mechanism of porous composite sandwich beam for orthopaedical application under three-point bending. *Compos Struct*. 2022;281:114983. doi:https://doi.org/10.1016/j.compstruct.2021.114983

333. Brazile B, Wang B, Wang G, et al. On the bending properties of porcine mitral, tricuspid, aortic, and pulmonary valve leaflets. *J Long Term Eff Med Implants*. 2015;25(1-2):41-53. doi:10.1615/JLongTermEffMedImplants.2015011741

334. Lam TV. The Mechanical Properties of Native Porcine Aortic and Pulmonary Heart Valve Leaflets. Published online 2004:200.

335. Crawford PT, Bordoni B. *Anatomy, Thorax, Aortic Valve*. StatPearls Publishing; 2021. Accessed October 15, 2024. https://www.ncbi.nlm.nih.gov/books/NBK559384/

336. Haugh MG, Murphy CM, O'Brien FJ. Novel freeze-drying methods to produce a range of collagen- glycosaminoglycan scaffolds with tailored mean pore sizes. *Tissue Eng - Part C Methods*. 2010;16(5):887-894. doi:10.1089/ten.tec.2009.0422

337. Tierney CM, Haugh MG, Liedl J, Mulcahy F, Hayes B, O'Brien FJ. The effects of collagen concentration and crosslink density on the biological, structural and mechanical properties of collagen-GAG scaffolds for bone tissue engineering. *J Mech*

Behav Biomed Mater. 2009;2(2):202-209. doi:https://doi.org/10.1016/j.jmbbm.2008.08.007

338. Liu T, Shi L, Gu Z, Dan W, Dan N. A novel combined polyphenol-aldehyde crosslinking of collagen film—Applications in biomedical materials. *Int J Biol Macromol*. 2017;101:889-895. doi:10.1016/j.ijbiomac.2017.03.166

339. Hu Y, Liu L, Gu Z, Dan W, Dan N, Yu X. Modification of collagen with a natural derived cross-linker, alginate dialdehyde. *Carbohydr Polym*. 2014;102(1):324-332. doi:10.1016/j.carbpol.2013.11.050

340. Yang C, Dan N, You W, et al. Modification of collagen-chitosan membrane by oxidation sodium alginate and in vivo/ in vitro evaluation for wound dressing application. *Int J Polym Anal Charact*. 2019;24(7):619-629. doi:10.1080/1023666X.2019.1648637

341. Du T, Chen Z, Li H, et al. Modification of collagen-chitosan matrix by the natural crosslinker alginate dialdehyde. *Int J Biol Macromol*. 2016;82:580-588. doi:10.1016/j.ijbiomac.2015.10.039

342. Han SB, Kim JK, Lee G, Kim DH. Mechanical Properties of Materials for Stem Cell Differentiation. *Adv Biosyst*. 2020;4(11). doi:10.1002/adbi.202000247